

Photochemical Activation of Chlorine and Bromine from Iron-doped Saline Media

DISSERTATION

zur Erlangung des Doktorgrades

Dr. rer. nat.

an der Fakultät für Biologie, Chemie und Geowissenschaften
der Universität Bayreuth

vorgelegt von

Julian Daniel Wittmer

geboren am 17.01.1987 in Heidelberg

Bayreuth, Oktober 2015

Die vorliegende Arbeit wurde in der Zeit von Dezember 2012 bis Oktober 2015 in Bayreuth an der Forschungsstelle für Atmosphärische Chemie unter Betreuung von Herrn Professor Dr. Cornelius Zetzsch angefertigt.

Vollständiger Abdruck der von der Fakultät für Biologie, Chemie und Geowissenschaften der Universität Bayreuth genehmigten Dissertation zur Erlangung des akademischen Grades eines Doktors der Naturwissenschaften (Dr. rer. nat.)

Disseration eingereicht am: 14.10.2015

Zulassung durch das Leitungsgremium: 21.10.2015

Wissenschaftliches Kolloquium: 04.02.2016

Amtierender Direktor: Prof. Dr. Stefan Schuster

Prüfungsausschuss:

Prof. Dr. Cornelius Zetzsch (Erstgutachter)

Prof. Dr. Frank Keppler (Zweitgutachter)

Prof. Dr. Christoph Thomas (Vorsitz)

Prof. Dr. Andreas Held (Drittgutachter)

“Do or do not.

There is no try.”

Frank Oznowicz

Abstract

The multifaceted role of halogen chemistry in the troposphere gained increasing attention in the last two decades. In particular, the interaction of Reactive Halogen Species (RHS) with ozone (O_3) and nitrogen oxide (NO_x) cycles (producing particulate matter and O_3), as well as the consumption of methane (CH_4) and volatile organic compounds by chlorine atoms (Cl) in competition with OH radicals, or the initiation of sudden O_3 depletions by bromine (Br) atoms, are of major interest in atmospheric research. An important issue is the exploration and quantification of RHS sources and sinks, considering homogeneous and heterogeneous processes. The main focus of this work is the heterogeneous, photochemical formation of atomic Cl and Br in the presence of iron-doped saline media at various salt and gas-phase compositions. A Teflon smog chamber was employed to expose the samples to simulated sunlight under controlled conditions (air composition, temperature, relative humidity). The production of the radicals Cl, Br and OH was indirectly quantified by the radical clock method, monitoring the consumption of a test mixture of hydrocarbons with known rate constants for the reactions with these radicals.

In a first series of experiments, laboratory-modeled salt pans were spread on a Teflon sheet and irradiated in the Teflon chamber in a zero-air environment (<2 ppb NO_x , <1 ppb O_3 and <100 ppb CH_4) at 55–60 % relative humidity and 20°C. A fraction of 0.5 wt% of iron(III) chloride hexahydrate ($FeCl_3 \cdot 6H_2O$) in sodium chloride (NaCl) revealed a photochemical effect of iron by enhancing the production of atomic Cl from $\sim 4 \times 10^{10}$ atoms $cm^{-3} h^{-1}$ for pure NaCl to $\sim 50 \times 10^{10}$ atoms $cm^{-3} h^{-1}$ for the iron doped samples in the first hour of irradiation. This significant increase can be explained by the photolysis of Fe^{III} -Cl complexes, thus reducing Fe^{III} to Fe^{II} and forming Cl radicals (Cl^{\bullet}). The recombination of Cl^{\bullet} radicals leads to degassing of Cl_2 from the quasi-liquid layer of the humidified salt, and gas-phase photolysis forms the detected atoms. The iron-induced activation adds to the known activation processes by NO_x and O_3 that are responsible for the Cl production in the blank (iron-free) experiment. When 0.5 wt % NaBr were present in the salts, the Br source significantly increased from $\sim 3 \times 10^{10}$ atoms $cm^{-3} h^{-1}$ (iron-free blank) to $\sim 30 \times 10^{10}$ atoms $cm^{-3} h^{-1}$ (2 wt % $FeCl_3 \cdot 6H_2O$). The presence of sulfate, oxalate and catechol in the salt mixtures led to an inhibition of the halogen formation because of competing complexation of Fe^{III} and a scavenging of Cl^{\bullet} and OH^{\bullet} by sulfate already in the aqueous phase.

A second series of experiments was conducted with aerosol in order to transfer the rather local phenomena of iron-containing salt pans to the potentially more relevant effect of iron on sea-spray aerosol in the troposphere. Artificial seawater solutions, containing typical inorganic anions (Cl^- , Br^- , SO_4^{2-} , Na^+ , K^+ , Ca^{2+} , Mg^{2+}), were doped with Fe^{III} , nebulized and irradiated. The aerosol experiments allowed to link the halogen production with the active surface area. The observed Cl productions significantly increased with the amount of Fe^{III} added to the stock solution, whereas the production was below the detection limit for the iron-free run in zero air. The molar Fe^{III}/Cl^- stock ratios of 0.01, 0.02 and 0.08 resulted in Cl production rates of 0.7, 1.4 and 6.6×10^{21} atoms $cm^{-3} h^{-1}$, respectively. Adjusting the pH of the $Fe^{III}/Cl^- = 0.01$ sample from ~ 4 to ~ 2.2 enhanced the Cl production by almost an order of magnitude. This can be explained by the speciation properties of the iron complexes, which were evaluated by employing the pH-

REdox-EQuilibrium (PHREEQC) software for equilibrium modeling. Calculations for high ionic strengths demonstrated the dominant presence of $\text{Fe}^{\text{III}}\text{-Cl}$ complexes in the acidic pH range below 4.5 and the formation of $\text{Fe}^{\text{III}}\text{-hydroxy}$ complexes at higher pH. The effects of the atmospheric pollutants NO_x , O_3 and SO_2 were investigated in additional experiments. For $\text{Fe}^{\text{III}}/\text{Cl}^- = 0.08$, the presence of ~ 20 ppb NO_2 and ~ 630 ppb O_3 increased the Cl production to $>16 \times 10^{21}$ atoms $\text{cm}^{-3} \text{h}^{-1}$ and $>18 \times 10^{21}$ atoms $\text{cm}^{-3} \text{h}^{-1}$, respectively. The enhancement is caused by additional activation mechanisms, aerosol acidification by NO_x and interactions with the photo-Fenton cycle. SO_2 slightly inhibited the Cl formation due to complex formation and radical scavenging in the aqueous phase. Linking the observed Cl production rate to the estimated fraction of active Fe indicated the catalytic effect of iron as well as additional activation mechanisms. Moreover, the aerosol particles were sampled by an impactor and analyzed by a scanning-electron-microscope with an energy-dispersive X-ray detector (SEM-EDX), demonstrating the presence of an active $\text{Fe}^{\text{III}}\text{-Cl}$ salt layer that covers the aerosol particles.

The third series of experiments dealt with the behavior of solid iron oxide (Fe_2O_3) embedded in artificial sea salt aerosol or exposed to gaseous HCl. The Cl production of Fe_2O_3 in non-acidified sea salt strongly remained below the detection limit. Adjusting the pH to 2.6–1.9 led to rates of $(1\text{--}10) \times 10^{21}$ Cl atoms $\text{cm}^{-2} \text{h}^{-1}$ and demonstrated the dependence of produced Cl on the amount of dissolved iron in the liquid phase (and thus on the pH). The high estimated fraction of active iron (600–2000 %) indicated an efficient, rapid recycling process of the involved iron. Multiple freezing and thawing of the non-acidified Fe_2O_3 sample did not lead to significant production rates. In the absence of salt and presence of gaseous HCl, an efficient Cl formation on pure Fe_2O_3 aerosol was observed. HCl is absorbed and photochemically activated to produce atomic Cl in the gas phase. The measurements were compared with iron-free experiments, using silica (SiO_2) aerosol particles as an UV transparent blank and HCl in zero-air, to distinguish the known heterogeneous and homogeneous background productions from the iron-induced Cl production. The Cl production increased with the injected amount of HCl and was observed to range from 0.8×10^{21} atoms $\text{cm}^{-2} \text{h}^{-1}$ for ~ 40 ppb of HCl to $>40 \times 10^{21}$ atoms $\text{cm}^{-2} \text{h}^{-1}$ for ~ 340 ppb of HCl.

To assess the environmental significance of the measurements, the limitations of transferring the smog chamber experiments to the natural environments have to be considered for every study. For instance, the salt pan study can only qualitatively be applied on natural, rather local, occurrences such as the Australian salt lakes or the Dead Sea (Israel), where the iron-induced halogen release may play a significant role. Though, the role of Fe^{III} for the global Cl production from sea-salt aerosol is probably negligible, considering the low natural molar $\text{Fe}^{\text{III}}/\text{Cl}^-$ ratio and the high aerosol surface area to chamber volume ratio in the smog chamber. The Fe_2O_3 experiments indicate that iron-induced Cl formation may be important for mineral dust and combustion aerosol particles in marine environments and in the presence of gaseous HCl.

Zusammenfassung

Die vielfältige Rolle der troposphärischen Halogenchemie erfuhr in den letzten zwei Jahrzehnten ein steigendes Interesse, insbesondere die Wechselwirkung von reaktiven Halogenspezies (RHS) mit Ozon- (O_3) und Stickoxid- (NO_x) Kreisläufen (wobei O_3 und Partikel produziert werden), der Verbrauch von Methan (CH_4) und volatilen organischen Verbindungen durch Chloratome (Cl) in Konkurrenz zum Verbrauch durch OH Radikale, oder der Anstoß plötzlicher O_3 Abbauereignisse durch Bromatome (Br). Wichtige Aspekte sind die Erforschung und Quantifizierung von RHS-Quellen und -Senken unter Berücksichtigung homogener und heterogener Prozesse. Die vorliegende Arbeit konzentriert sich hauptsächlich auf die heterogene, photochemische Bildung von atomarem Cl und Br in Gegenwart von salz- und eisenhaltigen Medien unterschiedlicher Zusammensetzung. Die Proben wurden in einer Teflonkammer unter kontrollierten Bedingungen (Luftzusammensetzung, Temperatur, relative Feuchte) simuliertem Sonnenlicht ausgesetzt. Die Produktion von Cl- und Br-Atomen und OH Radikalen wurde anhand des Abbaus einer Testmischung aus Kohlenwasserstoffen, indirekt quantifiziert („Radical Clock“).

In einer ersten Reihe von Experimenten wurden synthetisch hergestellte Salzpflanzen auf einer Teflonfolie innerhalb der Teflonkammer verteilt und unter Nullluftbedingungen (<2 ppb NO_x , <1 ppb O_3 and <100 ppb CH_4) bei 55-60 % relativer Feuchte und einer Temperatur von $20^\circ C$ bestrahlt. Ein Anteil von 0,5 Gew% Eisen(III)-chlorid Hexahydrat ($FeCl_3 \cdot 6H_2O$) in Natriumchlorid (NaCl) zeigte den photochemischen Effekt von Eisen auf, indem sich die Chloratom-Produktion während der Bestrahlung in der ersten Stunde von $\sim 4 \times 10^{10}$ Atomen $cm^{-3} h^{-1}$ für reines NaCl auf $\sim 50 \times 10^{10}$ Atome $cm^{-3} h^{-1}$ für eisendotierte Proben steigerte. Dieser signifikante Anstieg kann durch die Photolyse von Fe^{III} -Cl Komplexe erklärt werden, die zu einer Reduktion von Fe^{III} zu Fe^{II} unter Bildung von Chlorradikalen (Cl^{\bullet}) führt. Die Rekombination von Cl^{\bullet} Radikalen führt zum Entweichen von Cl_2 aus der quasi-flüssigen Wasserhaut des feuchten Salzes und die anschließende Photolyse von Cl_2 resultiert in den detektierten Cl Atomen. Die eiseninduzierte Aktivierung wirkt zusätzlich zu den bekannten Aktivierungsprozessen über NO_x und O_3 die für die Cl-Produktion im Nullexperiment (ohne Eisenanteil) verantwortlich sind. In Gegenwart von 0,5 Gew% NaBr im Salz erhöhte sich die Br-Produktion deutlich von $\sim 3 \times 10^{10}$ Atomen $cm^{-3} h^{-1}$ (im eisenfreien Experiment) zu $\sim 30 \times 10^{10}$ Atome $cm^{-3} h^{-1}$ (2 Gew% $FeCl_3 \cdot 6H_2O$). Die Anwesenheit von Sulfat, Oxalat und Brenzcatechin in den Salzmischungen führte zu einer Hemmung der Halogenaktivierung durch konkurrierende Komplexbildung mit Fe^{III} und dem Einfangen von Cl^{\bullet} und OH^{\bullet} durch Sulfat in der Flüssigphase.

In einer zweiten Reihe von Experimenten wurde Aerosol untersucht, um die eher lokalen Phänomene von eisenhaltigen Salzpflanzen auf potenziell relevantere Effekte von Eisen in troposphärischem Seesalzaerosol zu übertragen. Künstlich hergestellte Seesalzlösungen mit typischen anorganischen Anionen (Cl^- , Br^- , SO_4^{2-} , Na^+ , K^+ , Ca^{2+} , Mg^{2+}) wurden mit Fe^{III} dotiert, vernebelt und bestrahlt. Die Aerosolexperimente ermöglichen den Bezug der Halogenproduktion auf die aktive Aerosoloberfläche. Die beobachtete Cl-Produktion erhöhte sich beträchtlich mit der Menge an hinzugegebenem Fe^{III} , während die Produktion für die eisenfreie Probe in Nullluft unter der Nachweisgrenze war. Die

molaren $\text{Fe}^{\text{III}}/\text{Cl}^-$ Verhältnisse von 0,01, 0,02 und 0,08 in der Ausgangslösung resultierten in Cl-Produktionen von jeweils 0,7, 1,4 und $6,6 \times 10^{21}$ Atomen $\text{cm}^{-3} \text{h}^{-1}$. Die Anpassung des pH-Wertes der Probe mit $\text{Fe}^{\text{III}}/\text{Cl}^- = 0,01$ von ~ 4 auf $\sim 2,2$ steigerte die Cl-Produktion um fast eine Größenordnung. Dies kann durch die Komplexbildungseigenschaften von Eisen erklärt werden, die mit der Software PHREEQC modelliert wurden. Die Berechnungen zeigten ein dominierendes Vorkommen von $\text{Fe}^{\text{III}}\text{-Cl}$ -Komplexen im sauren pH Bereich unter 4,5 und die Bildung von $\text{Fe}^{\text{III}}\text{-Hydroxy}$ -Komplexen bei höheren pH-Werten. Einflüsse der atmosphärischen Schadstoffe NO_x , O_3 und SO_2 wurden in zusätzlichen Experimenten untersucht. Bei $\text{Fe}^{\text{III}}/\text{Cl}^- = 0,08$ erhöhte die Anwesenheit von ~ 20 ppb NO_2 bzw. ~ 630 ppb O_3 die Cl-Produktion jeweils auf $>16 \times 10^{21}$ Atome $\text{cm}^{-3} \text{h}^{-1}$ bzw. $>18 \times 10^{21}$ Atome $\text{cm}^{-3} \text{h}^{-1}$. Die Steigerung wird verursacht durch die zusätzlichen Aktivierungsmechanismen, der Ansäuerung des Aerosols durch NO_x und der Wechselwirkung mit dem Photo-Fenton Zyklus. SO_2 hemmte die Cl-Produktion geringfügig aufgrund der Komplexbildung und des Einfangens der Radikale in der Flüssigphase. Der Bezug der beobachteten Cl-Produktionsraten auf den abgeschätzten Anteil des aktiven Eisens deutete auf den katalytischen Effekt sowie auf zusätzliche Aktivierungsmechanismen hin. Des Weiteren wurden die Aerosolpartikel durch einen Impaktor beprobt und mit energiedispersiver Röntgenspektroskopie untersucht, die einen Überzug der Aerosolpartikel mit einer aktiven $\text{Fe}^{\text{III}}\text{-Cl}$ Salzschrift zeigte.

Die dritte Reihe von Experimenten behandelte das Verhalten von festem Eisenoxid (Fe_2O_3) in künstlichem Seesalzaerosol und in Gegenwart von gasförmigem HCl. Die Cl-Produktion des nicht angesäuerten Seesalzaerosols mit Eisenoxid blieb unter der Nachweisgrenze. Eine pH-Anpassung zu 2,6–1,9 resultierte in Produktionsraten von $(1\text{--}10) \times 10^{21}$ Cl-Atomen $\text{cm}^{-2} \text{h}^{-1}$ und war abhängig von der Menge des in der Flüssigphase gelösten Eisens (und daher vom pH Wert). Der hohe abgeschätzte Anteil aktiven Eisens (600–2000 %) deutet auf ein effizientes und schnelles Recycling des beteiligten Eisens hin. Das mehrfache Einfrieren und Wiederauftauen der nicht angesäuerten Fe_2O_3 Probe führte zu nicht signifikanten Produktionsraten. In Abwesenheit von Salzen, aber Anwesenheit von gasförmigen HCl, konnte eine effiziente Cl-Bildung am reinen Fe_2O_3 -Aerosol beobachtet werden. HCl wird dabei aufgenommen und photochemisch aktiviert. Die Messungen wurden mit eisenfreien Experimenten an UV-transparentem Quarzglas-aerosol (SiO_2) und HCl in Nullluft verglichen, um den Anteil der homogenen und heterogenen Cl-Hintergrundproduktion abzuschätzen. Die Cl-Produktion erhöhte sich mit der injizierten Menge an HCl und reichte von $0,8 \times 10^{21}$ Atomen $\text{cm}^{-2} \text{h}^{-1}$ bei ~ 40 ppb HCl bis zu $>40 \times 10^{21}$ Atomen $\text{cm}^{-2} \text{h}^{-1}$ bei ~ 340 ppb HCl.

Um die Bedeutung der Ergebnisse auf die Umwelt zu beziehen, müssen die Einschränkungen der einzelnen Kammerstudien berücksichtigt werden. Die Salzpflanzenmessungen können zum Beispiel nur qualitativ auf natürliche und eher lokale Vorkommen wie die australischen Salzseen oder das Tote Meer (Israel) übertragen werden, wo die eiseninduzierte Halogenfreisetzung eine maßgebliche Rolle spielen könnte. Die Bedeutung von Fe^{III} für die globale Cl-Produktion aus Seesalzaerosol ist jedoch vernachlässigbar, wenn man das kleine natürliche $\text{Fe}^{\text{III}}/\text{Cl}^-$ Verhältnis und das hohe Verhältnis von Aerosoloberfläche zu Kammervolumen in der Smogkammer berücksichtigt. Die Fe_2O_3 -Experimente weisen darauf hin, dass eiseninduzierte Cl-Bildung für Mineralstäube und Verbrennungsaerosol in mariner Umgebung und in Gegenwart von gasförmigen HCl von Bedeutung sein könnte.

Content

List of Publications

Chapter 1: Extended Summary	1
1.1 Introduction and Background	1
1.1.1 Halogen Chemistry in the Troposphere	1
1.1.2 Heterogeneous Halogen Activation Mechanisms	4
1.1.3 Iron-Halide Occurrences	6
1.2 Objectives	9
1.3 Experimental	10
1.3.1 Teflon-Smog Chamber	10
1.3.2 Sample Preparation	11
1.3.3 Instrumentation	12
1.3.3 Radical-Clock Method to quantify Cl, Br and OH	16
1.4 Results and Discussion	17
1.4.1 Iron Speciation in highly Saline Media	17
1.4.2 Iron-Induced Halogen Formation from Laboratory Modeled Salt Pans	19
1.4.3 Iron-Induced Chlorine Formation from Artificial Sea-Salt Aerosol	23
1.4.4 Photochemical Activation of Chlorine by Iron-Oxide Aerosol	27
1.5 Conclusions and Outlook	30
1.6 Nomenclature	32
1.6.1 Acronyms	32
1.6.2 Symbols	33
1.7 Individual Contribution to the Included Manuscripts	35
1.8 Additional Contributions to not Included Publications	36
1.9 Appendix	37
1.10 References	47
Chapter 2:	59
Iron(III)-Induced Activation of Chloride and Bromide from Modeled Salt Pans	59
Abstract	60
2.1 Introduction	61
2.2 Experimental Setup and Methods	62
2.2.1 Smog Chamber and Its Analytical Instrumentation	62
2.2.2 Sample Preparation	63
2.2.3 Quantification of Cl, Br, and OH by the Radical Clock Method	63

2.3 Results and Discussion	65
2.3.1 Data Assessment and Evaluation	65
2.3.2 Blank Experiments with Iron-Free Salt Pans	69
2.3.3 FeCl ₃ ·6H ₂ O Containing Salts	72
2.3.4 Speciation	79
2.3.5 Environmental Significance	83
2.4 Conclusions	84
2.5 Associated Content	84
2.6 Acknowledgments	84
2.7 References	84
2.8 Supporting Information	92
2.8.1 Iron-free salt pans	93
2.8.2 FeCl ₃ containing salts	94
2.8.3 Speciation	96
2.8.4 References	98
Chapter 3:	99
Iron(III)-Induced Activation of Chloride from Artificial Sea-Salt Aerosol	99
Environmental Context	99
Abstract	100
3.1 Introduction	101
3.2 Experimental	102
3.2.1 Smog-Chamber Set-up	102
3.2.2 Sample Preparation and Chemicals used	103
3.2.3 Aerosol Production and Measurement	104
3.2.4 Data Analysis (Radical Clock)	105
3.3 Results and Discussion	106
3.3.1 Chamber Wall Effects	107
3.3.2 Iron(III)-Catalysed Cl Atom Production	110
3.3.3 Effects of NO ₂ , O ₃ , and SO ₂	111
3.3.4 Effect of pH and Fe ^{III} Speciation Chemistry	119
3.3.5 SEM-EDX Results	121
3.3.6 Fraction of Active Iron	122
3.3.7 Environmental Significance	123
3.4 Conclusions	124
3.5 Associated Content	125

	Content
3.6 Acknowledgements	125
3.7 References	126
3.8 Supplementary Material	133
Chapter 4:	139
Photochemical Activation of Chlorine by Iron-Oxide Aerosol	139
Abstract	140
4.1 Introduction	141
4.2 Experimental	142
4.3 Results and Discussion	146
4.3.1 Cl Production from Fe ₂ O ₃ in Artificial Sea-Salt Aerosol	146
4.3.2 Cl Production from HCl Uptake on Fe ₂ O ₃	150
4.4 Environmental Significance	156
4.5 Conclusions	157
4.6 References	158
Acknowledgements	163

List of Publications

The thesis consists of an extended summary on the topic including the performed research and additional information. Three research articles, accomplished in the framework of this thesis, are included in **Chapter 2, 3** and **4**, respectively.

I. Wittmer et al. (2015a):

Wittmer, J., Bleicher, S. and Zetzsch, C. Iron(III)-induced activation of chloride and bromide from modeled salt pans, J. Phys. Chem. A, 119(19), 4373–4385, doi: 10.1021/jp508006s.

II. Wittmer et al. (2015b):

Wittmer, J., Bleicher, S., Ofner, J. and Zetzsch, C. Iron(III)-induced activation of chloride from artificial sea-salt aerosol, Environ. Chem., 12(4), 461-475, doi: 10.1071/EN14279.

III. Wittmer and Zetzsch (2016):

Wittmer, J. and Zetzsch, C.: Photochemical activation of chlorine by iron-oxide aerosol, J. Atm. Chem., 10874, 1-18, doi: 10.1007/s10874-016-9336-6.

aldehydes and unsaturated hydrocarbons at lower reaction rates than Cl (Atkinson et al. 2007). Iodine compounds, emitted from natural and anthropogenic sources, also affect the catalytic ozone depletion and tend to form ultrafine aerosol particles. For more details on iodine chemistry please refer to a number of reviews on this topic and the references therein (Carpenter 2003; Platt and Hönninger 2003; Saiz-Lopez et al. 2012). Moreover, the inorganic fluorine chemistry is considered to have no large impact on the atmosphere since hydrogen fluoride (HF) is efficiently formed and trapped in the aqueous phase (von Glasow and Crutzen 2007).

To assess the significance of halogens, one has to consider their origin and chemical development in the atmosphere. Figure 1.1 summarizes the main sources, atmospheric processes and sinks of Cl and Br including the activation mechanisms induced by dissolved iron or gaseous NO_2 and O_3 . The main formation paths of RHO are (1) the heterogeneous activation (see section 1.1.2), (2) the homogeneous production by the oxidation of hydrogen halides with e.g. hydroxyl radicals (OH) or hydroperoxyl radicals (HO_2), and (3) the photolysis of halogen containing precursors. Once atomic halogens ($\text{X} = \text{Cl}, \text{Br}$) are present, their typical fate is the reaction with O_3 (R1.1) followed by the self-reaction of halogen oxides (XO , R1.2) to form again two X atoms (assuming the photolysis of the formed X_2). However, the ClO self-reaction mainly forms the photolabile Cl_2O_2 dimer (photolysis to Cl and OClO; Molina and Molina 1987). This cycle leads to the autocatalytic net depletion of O_3 ($2\text{O}_3 \rightarrow 3\text{O}_2$). The ClO and BrO cross-interaction contributes to the recycling of X by forming Br or the photolabile BrCl and OClO (R1.3; Le Bras and Platt 1995; Tuckermann et al. 1997). Another possible recycling path is the reduction of XO by nitrogen monoxide (NO; R1.4).



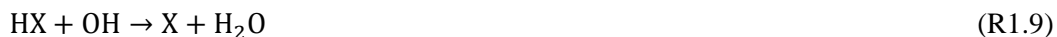
In the troposphere, this cycle is influenced by reactions with other oxidizing agents (e.g. HO_2) or pollutants (e.g. NO_2) to form reservoirs (HX, HOX, XONO_2) for inorganic halogen species (R1.5–R1.7; Atkinson et al. 2007).



The main sources of HO_2 are the reaction of OH with O_3 or another OH (from photolabile H_2O_2) or the oxidation of hydrocarbons (Warneck 1999). Moreover, the self-reaction of HO_2 can form the photolabile and highly soluble hydrogen peroxide (H_2O_2).



The halogen reservoirs can again take part in the halogen activation (see Figure 1.1). In the gas phase, they are mainly broken up by photolysis and the hydrogen halides are homogeneously reactivated by OH oxidation (R1.9),



whereas a variety of ways exist to heterogeneously reactivate the reservoirs to form RHS (see section 1.1.2 and Platt and Hönninger 2003).

The significance of reactions R1.1–R1.9 strongly depends on the oxidizing capacity of the troposphere, which is dominated by the sources and sinks of OH radicals. The main formation paths of OH in the troposphere are (1) the photolysis of O_3 to excited atomic oxygen ($\text{O}(^1\text{D})$) and O_2 at wavelengths below 340 nm (Dunlea and Ravishankara 2004) and the subsequent reaction of $\text{O}(^1\text{D})$ with H_2O (R1.10–R1.11), (2) the photolysis of nitrous acid (HONO, R1.12), mainly occurring in polluted air masses due to heterogeneous production (e.g. Harrison et al. 1996), (3) the photolysis of H_2O_2 (R1.13), and (4) the rapid radical recycling reaction via nitrogen monoxide (R1.14), already important at low pollution levels.



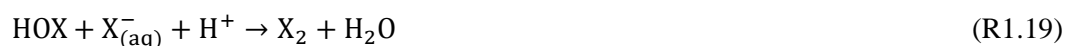
These sources are of relevance in this work since they are found to be responsible for the OH background production in the applied smog chamber (Bartolomei et al. 2015). A very minor portion of O_3 in the troposphere comes from the downward transport from the stratosphere, where it is formed by photolysis of oxygen. In reality, the tropospheric O_3 concentrations are strongly influenced by anthropogenic emissions of nitrogen oxides (mainly from combustion processes; Fishman and Crutzen 1978; Ehhalt and Drummond 1982), which may lead to enhanced O_3 (R1.15–1.17) and OH levels in the daytime (R1.10–R1.14). The photostationary state of nitrogen oxides and O_3 is also known as the Leighton relationship (Leighton 1961).



Here only the main reaction paths, relevant for the halogen chemistry, are illustrated. For a more detailed overview on the manifold reaction tree please refer to specific reviews (Wayne et al. 1995; von Glasow and Crutzen 2007; Finlayson-Pitts 2009).

1.1.2 Heterogeneous Halogen Activation Mechanisms

Compared to the homogeneous gas-phase activation of halogens (e.g. R1.9), the heterogeneous activation involves species that are present in the gaseous and aqueous phase. The aqueous phase is generally described by the Quasi-Liquid Microlayer (QLM) of an aerosol or salt crystal which represents the transition layer between the solid and gas phase. The hygroscopicity of a salt and the surrounding relative humidity determine the number of quasi-liquid microlayers (Finlayson-Pitts 2003; Ewing 2005; Buxmann et al. 2012). The combination of dissolved species, irradiation and uptake of gaseous species leads to the conversion of halides into less soluble oxidized species and the subsequent formation of gaseous RHS. Concerning sea-salt aerosol in marine areas, an important heterogeneous activation process involves the gaseous formation (R1.6) and uptake of hypochlorous or hypobromous acid (HOX; Fickert et al. 1999; Bloss et al. 2002). HOX is mainly scavenged by the QLM (Henry's law constant, $H^{cp} = 6.6 \times 10^2 \text{ M atm}^{-1}$ for HOCl and $> 1.3 \times 10^2 \text{ M atm}^{-1}$ for HOBr at 298 K; Sander 2015) or photolyzed to X and OH (Platt and Hönninger 2003). In the QLM, it leads to the formation of less soluble X_2 (H^{cp} at 298 K for $\text{Cl}_2 = 0.09 \text{ M atm}^{-1}$ and for $\text{Br}_2 = 0.73 \text{ M atm}^{-1}$; Sander 2015) or BrCl (XY) in dependence on the pH (Keene et al. 1998) and thus to an autocatalytic halogen activation (Hausmann and Platt 1994; Vogt et al. 1996) with the possible net reactions R1.18 and R1.19.



This reaction path is highly efficient for Br since the Cl activation needs a lower pH and is additionally limited by the reaction of gaseous Cl atoms with hydrocarbons, instead of O_3 , and subsequent formation of HCl (R1.20; Fickert et al. 1999).



where R denotes an organic radical. In the presence of polluted air masses, halogen nitrates (XONO_2) are formed from XO and NO_2 (R1.7) or nitryl halides (XNO_2) are formed heterogeneously (R1.22b). XONO_2 is either photolyzed to XO and NO_2 again, or hydrolyzed (even faster than HOX; Sander 2015) to form aqueous HOX (R1.21), being again available for reactions R1.18 and R1.19 (Hanson and Ravishankara 1993).



The hydrolysis of XONO_2 additionally strengthens the halogen activation by a decrease of the pH (formation of HNO_3), leading to a higher availability of H^+ and acid displacement reactions (Keene et al. 1999a; Fickert et al. 1999). Since XNO_2 is rather unreactive and only slightly soluble (H^{cp} at 298 K for $\text{ClNO}_2 = 0.05 \times 10^2 \text{ M atm}^{-1}$, for $\text{BrNO}_2 = 0.3 \times 10^2 \text{ M atm}^{-1}$; Sander 2015), it accumulates in the gas phase with photolysis as the only relevant sink. The slow heterogeneous uptake and potential formation of X_2 strongly depends on the salt composition (Frenzel et al. 1998; Schweitzer et al. 1999) and plays a minor role for natural sea salt as compared to other activation processes (Rossi 2003).

A further important effect of NO, NO₂ and O₃ in the gas phase is the formation of NO₃ and dinitrogen pentoxide (N₂O₅) that is readily hydrolyzed, forming 2HNO₃ and XNO₂ when halides are present (R1.22a and R1.22b; Zetzsch et al. 1988; Finlayson-Pitts et al. 1989; Zetzsch and Behnke 1992; Behnke et al. 1997).



The formation of XNO₂ (R1.22b) competes with the hydrolysis of N₂O₅ (R1.22a), which may lead to a halogen transfer into the gas phase by acid displacement of HX (Finlayson-Pitts 2003).

A further possible activation mechanism is the iron-induced photochemical formation of X₂ (Lim et al. 2006; Wittmer et al. 2015a). When Fe^{III} is dissolved in saline media, it forms photolabile Fe^{III}-X complexes (Millero et al. 1995; Nadtochenko and Kiwi 1998b). Table 1.1 lists the main complexes and their equilibrium constants (log₁₀ K) that represent the activity quotient. For convenience, the coordinated water molecules (H₂O)_x are omitted in the following (e.g. Fe(H₂O)₅Cl²⁺ is written as FeCl²⁺).

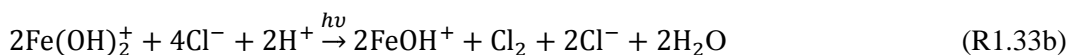
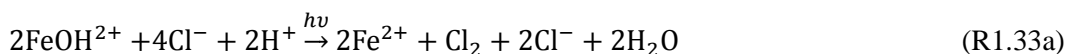
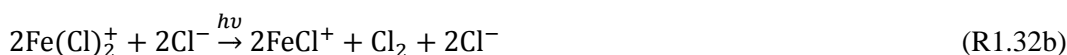
Table 1.1: Equilibrium constants of some typical Fe^{III}-hydroxy and Fe^{III}-halide complexes at an ionic strengths of zero and 298 K. Adapted from Wittmer et al. 2015a.

Equilibrium	log ₁₀ K	No.
Water		
Fe ³⁺ + H ₂ O ⇌ FeOH ²⁺ + H ⁺	-2.19	R1.23 ^A
Fe ³⁺ + 2H ₂ O ⇌ Fe(OH) ₂ ⁺ + 2H ⁺	-5.67	R1.24 ^A
Fe ³⁺ + 3H ₂ O ⇌ Fe(OH) ₃ + 3H ⁺	-12.0	R1.25 ^A
Fe ³⁺ + 4H ₂ O ⇌ Fe(OH) ₄ ⁻ + 4H ⁺	-21.6	R1.26 ^A
Chloride		
Fe ³⁺ + Cl ⁻ ⇌ FeCl ²⁺	1.48	R1.27 ^B
Fe ³⁺ + 2Cl ⁻ ⇌ FeCl ₂ ⁺	2.13	R1.28 ^C
Fe ³⁺ + 3Cl ⁻ ⇌ FeCl ₃	1.13	R1.29 ^D
Bromide		
Fe ³⁺ + Br ⁻ ⇌ FeBr ²⁺	0.61	R1.30 ^E
Fe ³⁺ + 2Br ⁻ ⇌ FeBr ₂ ⁺	0.2	R1.31 ^E

^ABaes and Mesmer (1976), ^BKester et al. (1975), ^CMartell and Smith (1976), ^DYatsimirskii and Vasil'ev (1960), ^ELister and Rivington (1955)

The speciation strongly depends on salinity, pH, and molar fractions in the media (see section 1.4.1). The low equilibrium constants for Fe^{III}-Br complexes and the dominant presence of Cl⁻ in most media mainly cause an activation of Cl⁻. The photolysis of FeCl²⁺ or FeCl₂⁺ reduces Fe^{III} to Fe^{II} and directly yields free chlorine atoms (Cl[•]) in the QLM of the salt crystals. The free Cl[•] reacts very fast with Cl⁻ to form Cl₂^{•-} (k_{Cl[•]+Cl⁻} = 2 × 10¹⁰ M⁻¹s⁻¹; Nadtochenko and Kiwi 1998a), which leads, after combination with another Cl[•] or

$\text{Cl}_2^{\bullet-}$, to a degassing of Cl_2 (H^{cp} at 298 K for $\text{Cl}_2 = 9.2 \times 10^{-2} \text{ M atm}^{-1}$; Sander 2015). An alternative, indirect pathway for chloride activation is the photolysis of the slightly less photoactive species FeOH^{2+} and $\text{Fe}(\text{OH})_2^+$ producing OH radicals (OH^{\bullet}) in the liquid that again can form Cl^{\bullet} via ClOH^{\bullet} . The net reactions are illustrated in R1.32 and R1.33. For a detailed discussion including kinetic considerations refer to Lim et al. (2006) or Wittmer et al. (2015a).



Due to a possible reoxidation of Fe^{II} by e.g. H_2O_2 or NO_3 in the aqueous phase, dissolved iron can have an autocatalytic effect on the halogen activation. Such a photo-Fenton like reaction cycle (illustrated in Figure 1.2) can lead to an enormous halogen release. The release is even enhanced in the presence of air pollutants, but also inhibited by photo-stable iron complexes, a shift in pH or precipitation of iron oxide (Wittmer et al. 2015a).

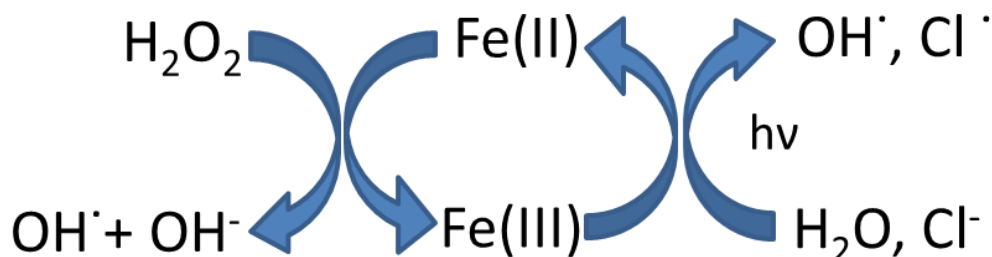


Figure 1.2: Photo-Fenton cycle of iron in the presence of oxidizing agents (e.g. H_2O_2) and irradiation, catalytically producing Cl^{\bullet} and OH^{\bullet} in the aqueous phase.

A number of additional, presumably less important mechanisms that may partly contribute to the RHS formation were explored in multiple studies and are summarized in several review articles (e.g. Rossi 2003; Finlayson-Pitts 2003). The description of these mechanisms is beyond the scope of this work.

1.1.3 Iron-Halide Occurrences

Iron (Fe , 55.8 g mol^{-1}) is the fourth most abundant element by mass in the earth's geosphere. It is of high relevance for our planet due to its biogeochemical diversity, ranging from iron ore to an essential micronutrient, is of high relevance for our planet. Thus, iron chemistry concerns geologists, biologists but also atmospheric scientists as Fe is naturally present in mineral aerosol particles (e.g. Mahowald et al. 2009) and is emitted more and more by the industry or transport sector in form of highly soluble combustion products (e.g. Luo et al. 2008). Generally, the fraction of dissolved iron is decisive for

further biogeochemical processes in terms of bioavailability or the photo-Fenton reaction cycle.

Mineral, iron-containing aerosol particles mainly originate from arid, vegetation-free regions like deserts or glacial flour. The produced aerosol particles are distributed in the whole troposphere and deposited by dry or wet deposition depending on particle size and density, turbulent transport and precipitation. During the long-range atmospheric transport, mineral dust aerosol coagulates with sea-salt aerosol (Andreae et al. 1986) and absorbs trace gases (e.g. SO₂, HCl, NO_x, O₃; Dentener et al. 1996). These processes are accelerated by cloud processing, where a mixture of minerals and sea salt is formed (Okada et al. 1990; Wurzler et al. 2000). The uptake of trace gases on the aerosol has been reported by several studies (Zhang and Iwasaka 2001; Sullivan et al. 2007b; Sullivan et al. 2007a; Arimoto et al. 2006; Murphy et al. 2006), detecting uptake products like chloride, sulfate and nitrate. For instance, Murphy et al. (2006) found chloride in mineral aerosol particles of the free troposphere. Many studies (Sullivan et al. 2007b; Sullivan et al. 2007a; Arimoto et al. 2006; Murphy et al. 2006; Zhang and Iwasaka 2001 and Sullivan et al. 2007b) provide evidence that chloride in mineral dust originates from the uptake of chlorine-containing gases, mainly in the form of HCl_(g). Therefore, chlorine chemistry can be considerably influenced when mineral aerosol particles pass the marine atmosphere, supported by a mean molar Cl⁻/Fe ratio of 100–200 in the marine aerosol of the central Atlantic (Warneck 1999). Aerosol particles have lifetimes from hours (particle diameter >6 μm), to days (2–6 μm), to weeks (< 2 μm) with a total average lifetime of about one week at a global atmospheric dust source of ~1700 Tg yr⁻¹ (Tegen and Fung 1994; Ginoux et al. 2001; Luo et al. 2003; Luo et al. 2008). Thus, mineral dust can be transported over long distances (e.g. from African deserts over the Atlantic to South America). Iron-containing aerosol particles are globally distributed in marine areas with minimum concentrations of 10⁻³ μg m⁻³ (South Atlantic, South Pacific) to maximum concentrations of 100 μg m⁻³ (North Atlantic, Indian Ocean; Figure 1.3; Mahowald et al. 2009). Moreover, the specific surface area is decisive to provide a reactive surface for heterogeneous reactions or to promote the solubility of the minerals. For instance, at particle diameters greater than 2.5 μm only a small fraction of hematite (Fe₂O₃) is dissolved (< 0.2 %), whereas a much higher fraction of iron dissolves in smaller particles (1–2 %) above the North Pacific Ocean (Ito and Feng 2010). The dissolution is a function of the acidity (acid mobilization), composition and size distribution of the particles, and further atmospheric processes like photooxidation, cloud formation and processing or temperature variations (Zhu et al. 1992; Zhuang et al. 1992; Meskhidze 2005; Shi et al. 2009; Baker and Croot 2010). As iron also originates from combustion (e.g. coal, blast furnaces, tropical fire; Luo et al. 2008) with a source strength ranging from 1.2 to 5.3 Tg yr⁻¹ (Ito and Feng 2010; Ito 2013; Wang et al. 2015), fine-mode combustion aerosol particles represent another potentially significant iron-halide occurrence when coming into contact with sea-salt aerosol or halogen containing trace gases. Although being less abundant than iron from mineral sources (41 to 74 Tg yr⁻¹; Ito 2013; Wang et al. 2015), combustion iron has a much higher soluble fraction (e.g. 77–81 % in oil combustion products compared to <1 % in mineral dust; Schroth et al. 2009). Therefore, even an estimated contribution of combustion iron of 5 % to the total atmospheric iron (Luo et al. 2008) can be of high relevance.

Rather local but abundant examples for iron in hypersaline media are salt lakes such as the Dead Sea (Israel), the Australian salt lakes (Long et al. 1992; Bowen et al. 2008; Krause et al. 2014), Don Juan Pond (Antarctica), the Great Salt Lake (Utah, USA), or the African salt lakes with iron concentrations in the range of 1 mg L^{-1} (Hammer 1986). The formation of reactive halogen species was detected above some of the lakes (Stutz et al. 2002; Holla et al. 2015). On a global scale, comparable amounts of water are stored in salt lakes and freshwater lakes (Hammer 1986) with a future trend towards increasing salinity caused by climate change (Williams 2002) or enhanced land use (Jolly et al. 2008). Iron halide chemistry will have an increasing importance in the future due to these circumstances.

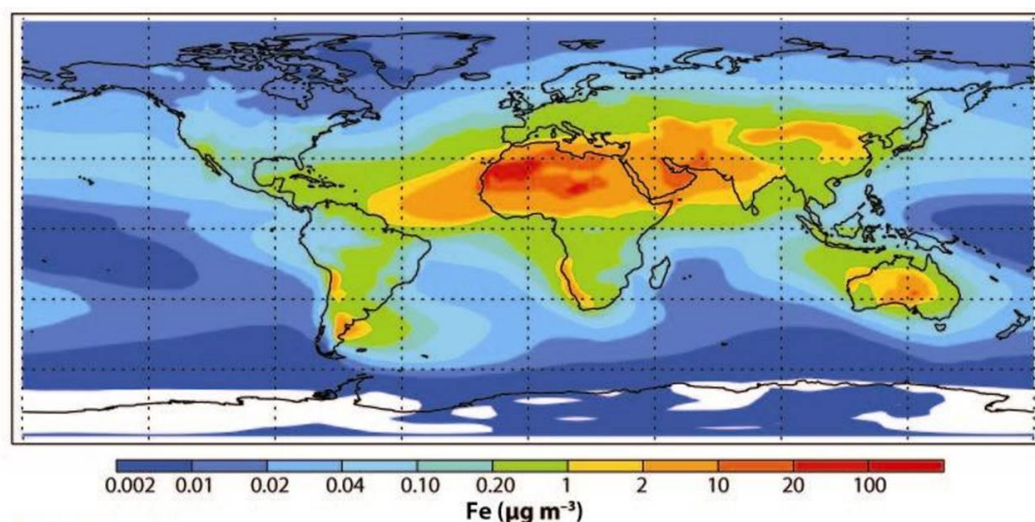


Figure 1.3: Modeled concentration of iron in surface aerosol particles ($\mu\text{g m}^{-3}$). Adopted from Mahowald et al. (2009).

Additionally, iron halides occur in coastal regions wetted by sea spray, in subtropical salt marshes (Soto-Jiménez and Páez-Osuna 2008) and other hypersaline environments containing iron from soil or deposition. In these regions they may locally impact the halogen chemistry. A relatively new, non-natural occurrence is the application of deicing road salt that was dramatically intensified in the last decades. For instance, 10–15 Tg year^{-1} rock salt were sold since the early 2000's in the United States, which is considerable when compared with the natural NaCl wet deposition of 2.2 Tg year^{-1} in the same area (Jackson and Jobbágy 2005) and a global chlorine source from sea-salt aerosol of $1785 \text{ Tg year}^{-1}$ (Keene et al. 1999b). Kim and Koretsky (2013) observed the presence of iron and a reduction to Fe^{II} in sediment cores of an urban kettle lake with simulated road salt deicers.

Besides hypersaline environments, a mixture of iron-containing aerosol and hydrogen halides can be found in volcanic plumes (Martin et al. 2008). Such an environment provides optimal conditions for the dissolution of particulate iron by condensation of the highly abundant acidic gases such as SO_2 , HCl, HF, or HBr (e.g. Wittmer et al. 2014). In the recent past, an intensive formation of RHS was observed in diluted volcanic plumes (Bobrowski et al. 2003; Gliß et al. 2015). Though, there is still a missing understanding of the responsible processes, as model calculations cannot completely explain the observations (Roberts et al. 2014; von Glasow 2010).

1.2 Objectives

The main goal of this thesis is to explore and quantify the iron-induced halogen release from highly saline media. In particular, the basic mechanism and the influence of atmospheric pollutants in the aqueous and gaseous phase shall be investigated with a special focus to the environmental significance.

To deal with these issues, smog chamber studies were applied with varying constituents including salt pans, artificial sea-salt aerosol, iron-oxide aerosol and a varying composition of the gas phase. Therefore, the thesis comprises three specific studies that assess the following topics and questions:

- What is the influence of dissolved iron (Fe_d) on the speciation in highly saline media?
- How is the molar Fe_d to halide ratio related to the iron-induced gaseous halogen production?
- Is recycling of iron observable?
- What is the influence of the pH on the dissolution and speciation characteristics of iron and on the halogen production?
- How do naturally occurring organic and inorganic contaminants (such as sodium sulfate, sodium oxalate or catechol) in the salt affect the halogen chemistry?
- Does the presence of gaseous pollutants (e.g. NO_2 , O_3 , SO_2) affect the halogen release mechanisms?
- Is the Cl activation by HCl absorption on iron-oxide aerosol possible?

Providing answers to these questions will contribute to the current understanding of the role of iron in saline environments in the context of halogen activation mechanisms and their relative importance and furthermore provide a data base to include this mechanism in atmospheric models.

1.3 Experimental

In order to investigate the iron-induced halogen production a series of experiments was performed in a Teflon-smog chamber. The experiments included (1) the irradiation of iron-doped salt pans with various compositions, (2) the investigation of artificial sea-salt aerosol containing dissolved Fe^{III} or partly dissolved Fe₂O₃, and (3) the exposure of pure Fe₂O₃ aerosol to gaseous HCl. In all cases, the produced gas-phase radicals (Cl, Br and OH) were quantified and compared to respective iron-free blank experiments. The experimental procedures and set-ups are briefly described in the following. For more detailed specifications please refer to Bleicher (2012), Buxmann et al. (2012), Wittmer et al. (2015a), Wittmer et al. (2015b) and Wittmer and Zetzsch (2015).

1.3.1 Teflon-Smog Chamber

The smog chamber consists of Teflon film (fluorinated ethylene propylene, FEP 200A, DuPont, film thickness: 54 μm) suspended in a cylindrical shape on three aluminum rings of 1.33 m diameter. The height of 2.5 m results in a theoretical volume of ~3500 L. In practice, the volume depends on the pressure differences between chamber interior and exterior based on the loose fixation of the foil. The whole construction is situated above a solar simulator consisting of 7 medium pressure arc lamps (Osram HMI 1200 W) with aluminum-coated reflectors. To obtain a spectrum comparable to atmospheric conditions, the light is filtered by a borosilicate glass filter (Schott, Tempax, 3 mm) for UV and by a ~2 cm water layer (connected to a heat exchanger) for infrared radiation. The spectrum was measured by a 2π spectroradiometer (Metcom; Bartolomei et al. 2015) and by a Czerny-Turner-Monochromator (Princeton Instruments, Acton 500 pro, f=500 mm, temperature stabilized at 25 °C) with a temperature controlled (-25°C) Hamamatsu detector (Bleicher 2012). The intensity was scaled on an absolute basis by NO₂ actinometry based on the photostationary Leighton relationship (see section 1.1.1) and the measured photolysis rate for NO₂. The result is the wavelength-dependent homogeneous actinic net flux $F(\lambda)$ within the inhomogeneous irradiated chamber (Figure 1.4). Together with the specific absorption cross-section σ and quantum yield Φ of a molecule A the photolysis rate J_A can be calculated:

$$J_A = \int \phi_A(\lambda, T) \sigma_A(\lambda, T) F(\lambda) d\lambda \quad (1.1)$$

The relevant photolysis rates are listed in Bleicher (2012) and Wittmer et al. (2015a).

The chamber is continuously flushed with zero air to replenish the air consumption of the analyzers and to avoid contamination by maintaining a slight overpressure within the chamber (monitored by a differential pressure sensor, Kalinsky Elektronik DS1). Continuous mixing of the chamber is guaranteed by a custom-built fan (PTFE-Teflon). The zero air is generated by passing ambient air through a compressor including particle filter and oil-separator, an air drier (Balston Filter Products, model 75–60), activated charcoal and a zero-air generator (cmc instruments, ZA 100k). The resulting hydrocarbon-free zero air has a dewing point of -70°C and impurities of <1 ppb of O₃, <0.5 ppb NO_x and <100 ppb of CH₄. If necessary, the air is humidified by passing a temperature-controlled three-neck bottle partly filled with deionized water (Seralpur pro

90 cm, $<0.055 \mu\text{S cm}^{-1}$). The whole set-up is situated in a temperature-controlled room allowing operational temperatures from 30°C down to -20°C . The temperature and relative humidity in the Teflon chamber are monitored by two light-shielded sensors at different heights (Rotronic, HC2-IC102) to observe potential thermic layering. After each aerosol experiment, the chamber walls were cleaned with deionized water and conditioned by generating high OH concentrations with >1 ppm O_3 (generated by a silent ozonizer, Sorbios GSG 12 discharging pure O_2 , $>99.995\%$), 50–80% RH and irradiation (4 additional UV lamps, Philips TUV 55 W, $\lambda = 253.7$ nm). At these conditions, the lifetime of O_3 is ~ 20 min and OH concentrations exceed 10^9 radicals cm^{-3} , indicated by the rapid depletion of CH_4 measured by a CH_4 analyzer (Bendix 8201). Before starting an experiment (salt pan or aerosol), the chamber was flushed for at least 10 h with zero air to remove the oxidation products from conditioning and the ambient air intruded during salt-pan insertion.

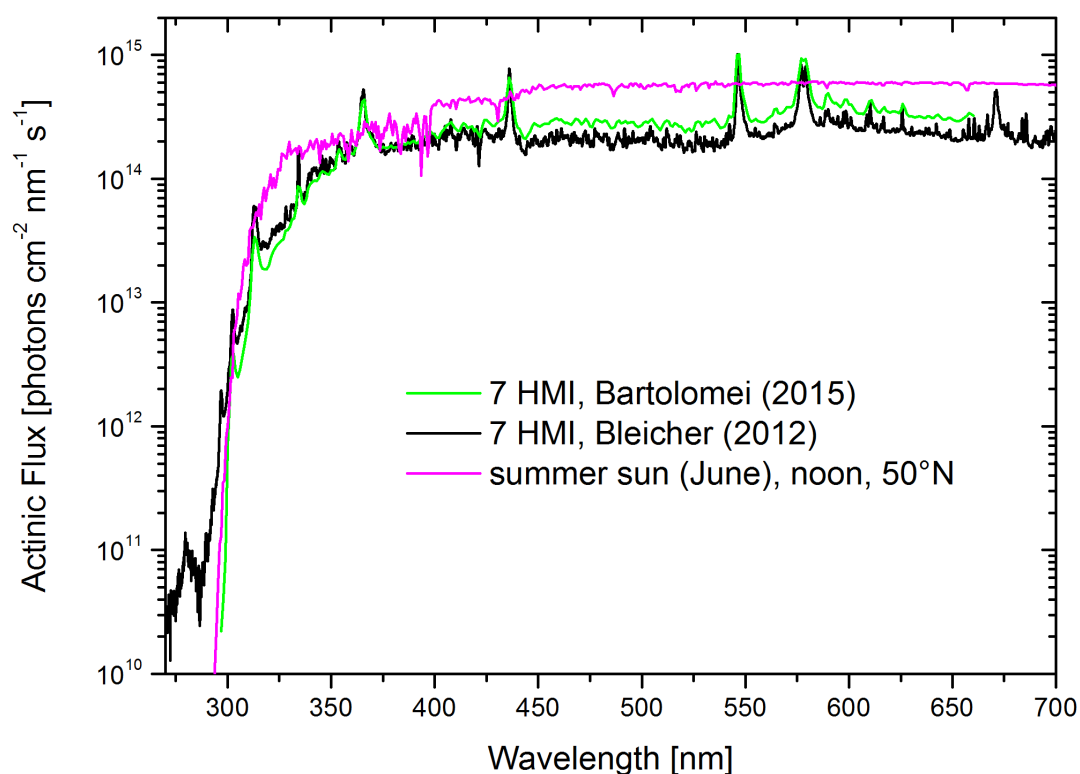


Figure 1.4: Actinic flux of the solar simulator measured by a 2π Metcom Spectroradiometer (Bartolomei et al. 2015) and by a Czerny-Turner-Monochromator (Princeton Instruments, Acton 500 pro, $f = 500$ mm, temperature stabilized at 25°C) with a Hamamatsu detector, cooled to -25°C (Bleicher 2012) in comparison to the radiative transfer model TUV (Madronich and Flocke 1999). The intensities of the measurements were normalized to $J_{\text{NO}_2} = 6.7 \times 10^{-3} \text{ s}^{-1}$ obtained by NO_2 actinometry.

1.3.2 Sample Preparation

Salt Pan Preparation

To prepare a salt pan, the amount of the desired salt mixture was first completely dissolved in bidistilled water and afterwards dried in an oven (flushed with zero air) on a Teflon sheet at 50°C for at least 70 h. Depending on the stickiness, the resulting salt crust

was milled in a ball mill (Retsch MM 2, Haan, Germany), ground in a (household salt mill) or spread untreated on a circular 0.3 m² Teflon sheet mounted in the middle of the chamber. In this way 13 samples were prepared with a sodium chloride (NaCl) bulk doped with various constituents, such as Fe^{III} chloride hexahydrate (FeCl₃·6H₂O), magnesium chloride (MgCl₂), sodium bromide (NaBr), sodium sulfate (Na₂SO₄), catechol (C₆H₆O₂), oxalic acid (H₂C₂O₄), or sodium oxalate (Na₂C₂O₄) and irradiated. After every experiment, the pH was estimated by adding 3 mL bidistilled water to 2 g of the salt crust to obtain a saturated solution from which the pH was determined by pH indicator strips (Merck). For more details on the investigated salt mixtures see section 4.2.

Aerosol Preparation and Production

The sample solutions were prepared by mixing various amounts of FeCl₃ (Merck, for synthesis, ≥98 % or Riedel-de Haën, sublimate, ≥99 %) or α-Fe₂O₃ (Sicotrans Orange, L2515D, BASF, specific surface = 152 m² g⁻¹) in artificial seawater (824 mg L⁻¹ NaCl, 314 mg L⁻¹ Na₂SO₄·10H₂O, 176 mg L⁻¹ MgCl₂, 52 mg L⁻¹ CaCl₂·2H₂O, 24 mg L⁻¹ KCl, 6.9 mg L⁻¹ NaHCO₃, 3.4 mg L⁻¹ KBr, 0.9 mg L⁻¹ H₃BO₃, and 0.1 mg L⁻¹ NaF; Kester et al. 1967). In case of Fe₂O₃, 17 mg were stirred into 100 mL of artificial seawater, forming a suspension. For some samples, the pH was adjusted by adding HCl (Sigma-Aldrich ACS, 37 %) in order to promote the iron dissolution and the associated Fe^{III}-Cl complex formation (see section 1.4.1). The prepared solutions were nebulized with an ultrasonic nebulizer (Quick Ohm QUV-HEV FT25/16-A, 35 W, 1.63 MHz) generating droplets in the μm range, that quickly come into equilibrium with the surrounding and evaporate to a saturated sea-salt solution (containing Fe₂O₃ agglomerates when applying Sicotrans Orange). The resulting particle number size distributions showed maxima between 290–480 nm (Figure 1.5), depending on the composition of the nebulized solution. A starting RH of 30–40 % was adjusted in the chamber before injecting the aerosol to avoid a crystallization of the saline aerosol (Siekman 2008). The injection took typically 30–60 minutes and (in order to avoid a dripping of the condensed droplets into the chamber) a heated transfer tube (made of copper) was applied. For the FeCl₃ and the corresponding blank samples, the impact of gaseous pollutants O₃, NO₂ (Rießner Gase, 104 vpm NO₂ with a purity of 98 % in synthetic air) and SO₂ was investigated (Rießner Gase, 0.99 % SO₂ with a purity of 99.98 % in N₂ with a purity of 99.999 %). In a further experimental series, suspensions of Fe₂O₃ and Aerosil 200 (Evonik Industries, specific surface = 200 m² g⁻¹) in deionized water were nebulized and exposed to various amounts of evaporated HCl (Sigma-Aldrich, ACS, 37 %).

1.3.3 Instrumentation

Gas Analyzers

The NO_x and O₃ concentrations in the chamber air were continuously monitored by chemiluminescence gas analyzers (EcoPhysics, CLD 88p, coupled with a photolytic converter, PLC 860, for NO and NO_x, and UPK 8001 for O₃). The UPK 8001 measures O₃ based on its reaction with ethene resulting in excited formaldehyde and the emitted photons are detected. The O₃ analyzer was calibrated in parallel by an absorption measurement at 254 nm in a 10 cm cuvette with zero air in the reference channel in an Uvikon XL. The calibration of the EcoPhysics analyzer and its converter efficiency was

performed by gas-phase titration of NO with O₃. The instruments are described in detail in Bleicher (2012).

Aerosol Measurement

During the experiments, the aerosol number size distributions were monitored by an electrostatic classifier (TSI, 3071) in combination with a bipolar neutralizer (⁸⁵Kr) and a condensation nucleus counter (TSI, 3020). Scanning and data evaluation was performed by a custom written software from Heinz-Ulrich Krüger (Balzer 2012).

Having passed the neutralizer, the particles exhibit a known bipolar charge distribution. With increasing particle size, it becomes more probable that the particles carry multiple charges (2e, 3e, etc.). Assuming the charge equilibrium according to Boltzmann, the fraction of particles carrying up to two elementary charges can be estimated by approximating the charge distributions with a logarithmic distribution of particle sizes from 1 to 1000 nm (Wiedensohler 1988):

$$f(N) = 10 \left[\sum_{i=0}^5 a_i(N) (\log D_p)^i \right] \quad (1.2)$$

Here, $a_i(N)$ are approximation coefficients listed in Wiedensohler 1988, N is the number of elementary charge units on a particle and D_p is the particle mobility diameter. Equation 1.2 is valid for the size ranges from 1 nm to 1000 nm for $N = -1, 0, 1$ and for the size ranges from 20 nm to 1000 nm for $n_p = -2, 2$. Particles smaller than 20 nm carry mostly one elementary charge, whereas for particles larger than 70 nm a triple charge becomes probable. The fraction of triply and higher charged particles can be calculated after Gunn and Woessner 1956:

$$f(n_p) = \frac{e}{\sqrt{4\pi^2 \epsilon_0 D_p kT}} \times \exp \frac{- \left[n_p - \frac{2\pi \epsilon_0 D_p kT}{e^2} \ln \left(\frac{c_{NI+} Z_{I+}}{c_{NI-} Z_{I-}} \right) \right]^2}{2 \frac{2\pi \epsilon_0 D_p kT}{e^2}} \quad (1.3)$$

where e = elementary charge, ϵ_0 = dielectric constant, k = Boltzmann's constant, T = temperature, $c_{I\pm}$ = ion concentration, and $Z_{I\pm}$ = ion mobility. Equations 1.2 and 1.3 are used for the multiple charge correction in our software.

Within the electrostatic classifier, a quasi-monodisperse particle size distribution is obtained based on the different electrical mobilities of the charged and former polydisperse aerosol. The classifier consists of two concentric electrodes whose voltage can be adjusted in order to scan through various electrical mobilities. In dependence of the diameter and the charge, the electrical mobility is defined as

$$Z_p = \frac{n_p e C}{3\pi \mu D_p} \quad (1.4)$$

where Z_p is the electrical mobility of the particle, n_p is the particle charge in elementary units, μ is the viscosity of air and C is the slip correction factor (Liu and Pui 1975). The slip correction considers the mean free path of air molecules, which is not negligible for particles smaller than 10 μm . In practice, the electrical mobility selection includes all aerosol particles whose mobility lies within a certain narrow range $Z_p \pm \Delta Z_p$, typically described by a transfer function which ideally has a triangular shape (maximum at Z_p). The half-width of the transfer function is given by

$$\Delta Z_p = \frac{(q_a + q_s) \cdot \ln\left(\frac{r_2}{r_1}\right)}{2\pi V L} \quad (1.5)$$

where q_a is the aerosol flow rate, q_s the sampling flow rate, r_1 the outer radius of the classifier center rod, r_2 the inner radius of the classifier housing, L the distance between the mid-planes of the classifier entrance slit and sampling slit and V the classifier center rod voltage (Knutson and Whitby 1975). Figure 1.5 illustrate typical, multiple charge corrected number size distributions of several aerosol types applied. The origin of these more or less pronounced bi- or trimodal distributions is probably the laminar and turbulent coagulation of droplets, especially at high precursor temperatures, droplet number concentrations and carrier gas flow rates (Wang et al. 2008) that apply to the nebulizer used.

Additionally, the generated aerosol particles were sampled by a Sioutas cascade impactor (SKC, aerodynamic diameter ranges: $>2.5 \mu\text{m}$, $1\text{--}2.5 \mu\text{m}$, $0.5\text{--}1 \mu\text{m}$, $0.25\text{--}0.5 \mu\text{m}$ and $<0.25 \mu\text{m}$; Misra et al. 2002) and subsequently analyzed by SEM-EDX (Scanning-Electron-Microscope with an Energy-Dispersive X-ray detector; Lohninger and Ofner 2014). The resulting images demonstrate the small particle size of the iron oxide powder, forming agglomerates during nebulization of the suspension in water (Figure 1.6a) and the composition of sea-salt particles including dissolved iron species (Figure 1.6b).

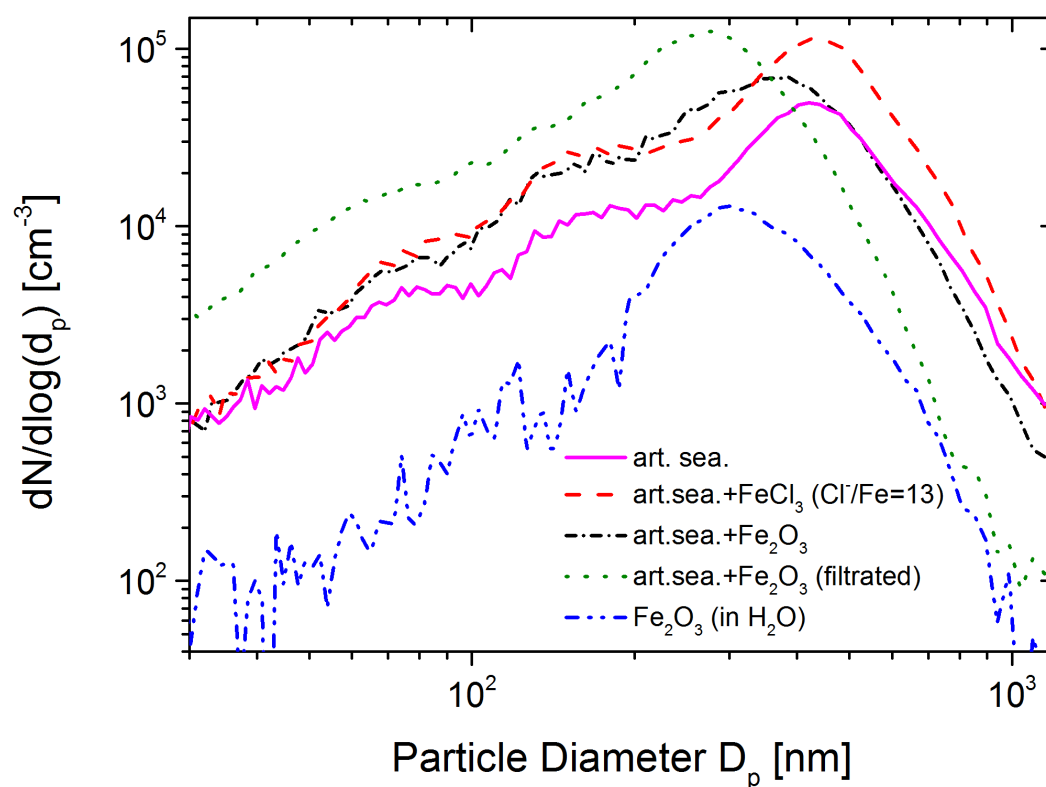


Figure 1.5: Typical, multiple-charge corrected number size distributions for aerosol particles obtained by the nebulization of artificial seawater (art.sea.), iron-containing (FeCl_3 or Fe_2O_3) art. sea. mixtures and pure suspensions of Fe_2O_3 in water. Adopted and merged from Wittmer et al. (2015b) and Wittmer and Zetzsch (2015).

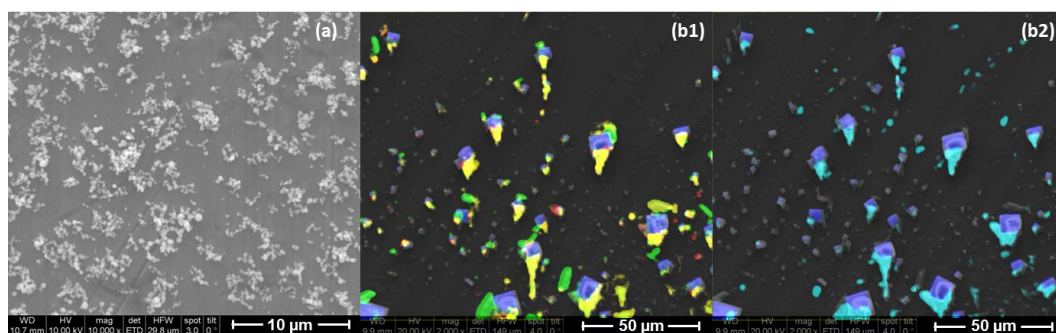


Figure 1.6: SEM (-EDX) images of the pure iron oxide sample (a) and the FeCl_3 doped artificial sea-salt sample (b). Color coding: NaCl – blue, CaSO_4 – green, MgCl_2 – yellow, KCl – red, FeCl_3 – turquoise. Image adopted and modified from Wittmer et al. (2015b).

1.3.3 Radical-Clock Method to Quantify Cl, Br and OH

To detect and quantify the produced halogen atoms and OH radicals in the smog chamber, the radical clock method was applied (Behnke et al. 1988; Zetzsch and Behnke 1993). The method is based on monitoring the consumption of selected hydrocarbons (HC_i ; 2,2-dimethylpropane, 2,2-dimethylbutane, 2,2,4-trimethylpentane, toluene), having different reactivities towards Cl, Br and OH. After focusing with a custom-built liquid nitrogen cryotrap enrichment (sampling flow 100 mL min^{-1} dried by a Nafion dryer), the hydrocarbons are quantified by a GC-FID (Gas Chromatography with a Flame Ionization Detector) using an Al_2O_3 -PLOT column. A temperature gradient of 50°C min is applied to heat the column from 160°C to 200°C after a runtime of 3 min, resulting in a total time interval of 15 min. The obtained time profiles are corrected for dilution (by the inert dilution standard perfluorohexane) and fitted with an appropriate differentiable analytical function. Finally, the unknown time profiles of Cl, Br and OH are determined by dissolving the overdetermined system of i differential equations including four HC_i profiles and their respective reaction rate constants ($k_{\text{Cl}+\text{HC}_i}$, $k_{\text{Br}+\text{HC}_i}$, $k_{\text{OH}+\text{HC}_i}$; listed in Wittmer et al. 2015a) towards the three radicals:

$$-\frac{d\ln[\text{HC}_i]}{dt} = k_{\text{Cl},i}[\text{Cl}] + k_{\text{Br},i}[\text{Br}] + k_{\text{OH},i}[\text{OH}] \quad (1.6)$$

The possible solutions of the overdetermined system are arithmetically averaged and the standard deviation of the mean is given as uncertainty. Assuming a photostationary steady state and equalizing sources and sinks allows to calculate the production rate dQ_X/dt ($X = \text{Cl, Br, or OH}$) and the corresponding total production Q_X (by integrating) of each radical in order to correct the quasistationary concentrations for the burden of the HCs.

$$\frac{dQ_X}{dt} = \sum_i k_{X+\text{HC}_i}[\text{HC}_i]_t[X]_t \quad (1.7)$$

A basic uncertainty in this consideration is the reactivity of the HC_i degradation products that may contribute to the radical sink. To account for this additional sink in the system (leading to an underestimation of dQ_X/dt), a maximal value of dQ_X/dt can be calculated by assuming a constant total reactivity towards each radical ($\sum_i k_{X+\text{HC}_i}[\text{HC}_i]_0$). This implies that the degradation products have the same reactivity as the initial reactivity of the HC_i and is mainly valid for Cl in the early stage of the experiment (Wittmer et al. 2015b). A comparison to the calculation of dQ_X/dt based on the actual dilution corrected $[\text{HC}]_i$ values results in a minimal and maximal value for the radical production.

Considering the aerosol experiments, the production (rate) can be multiplied by the chamber volume V_{ch} and normalized by the actual active surface area $A_{\text{eff}}(t)$ to obtain the absolute production rate dQ_{abs}/dt in $\text{atoms cm}^{-2} \text{ s}^{-1}$. The same applies for the total production Q_{abs} .

$$\frac{dQ_{\text{abs}}}{dt} = \frac{\frac{dQ_X}{dt} \times V_{\text{Ch}}}{A_{\text{eff}}(t)} \quad (1.8)$$

$A_{\text{eff}}(t)$ is the sum of (1) the actual measured aerosol surface ($A(t)$), (2) the active, wall-deposited surface area during injection, assuming an approximately linear increase of $A(t)$ during the injection time ($\Delta t_{\text{inj}} = t_{\text{inj, end}} - t_{\text{inj, start}}$), and (3) the active, deposited surface area after injection ($A_{0, \text{inj}}$) from the time on when the injection ends (t_{inj}). The respective deposition depends on the determined surface deposition lifetime τ_s (e.g. art. sea salt: 31100 s, iron doped art. sea salt: 8820 s, Fe_2O_3 aerosol: 4510 s; Wittmer et al. 2015b) and the factor 0.2 is the determined fraction of deposited surface that actively contributes to Q_x (Wittmer et al. 2015b).

$$A_{\text{eff}}(t) = A(t) + 0.2 \times \left(\int_{t_{\text{inj, start}}}^{t_{\text{inj, end}}} \left(\frac{\Delta A_{0, \text{inj}}}{\Delta t_{\text{inj}}} \times \frac{t}{\tau_s} \right) dt + A_{0, \text{inj}} \times \left(1 - \exp\left(-\frac{t_{\text{inj}}}{\tau_s}\right) \right) \right) \quad (1.9)$$

As the electrostatic classifier produced flashovers caused by the high RH in the course of some experiments, $A(t)$ could not always be determined continuously. Therefore it is replaced by the measurement at the beginning of the irradiation and the (aerosol-type dependent) surface deposition rate

$$A(t) = A_{0, \text{light}} \times \exp\left(-\frac{t_{\text{light}}}{\tau_s}\right) \quad (1.10)$$

1.4 Results and Discussion

1.4.1 Iron Speciation in Highly Saline Media

When iron is dissolved in saline water, it tends to form complexes with the available ligands. In particular, the speciation of these complexes depends on the pH, salinity and temperature and may promote the dissolution process (Zhu et al. 1992; Baker and Croot 2010). An important aspect is the influence of the photolabile Fe^{III} -halide and Fe^{III} -hydroxy complex formation in highly concentrated brines or in saline aerosol on the observed change in Q_x and Q_{abs} with pH and salt composition. To derive the speciation and relate it to Q_x and Q_{abs} , an equilibrium model was set up employing the software PHREEQC (pH Redox-EQuilibrium written in C; Parkhurst and Appelo 1999). The activity coefficients for Fe^{3+} , Na^+ , Cl^- , SO_4^{2-} , HSO_4^- , and Br^- were corrected for the ionic strength by the Pitzer ion interaction approach (Pitzer 1973; Tosca et al. 2005) complemented by the extended Debye-Hückel equation (Hückel 1925; Truesdell and Jones 1973) when the Pitzer parameters were not available. The Pitzer approach is well-suited for very high ionic strengths, whereas the extended Debye-Hueckel equation is generally limited to ionic strengths $< 1 \text{ mol L}^{-1}$ but at predominant presence of Cl^- still gives reliable results (Crowe and Longstaffe 1987; Merkel and Planer-Friedrich 2008). The Debye-Hueckel theory considers single ion activities surrounded by a spherical ionic cloud of opposite charge, while the Pitzer theory additionally includes a virial expansion, describing the interactions amongst ions and solvent. The applied PHREEQC database file is listed in the Appendix. The equilibrium calculation was used to describe the initial equilibrium conditions at the beginning of the experiment. For kinetic considerations including the formation path of degassing halogens, please refer to Balmer and Sulzberger (1999), de Laat and Le (2005) or Machulek et al. (2009). The resulting speciation graphs of the equilibrium model are shown in Figure 1.7. Comparing Figure 1.7a and Figure 1.7b reveals the effect of high ionic strengths on the complex formation.

In the low concentrated stock solution only a small fraction of the decisive Fe^{III} -Cl complexes is formed, whereas at high ionic strengths (with the simplified assumption of saturation in Cl^- with 6.1 mol L^{-1} and unchanged molar ratios), the Fe^{III} -Cl complexes dominate in the acidic pH range from 1 to 4.5. The presence of Fe^{III} -hydroxy complexes at higher pH is comparable for low and high ionic strengths. Figure 1.7b displays the representative speciation for the QLM of the hygroscopic salt crystals in a salt pan or the liquid aerosol phase. The measured pH ranges of the saturated water layer (98 g NaCl salt pan doped with 2 g $\text{FeCl}_3 \cdot 6\text{H}_2\text{O}$) and the aerosol stock solution (1 L artificial seawater doped with 0.05 g FeCl_3) are indicated by the colored areas. At both pH ranges of the samples, FeCl_2^+ and FeCl^+ represent the highest fraction of Fe^{III} species, having a much higher absorbance and quantum yield for photodissociation than the Fe^{III} -hydroxy complexes (Nadtochenko and Kiwi 1998a; Nadtochenko and Kiwi 1998b; Vione et al. 2005). Fe^{III} -Br complexes have an even higher absorbance (Rabinowitch and Stockmayer 1942) but show a negligible contribution (below 10^{-3}) at molar Cl^-/Br^- ratios of 150 (salt pan with NaBr addition; Wittmer et al. 2015a) and 997 (artificial seawater; Figure 1.7). The influence of other anions (contained in the artificial seawater) on the Fe^{III} complexation becomes negligible at high ionic strengths in a Cl^- dominated medium, even if a significant fraction is present in the stock solution (e.g. FeSO_4^+ ; Figure 1.7a). A rather important effect, which slows down the chloride activation, is the scavenging of Cl^- by sulfate anions shown by Machulek et al. (2009). The situation changes when organic constituents are added to such a system. Oxalate and catechol form a dominant fraction of iron complexes and thus inhibit the iron-induced Cl production (Wittmer et al. 2015a). In general, a pH below 4 facilitates the formation of degassing Cl_2 instead of HOCl, which dominates at pH 4–7. However, with decreasing pH, the fractions of Fe^{III} -hydroxy complexes and thus the OH^\bullet formation decrease considerably, inhibiting the reoxidation of Fe^{II} by H_2O_2 (formed via $\text{OH}^\bullet + \text{OH}^\bullet$). This can be proven by considering the fraction of active iron involved in the gaseous Cl production (see section 4.4 or Wittmer and Zetzsch 2015), or by the inhibiting effect of Cl^- anions on the photo-Fenton process (Machulek et al. 2007).

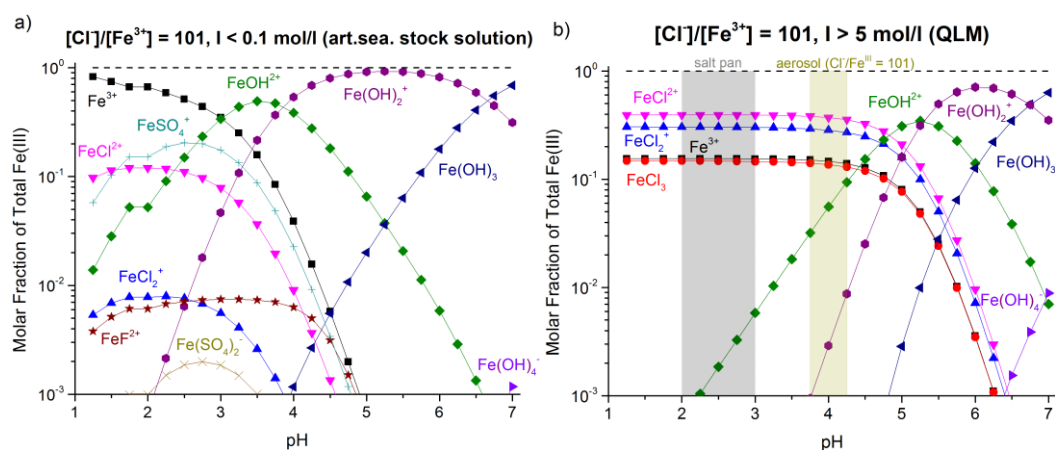


Figure 1.7: Molar fraction of the Fe^{III} species related to the total Fe^{III} content as function of the pH for the artificial seawater stock solution before nebulizing (a) and the highly concentrated aqueous phase of the salt pan or aerosol QLM (b) calculated by the PHREEQC equilibrium model. The dashed line indicates a molar fraction of 1. Adopted and modified from Wittmer et al. (2015b).

1.4.2 Iron-Induced Halogen Formation from Laboratory Modeled Salt Pans

Blank Experiments

In a first experimental series, blank experiments were conducted by applying iron-free salt pans with various constituents. Most of the measurements were close to the detection limit of 10^4 Cl atoms cm^{-3} and 10^9 Br atoms cm^{-3} . Some slight differences in the Cl production were detected by adding 0.5 g of NaBr to 99.5 g of NaCl ($Q_{\text{Cl}} = 1.6\text{--}1.7 \times 10^{10} \text{ cm}^{-3} \text{ h}^{-1}$), 5 g of $\text{MgCl}_2 \cdot 6\text{H}_2\text{O}$ to 95 g of NaCl ($Q_{\text{Cl}} = 1.9\text{--}2.0 \times 10^{10} \text{ cm}^{-3} \text{ h}^{-1}$) and 2 g of $\text{Na}_2\text{C}_2\text{O}_4$ to 98 g of NaCl ($Q_{\text{Cl}} = 2.7\text{--}2.8 \times 10^{10} \text{ cm}^{-3} \text{ h}^{-1}$), compared to the pure NaCl sample ($Q_{\text{Cl}} = 4.1\text{--}4.2 \times 10^{10} \text{ cm}^{-3} \text{ h}^{-1}$). The reasons why a Cl production was observed in a zero air environment are probably the bromide impurities in NaCl ($\text{Br}^- \leq 0.01\%$, according to the manufacturer Sigma Aldrich S9888, $\geq 99.0\%$) in combination with the observed NO_x impurities of up to 2 ppb. NO_x in the chamber air originates from the zero air (< 0.5 ppb), the HONO production of the Teflon walls (Bartolomei et al. 2015) and the air intrusion due to the opening of the chamber when changing the salt pan. The NO_x impurities may activate Cl^- heterogeneously by formation of ClNO ($J_{\text{ClNO}} = 1.8 \times 10^{-3} \text{ s}^{-1}$) on the solid salt (Vogt and Finlayson-Pitts 1995) or ClNO_2 ($J_{\text{ClNO}_2} = 2 \times 10^{-4} \text{ s}^{-1}$) in the presence of O_3 and thus N_2O_5 according to R1.22b. In the course of irradiation, up to 15 ppb O_3 were formed by the Leighton relationship (R1.15–R.17) and by the regeneration of NO with peroxy radicals (RO_2) or HO_2 (R1.14). The additional formation of ClONO_2 (R1.7) may also enhance the Cl^- activation (R1.21). Moreover, the bromide impurities are enriched on the crystal surface (Zangmeister et al. 2001) and may be responsible for the release of photolabile BrCl ($J_{\text{BrCl}} = 7 \times 10^{-3} \text{ s}^{-1}$) at high Cl^-/Br^- ratios according to R1.18 (Fickert et al. 1999). The potentially formed Br atoms were not detected, due to the low detection limit based on the low reactivity of the HCs toward Br (Wittmer et al. 2015a). However, when 0.5 g of NaBr were added to 99.5 g of NaCl, a significant Br production was observed ($Q_{\text{Br}} = 2.6\text{--}3.1 \times 10^{10} \text{ cm}^{-3} \text{ h}^{-1}$), whereas the Cl production was slightly lower compared to the pure NaCl sample ($Q_{\text{Cl}} = 1.6\text{--}1.7 \times 10^{10} \text{ cm}^{-3} \text{ h}^{-1}$; Figure 1.8). The main reason for this observation is probably the Br^- surface enrichment and the favored production of Br_2 instead of BrCl at these low Cl^-/Br^- ratios (Fickert et al. 1999). Additionally, the uptake of O_3 or of OH and subsequent release of Br_2 and BrCl may partly contribute to the observations (Hirokawa et al. 1998; Mochida et al. 2000; Frinak and Abbatt 2006, Jonathan P. D. 2006; Park et al. 2009; Nissenon et al. 2014).

The addition of MgCl_2 and $\text{Na}_2\text{C}_2\text{O}_4$ caused a slightly lower Cl production, which could be caused by the shift in pH. Adding 2 g of catechol to 98 g of NaCl did not result in a detectable Cl production.

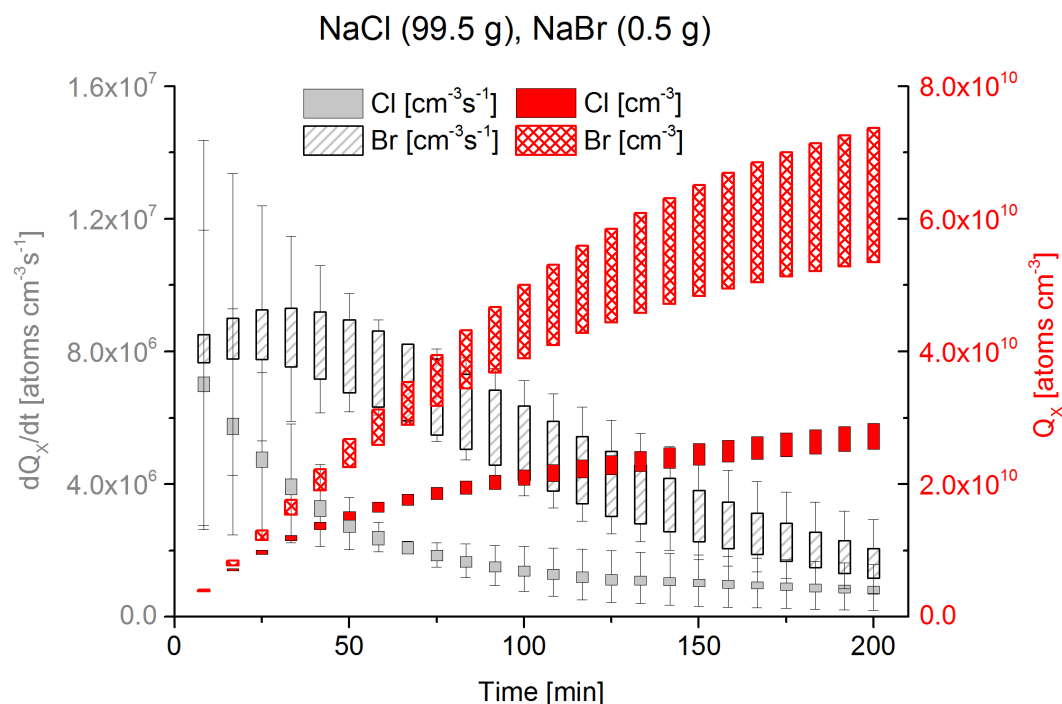


Figure 1.8: Production rates dQ_x/dt (grey) and integrated total production Q_x (red) of Cl and Br during the iron-free blank experiment with a mixture of 99.5 g of NaCl and 0.5 g of NaBr in the salt pan. The lower and upper margins of the bars represent the minimal and maximal values. For the dQ_x/dt , the negative minimum and the positive maximum uncertainties are included as thin error bars. Adopted and modified from Wittmer et al. (2015a).

FeCl₃·6H₂O containing Salt Pans

Adding FeCl₃·6H₂O to the salt mixtures significantly enhanced the observed Cl production. For instance, adding 2 g of FeCl₃·6H₂O to 98 g of NaCl led to a total consumption of the HCs within 30 min with an estimated Cl source of $(8\text{--}50) \times 10^{11} \text{ cm}^{-3} \text{ h}^{-1}$ (based on only two measurement points). A second irradiation (after 24 h flushing with humidified zero air) still showed a Cl production rate up to 30 times higher and a total production 10–20 times higher ($Q_{\text{Cl}} = 63\text{--}89 \times 10^{10} \text{ cm}^{-3} \text{ h}^{-1}$) compared to the NaCl blank sample. In an additional experiment, a freshly prepared salt pan with the same composition was irradiated for 12 h in the presence of ~9 ppm CH₄ without HC addition at constant conditions (RH = 60 %, T = 20°C, dilution flow = 3.2 L min⁻¹). The hardly detectable CH₄ depletion (based on the slow reaction rate $k_{\text{CH}_4, \text{Cl}} = 9.65 \times 10^{-14}$ at 20°C; Atkinson et al. 1997) from 8842 ppb to 8731 ppb within the first hour lead to a rough estimate of a total Cl production of $(2\text{--}3) \times 10^{12} \text{ cm}^{-3}$ (correcting the calculated quasistationary Cl concentration of $(3\text{--}4) \times 10^7 \text{ cm}^{-3}$ for the CH₄ burden and integrating over 3600 s).

When CH₄ reacts with Cl atoms, the ¹²CH₄ isotopomer is slightly faster removed than ¹³CH₄, leading to an enrichment of ¹²CH₄. To prove the CH₄ + Cl reaction in the salt pan experiment, the ¹²C/¹³C fractionation was determined by GC/C/IRMS (gas chromatography/combustion/isotope ratio mass spectrometry, described in Greule et al. (2012)) at the MPIC Mainz, Germany. The result was compared to the determination of the ¹²C/¹³C kinetic isotope effect (KIE, ratio of the rate constants of light and heavy isotopes) in the chamber set-up measured by manual Cl₂ injection (Rießner Gase, 0.971

% Cl₂ in N₂) with constant irradiation in the presence of ~9 ppm CH₄ in a zero air environment at 20°C. The air samples were taken hourly in pre-evacuated (<10⁻⁵ torr), electropolished 2 L stainless steel canisters. The resulting Rayleigh plot (Figure 1.9) leads to a KIE of 57 ‰ (represented by the slope; Saueressig et al. 1995) that roughly agrees with literature values of 58–66 ‰ at 25°C (Feilberg et al. 2005 and references therein). Including the air sample after 12 h irradiation of the salt pan in the Rayleigh plot illustrates a slight depletion in ¹²C which is a hint towards the reaction of CH₄ with Cl.

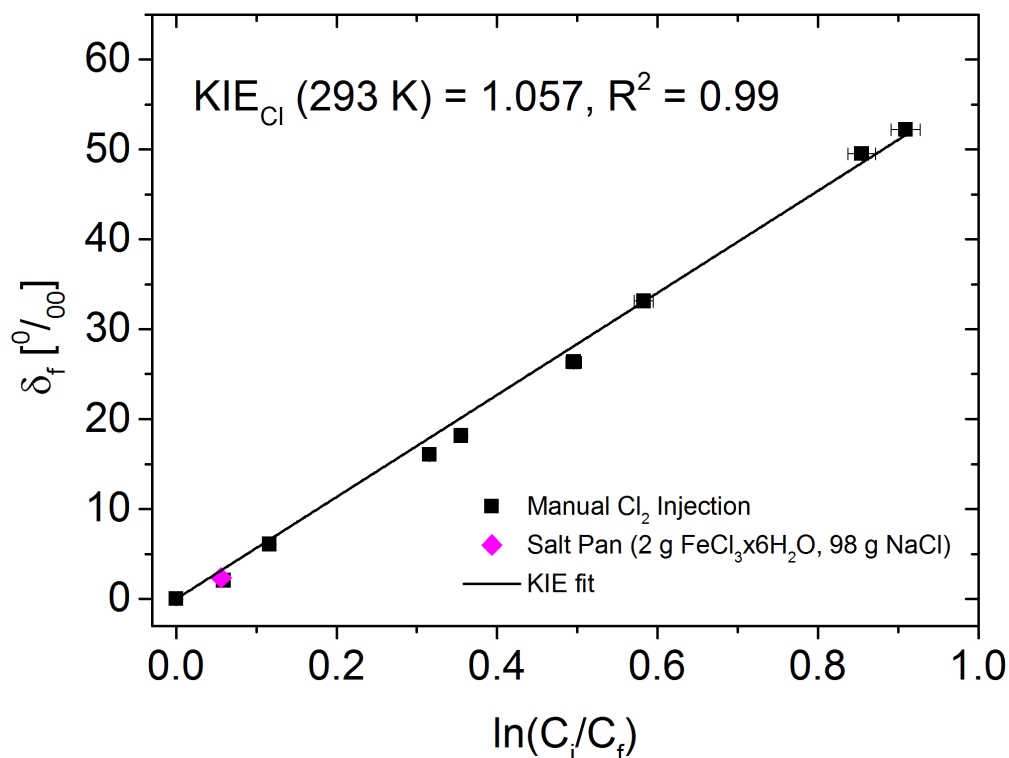


Figure 1.9: ¹²C/¹³C (R) isotope fractionation during the reaction of CH₄ with Cl in the manual Cl₂ injection experiment and the iron-containing salt pan experiment. C_i and C_f are the initial and actual CH₄ concentrations. δ_f represents the shift in δ¹³C ((R_{sample}/R_{standard}-1)×1000) by subtracting the initial δ¹³C value at the beginning of the experiment from the actual δ¹³C value.

Reducing the added FeCl₃·6H₂O from 2 g to 0.5 g, resulted in a slight decrease of the Cl source to $Q_{\text{Cl}} = (52\text{--}57) \times 10^{10} \text{ cm}^{-3}$ in the first 60 min of irradiation. The increase of the Cl production by more than one order of magnitude, when adding 0.5 g or 2 g of FeCl₃·6H₂O, proves the effect of Fe^{III} on the Cl activation as described in section 1.1.2. The additional drop in pH from ~5 of the NaCl sample to 2–2.5 of the iron-containing sample, causes optimal speciation conditions and supports the degassing of Cl₂ (see section 1.4.1). A possible regeneration of iron by reoxidation (and thus reactivation) of Fe^{II} was investigated by repeated irradiation of the 0.5 g FeCl₃·6H₂O/99.5 g NaCl mixture. The procedure of irradiation with a subsequent dark period of 1 to 7 days was performed 5 times (see Wittmer et al. 2015a). Even if a systematic tendency towards a changed Cl production as a function of number of irradiations or regeneration time was hardly noticeable, the experiments confirmed an enhanced Cl activation compared to the NaCl blank in each run. The minimum Q_{Cl} was $\geq 10^{11} \text{ cm}^{-3}$ after 100 min of irradiation of the iron doped salt pan in contrast to $(5.8\text{--}5.9) \times 10^{10} \text{ cm}^{-3}$ for 100 g of NaCl.

Figure 1.10 summarizes the results of the experiments and includes the additions of NaBr, Na₂C₂O₄, Na₂SO₄ and H₂C₂O₄ to the iron-free and iron-containing salt mixtures. The Na₂C₂O₄ (2 g)/FeCl₃·6H₂O (2 g)/NaCl (96 g) mixture showed a significantly lower Cl production ($Q_{Cl} = 6.7\text{--}6.9 \times 10^{10} \text{ cm}^{-3} \text{ h}^{-1}$), compared to the FeCl₃·6H₂O (2 g)/NaCl (98 g) sample due to the effects of oxalate. In particular, sodium oxalate shifts the pH to a less acidic range, and oxalate anions form stable complexes dominating the Fe^{III}-Cl complexes (Wittmer et al. 2015a). In a subsequent run, including oxalic acid instead of sodium oxalate, the sensitivity towards the pH was demonstrated by the observation of a higher Cl production ($Q_{Cl} = 13\text{--}15 \times 10^{10} \text{ cm}^{-3} \text{ h}^{-1}$). An optimized ratio of oxalate and Fe^{III} at an acidic pH may provide a sustainable iron-induced Cl formation, by forming H₂O₂ from photolysis of Fe^{III}-oxalato complexes and reoxidizing Fe^{II} (Zuo and Hoigné 1992). An approximately constant Cl production until the end of irradiation indicates this process, accompanied by a strengthening of the photo-Fenton process. When 0.5 g NaBr was added to the iron-containing salt mixture, a Q_{Cl} -inhibiting effect was observed, comparable to the effect of NaBr addition during the blank experiment. Probably similar reasons account for the decrease in Q_{Cl} to $(11\text{--}12) \times 10^{10} \text{ cm}^{-3} \text{ h}^{-1}$. However, Q_{Br} was ~12 times higher than in the absence of Fe^{III}. Possible explanations are the oxidation of Br⁻ by Cl₂ (Mochida et al. 1998), a preference of Br₂ release instead of BrCl at low pH and high Br⁻/Cl⁻ ratio (0.0067 mol mol⁻¹; Fickert et al. 1999) and an enhanced O₃ uptake with subsequent Br₂ formation in the presence of Fe^{III} (Sadanaga et al. 2001). The Na₂SO₄·10H₂O (5 g)/ FeCl₃·6H₂O (2 g)/NaCl (93 g) mixture resulted in a considerably reduced Cl source ($Q_{Cl} = 5\text{--}5.2 \times 10^{10} \text{ cm}^{-3} \text{ h}^{-1}$). The yellow color of the salt indicated a sulfate complex formation, potentially reducing the light intensity in the sensitive spectral region of the Fe^{III}-Cl complexes. A probably much stronger effect of dissolved SO₄²⁻ and HSO₄⁻ ions on Q_{Cl} is the scavenging of Cl[•] and OH[•] already in the liquid phase (Machulek et al. 2009). As a consequence, the production of sulfate anion radicals is preferred and the Cl₂ formation inhibited. Moreover, when Fe^{II} is formed during irradiation, it tends to form FeSO₄ complexes with sulfate ions (log K = 1.35; de Laat et al. 2004). The salt mixture doped with both, sulfate and oxalate, showed a combination of these effect (complexation + radical scavenging) and led to a drastic reduction of Q_{Cl} to $(1.4\text{--}1.5) \times 10^{10} \text{ cm}^{-3} \text{ h}^{-1}$ (Figure 1.10). An addition of 2 g of catechol had even stronger negative effects, yielding a Cl production below the detection limit. Catechol is highly soluble and acts as a reducing agent, forming extremely stable complexes with iron (Hider et al. 1981).

In all experiments (iron-free and iron-containing) a slight decrease of dQ_X/dt with time could be observed, probably caused by drying of the salt in the course of irradiation. A further explanation is the scavenging of radical intermediates like Cl[•], ClOH[•], Cl₂^{•-} and OH[•] by Fe^{II}, reducing the efficiency of the iron-induced halogen production with time. To roughly estimate the fraction of active iron involved in the photoproduction of Cl, Fe^{III} recycling and additional Cl activation processes were neglected, therefore assuming that each Fe^{III} produces ½ degassing Cl₂. For example, the FeCl₃·6H₂O (0.5 g)/NaCl (99.5 g) mixture resulted in a portion of ~0.17 % active iron, whereas the second irradiation of the FeCl₃·6H₂O (2 g)/NaCl (98 g) mixture yielded ~0.06 %. These low values are expected due to the large inactive bulk in the salt pans and the associated small fraction of active salt crust covered by a QLM. However, the specific surface of a salt pan and the number of microlayers are difficult to determine (Buxmann et al. 2012; Balzer 2012). Hence,

aerosol experiments allow a more quantitative evaluation of the iron-salt interaction (sections 1.4.3 and 1.4.4; Wittmer et al. 2015b; Wittmer and Zetzsch 2015).

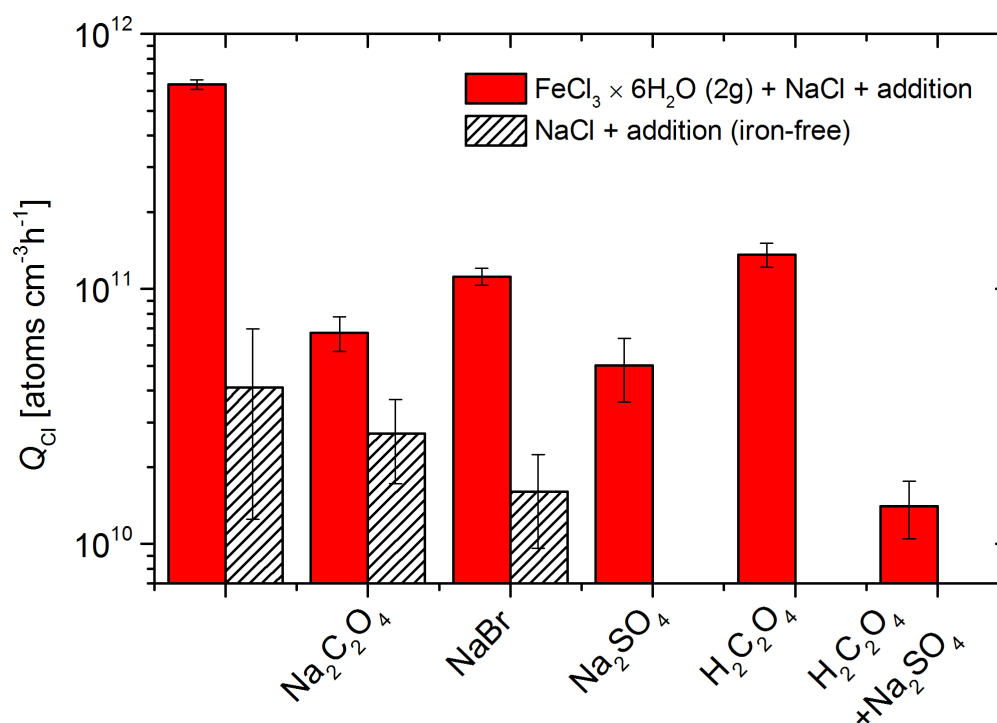


Figure 1.10: Overview on the total minimum Cl source in the 1st hour of the experiments irradiating iron-free and iron-containing salt pans with various additions.

1.4.3 Iron-Induced Chlorine Formation from Artificial Sea-Salt Aerosol

Fe^{III}-catalyzed Cl Activation

The irradiation of Fe^{III}-doped artificial sea-salt aerosol allowed to relate the produced amount of Cl to the active aerosol surface area according to equation 1.8. All experiments were conducted in the same manner: HC injection, 40–60 min waiting period, 30–50 min aerosol injection at 21±1 °C and RH ≥40 % (increasing to 70–90 % due to nebulization), 15 min waiting period, at least 180 min irradiation.

The iron-free blank experiments, applying artificial sea salt and NaCl aerosol particles led to Cl and Br concentrations close to the detection limit (Cl ~ 10⁴ cm⁻³, Br ~ 10⁹ cm⁻³) at initial aerosol surfaces of 0.01 and 0.023 m² m⁻³, respectively. Weighing 0.14 g of FeCl₃ into 1 L of artificial seawater (molar Cl⁻/Fe^{III} = 955) did not show a significant increase in Cl. The stepwise increase of the FeCl₃ addition to obtain Cl⁻/Fe^{III} ratios of (1) 101, (2) 51 and (3) 13 resulted in a corresponding increase in the total Cl production of (1) (0.7–0.8) × 10²¹ atoms cm⁻², (2) (1.4–1.5) × 10²¹ atoms cm⁻², and (3) (6.6–8.7) × 10²¹ atoms cm⁻² in the first 60 min of irradiation (Figure 1.11). The disproportionally stronger increase in Cl production compared to the increase in Cl⁻/Fe^{III} is probably caused by the observed shift in pH. The pH of the respective stock solutions decreased from 3.9–4.2 (1), to 3.3–3.6 (2) and 1.9–2.2 (3), promoting the Fe^{III}-Cl complex formation and Fe^{III} recycling (see section

1.4.1). In fact, adjusting the pH of the $\text{Fe}^{\text{III}}/\text{Cl}^- = 101$ mixture to 2.1–2.3 by adding HCl (Sigma-Aldrich, ACS 32 %) increased Q_{abs} to $(5.3\text{--}5.8) \times 10^{21}$ atoms $\text{cm}^{-2} \text{h}^{-1}$. Here, the low fraction of $\text{Fe}^{\text{III}}\text{-Cl}$ complexes in the unadjusted sample can explain the observation with regard to a fraction of less than 5 % in the stock solution at low ionic strength (Figure 1.7a) and the necessary time to reach the speciation equilibrium in the aerosol.

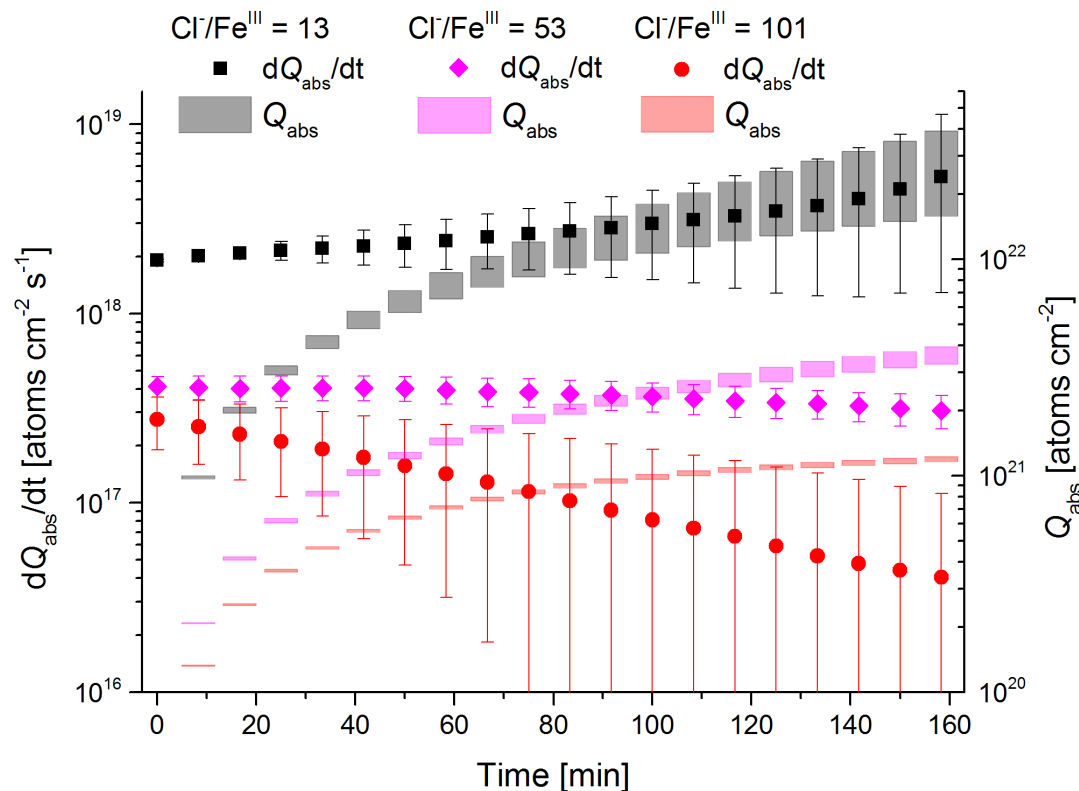


Figure 1.11: Absolute gaseous mean Cl production rate (dQ_{abs}/dt) and time integrated total minimum and maximum Cl production Q_{abs} per cm^2 of aerosol surface during the experiments with Fe^{III} -doped art. seawater at various Fe^{III} concentrations: $\text{Cl}^-/\text{Fe}^{\text{III}} = 13$ (black), 53 (magenta), 101 (red). The light was switched on at 0 min. Adopted from Wittmer et al. (2015b).

A higher Cl formation rate could be observed from a $\text{NaCl}/\text{FeCl}_3$ sample ($\text{Cl}^-/\text{Fe}^{\text{III}} = 13$, $Q_{\text{abs}} = 8.7\text{--}13 \times 10^{21}$ atoms $\text{cm}^{-2} \text{h}^{-1}$) compared to the respective artificial seawater sample. The presence of additional ions (e.g. sulfate) resulted in comparable effects to the salt pan experiments when Na_2SO_4 was added.

In contrast to the salt pan experiments (section 1.4.2), the Cl production by the aerosol showed more constant production rates with time (Figure 1.11). One reason is the weak drying and heating effect (compared to the salt pans) concerning the liquid aerosol particles at $\text{RH} > 70\%$ being above their efflorescence point (Warneck 1999) and showing no significant change of the size distribution with time (Chapter 3, Figure S3.1). Further, the aerosol particles are nearly homogeneously distributed within the chamber and thus provide a homogeneous mixture of reactants in contrast to a rather local RHS source from the salt pans.

Effects of NO₂, O₃, SO₂

In this series of experiments, the impact of typical atmospheric pollutants and trace gases on the iron-induced halogen activation was investigated. The same salt mixtures as described in the last section were irradiated in the presence 20 ppb NO_x, 630 ppb O₃, 20 or >200 ppb SO₂, respectively. Indeed, these concentrations are elevated in comparison to the marine boundary layer (MBL). Nevertheless, the achieved ratio of pollutant to aerosol concentration (2–6 mg m⁻³) is approximately in agreement with marine conditions.

In case of NO₂ addition, a fast formation of O₃ was observed during irradiation, based on reactions R1.15–R1.17. Due to the reoxidation of NO by HO₂ (R1.14), formed during HC depletion, the O₃ mixing ratio even exceeds the initial NO₂ mixing ratio. The Cl concentration remained below the detection limit during the iron-free blank experiment, therefore, the additional activation mechanisms induced by potential NO₃ and N₂O₅ formation (only in the presence of O₃ during irradiation) do only play a minor role. However, for Fe^{III}-doped sea-salt aerosol (Cl⁻/Fe^{III} = 13) and 20 ppb NO₂, an enhanced Cl production of $Q_{\text{abs}} = (16\text{--}52) \times 10^{21}$ atoms cm⁻² h⁻¹ was detected (Figure 1.12). Based on the simultaneous fast depletion of NO_x and NO in the gas phase, the formation and uptake of XONO₂ (R1.7, R1.21) could be responsible for an additional Cl₂ and BrCl formation (R1.18, R1.19), whereas the formation of XNO₂ probably plays a minor role (see section 1.1.2 or Rossi 2003). Moreover, the gaseous formation and uptake of HNO₃ by the reaction of NO₂ and OH may contribute to the Cl production cycle by aerosol acidification (supporting Fe^{III}-Cl complex formation and acid displacement of HCl) and reoxidation of Fe^{II} through photolysis in the aqueous phase (Vione et al. 2006). The HCl degassing and subsequent Cl formation by reaction with OH (R1.9) is estimated to be negligible (Zetzsch and Behnke 1993; Wittmer et al. 2015b).

The presence of O₃ significantly enhanced the halogen activation already in the blank experiment ($Q_{\text{abs,Cl}} = 3.1\text{--}4.9 \times 10^{21}$ atoms cm⁻² h⁻¹, $Q_{\text{abs,Br}} = 1.6\text{--}2.8 \times 10^{21}$ atoms cm⁻² h⁻¹). The observed O₃ destruction (lifetime ~ 10⁴ s) during irradiation indicates the autocatalytic O₃ destruction via R1.1, R1.6, R1.18 and R1.19 and subsequent heterogeneous halogen activation. Moreover, the presence of O₃ (R1.10, R1.11) may contribute to the halogen activation by formation and uptake of NO₃ and N₂O₅ (with 3–5 ppb of NO_x present after aerosol injection; Wittmer et al. 2015b) and a subsequent X₂ or XNO₂ release (R1.22; Finlayson-Pitts et al. 1989; Fenter et al. 1996; Rudich et al. 1996; Behnke et al. 1997; Thornton et al. 2010), or by direct uptake of OH and subsequent X₂ release (Knipping et al. 2000). The application of the iron-containing sample led to a four times faster O₃ destruction and to a disproportionately large increase in Q_{abs} ($Q_{\text{abs,Cl}} = 18\text{--}45 \times 10^{21}$ atoms cm⁻² h⁻¹, $Q_{\text{abs,Br}} = 3\text{--}8.1 \times 10^{21}$ atoms cm⁻² h⁻¹) compared to the increase when O₃ was added to the blank sample. Possible explanations for this observation are the lower aerosol pH that promotes the autocatalytic halogen release, the enhanced O₃ uptake in the presence of dissolved Fe^{III} (Sadanaga et al. 2001) and the enhanced formation and uptake of H₂O₂ (R1.8) induced by O₃, that may oxidize Fe^{II} back to Fe^{III}.

The SO₂ experiments showed an inhibiting impact on the measured Cl production. With increasing SO₂ mixing ratios, the production decreased ($Q_{\text{abs}} = 6\text{--}6.7 \times 10^{21}$ atoms cm⁻² h⁻¹ at ~20 ppb SO₂ and $Q_{\text{abs}} = 4\text{--}4.5 \times 10^{21}$ atoms cm⁻² h⁻¹ at >200 ppb SO₂). A SO₂ uptake and formation of bisulfite or sulfate (oxidation catalyzed by Fe^{III}; Novič et al. 1996)

explains the inhibition of the halogen activation in the liquid phase by the reaction of HOX with sulfite (Troy and Margerum 1991) or by the radical scavenging of sulfate (Machulek et al. 2009; Wittmer et al. 2015a). A significant uptake of SO₂ on sea-salt aerosol particles was reported by e.g. Gebel et al. (2000) and Hoppel et al. (2001). A further effect is the gas-phase oxidation of SO₂ by OH ($k_{\text{SO}_2+\text{OH}} = 1.3 \times 10^{-12} \text{ cm}^3 \text{ molecules}^{-1} \text{ s}^{-1}$ at 25°C; Atkinson et al. 2004) reducing the OH concentrations (Wittmer et al. 2015b) and thus intervening in the formation of HO₂ and H₂O₂, which are important agents for halogen activation (see section 1.1.1 and 1.1.2).

Fraction of Active Iron

Combining the measured liquid water content at the beginning of irradiation (LWC₀, corrected for the tare volume of the ions; see Wittmer et al. 2015b) with the minimum total Cl production Q_{Cl} and an assumed saturated Cl⁻ concentration in the aerosol (~6.1 mol L⁻¹) at a given Cl⁻/Fe^{III} ratio ($R_{\text{Cl/Fe}}$) allows to roughly estimate the minimum fraction of active iron (λ_{Fe}) involved in the Cl production:

$$\lambda_{\text{Fe}} = \frac{Q_{\text{Cl},\text{min}} \times R_{\text{Cl/Fe}}}{\text{LWC}_0 \times 6.1 \times N_{\text{A}}} \quad (1.11)$$

where N_{A} is the Avogadro constant ($6 \times 10^{23} \text{ mol}^{-1}$). The iron recycling effects (each Fe^{III} ion produces ½ Cl₂) and secondary activation mechanisms are excluded in this approach. Figure 1.12 summarizes the observed minimum and maximum absolute productions combined with the estimated minimum λ_{Fe} during the 1st hour for each experiment with iron-doped artificial sea-salt aerosol. The comparable λ_{Fe} of ~ 50 % for the samples with varying Cl⁻/Fe^{III} ratio in zero air indicates similar activation mechanisms. The increase of λ_{Fe} and Q_{abs} in the presence of NO_x and O₃ is a phenomenon caused by the additional activation mechanisms (see previous section). The inhibiting effect of high SO₂ mixing ratios decreases both, Q_{abs} and λ_{Fe} . The decrease in pH of the Cl⁻/Fe^{III} = 101 sample raised the fraction of active iron to more than 100 %. Excluding additional activation mechanisms induced by NO_x and O₃, this is a consequence of the higher fraction of Fe-Cl complexes and also an evidence for the iron recycling process (reoxidation of Fe^{II}). In comparison to the estimated active iron fractions from 0.06–0.17 % in the salt pan experiments (section 1.4.2), the high efficiency of the aerosol is evident, as the salt pans contain most of the iron in the inactive bulk.

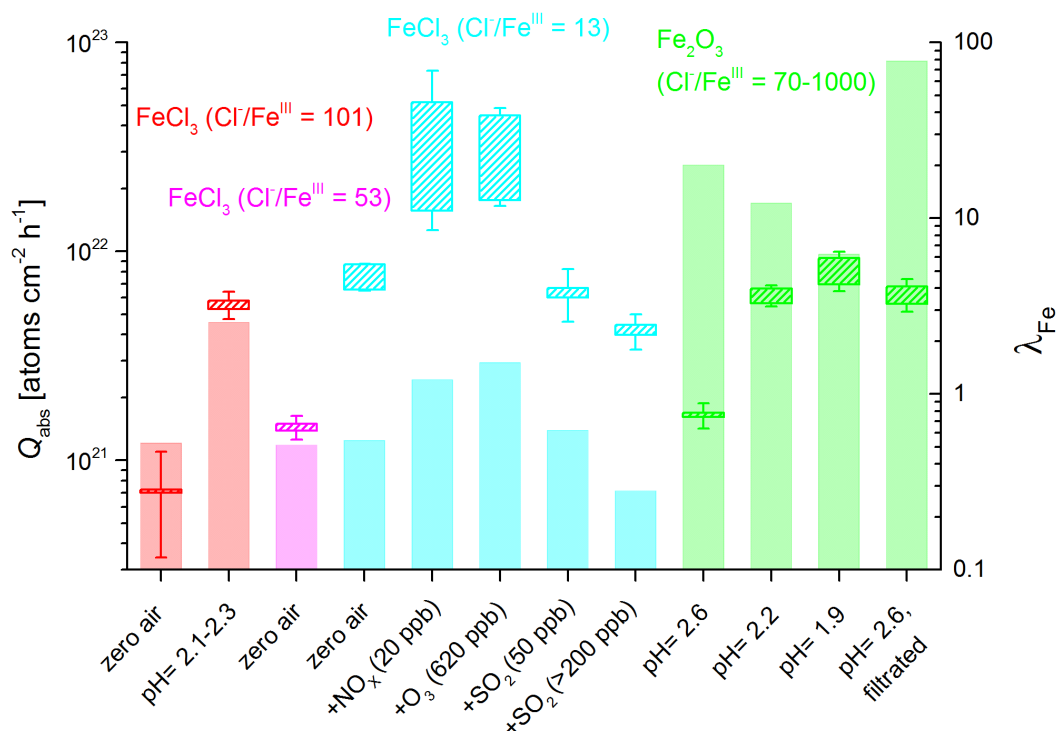


Figure 1.12: Overview of the minimum and maximum absolute Cl production Q_{abs} [atoms cm⁻² h⁻¹] over the first hour (hatched boxes) and the corresponding fraction of active Fe^{III} (λ_{Fe} , filled bars) for each experiment with FeCl₃ or Fe₂O₃ containing art. seawater samples at various pH or various air contaminants (NO_x, O₃, SO₂). Adopted and modified from Wittmer et al. (2015b).

1.4.4 Photochemical Activation of Chlorine by Iron-Oxide Aerosol

Fe₂O₃ in Artificial Sea Salt

In this series of experiments, the activity of Fe₂O₃ (Sicotrans Orange, L2515D, BASF, specific surface area: 152 m² g⁻¹ determined by BET measurement at the Faculty of Engineering Sciences, University of Bayreuth) in an artificial sea-salt matrix was investigated. After adding 17 mg of Fe₂O₃ to 100 mL artificial seawater, the pH of three samples was adjusted to 2.6, 2.2 and 1.9 (measured by a pH meter, pH 3110, WTW) by adding 30, 55 and 110 μL of HCl (Sigma-Aldrich ACS, 37%), respectively. The pH adjustment was done to promote the dissolution, which proceeds via R.1.34 and further forms Fe^{III}-Cl and hydroxy complexes (see section 1.4.1 and Figure 1.7):



The amount of dissolved iron (Fe_d) was determined by passing the respective sample aliquot through a 0.025 μm filter (Whatman Anotop 10 Plus) combined with a 0.45 μm pre-filter (Millipore) and by subsequent quantification by ICP-OES (Central Analytics, BayCEER, University of Bayreuth). Since the reference measurements without pH adjustment did not lead to detectable amounts of Fe_d , the contribution of iron colloids smaller than 0.025 μm is thus considered to be negligible. The resulting Fe_d concentrations after 7 days of equilibration time were 0.031 (pH 2.6, Cl⁻/ Fe_d ~1031), 0.21 (pH 2.2, Cl⁻/ Fe_d ~166) and 0.58 (pH 1.9, Cl⁻/ Fe_d ~71) mmol L⁻¹. These results demonstrate the high pH dependency of Fe_d (see also Zhu et al. 1992). The equilibration

time is of importance since the Fe_d concentration increases with time, whereas after 7 days an equilibrium is approached (Kuma et al. 1996; Liu and Millero 2002). The reference sample without pH adjustment did not show detectable amounts of Fe_d ($<0.001 \text{ mmol L}^{-1}$) and the Cl production of the corresponding aerosol was below the detection limit. An acceleration of the dissolution by freezing at -20°C for 1–3 h and thawing at 20°C for five times, did not result in detectable amounts, although an increase of factor 2 of the dissolution rate is reported in literature (Jeong et al. 2012). However, the Fe_d remains below the significant fraction of $\sim 1\%$ from the amount of added Fe_2O_3 to obtain $\text{Cl}/\text{Fe}_d < 1031$, which is needed for a reliable detection of the Cl production (Wittmer and Zetzsch 2015).

The nebulization and irradiation of the pH adjusted samples led to a significant Cl production of $(1.6\text{--}1.7) \times 10^{21} \text{ atoms cm}^{-2}$ (pH 2.6), $(5.6\text{--}6.6) \times 10^{21} \text{ atoms cm}^{-2}$ (pH 2.2) and $(7.0\text{--}9.3) \times 10^{21} \text{ Cl atoms cm}^{-2}$ (pH 1.9) during the 1st hour of irradiation, indicated in Figure 1.12. The nonlinear increase of Q_{abs} with increasing acidity may be caused by the parallel decrease of λ_{Fe} (Figure 1.12, 20 for pH 2.6, 12 for pH 2.2, 6 for pH 1.9, calculated according to equation 1.11). This observation is in contrast to FeCl_3 in artificial sea salt, where λ_{Fe} increased with decreasing pH. Though, the iron oxide samples are in the pH range with a low fraction of Fe^{III} -hydroxy (FeOH^{2+} , $\text{Fe}(\text{OH})_2^+$) complexes (see section 1.4.1), where the photochemical formation of OH^\bullet radicals (and thus H_2O_2) and Fe^{II} reoxidation is inhibited (Kiwi et al. 2000; Machulek et al. 2006). The systematically higher λ_{Fe} values of the Fe_2O_3 containing samples (compared to the FeCl_3 solutions) could be explained by the slightly larger specific surface area considering the smaller mean particle diameter (Figure 1.5) and the porous structure of the Fe_2O_3 agglomerates (Figure 1.6a). In order to investigate the influence of the particulate Fe_2O_3 phase, a filtrated aliquot of the pH 2.6 sample was nebulized and irradiated in an additional experiment. The observed strong increase in Q_{abs} ($5.6\text{--}6.8 \times 10^{21} \text{ Cl atoms cm}^{-2} \text{ h}^{-1}$) and in λ_{Fe} (7800 %) may again originate from the smaller mean particle diameter (Figure 1.5) and an enhanced availability of dissolved iron.

Cl Formation by HCl Uptake on Fe_2O_3 Aerosol

In the experiments, pure hydrated Fe_2O_3 aerosol particles were generated by nebulization of a Fe_2O_3 -water suspension and subsequently exposed to various mixing ratios of gaseous HCl (Sigma-Aldrich ACS, 37%). HCl was injected by a syringe into a heated glass injection port flushed with zero air. The main challenge in these experiments was the estimation of heterogeneous and homogeneous background Cl production that contributed to the total detected Cl production. Therefore, blank experiments were conducted including the injection of 5 μL HCl in the presence and absence of SiO_2 aerosol particles. The aerosol-free experiment revealed a homogeneous background production of $(2.6\text{--}2.7) \times 10^{10} \text{ Cl atoms cm}^{-3} \text{ h}^{-1}$ according to the reaction R1.9. The theoretical production rate at a detected OH concentration of $\sim 2 \times 10^6 \text{ cm}^{-3}$ and with the reaction rate $k_{\text{HCl+OH}} = 7.6 \times 10^{-13} \text{ cm}^3 \text{ molecules}^{-1} \text{ s}^{-1}$ at 20°C (Atkinson et al. 2007) for the injected amount of 5 μL HCl ($\sim 345 \text{ ppb}$) is $4.6 \times 10^{10} \text{ atoms cm}^{-3} \text{ h}^{-1}$. Compared to the measured rate of $(2.6\text{--}2.7) \times 10^{10} \text{ Cl atoms cm}^{-3} \text{ h}^{-1}$, the determined reproducibility (ρ) of 56–59 % is probably caused by injection and wall losses of HCl. In the presence of SiO_2 , an enhanced Cl production of $(1.1\text{--}1.2) \times 10^{11} \text{ Cl atoms cm}^{-3} \text{ h}^{-1}$ (related to the aerosol surface: $2.6\text{--}2.7 \times 10^{21} \text{ Cl atoms cm}^{-2} \text{ h}^{-1}$) was observed. In agreement with the

results of Zetzsch and Behnke (1993), this was caused by additional heterogeneous activation mechanisms (see section 1.1.2). For instance, HOCl and Cl^- produce Cl_2 (R1.19) on aerosol particles in the absence of bromide when acidified by HCl uptake (Vogt et al. 1996; Rossi 2003). Moreover, Knipping et al. (2000) report an uptake of OH and a subsequent Cl_2 formation from the primarily formed ClOH^* (section 1.1.2).

Subtracting the homogeneous fraction from the SiO_2 experiment leads to the pure heterogeneous background production of $Q_{\text{bg,het}} = (2.0\text{--}2.1) \times 10^{21}$ Cl atoms $\text{cm}^{-2} \text{h}^{-1}$. To account for the background production in the Fe_2O_3 aerosol experiments, an effective (absolute) Cl production (Q_{eff}) is determined by considering the homogeneous and heterogeneous fraction (4.3).

$$Q_{\text{eff}}(t) = \frac{(Q_{\text{Cl}}(t) - \rho \times [\text{OH}] \times [\text{HCl}] \times k_{\text{HCl+OH}} \times t) \times V_{\text{Ch}}}{A_{\text{eff}}(t)} - Q_{\text{bg,het}}(t) \quad (1.12)$$

where $Q_{\text{Cl}}(t)$ is the integrated total Cl production (atoms cm^3) at time t (section 1.3.3), $[\text{OH}]$ and $[\text{HCl}]$ are the quasistationary OH and HCl concentrations (assumed to be constant), V_{Ch} is the chamber volume, $A_{\text{eff}}(t)$ is the effective surface area (section 1.3.3), and $Q_{\text{bg,het}}$ the integrated heterogeneous background production at time t (Wittmer and Zetzsch 2015).

The Fe_2O_3 experiment with 5 μL HCl injection resulted in a Q_{eff} of $(4.1\text{--}4.9) \times 10^{22}$ atoms $\text{cm}^{-3} \text{h}^{-1}$ at $[\text{OH}] = 5 \times 10^6 \text{ cm}^{-3}$ and $\text{RH} = 61 \%$. Decreasing the amount of HCl to 3.5, 1.2, and 0.6 μL yielded an appropriate decrease in Q_{eff} to (13–14), (2.8–2.9) and (0.7–0.8) $\times 10^{21}$ atoms $\text{cm}^{-3} \text{h}^{-1}$, respectively (Figure 1.13) at $[\text{OH}] = (4.6\text{--}7.4) \times 10^6 \text{ cm}^{-3}$ and $\text{RH} = 52\text{--}61 \%$. In addition, a high and low RH run at the same amount of HCl injected showed a strong dependency of Q_{eff} on RH. With decreasing RH, Q_{eff} increased from $(2.3\text{--}2.8) \times 10^{21}$ atoms $\text{cm}^{-3} \text{h}^{-1}$ ($\text{RH} = 76 \%$) to $(78\text{--}91) \times 10^{21}$ atoms $\text{cm}^{-3} \text{h}^{-1}$ ($\text{RH} = 42 \%$). Whereas the number of water layers on the particles changes only slowly in this RH range (Cwiertny et al. 2008), the adsorbed water on the Teflon wall is known to increase exponentially with increasing RH (Svensson et al. 1987; Wahner et al. 1998), intensifying the wall sink of HCl and thus reducing the Cl production. The Cl yields calculated by the molar ratio of Cl produced in the first 200 min of irradiation (corrected for the homogeneous background) and the injected molar amount of HCl, resulted in a range of 2–5 %, except for the high RH experiment (below 1 %). These yields were independent of the provided surface area which varied from $(1\text{--}6) \times 10^{-3} \text{ m}^2 \text{ m}^{-3}$.

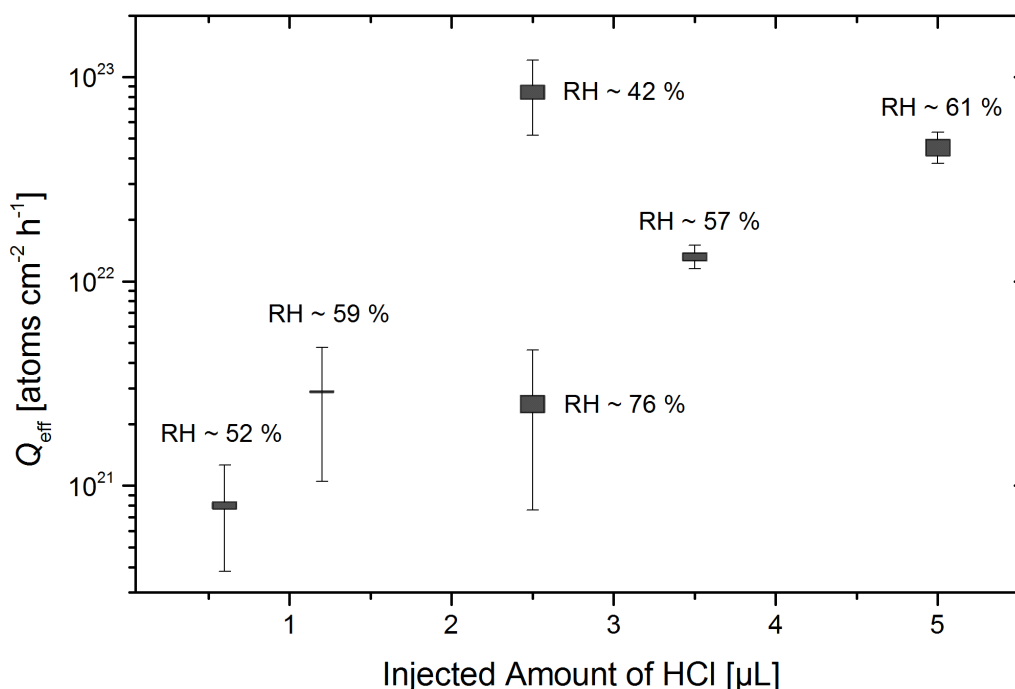


Figure 1.13: Total amount of Cl atoms per hour and per cm² aerosol surface of Fe₂O₃ (corrected for the heterogeneous and homogeneous background) produced at various HCl concentrations. The RH is labeled for each experiment. The lower and upper margins of the bars represent the minimal and maximal values. The error bars represent the respective negative minimum and the positive maximum uncertainty. Adopted from Wittmer and Zetzsch (2015).

1.5 Conclusions and Outlook

Up to now, the role of iron in halogen-activation processes was not in the focus of atmospheric research. The present atmospheric models largely do not consider the chemical activity of iron in aerosol particles in terms of gaseous halogen production. The present work performs the first efforts to clarify the relevance of iron induced halogen formation in natural environments and helps to estimate a potential contribution to the RHS formation in saline environments with a large iron burden. Therefore, the behavior of iron in saline media at different conditions was systematically explored, from speciation model to measurement. The calculated speciation showed a large fraction of photolabile Fe-Cl complexes in chloride dominated media at high ionic strength for pH values below 4.5. In the less acidic range the Fe-hydroxy complexes become dominant. This general constellation is only disturbed by strong organic ligands (e.g. oxalate or catechol), whereas a fraction of other inorganic anions (SO₄²⁻, Br⁻, F⁻), as present in seawater, has no considerable influence on iron speciation at high salinities. Dissolved sulfate anions rather scavenge the produced radicals already in the aqueous phase and thus inhibit the halogen activation.

The investigation of Fe^{III}-doped salt pans revealed a promoting effect of Fe^{III} on gaseous Cl and Br production and the influence of inorganic and organic contaminants. A five times repeated irradiation of an iron-containing salt pan resulted in an elevated Cl production, compared to an iron-free sample, due to the recycling of Fe^{III}. The Cl source increased with Fe^{III} content and decreased in the presence of Br⁻, SO₄²⁻, oxalate and

catechol due to speciation and pH effects, radical scavenging, or the surface enrichment and preference of bromide activation at low Cl^-/Br^- ratios (Wittmer et al. 2015a).

In the second study (Wittmer et al. 2015b), Fe^{III} -doped artificial sea-salt aerosol was exposed to simulated sunlight and various trace-gas pollutants (NO_x , O_3 , SO_2). The application of aerosol particles allowed to quantify atomic halogen production in relation to the reactive surface area. The Cl production significantly increased with the Fe^{III} -load in the aerosol from $(0.7\text{--}9) \times 10^{21}$ Cl atoms $\text{cm}^{-2} \text{h}^{-1}$ for $\text{Cl}^-/\text{Fe}^{\text{III}}$ ratios ranging from 101–13. NO_x and O_3 additions considerably enhanced the activation process, whereas the presence of SO_2 slightly inhibited the chlorine release. Moreover, an acidification of the stock solution from pH ~ 4 to ~ 2.2 led to an increase of gaseous Cl formation by almost an order of magnitude and therefore provided evidence for the speciation effects. An estimate of the fraction of iron involved in the Cl production resulted in values around 50 % with a significant rise to >100 % when NO_x and O_3 were present, indicating their reinforcing effect and the additional activation mechanisms.

The third study (Wittmer and Zetzsch 2015) deals with the behavior of solid iron oxide, embedded in a sea-salt matrix, and with the role of pure iron-oxide aerosol, exposed to gaseous HCl. As for the standard mixture of Fe_2O_3 and artificial seawater, no significant amount of dissolved iron and thus no Cl production could be detected without acidification. Adjusting the pH below 3, an enhanced iron dissolution (increasing with acidity) accompanied by strong gaseous Cl productions in the range of $(1\text{--}10) \times 10^{21}$ Cl atoms $\text{cm}^{-2} \text{h}^{-1}$ were observed. The fractions of active iron ranging between 600 and 2000 % prove the recycling effect iron. Furthermore, the iron-induced Cl production could also be demonstrated for gaseous HCl that is absorbed on iron-oxide aerosol particles.

Especially the last finding is of high relevance for atmospheric processes in terms of iron containing mineral dust and combustion-aerosol particles in marine environments with a steady presence of HCl. The observed Cl^- enrichment in mineral dust during atmospheric processing (Sullivan et al. 2007b) is a further hint at a significant atmospheric role of this process. Though, mineral dust contains ~ 3.5 % of iron on average (Duce and Tindale 1991), and the HCl uptake is mainly ascribed to the reaction with $\text{CaCO}_{3(\text{s})}$ (Tobo et al. 2009). Considering the natural iron content in sea-salt aerosol, the mean molar Cl^-/Fe ratio of 100–200 (Central Atlantic; Warneck 1999) suggests a significant effect of iron with regard to a low aerosol pH (Keene et al. 1998). However, smog chambers typically provide a much higher aerosol-surface to air-volume ratio compared to the MBL. The present chamber experiments showed a 20–200 times larger aerosol-surface area than in the MBL and an additional enrichment of the produced gas-phase species. Hence, the iron-induced halogen production may have rather local impacts when particles with a large Fe^{III} burden come into contact with highly saline media (see section 1.1.3).

To integrate the findings of this thesis into a larger context, the results should be reproduced by a chemical box model and, in a further step, applied for global model calculations (e.g. Herrmann et al. 2003; Tilgner et al. 2013) to estimate the contribution of iron-induced Cl formation to the tropospheric budget of atomic Cl. To facilitate the incorporation into the models, the experimental conditions can be adapted to natural conditions by applying natural mineral-dust aerosol or by a systematic investigation of natural salt samples.

1.6 Nomenclature

1.6.1 Acronyms

CFC	Chlorofluorocarbon
Fe_D	Dissolved iron
FEP	Fluorinated ethylene propylene
GC	Gas chromatography
HC	Hydrocarbon
HMI	Hydrargyrum medium-pressure arc iodide
KIE	Kinetic isotope effect
LWC	Liquid water content
MBL	Marine boundary layer
NO_x	Nitrogen oxides: NO and NO ₂
ppm	Parts per million
ppb	Parts per billion
ppt	Parts per trillion
TUV	Tropospheric ultraviolet and visible radiation model
UV	Ultraviolet
QLM	Quasi-liquid microlayer
RH	Relative humidity
RHS	Reactive halogen species
SEM-EDX	Scanning electron microscope with an energy dispersive X-ray detector
VOC	Volatile organic compound
X	Halogens: Cl and Br

1.6.2 Symbols

A	Measured aerosol-surface area [cm^2]
A_{eff}	Effective active surface area [cm^2]
$a_i(N)$	Approximation coefficient for $f(N)$
C	Slip-correction factor
$c_{\text{I}\pm}$	Ion concentration
D_p	Particle mobility diameter [nm]
e	Elementary charge [1.6×10^{-19} C]
F	Actinic flux [photons $\text{cm}^{-2} \text{nm}^{-1} \text{s}^{-1}$]
$f(N)$	Particle charge distribution
H^{cp}	Henry's law constant c/p (concentration of a species in the aqueous phase/partial pressure in the gas phase) [$\text{mol m}^{-3} \text{Pa}^{-1}$]
J_A	Photolysis rate of a molecule A [s^{-1}]
K	Equilibrium constant; concentration ratio of involved species
k	Boltzmann's constant [1.38×10^{-23} J K^{-1}]
k_{X+Y}	2 nd order reaction rate constant between species X and Y [$\text{cm}^3 \text{molecules}^{-1} \text{s}^{-1}$]
N_A	Avogadro's constant [$6 \times 10^{23} \text{mol}^{-1}$]
n_p	Number of elementary charge units on a particle
Q_{abs}	Absolute radical production [atoms cm^{-2}]
dQ_{abs}/dt	Absolute radical production rate [atoms $\text{cm}^{-2} \text{s}^{-1}$]
Q_{eff}	Effective Cl atom production considering the homogeneous and heterogeneous background [atoms cm^{-2}]
$Q_{\text{bg,heter}}$	Heterogeneous absolute Cl background production [atoms cm^{-2}]
Q_X	Total radical production [atoms cm^{-3}]
dQ_X/dt	Radical production rate [atoms $\text{cm}^{-3} \text{s}^{-1}$]
q_a	Aerosol flow rate [$\text{cm}^3 \text{s}^{-1}$]
q_s	Sampling flow rate [$\text{cm}^3 \text{s}^{-1}$]

$R_{Cl/Fe}$	Molar chloride to iron ratio
r_1	Outer radius of the classifier center-rod [cm]
r_2	Inner radius of the classifier housing [cm]
t	Time [s]
T	Temperature [K or °C]
V	Classifier center-rod voltage [V]
V_{Ch}	Teflon chamber volume [cm ³]
$Z_{I\pm}$	Ion mobility
Z_P	Electrical mobility
ϵ_0	Dielectric constant [F m ⁻¹]
λ_{Fe}	Mole fraction of active iron
λ	Wavelength [nm]
μ	Viscosity of air [Pa s]
ρ	Reproducibility of injected HCl [%]
σ	Absorption cross-section [cm ² molecules ⁻¹]
τ_s	Surface-deposition lifetime [s]
Φ	Quantum yield

1.7 Individual Contribution to the Included Manuscripts

Manuscript 1 (chapter 2)

Wittmer, J., Bleicher, S. and Zetzsch, C.: Iron(III)-induced activation of chloride and bromide from modeled salt pans, **2015**, *J. Phys. Chem. A*, 119(19), 4373–4385, doi: 10.1021/jp508006s.

J. Wittmer	50 %	Experiment execution, data evaluation and interpretation, manuscript writing and editing
S. Bleicher	40 %	Experiment design and execution, data interpretation and discussion
C. Zetzsch	10 %	Idea, discussion and manuscript editing
F. D. Oeste		Idea and discussion

Manuscript 2 (chapter 3)

Wittmer, J., Bleicher, S., Ofner, J. and Zetzsch, C.: Iron(III)-induced activation of chloride from artificial sea-salt aerosol, **2015**, *Environ. Chem.*, 12(4), 461–475, doi: 10.1071/EN14279.

J. Wittmer	77 %	Experiment design and execution, data interpretation, manuscript writing and editing
S. Bleicher	5 %	Discussion and comments to improve the manuscript
J. Ofner	3 %	SEM-EDX measurements and interpretation
C. Zetzsch	15 %	Discussion and manuscript editing
F. D. Oeste		Idea and discussion

Manuscript 3 (chapter 4)

Wittmer, J. and Zetzsch, C.: Photochemical activation of chlorine by iron-oxide aerosol, submitted to *Atm. Chem.*, **2015**.

J. Wittmer	90 %	Experiment design and execution, data interpretation, manuscript writing and editing
C. Zetzsch	10 %	Discussion and comments to improve the manuscript

1.8 Additional Contributions to not Included Publications

- Bartolomei, V., Gomez Alvarez, E., **Wittmer, J.**, Tlili, S., Streckowski, R., Temime-Roussel, B., Quivet, E., Wortham, H., Zetzsch, C., Kleffmann, J., Gligorovski, S.: Combustion processes as a source of high levels of indoor hydroxyl radicals through the photolysis of nitrous acid, **2015**, *Environ. Sci. Technol.* 49(11), 6599–6607, doi: 10.1021/acs.est.5b01905
- **Wittmer, J.**, Bobrowski, N., Liotta, M., Giuffrida, G., Calabrese, S., Platt, U.: Active alkaline traps to determine acidic-gas ratios in volcanic plumes: Sampling techniques and analytical methods, **2014**, *Geochem. Geophys. Geosyst.* 15(7), 2797–2820. doi: 10.1002/2013GC005133

1.9 Appendix

PHREEQC database for equilibrium calculations. Data composed from Allison et al. 1991) and Tosca et al.; 2005).

SOLUTION_MASTER_SPECIES

H	H+	-1.	H	1.008
H(1)	H+	-1.	0.0	
E	e-	0.0	0.0	0.0
F	F-		0	18.9984
18.9984				
S(-2)	HS-		1.0	32.064
O	H2O	0.0	O	16.00
O(-2)	H2O	0.0	0.0	
Ca	Ca+2	0.0	Ca	40.08
Mg	Mg+2	0.0	Mg	24.305
Na	Na+	0.0	Na	22.9898
K	K+	0.0	K	39.0983
Fe	Fe+3		0.0	55.847
Fe(+2)	Fe+2		0.0	55.847
Fe(+3)	Fe+3		-2.0	55.847
Mn	Mn+2	0.0	Mn	54.938
Ba	Ba+2	0.0	Ba	137.33
Sr	Sr+2	0.0	Sr	87.62
Cl	Cl- 0.0	Cl		35.453
C	CO3-2	2.0	HCO3	12.0111
C(4)	CO3-2	2.0	HCO3	12.0111
Alkalinity	CO3-2	1.0	Ca0.5(CO3)0.5	50.05
S	SO4-2	0.0	SO4	32.064
S(6)	SO4-2	0.0	SO4	
B	B(OH)3	0.0	B	10.81
Li	Li+	0.0	Li	6.941
Br	Br-	0.0	Br	79.904

SOLUTION_SPECIES

H+ = H+

	log_k	0.000
	-dw	9.31e-9
e- = e-		
	log_k	0.000
H2O = H2O		
	log_k	0.000
Ca+2 = Ca+2		
	log_k	0.000
	-dw	0.793e-9
	-millero	-19.69 0.1058 -0.001256 1.617 -0.075
0.0008262		
Mg+2 = Mg+2		
	log_k	0.000
	-dw	0.705e-9
	-millero	-22.32 0.0868 -0.0016 2.017 -0.125
0.001457		
Na+ = Na+		
	log_k	0.000
	-dw	1.33e-9
	-millero	-3.46 0.1092 -0.000768 2.698 -0.106
0.001651		
K+ = K+		
	log_k	0.000
	-dw	1.96e-9
	-millero	7.26 0.0892 -0.000736 2.722 -0.101
0.00151		
Fe+2 = Fe+2		
	log_k	0.000
	-dw	0.719e-9
Fe+3 = Fe+3		
	log_k	0
	-dw	0.719e-9
Fe+3 + e- = Fe+2		
	log_k	13.032
	delta_h	-10 kcal
F- = F-		
	log_k	0
	delta_h	0 kcal

	-gamma	3.5	0.0
SO4-2 + 9H+ + 8e- = HS- + 4H2O			
	log_k	33.66	
	delta_h	-60.14 kcal	
	-gamma	3.5	0.0
Mn+2 = Mn+2			
	log_k	0.000	
	-dw	0.688e-9	
Cl- = Cl-			
	log_k	0.000	
	-dw	2.03e-9	
	-millero	16.37 0.0896 -0.001264 -1.494 0.034	
-0.000621			
CO3-2 = CO3-2			
	log_k	0.000	
	-dw	0.955e-9	
	-millero	-8.74 0.300 -0.004064 5.65; # d is value for 25	
		oC, e and f not reported by Millero, 2000	
SO4-2 = SO4-2			
	log_k	0.000	
	-dw	1.07e-9	
	-millero	9.26 0.284 -0.003808 0.4348 -	
0.0099143 -8.4762e-05			
B(OH)3 = B(OH)3			
	log_k	0.000	
	-dw	1.1e-9	
	-millero	36.56 0.130 -0.00081 # d, e and f not	
		reported by Millero, 2000	
Br- = Br-			
	log_k	0.000	
	-dw	2.01e-9	
	-millero	22.98 0.0934 -0.000968 -1.675 0.05 -	
0.001105			
H2O = OH- + H+			
	log_k	-13.998	
	delta_h	13.345 kcal	
#	-analytic	-283.971	-0.05069842
13323.0	102.24447	-1119669.0	

```

-dw      5.27e-9
CO3-2 + H+ = HCO3-
  log_k   10.3393
  delta_h -3.561 kcal
  -analytic 107.8975    0.03252849 -
5151.79  -38.92561    563713.9
  -dw      1.18e-9
  -millero 21.07  0.185  -0.002248  2.29 -
0.006644 -3.667E-06
CO3-2 + 2 H+ = CO2 + H2O
  log_k   16.6767
  delta_h -5.738 kcal
  -analytic 464.1925    0.09344813 -
26986.16 -165.75951    2248628.9
  -dw      1.92e-9
#CO3-2 + 2 H+ = CO2 + H2O
#   log_k   16.681
#   delta_h -5.738 kcal
#   -analytic 464.1965    0.09344813 -
26986.16 -165.75951    2248628.9
SO4-2 + H+ = HSO4-
  log_k   1.979
  delta_h 4.91 kcal
  -analytic -5.3585    0.0183412  557.2461
  -dw      1.33e-9
B(OH)3 + H2O = B(OH)4- + H+
  log_k   -9.239
  delta_h 0 kcal
3B(OH)3 = B3O3(OH)4- + 2H2O + H+
  log_k   -7.528
  delta_h 0 kcal
4B(OH)3 = B4O5(OH)4-2 + 3H2O + 2H+
  log_k   -16.134
  delta_h 0 kcal
Ca+2 + B(OH)3 + H2O = CaB(OH)4+ + H+
  log_k   -7.589
  delta_h 0 kcal
Mg+2 + B(OH)3 + H2O = MgB(OH)4+ + H+

```

```

  log_k   -7.840
  delta_h 0 kcal
Ca+2 + F- = CaF+
  log_k   0.94
  delta_h 3.798 kcal
  -gamma 5 0
Ca+2 + SO4-2 = CaSO4
  log_k   2.309
  delta_h 1.47 kcal
  Ca+2 + H2O = CaOH+ + H+
  log_k   -12.598
  delta_h 14.535 kcal
  -gamma 6 0
Ca+2 + CO3-2 + H+ = CaHCO3+
  log_k   11.33
  delta_h 1.79 kcal
  -gamma 6 0
  -analytical -9.448  0.03709  2902.39
Ca+2 + CO3-2 = CaCO3
  log_k   3.151
  delta_h 3.547 kcal
  -analytic -1228.806    -0.299440
35512.75  485.818
  -dw 4.46e-10 # complexes: calc'd with
the Pikal formula
Mg+2 + H2O = MgOH+ + H+
  log_k   -11.809
  delta_h 15.419 kcal
Mg+2 + CO3-2 = MgCO3
  log_k   2.928
  delta_h 2.535 kcal
  -analytic -32.225  0.0  1093.486
12.72433
  -dw 4.21e-10
Mg+2 + F- = MgF+
  log_k   1.82
  delta_h 4.674 kcal
  -gamma 4.5 0

```

```

Mg+2 + CO3-2 + H+ = MgHCO3+
  log_k   11.4
  delta_h -2.43 kcal
  -gamma 4 0
Mg+2 + SO4-2 = MgSO4
  log_k   2.25
  delta_h 1.399 kcal
Na+ + CO3-2 = NaCO3-
  log_k   1.268
  delta_h 8.911 kcal
  -gamma 5.4 0
Na+ + F- = NaF
  log_k   -0.79
  delta_h 0 kcal
Na+ + CO3-2 + H+ = NaHCO3
  log_k   10.08
  delta_h 0 kcal
K+ + SO4-2 = KSO4-
  log_k   0.85
  delta_h 2.25 kcal
  -gamma 5.4 0
Na+ + SO4-2 = NaSO4-
  log_k   0.7
  delta_h 1.12 kcal
  -gamma 5.4
SO4-2 + H+ = HSO4-
  log_k   1.987
  delta_h 4.91 kcal
  -gamma 4.5 0
  -analytical -5.3505  0.0183412  557.2461
CO3-2 + 2H+ = H2CO3
  log_k   16.681
  delta_h -2.247 kcal
F- + H+ = HF
  log_k   3.169
  delta_h 3.46 kcal
2F- + H+ = HF2-
  log_k   3.749

```

delta_h 4.55 kcal
 -gamma 3.5 0
 $2F^- + 2H^+ = H_2F_2$
 log_k 6.768
 delta_h 0 kcal
 $Fe^{+3} + SO_4^{2-} = FeSO_4$
 log_k 3.92
 delta_h 3.91 kcal
 -gamma 5 0
 $Fe^{+3} + 2SO_4^{2-} = Fe(SO_4)_2$
 log_k 5.42
 delta_h 4.6 kcal
 $H^+ + HSO_4^- = H_2SO_4$
 log_k -3.00
 $H^+ + Cl^- = HCl$
 log_k -6
 $Fe^{+3} + Cl^- = FeCl$
 log_k 1.48
 delta_h 5.6 kcal
 -gamma 5 0
 $Fe^{+3} + 2Cl^- = FeCl_2$
 log_k 2.13
 delta_h 0 kcal
 -gamma 5 0
 $Fe^{+3} + 3Cl^- = FeCl_3$
 log_k 1.13
 delta_h 0 kcal
 -gamma 5.4 0
 $Fe^{+3} + F^- = FeF$
 log_k 6.199
 delta_h 2.699 kcal
 -gamma 5 0
 $Fe^{+3} + 2F^- = FeF_2$
 log_k 10.8
 delta_h 4.8 kcal
 -gamma 5 0
 $Fe^{+3} + 3F^- = FeF_3$
 log_k 14

delta_h 5.399 kcal
 $Fe^{+3} + H_2O = FeOH^{2+} + H^+$
 log_k -2.19
 delta_h 10.399 kcal
 -gamma 5.4 0
 $Fe^{+3} + 2H_2O = Fe(OH)_2^{+} + 2H^+$
 log_k -5.67
 delta_h 0 kcal
 -gamma 5.4 0
 $Fe^{+3} + 3H_2O = Fe(OH)_3 + 3H^+$
 log_k -12.0
 delta_h 0 kcal
 -gamma 5.4 0
 $Fe^{+3} + 4H_2O = Fe(OH)_4^{-} + 4H^+$
 log_k -21.6
 delta_h 0 kcal
 -gamma 5.4 0
 $Fe^{+3} + Br^- = FeBr$
 log_k 0.61
 delta_h 5 kcal
 $Fe^{+3} + 2Br^- = FeBr_2$
 log_k 0.2
 delta_h 2 kcal
 $HS^- + H^+ = H_2S$
 log_k 6.994
 delta_h -5.3 kcal
 -analytical -11.17 0.02386 3279.0
 $HS^- = S^{2-} + H^+$
 log_k -12.918
 delta_h 12.1 kcal
 -gamma 5 0
 $B(OH)_3 = H_2BO_3^- + H^+$
 log_k -9.24
 delta_h 3.224 kcal
 -gamma 2.5 0
 -analytical 24.3919 0.012078 -1343.9 -
 13.2258
 $B(OH)_3 + F^- = BF(OH)_3$

log_k -0.399
 delta_h 1.85 kcal
 -gamma 2.5 0
 $B(OH)_3 + 2F^- + H^+ = BF_2(OH)_2^- + H_2O$
 log_k 7.63
 delta_h 1.635 kcal
 -gamma 2.5 0
 $B(OH)_3 + 3F^- + 2H^+ = BF_3OH^- + 2H_2O$
 log_k 13.667
 delta_h -1.58 kcal
 -gamma 2.5 0
 $B(OH)_3 + 4F^- + 3H^+ = BF_4^- + 3H_2O$
 log_k 20.274
 delta_h -1.795 kcal
 -gamma 2.5 0

PHASES

Anhydrite

$CaSO_4 = Ca^{+2} + SO_4^{2-}$
 log_k -4.362
 -analytical 422.950 0.0 -18431. -
 147.708

Aragonite

$CaCO_3 = CO_3^{2-} + Ca^{+2}$
 log_k -8.336
 delta_h -2.589 kcal
 -analytical -171.8607 -.077993 2903.293

71.595

Arcaelite

$K_2SO_4 = + 1.0000 SO_4^{2-} + 2.0000 K^+$
 log_k -1.776
 -analytical 2.823 0.0 -1371.2

Bischofite

$MgCl_2 \cdot 6H_2O = + 1.0000 Mg^{++} + 2.0000 Cl^- + 6.0000 H_2O$
 log_k 4.455
 -analytical 3.524 0.0 277.6

Bloedite
 $\text{Na}_2\text{Mg}(\text{SO}_4)_2 \cdot 4\text{H}_2\text{O} = + 1.0000 \text{ Mg}^{++} + 2.0000 \text{ Na}^+ + 2.0000 \text{ SO}_4^{--} + 4.0000 \text{ H}_2\text{O}$
 log_k -2.347
 -delta_H 0 # Not possible to calculate enthalpy of reaction Bloedite

Brucite
 $\text{Mg}(\text{OH})_2 = + 1.0000 \text{ Mg}^{++} + 2.0000 \text{ OH}^-$
 log_k -10.88
 -delta_H 4.85 kcal/mol
 # -analytic -1.0280e+002 -1.9759e-002
 9.0180e+003 3.8282e+001 1.4075e+002
 # -Range: 0-300

Burkeite
 $\text{Na}_6\text{CO}_3(\text{SO}_4)_2 = + 1.0000 \text{ CO}_3^{--} + 2.0000 \text{ SO}_4^{--} + 6.0000 \text{ Na}^+$
 log_k -0.772

Calcite
 $\text{CaCO}_3 = \text{CO}_3^{--} + \text{Ca}^{+2}$
 log_k -8.406
 delta_h -2.297 kcal
 -analytic -171.8329 -0.077993
 2839.319 71.595

Carnallite
 $\text{KMgCl}_3 \cdot 6\text{H}_2\text{O} = \text{K}^+ + \text{Mg}^{++} + 3\text{Cl}^- + 6\text{H}_2\text{O}$
 log_k 4.330

Dolomite
 $\text{CaMg}(\text{CO}_3)_2 = \text{Ca}^{+2} + \text{Mg}^{+2} + 2 \text{CO}_3^{--}$
 log_k -17.083
 delta_h -9.436 kcal

Epsomite
 $\text{MgSO}_4 \cdot 7\text{H}_2\text{O} = \text{Mg}^{+2} + \text{SO}_4^{--} + 7 \text{H}_2\text{O}$
 log_k -1.881
 -analytical 1.718 0.0 -1073.

Gaylussite

$\text{CaNa}_2(\text{CO}_3)_2 \cdot 5\text{H}_2\text{O} = \text{Ca}^{+2} + 2 \text{CO}_3^{--} + 2 \text{Na}^+ + 5 \text{H}_2\text{O}$
 log_k -9.421

Glaserite
 $\text{NaK}_3(\text{SO}_4)_2 = \text{Na}^+ + 3\text{K}^+ + 2\text{SO}_4^{--}$
 log_k -3.803

Glauberite
 $\text{Na}_2\text{Ca}(\text{SO}_4)_2 = \text{Ca}^{+2} + 2 \text{Na}^+ + 2 \text{SO}_4^{--}$
 log_k -5.245

Gypsum
 $\text{CaSO}_4 \cdot 2\text{H}_2\text{O} = \text{Ca}^{+2} + \text{SO}_4^{--} + 2 \text{H}_2\text{O}$
 log_k -4.581
 delta_h -0.109 kcal
 -analytic 90.318 0.0 -4213. -
 32.641

Halite
 $\text{NaCl} = \text{Cl}^- + \text{Na}^+$
 log_k 1.570
 -analytic -713.4616 -.1201241 37302.21
 262.4583 -2106915.

Hexahydrate
 $\text{MgSO}_4 \cdot 6\text{H}_2\text{O} = \text{Mg}^{+2} + \text{SO}_4^{--} + 6 \text{H}_2\text{O}$
 log_k -1.635
 -analytic -62.666 0.0 1828.
 22.187

Kainite
 $\text{KMgClSO}_4 \cdot 3\text{H}_2\text{O} = \text{Cl}^- + \text{K}^+ + \text{Mg}^{+2} + \text{SO}_4^{--} + 3 \text{H}_2\text{O}$
 log_k -0.193

Kalicinite
 $\text{KHCO}_3 = \text{K}^+ + \text{H}^+ + \text{CO}_3^{--}$
 log_k -10.058

Kieserite
 $\text{MgSO}_4 \cdot \text{H}_2\text{O} = \text{Mg}^{+2} + \text{SO}_4^{--} + \text{H}_2\text{O}$
 log_k -0.123

Labile_S

$\text{Na}_4\text{Ca}(\text{SO}_4)_3 \cdot 2\text{H}_2\text{O} = 4\text{Na}^+ + \text{Ca}^{+2} + 3\text{SO}_4^{--} + 2 \text{H}_2\text{O}$
 log_k -5.672

Leonhardite
 $\text{MgSO}_4 \cdot 4\text{H}_2\text{O} = \text{Mg}^{+2} + \text{SO}_4^{--} + 4\text{H}_2\text{O}$
 log_k -0.887

Leonite
 $\text{K}_2\text{Mg}(\text{SO}_4)_2 \cdot 4\text{H}_2\text{O} = \text{Mg}^{+2} + 2 \text{K}^+ + 2 \text{SO}_4^{--} + 4 \text{H}_2\text{O}$
 log_k -3.979

Magnesite
 $\text{MgCO}_3 = \text{CO}_3^{--} + \text{Mg}^{+2}$
 log_k -7.834
 delta_h -6.169

Mirabilite
 $\text{Na}_2\text{SO}_4 \cdot 10\text{H}_2\text{O} = \text{SO}_4^{--} + 2 \text{Na}^+ + 10 \text{H}_2\text{O}$
 log_k -1.214
 -analytic -3862.234 -1.19856 93713.54
 1577.756 0.

Misenite
 $\text{K}_8\text{H}_6(\text{SO}_4)_7 = 6 \text{H}^+ + 7 \text{SO}_4^{--} + 8 \text{K}^+$
 log_k -10.806

Nahcolite
 $\text{NaHCO}_3 = \text{CO}_3^{--} + \text{H}^+ + \text{Na}^+$
 log_k -10.742

Natron
 $\text{Na}_2\text{CO}_3 \cdot 10\text{H}_2\text{O} = \text{CO}_3^{--} + 2 \text{Na}^+ + 10.0000 \text{ H}_2\text{O}$
 log_k -0.825

Nesquehonite
 $\text{MgCO}_3 \cdot 3\text{H}_2\text{O} = \text{CO}_3^{--} + \text{Mg}^{+2} + 3 \text{H}_2\text{O}$
 log_k -5.167

CO2(g)
 $\text{CO}_2 = \text{CO}_2$
 log_k -1.468
 -analytic 108.3865 0.01985076 -
 6919.53 -40.45154 669365.0

Pentahydrate	MgSO4:5H2O = Mg+2 + SO4-2 + 5 H2O				
	log_k	-1.285			
Pirssonite	Na2Ca(CO3)2:2H2O = 2Na+ + Ca+2 + 2CO3-2 + 2 H2O				
	log_k	-9.234			
Polyhalite	K2MgCa2(SO4)4:2H2O = 2K+ + Mg+2 + 2Ca+2 + 4SO4-2 + 2 H2O				
	log_k	-13.744			
Portlandite	Ca(OH)2 = Ca+2 + 2 OH-				
	log_k	-5.190			
Schoenite	K2Mg(SO4)2:6H2O = 2K+ + Mg+2 + 2SO4-2 + 6H2O				
	log_k	-4.328			
Sylvite	KCl = K+ + Cl-				
	log_k	0.900			
	-analytic	3.984	0.0	-919.55	
Syngenite	K2Ca(SO4)2:H2O = 2K+ + Ca+2 + 2SO4-2 + H2O				
	log_k	-7.448			
Trona	Na3H(CO3)2:2H2O = 3 Na+ + H+ + 2CO3-2 + 2H2O				
	log_k	-11.384			
Borax	Na2(B4O5(OH)4):8H2O + 2 H+ = 4 B(OH)3 + 2 Na+ + 5 H2O				
	log_k	12.464			
Boric_acid,s	B(OH)3 = B(OH)3				
	log_k	-0.030			
KB5O8:4H2O					

	KB5O8:4H2O + 3H2O + H+ = 5B(OH)3 + K+				
	log_k	4.671			
K2B4O7:4H2O	K2B4O7:4H2O + H2O + 2H+ = 4B(OH)3 + 2K+				
	log_k	13.906			
NaBO2:4H2O	NaBO2:4H2O + H+ = B(OH)3 + Na+ + 3H2O				
	log_k	9.568			
NaB5O8:5H2O	NaB5O8:5H2O + 2H2O + H+ = 5B(OH)3 + Na+				
	log_k	5.895			
Teepelite	Na2B(OH)4Cl + H+ = B(OH)3 + 2Na+ + Cl- + H2O				
	log_k	10.840			
H2O(g)	H2O = H2O				
	log_k	1.51			
	delta_h	-44.03	kJ		
#	Stumm and Morgan, from NBS and Robie, Hemmingway, and Fischer (1978)				
PITZER					
-B0					
Na+	Cl-	0.0765	-777.03	-4.4706	
		0.008946	-3.3158E-6		
K+	Cl-	0.04835	0	0	
5.794E-4					
Mg+2	Cl-	0.35235	0	0	-
1.943E-4					
Ca+2	Cl-	0.3159	0	0	-
1.725E-4					
MgOH+	Cl-	-0.1			

H+	Cl-	0.1775	0	0	-
3.081E-4					
Li+	Cl-	0.1494	0	0	-
1.685E-4					
Sr+2	Cl-	0.2858	0	0	
0.717E-3					
Fe+2	Cl-	0.40942			
Fe+3	Cl-	0.34082			
Fe+3	SO4-2	0.56622			
Fe+3	HSO4-	0.34082			
Mn+2	Cl-	0.327225			
Ba+2	Cl-	0.2628	0	0	
0.6405E-3					
CaB(OH)4+	Cl-	0.12			
MgB(OH)4+	Cl-	0.16			
Na+	Br-	0.0973	0	0	
7.692E-4					
K+	Br-	0.0569	0	0	
7.39E-4					
H+	Br-	0.1960	0	0	-
2.049E-4					
Mg+2	Br-	0.4327	0	0	-
5.625E-5					
Ca+2	Br-	0.3816	0	0	-
5.2275E-4					
Li+	Br-	0.1748	0	0	-
1.819E-4					
Sr+2	Br-	0.331125	0	0	-
0.32775E-3					
Ba+2	Br-	0.31455	0	0	-
0.33825E-3					
Na+	SO4-2	0.01958	0	0	
2.367E-3					
K+	SO4-2	0.04995	0	0	
1.44E-3					
Mg+2	SO4-2	0.221	0	0	-
0.69E-3					
Ca+2	SO4-2	0.2			

Chapter 1 – Extended Summary

H+	SO4-2	0.0298			
Li+	SO4-2	0.136275	0	0	
0.5055E-3					
Sr+2	SO4-2	0.200	0	0	-
2.9E-3					
Fe+2	SO4-2	0.2568			
Mn+2	SO4-2	0.2065			
Na+	HSO4-	0.0454			
K+	HSO4-	-0.0003			
Mg+2	HSO4-	0.4746			
Ca+2	HSO4-	0.2145			
H+	HSO4-	0.2065			
Fe+2	HSO4-	0.4273			
Na+	OH-	0.0864	0	0	
7.00E-4					
K+	OH-	0.1298			
Ca+2	OH-	-0.1747			
Li+	OH-	0.015			
Ba+2	OH-	0.17175			
Na+	HCO3-	0.0277	0	0	
1.00E-3					
K+	HCO3-	0.0296	0	0	
0.996E-3					
Mg+2	HCO3-	0.329			
Ca+2	HCO3-	0.4			
Sr+2	HCO3-	0.12			
Na+	CO3-2	0.0399	0	0	
1.79E-3					
K+	CO3-2	0.1488	0	0	
1.788E-3					
Na+	B(OH)4-	-0.0427			
Na+	B3O3(OH)4-	-0.056			
Na+	B4O5(OH)4-2	-0.11			
K+	B(OH)4-	0.035			
K+	B3O3(OH)4-	-0.13			
K+	B4O5(OH)4-2	-0.022			
-B1					

Na+	Cl-	0.2664	0	0	
6.1608E-5					
1.0715E-6					
K+	Cl-	0.2122	0	0	
10.71E-4					
Mg+2	Cl-	1.6815	0	0	
3.6525E-3					
Ca+2	Cl-	1.614	0	0	
3.9E-3					
MgOH+	Cl-	1.658			
H+	Cl-	0.2945	0	0	
1.419E-4					
Li+	Cl-	0.3074	0	0	
5.366E-4					
Sr+2	Cl-	1.667	0	0	
2.8425E-3					
Fe+2	Cl-	1.99612			
Fe+3	Cl-	1.6285			
Fe+3	SO4-2	12.16131			
Fe+3	HSO4-	1.6285			
Mn+2	Cl-	1.55025			
Ba+2	Cl-	1.49625	0	0	
3.2325E-3					
Na+	Br-	0.2791	0	0	
10.79E-4					
K+	Br-	0.2212	0	0	
17.40E-4					
H+	Br-	0.3564	0	0	
4.467E-4					
Mg+2	Br-	1.753	0	0	
3.8625E-3					
Ca+2	Br-	1.613	0	0	
6.0375E-3					
Li+	Br-	0.2547	0	0	
6.636E-4					
Sr+2	Br-	1.7115	0	0	
6.5325E-3					
Ba+2	Br-	1.56975	0	0	
6.78E-3					

Na+	SO4-2	1.113	0	0	
5.6325E-3					
K+	SO4-2	0.7793	0	0	
6.6975E-3					
Mg+2	SO4-2	3.343	0	0	
1.53E-2					
Ca+2	SO4-2	3.1973	0	0	
5.46E-2					
Li+	SO4-2	1.2705	0	0	
1.41E-3					
Sr+2	SO4-2	3.1973	0	0	
27.0E-3					
Fe+2	SO4-2	3.063			
Mn+2	SO4-2	2.9511			
Na+	HSO4-	0.398			
K+	HSO4-	0.1735			
Mg+2	HSO4-	1.729			
Ca+2	HSO4-	2.53			
H+	HSO4-	0.5556			
Fe+2	HSO4-	3.48			
Na+	OH-	0.253	0	0	
1.34E-4					
K+	OH-	0.32			
Ca+2	OH-	-0.2303			
Li+	OH-	0.14			
Ba+2	OH-	1.2			
Na+	HCO3-	0.0411	0	0	
1.10E-3					
K+	HCO3-	-0.013	0	0	
1.104E-3					
Mg+2	HCO3-	0.6072			
Ca+2	HCO3-	2.977			
Na+	CO3-2	1.389	0	0	
2.05E-3					
K+	CO3-2	1.43	0	0	
2.051E-3					
Na+	B(OH)4-	0.089			
Na+	B3O3(OH)4-	-0.910			

Na+	B4O5(OH)4-2	-0.40				
K+	B(OH)4-	0.14				
-B2						
Mg+2	SO4-2	-37.23	0	0	-	
0.253						
Ca+2	SO4-2	-54.24	0	0	-	
0.516						
Sr+2	SO4-2	-54.24	0	0	-0.42	
Fe+2	SO4-2	-42.0				
Fe+2	HSO4-	1.7199				
Fe+2	Cl-	0.34439				
Fe+3	Cl-	1.7199				
Fe+3	SO4-2	3.0751				
Fe+3	HSO4-	1.7199				
Mn+2	SO4-2	-40.0				
Ca+2	OH-	-5.72				
-CO						
Na+	Cl-	0.00127	33.317	0.09421	-	
4.655E-5						
K+	Cl-	-0.00084	0	0	-	
5.095E-5						
Mg+2	Cl-	0.00519	0	0	-	
1.64933E-4						
Ca+2	Cl-	-0.00034				
H+	Cl-	0.0008	0	0		
6.213E-5						
Li+	Cl-	0.00359	0	0	-	
4.520E-5						
Sr+2	Cl-	-0.00130				
Fe+2	Cl-	0.02643				
Fe+3	Cl-	-0.014				
Fe+2	SO4-2	0.0209				
Fe+3	SO4-2	0.000524				
Fe+3	HSO4-	-0.014				
Mn+2	Cl-	-0.0204972				
Ba+2	Cl-	-0.0193782	0	0	-	
1.53796E-4						

Na+	Br-	0.00116	0	0	-	
9.30E-5						
K+	Br-	-0.00180	0	0	-	
7.004E-5						
H+	Br-	0.00827	0	0	-	
5.685E-5						
Mg+2	Br-	0.00312				
Ca+2	Br-	-0.00257				
Li+	Br-	0.0053	0	0	-	
2.813E-5						
Sr+2	Br-	0.00122506				
Ba+2	Br-	-0.0159576				
Na+	SO4-2	0.00497	0	0	-	
4.87904E-4						
Mg+2	SO4-2	0.025	0	0		
0.523E-3						
H+	SO4-2	0.0438				
Li+	SO4-2	-0.00399338	0	0	-	
2.33345E-4						
Mn+2	SO4-2	0.01636				
Na+	OH-	0.0044	0	0	-	
18.94E-5						
K+	OH-	0.0041				
K+	HCO3-	-0.008				
Na+	CO3-2	0.0044				
K+	CO3-2	-0.0015				
Na+	B(OH)4-	0.0114				
-THETA						
Na+	Fe+3	-0.07				
H+	Fe+3		-0.07			
K+	Fe+3		-0.07			
K+	Fe+2		-0.18			
Ca+2	Fe+2		0.007			
Fe+2	Fe+3		-0.05			
Mg+2	Fe+2	-0.06				
Na+	FeOH+2					
K+	Na+	-0.012				

Mg+2	Na+	0.07				
Ca+2	Na+	0.07				
Sr+2	Na+	0.051				
H+	Na+	0.036				
Ca+2	K+	0.032				
H+	K+	0.005				
Ca+2	Mg+2	0.007				
H+	Mg+2	0.1				
H+	Ca+2	0.092				
SO4-2	Cl-	0.02				
HSO4-	Cl-	-0.006				
OH-	Cl-	-0.05				
HCO3-	Cl-	0.03				
CO3-2	Cl-	-0.02				
B(OH)4-	Cl-	-0.065				
B3O3(OH)4-	Cl-	0.12				
B4O5(OH)4-2	Cl-	0.074				
OH-	Br-	-0.065				
OH-	SO4-2	-0.013				
HCO3-	SO4-2	0.01				
CO3-2	SO4-2	0.02				
B(OH)4-	SO4-2	-0.012				
B3O3(OH)4-	SO4-2	0.10				
B4O5(OH)4-2	SO4-2	0.12				
CO3-2	OH-	0.1				
CO3-2	HCO3-	-0.04				
B3O3(OH)4-	HCO3-	-0.10				
B4O5(OH)4-2	HCO3-	-0.087				
-LAMDA						
Na+	CO2	0.1				
K+	CO2	0.051				
Mg+2	CO2	0.183				
Ca+2	CO2	0.183				
Cl-	CO2	-0.005				
SO4-2	CO2	0.097				
HSO4-	CO2	-0.003				
Na+	B(OH)3	-0.097				

Chapter 1 – Extended Summary

K+	B(OH)3	-0.14		
Cl-	B(OH)3	0.091		
SO4-2	B(OH)3	0.018		
B3O3(OH)4-	B(OH)3	-0.20		
-ZETA				
H+	Cl-	B(OH)3	-0.0102	
Na+	SO4-2	B(OH)3	0.046	
-PSI				
Fe+3	H+	Cl-	-0.004	
Na+		Fe+2	SO4-2	-0.015
Fe+2	Fe+3	SO4-2	-0.05	
Fe+2	Fe+3	Cl-	0.012	
Na+		Fe+2	Cl-	-0.01
Na+		Fe+3	SO4-2	-0.01
Na+		Fe+3	Cl-	-0.004
Na+	K+	Cl-	-0.0018	
Na+	K+	Br-	-0.0022	
Na+	K+	SO4-2	-0.010	
Na+	K+	HCO3-	-0.003	
Na+	K+	CO3-2	0.003	
Na+	Ca+2	Cl-	-0.007	
Na+	Sr+2	Cl-	-0.0021	
Na+	Ca+2	SO4-2	-0.055	
Na+	Mg+2	Cl-	-0.012	
Na+	Mg+2	SO4-2	-0.015	
Na+	H+	Cl-	-0.004	
Na+	H+	Br-	-0.012	
Na+	H+	HSO4-	-0.0129	
K+	Ca+2	Cl-	-0.025	
K+	Mg+2	Cl-	-0.022	
K+	Mg+2	SO4-2	-0.048	
K+	H+	Cl-	-0.011	
K+	H+	Br-	-0.021	
K+	H+	SO4-2	0.197	
K+	H+	HSO4-	-0.0265	
K+		Fe+2	Cl-	0.003
K+		Fe+3	Cl-	-0.01

K+	Fe+3	SO4-2		-0.03
K+	Fe+2	SO4-2		-0.03
Ca+2	Mg+2	Cl-	-0.012	
Ca+2	Fe+2	SO4-2	0.024	
Ca+2	Fe+3	SO4-2	0.03	
Ca+2	Fe+2	Cl-	-0.012	
Ca+2	Mg+2	SO4-2	0.024	
Ca+2	H+	Cl-	-0.015	
Mg+2	MgOH+	Cl-	0.028	
Mg+2	H+	Cl-	-0.011	
Mg+2	H+	HSO4-	-0.0178	
Mg+2	Fe+2	Cl-	-0.012	
Mg+2	Fe+3	Cl-	-0.024	
Cl-	SO4-2	Fe+2	-0.004	
Cl-	Br-	K+	0.0000	
Cl-	SO4-2	Na+	0.0014	
Cl-	SO4-2	Ca+2	-0.018	
Cl-	SO4-2	Mg+2	-0.004	
Cl-	HSO4-	Na+	-0.006	
Cl-	HSO4-	H+	0.013	
Cl-	OH-	Na+	-0.006	
Cl-	OH-	K+	-0.006	
Cl-	OH-	Ca+2	-0.025	
Cl-	HCO3-	Na+	-0.015	
Cl-	HCO3-	Mg+2	-0.096	
Cl-	CO3-2	Na+	0.0085	
Cl-	CO3-2	K+	0.004	
Cl-	B(OH)4-	Na+	-0.0073	
Cl-	B3O3(OH)4-	Na+	-0.024	
Cl-	B4O5(OH)4-2	Na+	0.026	
SO4-2	HSO4-	Na+	-0.0094	
SO4-2	HSO4-	K+	-0.0677	
SO4-2	HSO4-	Mg+2	-0.0425	
SO4-2	OH-	Na+	-0.009	
SO4-2	OH-	K+	-0.050	
SO4-2	HCO3-	Na+	-0.005	
SO4-2	HCO3-	Mg+2	-0.161	
SO4-2	CO3-2	Na+	-0.005	

SO4-2	CO3-2	K+	-0.009	
SO4-2	HSO4-	Fe+2	-0.0425	
OH-	CO3-2	Na+	-0.017	
OH-	CO3-2	K+	-0.01	
OH-	Br-	Na+	-0.018	
OH-	Br-	K+	-0.014	
HCO3-	CO3-2	Na+	0.002	
HCO3-	CO3-2	K+	0.012	
-V0v				
Na+	Cl-		16.68	
K+	Cl-		26.87	
Ca+2	Cl-		17.4193	
Mg+2	Cl-		13.734	
Na+	SO4-2		11.787	
K+	SO4-2		32.167	
Ca+2	SO4-2		0	
Mg+2	SO4-2		-7.839	
Na+	HCO3-		23.181	
K+	HCO3-		33.371	
Ca+2	HCO3-		0	
Mg+2	HCO3-		0	
Na+	CO3-2		-6.48	
K+	CO3-2		13.9	
Ca+2	CO3-2		0	
Mg+2	CO3-2		0	
-B0v				
Na+	Cl-		1.2340e-5	
K+	Cl-		1.3949e-5	
Mg+2	Cl-		1.38330e-5	
Ca+2	Cl-		1.32870e-5	
Na+	SO4-2		5.308e-5	
K+	SO4-2		3.348e-5	
Mg+2	SO4-2		4.9329e-5	
Na+	HCO3-		-1.162e-5	
K+	HCO3-		-0.2705e-5	
Na+	CO3-2		5.98e-5	

```

K+   CO3-2  3.2889e-5

-B1v
K+   Cl-    2.3500E-06
Na+  SO4-2   1.2340E-04
K+   SO4-2   2.3800E-04
Mg+2 SO4-2   1.4838E-04
Na+  HCO3-   1.7800E-04
K+   HCO3-   1.6950E-04
Na+  CO3-2   8.1600E-05
K+   CO3-2   2.0700E-04
-B2v
Mg+2 SO4-2   1.6790E-02
-Cv
Na+  Cl-    -6.4500E-07
K+   Cl-    -8.6970E-07
Ca+2 Cl-    -2.1750E-07
Mg+2 Cl-    -3.5700E-07
Na+  SO4-2   -2.7940E-06
Mg+2 SO4-2   1.9200E-07
Na+  CO3-2   -3.2500E-06
K+   CO3-2   -7.4700E-07

EXCHANGE_MASTER_SPECIES
X    X-
EXCHANGE_SPECIES
X- = X-
log_k    0.0

Na+ + X- = NaX
log_k    0.0

K+ + X- = KX
log_k    0.7
delta_h -4.3 # Jardine & Sparks, 1984

Li+ + X- = LiX

```

```

log_k -0.08
delta_h 1.4 # Merriam & Thomas, 1956

Ca+2 + 2X- = CaX2
log_k 0.8
delta_h 7.2 # Van Bladel & Gheyl, 1980

Mg+2 + 2X- = MgX2
log_k 0.6
delta_h 7.4 # Laudelout et al., 1968

Mn+2 + 2X- = MnX2
log_k 0.52

Fe+2 + 2X- = FeX2
log_k 0.44

SURFACE_MASTER_SPECIES
Hfo_s Hfo_sOH
Hfo_w Hfo_wOH

SURFACE_SPECIES
# All surface data from
# Dzombak and Morel, 1990
#
# Acid-base data from table 5.7
#
# strong binding site--Hfo_s,

Hfo_sOH = Hfo_sOH
log_k 0.0

Hfo_sOH + H+ = Hfo_sOH2+
log_k 7.29 # = pKa1,int

Hfo_sOH = Hfo_sO- + H+
log_k -8.93 # = -pKa2,int

```

```

# weak binding site--Hfo_w

Hfo_wOH = Hfo_wOH
log_k 0.0

Hfo_wOH + H+ = Hfo_wOH2+
log_k 7.29 # = pKa1,int

Hfo_wOH = Hfo_wO- + H+
log_k -8.93 # = -pKa2,int

#####
##
#          CATIONS          #
#####
#
# Cations from table 10.1 or 10.5
#
# Calcium
Hfo_sOH + Ca+2 = Hfo_sOHCa+2
log_k 4.97

Hfo_wOH + Ca+2 = Hfo_wOCa+ + H+
log_k -5.85

#
# Derived constants table 10.5
#
# Magnesium
Hfo_wOH + Mg+2 = Hfo_wOMg+ + H+
log_k -4.6

# Iron
# Hfo_sOH + Fe+2 = Hfo_sOFe+ + H+
# log_k 0.7 # LFER using table 10.5

# Hfo_wOH + Fe+2 = Hfo_wOFe+ + H+
# log_k -2.5 # LFER using table 10.5

```

```
# Iron, strong site: Appelo, Van der Weiden, Tournassat
& Charlet, subm.
  Hfo_sOH + Fe+2 = Hfo_sOFe+ + H+
  log_k -0.95
# Iron, weak site: Liger et al., GCA 63, 2939, re-
optimized for D&M
  Hfo_wOH + Fe+2 = Hfo_wOFe+ + H+
  log_k -2.98

  Hfo_wOH + Fe+2 + H2O = Hfo_wOFeOH +
2H+
  log_k -11.55

#####
##
# ANIONS #
#####
##
#
# Anions from table 10.7
#
# Borate
  Hfo_wOH + B(OH)3 = Hfo_wH2BO3 + H2O
  log_k 0.62
#
# Anions from table 10.8
#
# Sulfate
  Hfo_wOH + SO4-2 + H+ = Hfo_wSO4- +
H2O
  log_k 7.78

  Hfo_wOH + SO4-2 = Hfo_wOHSO4-2
  log_k 0.79
#
# Carbonate: Van Geen et al., 1994 reoptimized for
HFO
```

```
# 0.15 g HFO/L has 0.344 mM sites == 2 g of Van
Geen's Goethite/L
#
# Hfo_wOH + CO3-2 + H+ = Hfo_wCO3- +
H2O
# log_k 12.56
#
# Hfo_wOH + CO3-2 + 2H+= Hfo_wHCO3 +
H2O
# log_k 20.62

END
MEAN GAM
CaCl2
CaSO4
CaCO3
Ca(OH)2
MgCl2
MgSO4
MgCO3
Mg(OH)2
NaCl
Na2SO4
NaHCO3
Na2CO3
NaOH
KCl
K2SO4
KHCO3
K2CO3
KOH
HCl
H2SO4
HBr

END
```

1.10 References

- Allison, J. D., Brown, D. S., Kevin, J., MINTEQA2/PRODEFA2, A Geochemical Assessment Model for Environmental Systems: Version 3.0 User's Manual. Environmental Research Laboratory, Office of Research and Development, US Environmental Protection Agency, Athens, Georgia, USA 1991
- Andreae, M. O., Charlson, R. J., Bruynseels, F., Storms, H., van Grieken, R., Maenhaut, W. Internal mixture of sea salt, silicates, and excess sulfate in marine aerosols. *Science* 1986, 232, 1620–1623. doi: 10.1126/science.232.4758.1620
- Arimoto, R., Kim, Y. J., Kim, Y. P., Quinn, P. K., Bates, T. S., Anderson, T. L., Gong, S., Uno, I., Chin, M., Huebert, B. J., Clarke, A. D., Shinozuka, Y., Weber, R. J., Anderson, J. R., Guazzotti, S. A., Sullivan, R. C., Sodeman, D. A., Prather, K. A., Sokolik, I. N. Characterization of Asian dust during ACE-Asia. *Global Planet. Change* 2006, 52, 23–56. doi: 10.1016/j.gloplacha.2006.02.013
- Atkinson, R., Baulch, D. L., Cox, R. A., Crowley, J. N., Hampson, R. F., Hynes, R. G., Jenkin, M. E., Rossi, M. J., Troe, J. Evaluated kinetic and photochemical data for atmospheric chemistry: Volume I - Gas phase reactions of O_x, HO_x, NO_x and SO_x species. *Atmos. Chem. Phys.* 2004, 4, 1461–1738. doi: 10.5194/acp-4-1461-2004
- Atkinson, R., Baulch, D. L., Cox, R. A., Crowley, J. N., Hampson, R. F., Hynes, R. G., Jenkin, M. E., Rossi, M. J., Troe, J. Evaluated kinetic and photochemical data for atmospheric chemistry: Volume III – Gas phase reactions of inorganic halogens. *Atmos. Chem. Phys.* 2007, 7, 981–1191. doi: 10.5194/acp-7-981-2007
- Atkinson, R., Baulch, D. L., Cox, R. A., Hampson, R. F., Kerr, J. A., Rossi, M. J., Troe, J. Evaluated kinetic, photochemical and heterogeneous data for atmospheric chemistry: supplement V. IUPAC subcommittee on gas kinetic data evaluation for atmospheric chemistry. *J. Phys. Chem. Ref. Data* 1997, 26, 521. doi: 10.1063/1.556011
- Baes, C. F., Mesmer, R. E., The hydrolysis of cations. Wiley, New York 1976
- Baker, A. R., Croot, P. L. Atmospheric and marine controls on aerosol iron solubility in seawater. *Marine Chem.* 2010, 120, 4–13. doi: 10.1016/j.marchem.2008.09.003
- Balmer, M. E., Sulzberger, B. Atrazine degradation in irradiated iron/oxalate systems: effects of pH and oxalate. *Environ. Sci. Technol.* 1999, 33, 2418–2424. doi: 10.1021/es9808705
- Balzer, N., Kinetische Untersuchungen der Halogen-Aktivierung einer simulierten Salzpflanze in einer Smogkammer, PhD thesis. Atmospheric Chemistry Research Laboratory, University of Bayreuth 2012. <https://epub.uni-bayreuth.de/162/>
- Barrie, L. A., Bottenheim, J. W., Schnell, R. C., Crutzen, P. J., Rasmussen, R. A. Ozone destruction and photochemical reactions at polar sunrise in the lower Arctic atmosphere. *Nature* 1988, 334, 138–141. doi: 10.1038/334138a0
- Bartolomei, V., Gomez Alvarez, E., Wittmer, J., Tlili, S., Streckowski, R., Temime-Roussel, B., Quivet, E., Wortham, H., Zetzsch, C., Kleffmann, J., Gligorovski, S. Combustion processes as a source of high levels of indoor hydroxyl radicals through the photolysis of nitrous acid. *Environ. Sci. Technol.* 2015, 49, 6599–6607. doi: 10.1021/acs.est.5b01905

- Behnke, W., George, C., Scheer, V., Zetzsch, C. Production and decay of ClNO₂ from the reaction of gaseous N₂O₅ with NaCl solution: Bulk and aerosol experiments. *J. Geophys. Res.* 1997, 102, 3795. doi: 10.1029/96JD03057
- Behnke, W., Holländer, W., Koch, W., Nolting, F., Zetzsch, C. A smog chamber for studies of the photochemical degradation of chemicals in the presence of aerosols. *Atmos. Environ.* 1988, 22, 1113–1120. doi: 10.1016/0004-6981(88)90341-1
- Bleicher, S., Zur Halogenaktivierung im Aerosol und in Salzpflanzen, PhD thesis. Atmospheric Chemistry Research Laboratory, University of Bayreuth 2012. <https://epub.uni-bayreuth.de/view/person/Bleicher=3ASergej=3A=3A.html>
- Bloss, W. J., Rowley, D. M., Cox, R. A., Jones, R. L. Rate coefficient for the BrO + HO₂ reaction at 298 K. *Phys. Chem. Chem. Phys.* 2002, 4, 3639–3647. doi: 10.1039/b201653b
- Bobrowski, N., Hönninger, G., Galle, B., Platt, U. Detection of bromine monoxide in a volcanic plume. *Nature* 2003, 423, 273–276
- Bowen, B. B., Benison, K. C., Oboh-Ikuenobe, F. E., Story, S., Mormile, M. R. Active hematite concretion formation in modern acid saline lake sediments, Lake Brown, Western Australia. *Earth and Planet. Sc. Lett.* 2008, 268, 52–63. doi: 10.1016/j.epsl.2007.12.023
- Buxmann, J., Balzer, N., Bleicher, S., Platt, U., Zetzsch, C. Observations of bromine explosions in smog chamber experiments above a model salt pan. *Int. J. Chem. Kinet.* 2012, 44, 312–326. doi: 10.1002/kin.20714
- Carpenter, L. J. Iodine in the marine boundary layer. *Chem. Rev.* 2003, 103, 4953–4962. doi: 10.1021/cr0206465
- Crowe, A. S., Longstaffe, F. J. Extension of geochemical modelling techniques to brines: coupling of the Pitzer equations to PHREEQE. *Solving ground water problems with models: an intensive three-day conference and exposition devoted exclusively to ground water modeling* 1987
- Cwiertny, D. M., Young, M. A., Grassian, V. H. Chemistry and photochemistry of mineral dust aerosol. *Annu. Rev. Phys. Chem.* 2008, 59, 27–51. doi: 10.1146/annurev.physchem.59.032607.093630
- de Laat, J., Le, T. G. Kinetics and modeling of the Fe(III)/H₂O₂ system in the presence of sulfate in acidic aqueous solutions. *Environ. Sci. Technol.* 2005, 39, 1811–1818. doi: 10.1021/es0493648
- de Laat, J., Le, T. G., Legube, B. A comparative study of the effects of chloride, sulfate and nitrate ions on the rates of decomposition of H₂O₂ and organic compounds by Fe(II)/H₂O₂ and Fe(III)/H₂O₂. *Chemosphere* 2004, 55, 715–723. doi: 10.1016/j.chemosphere.2003.11.021
- Dentener, F. J., Carmichael, G. R., Zhang, Y., Lelieveld, J., Crutzen, P. J. Role of mineral aerosol as a reactive surface in the global troposphere. *J. Geophys. Res.* 1996, 101, 22869. doi: 10.1029/96JD01818
- Duce, R. A., Tindale, N. W. Atmospheric transport of iron and its deposition in the ocean. *Limnol. Oceanogr.* 1991, 36, 1715–1726. doi: 10.4319/lo.1991.36.8.1715

- Dunlea, E. J., Ravishankara, A. R. Measurement of the rate coefficient for the reaction of O(1D) with H₂O and re-evaluation of the atmospheric OH production rate. *Phys. Chem. Chem. Phys.* 2004, 6, 3333. doi: 10.1039/b402483d
- Ehhalt, D. H., Drummond, J. W. The tropospheric cycle of NO_x. In: Georgii H.W., Jaeschke W. (eds.) *Chemistry of the Unpolluted and Polluted Troposphere*. pp 219–251. Springer Netherlands, Dordrecht 1982
- Ewing, G. E., H₂O on NaCl: From single molecule, to clusters, to monolayer, to thin film, to deliquescence. *Intermol Forces Clusters II Struct Bonding*, vol 116. Springer, Berlin Heidelberg 2005. http://dx.doi.org/10.1007/430_012
- Faxon, C. B., Allen, D. T. Chlorine chemistry in urban atmospheres: A review. *Environ. Chem.* 2013, 10, 221. doi: 10.1071/EN13026
- Feilberg, K. L., Griffith, David W. T., Johnson, M. S., Nielsen, C. J. The ¹³C and D kinetic isotope effects in the reaction of CH₄ with Cl. *Int. J. Chem. Kinet.* 2005, 37, 110–118. doi: 10.1002/kin.20058
- Fenter, F. F., Caloz, F., Rossi, M. J. Heterogeneous kinetics of N₂O₅ uptake on salt, with a systematic study of the role of surface presentation (for N₂O₅ and HNO₃). *J. Phys. Chem.* 1996, 100, 1008–1019. doi: 10.1021/jp9503829
- Fickert, S., Adams, J. W., Crowley, J. N. Activation of Br₂ and BrCl via uptake of HOBr onto aqueous salt solutions. *J. Geophys. Res.* 1999, 104, 23719. doi: 10.1029/1999JD900359
- Finlayson-Pitts, B. J. The tropospheric chemistry of sea salt: A molecular-level view of the chemistry of NaCl and NaBr. *Chem. Rev.* 2003, 103, 4801–4822
- Finlayson-Pitts, B. J. Halogens in the troposphere. *Anal. Chem.* 2009, 82, 770–776. doi: 10.1021/ac901478p
- Finlayson-Pitts, B. J., Ezell, M. J., Pitts, J. N. Formation of chemically active chlorine compounds by reactions of atmospheric NaCl particles with gaseous N₂O₅ and ClONO₂. *Nature* 1989, 337, 241–244. doi: 10.1038/337241a0
- Fishman, J., Crutzen, P. J. The origin of ozone in the troposphere. *Nature* 1978, 274, 855–858. doi: 10.1038/274855a0
- Frenzel, A., Scheer, V., Sikorski, R., George, C., Behnke, W., Zetzsch, C. Heterogeneous Interconversion Reactions of BrNO₂, ClONO₂, Br₂, and Cl₂. *J. Phys. Chem. A* 1998, 102, 1329–1337. doi: 10.1021/jp973044b
- Frinak, E. K., Abbatt, Jonathan P. D. Br₂ production from the heterogeneous reaction of gas-phase OH with aqueous salt solutions: Impacts of acidity, halide concentration, and organic surfactants. *J. Phys. Chem. A* 2006, 110, 10456–10464. doi: 10.1021/jp063165o
- Gebel, M. E., Finlayson-Pitts, B. J., Ganske, J. A. The uptake of SO₂ on synthetic sea salt and some of its components. *Geophys. Res. Lett.* 2000, 27, 887–890. doi: 10.1029/1999GL011152
- Ginoux, P., Chin, M., Tegen, I., Prospero, J. M., Holben, B., Dubovik, O., Lin, S.-J. Sources and distributions of dust aerosols simulated with the GOCART model. *J. Geophys. Res.* 2001, 106, 20255. doi: 10.1029/2000JD000053
- Gliß, J., Bobrowski, N., Vogel, L., Pöhler, D., Platt, U. OCIO and BrO observations in the volcanic plume of Mt. Etna – implications on the chemistry of chlorine and bromine

- species in volcanic plumes. *Atmos. Chem. Phys.* 2015, 15, 5659–5681. doi: 10.5194/acp-15-5659-2015
- Greule, M., Huber, S. G., Keppler, F. Stable hydrogen-isotope analysis of methyl chloride emitted from heated halophytic plants. *Atmos. Environ.* 2012, 62, 584–592. doi: 10.1016/j.atmosenv.2012.09.007
- Gunn, R., Woessner, R. H. Measurements of the systematic electrification of aerosols. *J. Colloid Sci.* 1956, 11, 254–259. doi: 10.1016/0095-8522(56)90050-2
- Hammer, U. T., Saline lake ecosystems of the world. Monographiae biologicae, v. 59. Dr. W. Junk Publishers, Dordrecht, Boston 1986
- Hanson, D. R., Ravishankara, A. R. Uptake of hydrochloric acid and hypochlorous acid onto sulfuric acid: solubilities, diffusivities, and reaction. *J. Phys. Chem.* 1993, 97, 12309–12319. doi: 10.1021/j100149a035
- Harrison, R. M., Peak, J. D., Collins, G. M. Tropospheric cycle of nitrous acid. *J. Geophys. Res.* 1996, 101, 14429. doi: 10.1029/96JD00341
- Hausmann, M., Platt, U. Spectroscopic measurement of bromine oxide and ozone in the high Arctic during Polar Sunrise Experiment 1992. *J. Geophys. Res.* 1994, 99, 25399. doi: 10.1029/94JD01314
- Herrmann, H., Majdik, Z., Ervens, B., Weise, D. Halogen production from aqueous tropospheric particles. *Chemosphere* 2003, 52, 485–502. doi: 10.1016/S0045-6535(03)00202-9
- Hider, R. C., Mohd-Nor, A. R., Silver, J., Morrison, I. E. G., Rees, L. V. C. Model compounds for microbial iron-transport compounds. Part 1: Solution chemistry and Mössbauer study of iron(II) and iron(III) complexes from phenolic and catecholic systems. *J. Chem. Soc., Dalton Trans.* 1981, 609–622. doi: 10.1039/DT9810000609
- Hirokawa, J., Onaka, K., Kajii, Y., Akimoto, H. Heterogeneous processes involving sodium halide particles and ozone: Molecular bromine release in the marine boundary layer in the absence of nitrogen oxides. *Geophys. Res. Lett.* 1998, 25, 2449–2452. doi: 10.1029/98GL01815
- Holla, R., Schmitt, S., Frieß, U., Pöhler, D., Zingler, J., Corsmeier, U., Platt, U. Vertical distribution of BrO in the boundary layer at the Dead Sea. *Environ. Chem.* 2015. doi: 10.1071/EN14224
- Hoppel, W., Pasternack, L., Caffrey, P., Frick, G., Fitzgerald, J., Hegg, D., Gao, S., Ambrusko, J., Albrechtinski, T. Sulfur dioxide uptake and oxidation in sea-salt aerosol. *J. Geophys. Res.* 2001, 106, 27575. doi: 10.1029/2000JD900843
- Hückel, E. Zur Theorie konzentrierterer wässriger Lösungen starker Elektrolyte. *Phys. Z.* 1925, 26, 93–147
- Ito, A. Global modeling study of potentially bioavailable iron input from shipboard aerosol sources to the ocean. *Global Biogeochem. Cycles* 2013, 27, 1–10. doi: 10.1029/2012GB004378
- Ito, A., Feng, Y. Role of dust alkalinity in acid mobilization of iron. *Atmos. Chem. Phys.* 2010, 10, 9237–9250. doi: 10.5194/acp-10-9237-2010
- Jackson, R. B., Jobbágy, E. G. From icy roads to salty streams. *Proc. Natl. Acad. Sci. USA* 2005, 102, 14487–14488. doi: 10.1073/pnas.0507389102

- Jeong, D., Kim, K., Choi, W. Accelerated dissolution of iron oxides in ice. *Atmos. Chem. Phys.* 2012, 12, 11125–11133. doi: 10.5194/acp-12-11125-2012
- Jolly, I. D., McEwan, K. L., Holland, K. L. A review of groundwater-surface water interactions in arid/semi-arid wetlands and the consequences of salinity for wetland ecology. *Ecohydrol.* 2008, 1, 43–58. doi: 10.1002/eco.6
- Keene, W. C., Khalil, M. Aslam K., Erickson, D. J., McCulloch, A., Graedel, T. E., Lobert, J. M., Aucott, M. L., Gong, S. L., Harper, D. B., Kleiman, G., Midgley, P., Moore, R. M., Seuzaret, C., Sturges, W. T., Benkovitz, C. M., Koropalov, V., Barrie, L. A., Li, Y. F. Composite global emissions of reactive chlorine from anthropogenic and natural sources: Reactive chlorine emissions inventory. *J. Geophys. Res.* 1999a, 104, 8429. doi: 10.1029/1998JD100084
- Keene, W. C., Khalil, M. Aslam K., Erickson, D. J., McCulloch, A., Graedel, T. E., Lobert, J. M., Aucott, M. L., Gong, S. L., Harper, D. B., Kleiman, G., Midgley, P., Moore, R. M., Seuzaret, C., Sturges, W. T., Benkovitz, C. M., Koropalov, V., Barrie, L. A., Li, Y. F. Composite global emissions of reactive chlorine from anthropogenic and natural sources: Reactive chlorine emissions inventory. *J. Geophys. Res.* 1999b, 104, 8429. doi: 10.1029/1998JD100084
- Keene, W. C., Sander, R., Pszenny, A. A., Vogt, R., Crutzen, P. J., Galloway, J. N. Aerosol pH in the marine boundary layer. *J. Aerosol Sci.* 1998, 29, 339–356. doi: 10.1016/S0021-8502(97)10011-8
- Kester, D. R., Byrne, R. H., Liang, Y.-J. Redox reactions and solution complexes of iron in marine systems. In: Church T.M. (ed.) *Marine Chemistry in the Coastal Environment*, vol 18. pp 56–79 1975
- Kester, D. R., Duedall, I. W., Connors, D. N., Pytkowicz, R. M. Preparation of artificial seawater. *Limnol. Oceanogr.* 1967, 12, 176–179. doi: 10.4319/lo.1967.12.1.0176
- Kim, S.-y., Koretsky, C. Effects of road salt deicers on sediment biogeochemistry. *Biogeochemistry* 2013, 112, 343–358. doi: 10.1007/s10533-012-9728-x
- Kiwi, J., Lopez, A., Nadochenko, V. Mechanism and kinetics of the OH-radical intervention during Fenton oxidation in the presence of a significant amount of radical scavenger (Cl). *Environ. Sci. Technol.* 2000, 34, 2162–2168. doi: 10.1021/es991406i
- Knipping, E. M., Lakin, M. J., Foster, K. L., Jungwirth, P., Tobias, D. J., Gerber, R. B., Dabdub, D., Finlayson-Pitts, B. J. Experiments and simulations of ion-enhanced interfacial chemistry on aqueous NaCl aerosols. *Science* 2000, 288, 301–306. doi: 10.1126/science.288.5464.301
- Knutson, E. O., Whitby, K. T. Aerosol classification by electric mobility: apparatus, theory, and applications. *J. Aerosol Sci.* 1975, 6, 443–451. doi: 10.1016/0021-8502(75)90060-9
- Krause, T., Tubbesing, C., Benzing, K., Schöler, H. F. Model reactions and natural occurrence of furans from hypersaline environments. *Biogeosciences* 2014, 11, 2871–2882. doi: 10.5194/bg-11-2871-2014
- Kuma, K., Nishioka, J. U., Matsunaga, K. Controls on iron(III) hydroxide solubility in seawater: The influence of pH and natural organic chelators. *Limnol. Oceanogr.* 1996, 41, 396–407. doi: 10.4319/lo.1996.41.3.0396

- Le Bras, G., Platt, U. A possible mechanism for combined chlorine and bromine catalyzed destruction of tropospheric ozone in the Arctic. *Geophys. Res. Lett.* 1995, 22, 599–602. doi: 10.1029/94GL03334
- Leighton, P. A. Photochemistry of air pollution. In: Loebel E.M. (ed.) "Physical Chemistry" series of monographs, vol 9. p 300. Academic Press, New York and London 1961
- Lim, M., Chiang, K., Amal, R. Photochemical synthesis of chlorine gas from iron(III) and chloride solution. *J. Photochem. Photobiol., A* 2006, 183, 126–132. doi: 10.1016/j.jphotochem.2006.03.005
- Lister, M. W., Rivington, D. E. Some ferric halide complexes, and ternary complexes with thiocyanate ions. *Can. J. Chem.* 1955, 33, 1603–1613. doi: 10.1139/v55-194
- Liu, B., Pui, D. On the performance of the electrical aerosol analyzer. *J. Aerosol Sci.* 1975, 6, 249–264. doi: 10.1016/0021-8502(75)90093-2
- Liu, X., Millero, F. J. The solubility of iron in seawater. *Marine Chem.* 2002, 77, 43–54. doi: 10.1016/S0304-4203(01)00074-3
- Lohninger, H., Ofner, J. Multisensor hyperspectral imaging as a versatile tool for image-based chemical structure determination. *Spectrosc. Eur.* 2014, 6–10
- Long, D. T., Fegan, N. E., McKee, J. D., Lyons, W. B., Hines, M. E., Macumber, P. G. Formation of alunite, jarosite and hydrous iron oxides in a hypersaline system: Lake Tyrrell, Victoria, Australia. *Chem. Geol.* 1992, 96, 183–202. doi: 10.1016/0009-2541(92)90128-R
- Luo, C., Mahowald, N., Bond, T., Chuang, P. Y., Artaxo, P., Siefert, R., Chen, Y., Schauer, J. Combustion iron distribution and deposition. *Global Biogeochem. Cycles* 2008, 22, n/a. doi: 10.1029/2007GB002964
- Luo, C., Mahowald, N., del Corral, J. Sensitivity study of meteorological parameters on mineral aerosol mobilization, transport, and distribution. *J. Geophys. Res.* 2003, 108. doi: 10.1029/2003JD003483
- Machulek, A., Moraes, J. E. F., Vautier-Giongo, C., Silverio, C. A., Friedrich, L. C., Nascimento, C. A. O., Gonzalez, M. C., Quina, F. H. Abatement of the inhibitory effect of chloride anions on the photo-Fenton process. *Environ. Sci. Technol.* 2007, 41, 8459–8463. doi: 10.1021/es071884q
- Machulek, A., Moraes, José Ermírio F, Okano, L. T., Silvério, C. A., Quina, F. H. Photolysis of ferric ions in the presence of sulfate or chloride ions: implications for the photo-Fenton process. *Photochem. Photobiol. Sci.* 2009, 8, 985–991. doi: 10.1039/b900553f
- Machulek, A., Vautier-Giongo, C., Moraes, José E F, Nascimento, Claudio A O, Quina, F. H. Laser flash photolysis study of the photocatalytic step of the photo-Fenton reaction in saline solution. *J. Photochem. Photobiol.* 2006, 82, 208–212. doi: 10.1562/2005-05-28-RA-548
- Madronich, S., Flocke, S. The role of solar radiation in atmospheric chemistry. In: Hutzinger O., Boule P. (eds.) *Environmental Photochemistry*, 2 / 2L. pp 1–26. Springer, Berlin Heidelberg 1999
- Mahowald, N. M., Engelstaedter, S., Luo, C., Sealy, A., Artaxo, P., Benitez-Nelson, C., Bonnet, S., Chen, Y., Chuang, P. Y., Cohen, D. D., Dulac, F., Herut, B., Johansen, A.

- M., Kubilay, N., Losno, R., Maenhaut, W., Paytan, A., Prospero, J. M., Shank, L. M., Siefert, R. L. Atmospheric iron deposition: global distribution, variability, and human perturbations. *Ann. Rev. Mar. Sci.* 2009, 1, 245–278. doi: 10.1146/annurev.marine.010908.163727
- Martell, A. E., Smith, R. M., Critical Stability Constants. Volume 4. Inorganic Complexes. Plenum, New York 1976
- Martin, R. S., Mather, T. A., Pyle, D. M., Power, M., Allen, A. G., Aiuppa, A., Horwell, C. J., Ward, E. P. W. Composition-resolved size distributions of volcanic aerosols in the Mt. Etna plumes. *J. Geophys. Res.* 2008, 113. doi: 10.1029/2007JD009648
- Merkel, B., Planer-Friedrich, B., Groundwater Geochemistry: A Practical Guide to Modeling of Natural and Contaminated Aquatic Systems. Springer, Berlin Heidelberg 2008
- Meskhidze, N. Dust and pollution: A recipe for enhanced ocean fertilization? *J. Geophys. Res.* 2005, 110. doi: 10.1029/2004JD005082
- Millero, F. J., Yao, W., Aicher, J. The speciation of Fe(II) and Fe(III) in natural waters. *Marine Chem.* 1995, 50, 21–39. doi: 10.1016/0304-4203(95)00024-L
- Misra, C., Singh, M., Shen, S., Sioutas, C., Hall, P. M. Development and evaluation of a personal cascade impactor sampler (PCIS). *J. Aerosol Sci.* 2002, 33, 1027–1047. doi: 10.1016/S0021-8502(02)00055-1
- Mochida, M., Hirokawa, J., Akimoto, H. Unexpected large uptake of O₃ on sea salts and the observed Br₂ formation. *Geophys. Res. Lett.* 2000, 27, 2629–2632. doi: 10.1029/1999GL010927
- Mochida, M., Hirokawa, J., Kajii, Y., Akimoto, H. Heterogeneous reactions of Cl₂ with sea salts at ambient temperature: Implications for halogen exchange in the atmosphere. *Geophys. Res. Lett.* 1998, 25, 3927–3930. doi: 10.1029/1998GL900100
- Molina, L. T., Molina, M. J. Production of chlorine oxide (Cl₂O₂) from the self-reaction of the chlorine oxide (ClO) radical. *J. Phys. Chem.* 1987, 91, 433–436. doi: 10.1021/j100286a035
- Molina, M. J., Rowland, F. S. Stratospheric sink for chlorofluoromethanes: Chlorine atom-catalysed destruction of ozone. *Nature* 1974, 249, 810–812. doi: 10.1038/249810a0
- Murphy, D. M., Cziczo, D. J., Froyd, K. D., Hudson, P. K., Matthew, B. M., Middlebrook, A. M., Peltier, R. E., Sullivan, A., Thomson, D. S., Weber, R. J. Single-particle mass spectrometry of tropospheric aerosol particles. *J. Geophys. Res.* 2006, 111. doi: 10.1029/2006JD007340
- Nadtochenko, V., Kiwi, J. Primary photochemical reactions in the photo-fenton system with ferric chloride. 1. A case study of xylydine oxidation as a model compound. *Environ. Sci. Technol.* 1998a, 32, 3273–3281. doi: 10.1021/es970962e
- Nadtochenko, V. A., Kiwi, J. Photolysis of FeOH²⁺ and FeCl²⁺ in aqueous solution. photodissociation kinetics and quantum yields. *Inorg. Chem.* 1998b, 37, 5233–5238. doi: 10.1021/ic9804723
- Nissenson, P., Wingen, L. M., Hunt, S. W., Finlayson-Pitts, B. J., Dabdub, D. Rapid formation of molecular bromine from deliquesced NaBr aerosol in the presence of

- ozone and UV light. *Atmos. Environ.* 2014, 48, 491–506. doi: 10.1016/j.atmosenv.2014.02.056
- Novič, M., Grgić, I., Poje, M., Hudnik, V. Iron-catalyzed oxidation of s(IV) species by oxygen in aqueous solution: Influence of pH on the redox cycling of iron. *Atmos. Environ.* 1996, 30, 4191–4196. doi: 10.1016/1352-2310(96)00137-9
- Okada, K., Naruse, H., Tanaka, T., Nemoto, O., Iwasaka, Y., Wu, P.-M., Ono, A., Duce, R. A., Uematsu, M., Merrill, J. T., Arao, K. X-ray spectrometry of individual Asian dust-storm particles over the Japanese islands and the North Pacific Ocean. *Atmos. Environ. A* 1990, 24, 1369–1378. doi: 10.1016/0960-1686(90)90043-M
- Park, J.-H., Christov, C. I., Ivanov, A. V., Molina, M. J. On OH Uptake by Sea Salt under Humid Conditions. *Geophys. Res. Lett.* 2009, 36, L02802. doi: 10.1029/2008GL036160
- Parkhurst, D. L., Appelo, C. A. User's guide to PHREEQC (Version 2): A computer program for speciation, batch-reaction, one-dimensional transport, and inverse geochemical calculations 1999
- Pitzer, K. S. Thermodynamics of electrolytes. I. Theoretical basis and general equations. *J. Phys. Chem.* 1973, 77, 268–277. doi: 10.1021/j100621a026
- Platt, U., Hönninger, G. The role of halogen species in the troposphere. *Chemosphere* 2003, 52, 325–338. doi: 10.1016/S0045-6535(03)00216-9
- Rabinowitch, E., Stockmayer, W. H. Association of ferric ions with chloride, bromide and hydroxyl ions (a spectroscopic study). *J. Am. Chem. Soc.* 1942, 64, 335–347. doi: 10.1021/ja01254a034
- Roberts, T. J., Martin, R. S., Jourdain, L. Reactive bromine chemistry in Mount Etna's volcanic plume: the influence of total Br, high-temperature processing, aerosol loading and plume–air mixing. *Atmos. Chem. Phys.* 2014, 14, 11201–11219. doi: 10.5194/acp-14-11201-2014
- Rossi, M. J. Heterogeneous Reactions on Salts. *Chem. Rev.* 2003, 103, 4823-4882
- Rudich, Y., Talukdar, R. K., Ravishankara, A. R., Fox, R. W. Reactive uptake of NO₃ on pure water and ionic solutions. *J. Geophys. Res.* 1996, 101, 21023–21031. doi: 10.1029/96JD01844
- Sadanaga, Y., Hirokawa, J., Akimoto, H. Formation of molecular chlorine in dark condition: Heterogeneous reaction of ozone with sea salt in the presence of ferric ion. *Geophys. Res. Lett.* 2001, 28, 4433–4436. doi: 10.1029/2001GL013722
- Saiz-Lopez, A., Plane, John M C, Baker, A. R., Carpenter, L. J., von Glasow, R., Martín, Juan C Gómez, McFiggans, G., Saunders, R. W. Atmospheric chemistry of iodine. *Chem. Rev.* 2012, 112, 1773–1804. doi: 10.1021/cr200029u
- Sander, R. Compilation of Henry's law constants (version 4.0) for water as solvent. *Atmos. Chem. Phys.* 2015, 15, 4399–4981. doi: 10.5194/acp-15-4399-2015
- Saueressig, G., Bergamaschi, P., Crowley, J. N., Fischer, H., Harris, G. W. Carbon kinetic isotope effect in the reaction of CH₄ with Cl atoms. *Geophys. Res. Lett.* 1995, 22, 1225–1228. doi: 10.1029/95GL00881
- Schroth, A. W., Crusius, J., Sholkovitz, E. R., Bostick, B. C. Iron solubility driven by speciation in dust sources to the ocean. *Nature Geosci.* 2009, 2, 337–340. doi: 10.1038/ngeo501

- Schweitzer, F., Mirabel, P., George, C. Heterogeneous chemistry of nitril halides in relation to tropospheric halogen activation. *J. Atmos. Chem.* 1999, 34, 101–117. doi: 10.1023/A:1006249921480
- Shi, Z., Krom, M. D., Bonneville, S., Baker, A. R., Jickells, T. D., Benning, L. G. Formation of iron nanoparticles and increase in iron reactivity in mineral dust during simulated cloud processing. *Environ. Sci. Technol.* 2009, 43, 6592–6596. doi: 10.1021/es901294g
- Siekmann, F., Freisetzung von photolabilen und reaktiven Halogenverbindungen aus salzhaltigen Aerosolen unter simulierten troposphärischen Reinluftbedingungen in einer Aerosol-Smogkammer, PhD thesis. Atmospheric Chemistry Research Laboratory, University of Bayreuth 2008. <https://epub.uni-bayreuth.de/view/person/Siekmann=3AFrank=3A=3A.html>
- Soto-Jiménez, M. F., Páez-Osuna, F. Diagenetic processes on metals in hypersaline mudflat sediments from a subtropical saltmarsh (SE Gulf of California): Postdepositional mobility and geochemical fractions. *Appl. Geochem.* 2008, 23, 1202–1217. doi: 10.1016/j.apgeochem.2007.11.011
- Stutz, J., Ackermann, R., Fast, J. D., Barrie, L. Atmospheric reactive chlorine and bromine at the Great Salt Lake, Utah. *Geophys. Res. Lett.* 2002, 29, 18-1. doi: 10.1029/2002GL014812
- Sullivan, R. C., Guazzotti, S. A., Sodeman, D. A., Prather, K. A. Direct observations of the atmospheric processing of Asian mineral dust. *Atmos. Chem. Phys.* 2007a, 7, 1213–1236. doi: 10.5194/acp-7-1213-2007
- Sullivan, R. C., Guazzotti, S. A., Sodeman, D. A., Tang, Y., Carmichael, G. R., Prather, K. A. Mineral dust is a sink for chlorine in the marine boundary layer. *Atmos. Environ.* 2007b, 41, 7166–7179. doi: 10.1016/j.atmosenv.2007.05.047
- Svensson, R., Ljungström, E., Lindqvist, O. Kinetics of the reaction between nitrogen dioxide and water vapour. *Atmos. Environ.* 1987, 21, 1529–1539. doi: 10.1016/0004-6981(87)90315-5
- Tegen, I., Fung, I. Modeling of mineral dust in the atmosphere: Sources, transport, and optical thickness. *J. Geophys. Res.* 1994, 99, 22897. doi: 10.1029/94JD01928
- Thornton, J. A., Kercher, J. P., Riedel, T. P., Wagner, N. L., Cozic, J., Holloway, J. S., Dubé, W. P., Wolfe, G. M., Quinn, P. K., Middlebrook, A. M., Alexander, B., Brown, S. S. A large atomic chlorine source inferred from mid-continental reactive nitrogen chemistry. *Nature* 2010, 464, 271–274. doi: 10.1038/nature08905
- Tilgner, A., Bräuer, P., Wolke, R., Herrmann, H. Modelling multiphase chemistry in deliquescent aerosols and clouds using CAPRAM3.0i. *J. Atmos. Chem.* 2013, 70, 221-256. doi: 10.1007/s10874-013-9267-4
- Tobo, Y., Zhang, D., Nakata, N., Yamada, M., Ogata, H., Hara, K., Iwasaka, Y. Hygroscopic mineral dust particles as influenced by chlorine chemistry in the marine atmosphere. *Geophys. Res. Lett.* 2009, 36. doi: 10.1029/2008GL036883
- Tosca, N. J., McLennan, S. M., Clark, B. C., Grotzinger, J. P., Hurowitz, J. A., Knoll, A. H., Schröder, C., Squyres, S. W. Geochemical modeling of evaporation processes on Mars: Insight from the sedimentary record at Meridiani Planum. *Earth and Planet. Sc. Lett.* 2005, 240, 122–148. doi: 10.1016/j.epsl.2005.09.042

- Troy, R. C., Margerum, D. W. Non-metal redox kinetics: hypobromite and hypobromous acid reactions with iodide and with sulfite and the hydrolysis of bromosulfate. *Inorg. Chem.* 1991, 30, 3538–3543. doi: 10.1021/ic00018a028
- Truesdell, A. H., Jones, B. F., WATEQ, a computer program for calculating chemical equilibria of natural waters. US Department of the Interior, Geological Survey 1973
- Tuckermann, M., Ackermann, R., Gölz, C., Lorenzen-Schmidt, H., Senne, T., Stutz, J., Trost, B., Unold, W., Platt, U. DOAS-observation of halogen radical-catalysed Arctic boundary layer ozone destruction during the ARCTOC-Campaigns 1995 and 1996 in Ny-Ålesund, Spitsbergen. *Tellus B* 1997, 49, 533–555. doi: 10.1034/j.1600-0889.49.issue5.9.x
- Vione, D., Maurino, V., Minero, C., Calza, P., Pelizzetti, E. Phenol Chlorination and Photochlorination in the Presence of Chloride Ions in Homogeneous Aqueous Solution. *Environ. Sci. Technol.* 2005, 39, 5066–5075. doi: 10.1021/es0480567
- Vione, D., Maurino, V., Minero, C., Pelizzetti, E., Harrison, Mark A J, Olariu, R.-I., Arsene, C. Photochemical reactions in the tropospheric aqueous phase and on particulate matter. *Chem. Soc. Rev.* 2006, 35, 441–453. doi: 10.1039/b510796m
- Vogt, R., Crutzen, P. J., Sander, R. A mechanism for halogen release from sea-salt aerosol in the remote marine boundary layer. *Nature* 1996, 383, 327–330. doi: 10.1038/383327a0
- Vogt, R., Finlayson-Pitts, B. J. Unique photochemistry of surface nitrate. *J. Phys. Chem.* 1995, 99, 17269–17272. doi: 10.1021/j100047a035
- von Glasow, R. Atmospheric chemistry: Wider role for airborne chlorine. *Nature* 2010, 464, 168–169. doi: 10.1038/464168a
- von Glasow, R., Crutzen, P. J. Tropospheric halogen chemistry. *Treatise on Geochemistry* 2007, 1–67. doi: 10.1016/B0-08-043751-6/04141-4
- Wahner, A., Mentel, T. F., Sohn, M. Gas-phase reaction of N₂O₅ with water vapor: Importance of heterogeneous hydrolysis of N₂O₅ and surface desorption of HNO₃ in a large Teflon chamber. *Geophys. Res. Lett.* 1998, 25, 2169–2172. doi: 10.1029/98GL51596
- Wang, R., Balkanski, Y., Boucher, O., Bopp, L., Chappell, A., Ciais, P., Hauglustaine, D., Peñuelas, J., Tao, S. Sources, transport and deposition of iron in the global atmosphere. *Atmos. Chem. Phys.* 2015, 15, 6247–6270. doi: 10.5194/acp-15-6247-2015
- Wang, W.-N., Purwanto, A., Lenggono, I. W., Okuyama, K., Chang, H., Jang, H. D. Investigation on the correlations between droplet and particle size distribution in ultrasonic spray pyrolysis. *Ind. Eng. Chem. Res.* 2008, 47, 1650–1659. doi: 10.1021/ie070821d
- Warneck, P., Chemistry of the Natural Atmosphere. Academic press 1999
- Wayne, R. P., Poulet, G., Biggs, P., Burrows, J. P., Cox, R. A., Crutzen, P. J., Hayman, G. D., Jenkin, M. E., Le Bras, G., Moortgat, G. K., Platt, U., Schindler, R. N. Halogen oxides: Radicals, sources and reservoirs in the laboratory and in the atmosphere. *Atmos. Environ. A* 1995, 29, 2677–2881. doi: 10.1016/1352-2310(95)98124-Q

- Wiedensohler, A. An approximation of the bipolar charge distribution for particles in the submicron size range. *J. Aerosol Sci.* 1988, 19, 387–389. doi: 10.1016/0021-8502(88)90278-9
- Williams, W. D. Environmental threats to salt lakes and the likely status of inland saline ecosystems in 2025. *Envir. Conserv.* 2002, 29. doi: 10.1017/S0376892902000103
- Wittmer, J., Bleicher, S., Zetzsch, C. Iron(III)-induced activation of chloride and bromide from modeled salt pans. *J. Phys. Chem. A* 2015a, 119, 4373–4385. doi: 10.1021/jp508006s
- Wittmer, J., Bleicher, S., Ofner, J., Zetzsch, C. Iron(III)-induced activation of chloride from artificial sea-salt aerosol. *Environ. Chem.* 2015b, 12, 461–475. doi: 10.1071/EN14279
- Wittmer, J., Bobrowski, N., Liotta, M., Giuffrida, G., Calabrese, S., Platt, U. Active alkaline traps to determine acidic-gas ratios in volcanic plumes: Sampling techniques and analytical methods. *Geochem. Geophys. Geosyst.* 2014, 15, 2797–2820. doi: 10.1002/2013GC005133
- Wittmer, J., Zetzsch, C. Photochemical activation of chlorine by iron-oxide aerosol. *submitted to Atm. Chem.* 2015
- Wurzler, S., Reisin, T. G., Levin, Z. Modification of mineral dust particles by cloud processing and subsequent effects on drop size distributions. *J. Geophys. Res.* 2000, 105, 4501. doi: 10.1029/1999JD900980
- Yatsimirskii, K. B., Vasil'ev, V. P., Instability constants of complex compounds. Pergamon Press, Oxford 1960
- Zangmeister, C. D., Turner, J. A., Pemberton, J. E. Segregation of NaBr in NaBr/NaCl crystals grown from aqueous solutions: Implications for sea salt surface chemistry. *Geophys. Res. Lett.* 2001, 28, 995–998. doi: 10.1029/2000GL012539
- Zetzsch, C., Behnke, W. Heterogeneous photochemical sources of atomic Cl in the troposphere. *Ber. der Bunsengesell. für physikal. Chemie* 1992, 96, 488–493. doi: 10.1002/bbpc.19920960351
- Zetzsch, C., Behnke, W. Heterogeneous reactions of chlorine compounds. In: Niki H., Becker K.H. (eds.) *The Tropospheric Chemistry of Ozone in the Polar Regions*. pp 291–306. Springer, Berlin, Heidelberg 1993
- Zetzsch, C., Pfahler, G., Behnke, W. Heterogeneous formation of chlorine atoms from NaCl in a photosmog system. *J. Aerosol Sci.* 1988, 19, 1203–1206. doi: 10.1016/0021-8502(88)90136-X
- Zhang, D., Iwasaka, Y. Chlorine deposition on dust particles in marine atmosphere. *Geophys. Res. Lett.* 2001, 28, 3613–3616. doi: 10.1029/2001GL013333
- Zhu, X., Prospero, J. M., Millero, F. J., Savoie, D. L., Brass, G. W. The solubility of ferric ion in marine mineral aerosol solutions at ambient relative humidities. *Marine Chem.* 1992, 38, 91–107. doi: 10.1016/0304-4203(92)90069-M
- Zhuang, G., Yi, Z., Duce, R. A., Brown, P. R. Chemistry of iron in marine aerosols. *Global Biogeochem. Cycles* 1992, 6, 161–173. doi: 10.1029/92GB00756
- Zuo, Y., Hoigné, J. Formation of hydrogen peroxide and depletion of oxalic acid in atmospheric water by photolysis of iron(III)-oxalato complexes. *Environ. Sci. Technol.* 1992, 26, 1014–1022. doi: 10.1021/es00029a022

Chapter 2:

Iron(III)-Induced Activation of Chloride and Bromide from Modeled Salt Pans

Julian Wittmer¹, Sergej Bleicher^{1,2} and Cornelius Zetzsch¹

[1] Atmospheric Chemistry Research Unit, BayCEER, University of Bayreuth, Dr. Hans-Frisch Straße 1-3, 95448 Bayreuth, Germany

[2] Now at: Department of Forensic Toxicology, Synlab MVZ Weiden GmbH, Zur Kesselschmiede 4, 92637 Weiden, Germany

Reproduced with permission from Wittmer, J., Bleicher, S., Zetzsch, C. Iron(III)-induced activation of chloride and bromide from modeled salt pans. J. Phys. Chem. A 119(19), 4373–4385 (2015b). doi: 10.1021/jp508006s. Copyright 2015 American Chemical Society.

Full text article: <http://pubs.acs.org/doi/abs/10.1021/jp508006s>

Special Issue: Mario Molina Festschrift

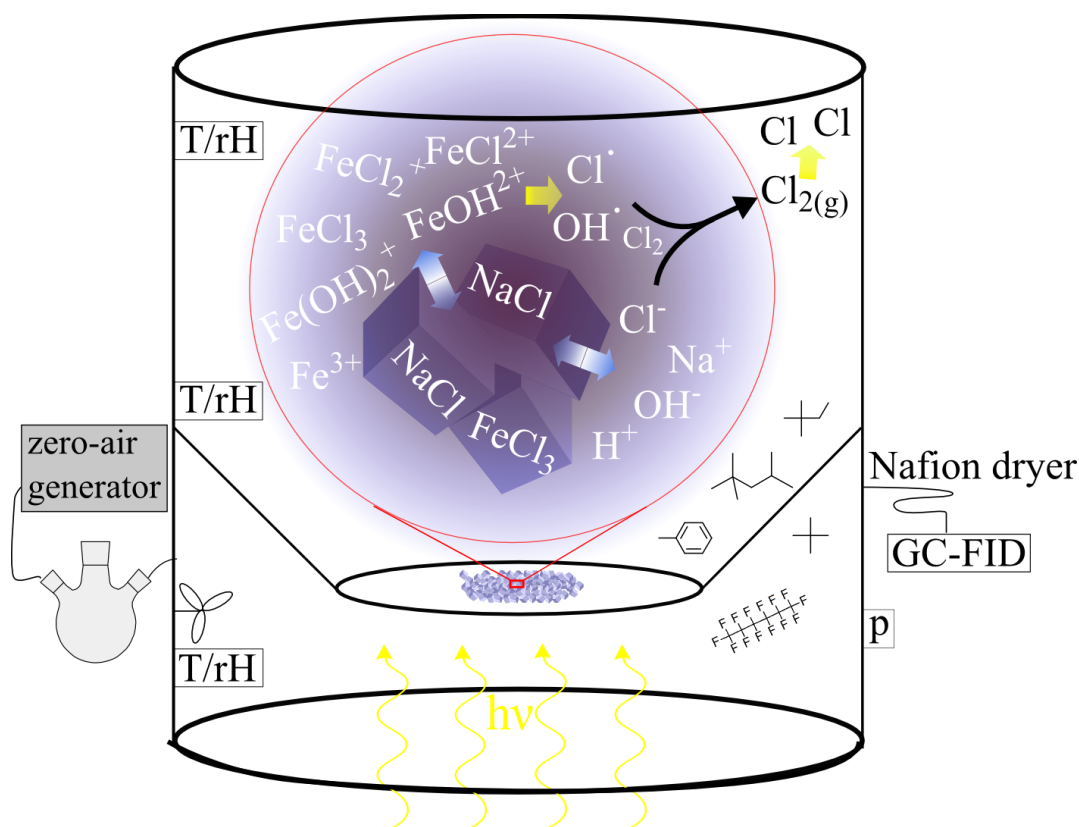
Received: August 7, 2014

Revised: September 18, 2014

Published: September 22, 2014

Abstract

The photochemistry of halides in sea spray aerosol, on salt pans, and on other salty surfaces leads to a formation of reactive halogen species. We investigated the photochemical formation of atomic chlorine (Cl) and bromine (Br) in the gas phase in the presence of laboratory-modeled salt pans consisting of sodium chloride doped with iron(III) chloride hexahydrate (0.5 and 2 wt %). The samples were spread on a Teflon sheet and exposed to simulated sunlight in a Teflon smog chamber in purified, humidified air in the presence of a test mixture of hydrocarbons at the ppb level to determine Cl, Br, and OH formation by the radical clock method. Driven by the photolytic reduction of Fe(III) to Fe(II), the production rates of the Fe(III)-doped NaCl salt samples (up to 10^7 atoms $\text{cm}^{-3} \text{s}^{-1}$) exceeded the release of Cl above a pure NaCl sample by more than an order of magnitude in an initially O_3 -free environment at low NO_x . In bromide-doped samples (0.5 wt % NaBr), a part of the Cl release was replaced by Br when Fe(III) was present. Additions of sodium sulfate, sodium oxalate, oxalic acid, and catechol to NaCl/ FeCl_3 samples were found to restrain the activation of chloride.



2.1 Introduction

Besides the hydroxyl radical (OH), chlorine atoms (Cl) are an important oxidant in the troposphere, particularly in marine environments.¹⁻⁴ Despite the importance of Cl for the ozone destruction mechanism in the stratosphere,^{5,6} the multifaceted role of atomic Cl in the lower part of the atmosphere as a depletion reagent for ozone or as an initiator of photochemistry in the early morning was rather underestimated and came into focus in the last 2 decades.^{1,7} Newer studies show an impact of reactive halogen species from the occurrence of nitryl chloride (ClNO₂) even in continental regions.^{8,9} Chlorine atoms are an effective consumer of volatile organic compounds (VOCs) and also influence the cycles of ozone (O₃) and nitrogen oxides (NO_x). Among the VOCs, the short-lived greenhouse gas methane (CH₄) is of major interest in climate research to date. Atomic Cl has a 16 times faster reaction rate constant toward methane in comparison to hydroxyl radicals at 298 K.¹⁰ Moreover, the behavior of the isotope enrichment, $\delta^{13}\text{C}$, of CH₄ in the tropospheric background can be ascribed to the reaction with atomic Cl representing a sink for CH₄ of 19 Tg yr⁻¹ that corresponds to 3.3% of total CH₄.¹¹⁻¹³ Levine et al.¹⁴ suggest that Cl could have been responsible for about 10% of the glacial–interglacial change in the isotopic composition of CH₄. A main question is therefore to determine and quantify the sources of atomic chlorine and their dependencies. The natural processes that are responsible for the activation of chloride in the liquid or solid phase into a gaseous form are only partly understood, and decisive inorganic halogen species (e.g., ClNO, BrNO, ClONO₂, BrONO₂, ClOH, HOBr) have not been detected yet in the troposphere,¹⁵ although the dependence on various parameters like pH,¹⁶ bromine content,¹⁷ and the concentrations of NO_x and O₃^{18,19} has been investigated.

High concentrations of reactive halogen species were observed in sea salt influenced environments, such as the Arctic. For example Jobson et al. calculated concentrations of $(0.39-7.7) \times 10^4$ Cl atoms cm⁻³ and $(0.3-6.1) \times 10^7$ Br atoms cm⁻³ for 1 day during their campaign at Alert, Northwest Territories,²⁰ by employing the radical clock technique during ozone depletion events.^{17,18,21} Combined with the measured concentrations of C₂–C₆ hydrocarbons and their reaction rates toward Cl and Br given by Jobson et al.,²⁰ this requires production rates of $(0.2-3.6) \times 10^5$ Cl atoms cm⁻³ s⁻¹ and $(0.2-3.3) \times 10^5$ Br atoms cm⁻³ s⁻¹ at least (not considering the contributions of other trace gases to the total reactivity of the atmosphere against Cl and Br). Furthermore, several studies detected reactive halogen species (including the molecular halogens) on coastal sites of the Arctic^{3,22-25} above salt lakes and salt covered areas such as the Dead Sea, Israel, or the Great Salt Lake, UT (U.S.A.),²⁶⁻²⁸ and also in volcanic plumes.^{29,30}

More than a century ago, Eder³¹ observed a catalytic effect of iron on chloride activation in solid salt and in the liquid phase when exposed to sunlight. In particular, the formation of iron(II) and aqueous Cl₂^{•-} radicals (due to the photodecomposition of iron(III) complexes in chloride-containing solutions) has been manifested by several studies³²⁻³⁶ that mainly concentrate on the detection of atomic chlorine formed in the aqueous phase but also observed the degassing of chlorine molecules (Cl₂) formed via combination of Cl₂^{•-}.³⁷ The speciation and photochemistry in the quasi-liquid microlayer (QLM) on the salt crystals are decisive for the halogen release. Depending on the composition of the salt and the humidity, water adsorbs on the crystals and forms and modifies the thickness and

properties of the QLM.^{38,39} The photolytic reduction of Fe(III) to Fe(II) plays a key role in the photo-Fenton reaction, together with hydrogen peroxide (H₂O₂), that is responsible for the reoxidation to Fe(III). However, the photo-Fenton reaction is inhibited at high salinity due to the formation of Fe-Cl complexes and the scavenging of OH radicals by Cl⁻, both forming the less reactive Cl₂^{•-} radical anion and lowering the combination of OH[•] to H₂O₂.^{35,40}

The present study deals with the photoinduced formation and release of Cl₂, BrCl, and Br₂ from humidified salts (in an O₃ free environment at low NO_x), detected indirectly in the form of Cl and Br atoms. In order to reproduce natural processes, the effects of several inorganic (Mg²⁺, Br⁻, SO₄²⁻) and organic (C₂O₄²⁻, C₆H₆O₂) constituents of natural salts are investigated in this work. In particular, an inhibiting impact of sulfate on the photo-Fenton reaction is known.³⁴ Moreover, bromide, which is far easier to oxidize than chloride, stimulates the activation of chloride.^{16,17} Even small amounts of bromide have a high impact on the chloride chemistry, whereas the impact of bromide on the iron induced chloride activation is still unclear and experimentally investigated in this work for the first time. Hypobromous acid (HOBr) combines with Br⁻ to form Br₂ but may also form bromine monochloride (BrCl) in the predominant presence of Cl⁻. Br₂ and BrCl are released to the gas phase, depending on the pH, and are photolyzed by sunlight to atomic Br and Cl, respectively. Organic compounds like oxalic acid (H₂C₂O₄) or catechol (C₆H₆O₂) are known to influence iron ions by complexation^{41,42} and thus intervene in the photoproduction of aqueous halogens and OH radicals.⁴³ Additionally, oxalate acts as a scavenger of OH[•].⁴⁴ The iron-catechol complexes are strongly colored and thus change the light absorbing properties of the salt samples.^{45,46}

2.2 Experimental Setup and Methods

2.2.1 Smog Chamber and Its Analytical Instrumentation

Measurements are performed in a cylindrical smog chamber made of Teflon film (FEP 200A, DuPont) that is fixed on three aluminum rings of 1.33 m diameter and combines two widths of the Teflon film to obtain a height of 2.5 m. This leads to a volume of more than 3500 L (slightly dependent on the internal pressure) and a surface to volume ratio of 3.8 m⁻¹.⁴⁷ The whole construction is suspended above an IR filter (2 cm of deionized water), an UV filter (3 mm of borosilicate glass), and bifocal reflectors with seven medium pressure arc lamps (Osram HMI, 1.2 kW each) to reproduce the actinic flux of the summer sun at 50° latitude.⁴⁸ Because the lamps have a heat-up time of 3 min until they attain their full intensity, they were covered during this time and rapidly uncovered at the beginning of the experiment.

To replenish the air consumption of the gas analyzers and warrant the zero air environment, a slight overpressure of 0.5–2 Pa (differential pressure sensor, Kalinsky Elektronik DS1) is maintained by a continuous flow of hydrocarbon-free zero air (zero-air-generator, cmc instruments, <1 ppb O₃, <0.5 ppb NO_x, <100 ppb CH₄) controlled by a mass flow controller (Tylan FC2910). Before flowing into the chamber, the zero air is humidified by a three-necked flask that is filled with bidistilled water and placed on a heater. In this way, the humidity can be adjusted by the water temperature in the flask. All experiments in this study were conducted at constant conditions at 20°C and 55–60%

relative humidity (RH), which was monitored by sensors (Driesen + Kern DKRF400X-P) at three levels of the chamber (top, middle, and bottom). Continuous mixing was achieved by a custom built fan (made of PTFE-Teflon), placed directly below the zero air inlet to achieve mixing times of 3–4 min. Furthermore, the smog chamber was equipped with an analyzer for NO (EcoPhysics, CLD 88p), coupled with a photolytic converter for NO_x (EcoPhysics, PLC 860), and with two O₃ analyzers (UPK 8001 and Thermo Fisher Scientific 49i). A more detailed description of the smog chamber and its analytical instrumentation can be found elsewhere.^{47,48}

2.2.2 Sample Preparation

The salt pans were prepared by solving the desired amount of compound in 500 mL of bidistilled water under gentle warming (below 50°C) to allow complete dissolution. In order to obtain a crystallized salt sample, the turbid brine, containing various brownish iron(III) species as the hydrolysis product,⁴⁹ was dried on a Teflon sheet (FEP 200A, DuPont) in a wide beaker (diameter 225 mm) at 50°C for at least 70 h under a constant zero air flow. The crust above the brine was broken every 24 h in order to achieve total dryness. Afterward, the residue was either milled in a ball mill (Retsch MM 2, Haan, Germany) or ground in a household salt mill or used as an untreated polycrystalline salt, depending on the hygroscopicity and thus the stickiness of the salt mixture. Each sample was spread on a circular 0.3 m² Teflon sheet mounted in the chamber. Before starting the irradiation, the chamber was flushed for at least 10 h by 30 L/min of humidified zero air (55–60% RH) in order to provide the humidification of the salt and to get rid of the inherent air intrusion during the insertion of the salt pan. The chemicals used were NaCl ACS (Sigma-Aldrich), MgCl₂·6H₂O (VWR), NaBr Suprapur (Merck), Na₂SO₄·10H₂O ACS (Merck), Na₂C₂O₄ ACS (Alfa Aesar), H₂C₂O₄·2H₂O (Merck), C₆H₆O₂ (Merck), and Fe(III)Cl₃·6H₂O ACS (Sigma Aldrich).

All in all, a total of 13 salt samples, different in their composition, were investigated under similar conditions, whereas some of them were irradiated twice or up to five times. The pH was determined afterward by adding about 2 g of the salt to 3 mL of bidistilled water in order to obtain a saturated solution and a rough estimate of the pH in the QLM on the salt crystals, especially with respect to relative differences of the salt samples and the thereby induced complex formation. Nonbleeding pH indicator strips (Merck, special indicator pH 0–2.5, 2.5–4.5 and 4.0–7.0) were employed, assuming an uncertainty of ± 0.5.

2.2.3 Quantification of Cl, Br, and OH by the Radical Clock

Method

Once gaseous Cl₂, BrCl, and Br₂ molecules were present, they were rapidly photolyzed to atoms by the solar simulator in our setup ($J_{\text{Cl}_2} = 1.55 \times 10^{-3} \text{ s}^{-1}$, $J_{\text{BrCl}} = 7 \times 10^{-3} \text{ s}^{-1}$, $J_{\text{Br}_2} = 1.7 \times 10^{-2} \text{ s}^{-1}$).⁴⁷ To quantify the concentrations of Cl, Br, and OH in the gas phase, the radical clock method^{50,51} was applied after smoothing the observed time profiles of the hydrocarbons⁴⁸ and was extended to bromine atoms when bromide was involved. This was achieved by monitoring the depletion of an inert dilution standard (n-perfluorohexane, PFH) and the consumption of selected hydrocarbons (HC_i), namely, 2,2-dimethylpropane (DMP), 2,2-dimethylbutane (DMB), 2,2,4-trimethylpentane (TMP), and

toluene (Tol), every 15 min by gas chromatography, GC (Siemens Sichromat 2), using an Al₂O₃-PLOT column with 50 m, employing a temperature gradient of 50°C/min to heat from 160 to 200°C after 3 min of runtime, using 0.25 mL/min He as the carrier gas, a flame ionization detector (FID), a custom-built liquid nitrogen cryotrap enrichment for focusing the samples with a sampling flow of 100 mL/min for 3 min, and a Nafion dryer. The dilution flow (to maintain the overpressure and replenish the consumption by the gas analytics) was typically 5 L/min, leading to a mean residence time of 12 h of the gas in the chamber. The degradation of the HC_i in combination with the respective rate constants of their reactions with Cl (k_{Cl,i}), Br (k_{Br,i}), and OH (k_{OH,i}) (Supporting Information, Table S2.1) allows us to compute time profiles for Cl, Br, and OH by solving the system of *i* differential equations according to eq 2.1 after fitting an appropriate analytical function to the profile of each HC_i.

$$-\frac{d[\text{HC}]_i}{dt} = k_{\text{Cl},i}[\text{Cl}][\text{HC}]_i + k_{\text{Br},i}[\text{Br}][\text{HC}]_i + k_{\text{OH},i}[\text{OH}][\text{HC}]_i \quad (2.1)$$

Dividing by [HC]_i separates the variables (eq 2.2) and allows us to identify the contribution of each radical to the consumption of the HC_i after integration.

$$-\frac{d\ln[\text{HC}]_i}{dt} = k_{\text{Cl},i}[\text{Cl}] + k_{\text{Br},i}[\text{Br}] + k_{\text{OH},i}[\text{OH}] \quad (2.2)$$

Due to the use of four different HC species *i* to determine three unknown variables, the system is overdetermined. The single results are arithmetically averaged, and the standard deviations allow us to obtain a statistical uncertainty of the result. The steady state of the radicals and atoms, formed by the photochemical processes and consumed by the HCs and their degradation products, delivers concentrations that inversely depend on the initial amount of the HC_i injected (if wall loss and reactions with CH₄, O₃, and other constituents are neglected), forming a total reactivity of the system toward the respective radical ($\sum_i k_{\text{X},i}[\text{HC}]_i$; X = Cl, Br, or OH). The total production, Q_X, during the time τ can be calculated by equalizing the source and the sinks, assuming a photostationary, steady state (d[X]/dt = 0)

$$Q_X = \int_0^\tau \sum_i k_{\text{X},i}[\text{HC}]_{i,t}[\text{X}]_t dt \quad (2.3)$$

Adopting the initial HC concentrations, [HC]_{i,0}, and the rate constants of their reactions with the radical X as a constant total reactivity of the chamber contents toward X over the time of the experiment allows us to calculate a maximal value of X. Such an approximation assumes that the reactivity of the reaction products is the same as the reactivity of the HC_i, which is only valid in the early stage of each experiment at low consumption of the hydrocarbons. By using actually measured, dilution corrected [HC]_i values and neglecting any X-reactivity of the products, a minimal value of Q_X can be calculated.

2.3 Results and Discussion

Salt compositions, treatment, reactivity of the system, resulting Cl and Br sources, and the determined OH concentrations of the 18 performed experiments are listed in Table 2.1.

2.3.1 Data Assessment and Evaluation

The development of the gas chromatograms during experiment # 6.2 is illustrated in Figure 2.1.

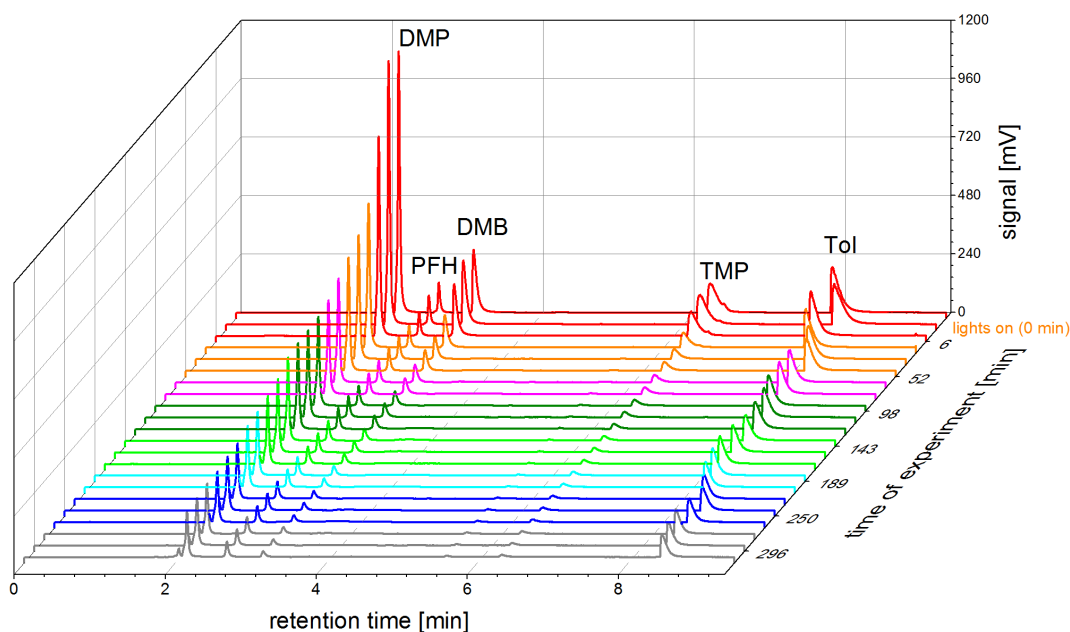


Figure 2.1: Evolution of the gas chromatograms from experiment #6.2 (2 g of $\text{FeCl}_3 \cdot 6\text{H}_2\text{O}$ /98 g of NaCl), showing the peaks of DMP, PFH, DMB, TMP, Tol, and an unidentified reaction product.

The peaks are manually integrated using the Chemstation software (HPCHEM-Agilent/Rev. B.04.03-SP1). The resulting peak areas of each measurement are corrected for dilution by the signal of the inert standard, PFH, and are shown in Figure 2.2.

The application of the (bi)exponential fit functions displayed in the figure in combination with eq 2.2 leads to smoothed time profiles for the Cl and OH concentrations (Br is below the detection limit in this experiment) that are shown in Figure 2.3. Due to the Cl dominated HC depletion and the low HC reactivity toward OH, the OH evaluation is errorprone and partly shows high uncertainties compared to the result of Cl. Eq 2.3 allows us to calculate the total source of Cl and OH (and Br if present). This principle was applied for the data evaluation of each experiment and led to the respective results that are discussed in the following sections.

Table 2.1: Salt Compositions, Irradiation Times, Total Initial Reactivity of the HCs in the Chamber against Cl and Br, Cl and Br Concentrations, and the Resulting Minimum and Maximum Cl and Br Sources (neglecting or considering degradation products, respectively), and OH Concentrations.

experiment no. ^a	composition (weight [g])	irradiation time [min]	initial Cl / Br reactivity (s ⁻¹)	Cl / Br concentration (10 ⁵ radicals cm ⁻³) ^h	Cl / Br - source Q _x (10 ¹⁰ atoms h ⁻¹ cm ⁻³)	OH concentration (10 ⁶ radicals cm ⁻³) ^h
# 1	NaCl (100) ^b	738	114	~5.8	4.1 – 4.2	~6
# 2	NaCl (95), MgCl ₂ ·6H ₂ O (5) ^b	760	62	~9.1	1.9 – 2.0	~10
# 3	NaCl (99.5), NaBr (0.5) ^b	474	60/0.0022	~ 8.5/~4084	1.6 – 1.7 / 2.6 – 3.1	~4.5
# 4	NaCl (98), Na ₂ C ₂ O ₄ (2) ^b	590	44	~1.8	2.7 – 2.8	~6.2
# 5	NaCl (98), C ₆ H ₆ O ₂ (2) ^c	432	41	n.d. ^e	n.d. ^e	~1.8
# 6.1	NaCl (98), FeCl ₃ ·6H ₂ O (2) ^c	30	73	~300 ^f	>79 – 500 ^f	n.d. ^g
# 6.2	NaCl (98), FeCl ₃ ·6H ₂ O (2) ^c	341	151	~18	63 – 89	~6.8
# 7.1	NaCl (99.5), FeCl ₃ ·6H ₂ O (0.5) ^c	300	284	~6	52 – 57	~3.1
# 7.2	NaCl (99.5), FeCl ₃ ·6H ₂ O (0.5) ^c	235	231	~390	130 – 230	~17
# 7.3	NaCl (99.5), FeCl ₃ ·6H ₂ O (0.5) ^c	306	195	~2.4	14 – 15	~1.5
# 7.4	NaCl (99.5), FeCl ₃ ·6H ₂ O (0.5) ^c	274	111	~6.2	19 – 21	~3.5
# 7.5	NaCl (99.5), FeCl ₃ ·6H ₂ O (0.5) ^c	165	86	~2.5	7.2 – 7.6	~4
# 8	NaCl (93), FeCl ₃ (2)·6 H ₂ O, Na ₂ SO ₄ ·10H ₂ O (5) ^b	311	71	~1.9	5 – 5.2	~3.5
# 9	NaCl (97.5), FeCl ₃ ·6H ₂ O (2), NaBr (0.5) ^b	666	353/0.0088	~1.5/~10195	11–12 / 27–32	~4.5
# 10	NaCl (96), FeCl ₃ ·6 H ₂ O (2), Na ₂ C ₂ O ₄ (2) ^d	214	235	~0.8	6.7 – 6.9	n.d. ^e
# 11	NaCl (96), FeCl ₃ ·6H ₂ O (2), C ₆ H ₆ O ₂ (2) ^d	220	297	n.d. ^e	n.d. ^e	~ 4
# 12	NaCl (96), FeCl ₃ ·6 H ₂ O (2), H ₂ C ₂ O ₄ ·2H ₂ O (2) ^d	129	85	~5.1	13 – 15	n.d. ^e
# 13	NaCl (91), FeCl ₃ ·6H ₂ O (2), Na ₂ SO ₄ ·10H ₂ O (5), H ₂ C ₂ O ₄ ·2H ₂ O (2) ^c	308	90	~0.5	1.4 – 1.5	~2.6

^aIn chronological order; two digits indicate multiple irradiations of the same sample. ^bMilled, ^cGround, ^dUntreated, ^eBelow the detection limit, ^fHCs disappeared within 30 min,

^gCannot be distinguished from Cl, ^hMean over the first hour

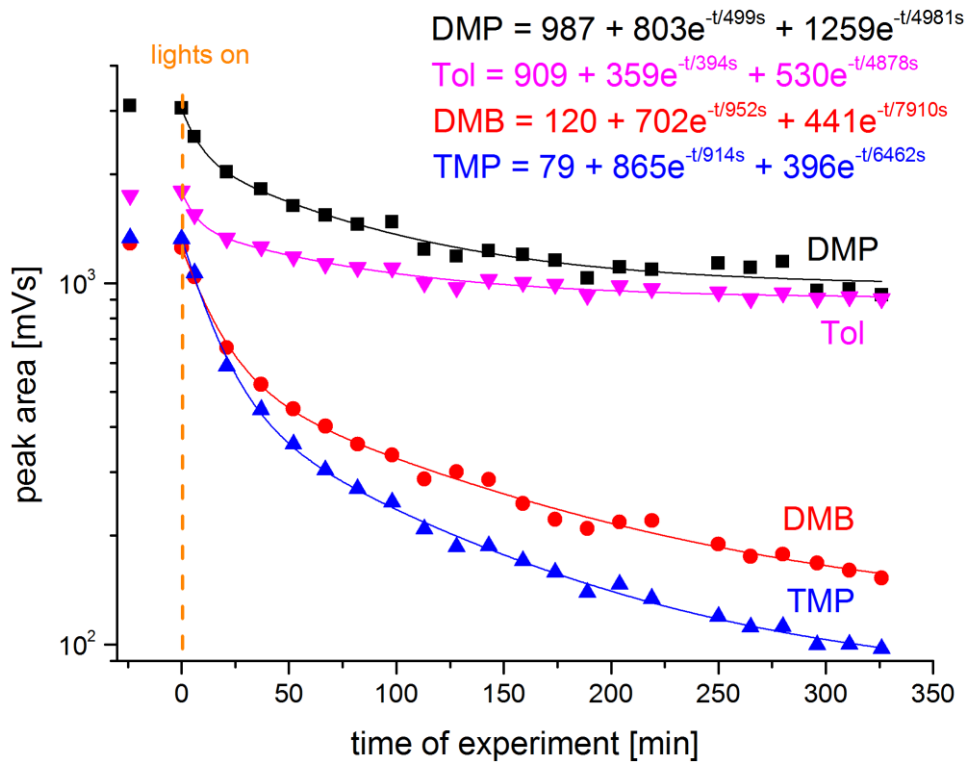


Figure 2.2: Dilution corrected time profiles of the integrated HC peak areas from experiment #6.2 (2 g $\text{FeCl}_3 \cdot 6\text{H}_2\text{O}$ /98 g NaCl).

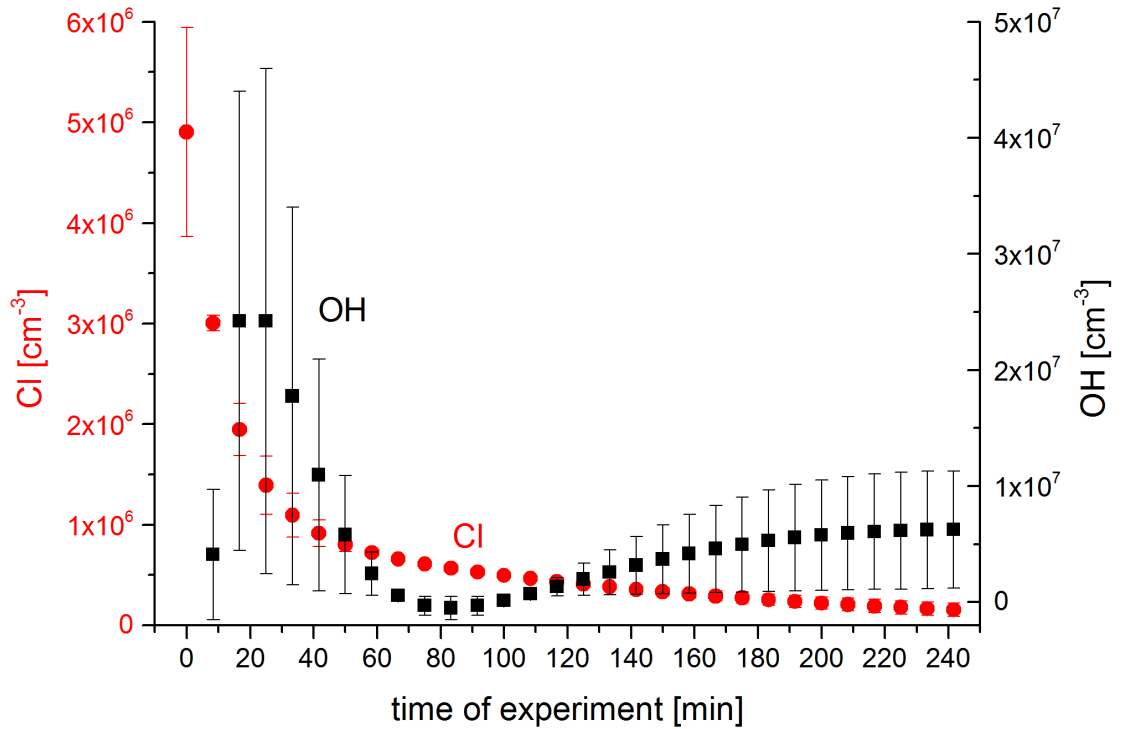


Figure 2.3: Resulting time profiles for the gaseous Cl and OH concentrations in the 2 g of $\text{FeCl}_3 \cdot 6\text{H}_2\text{O}$ /98 g of NaCl experiment #6.2.

Instead of using (bi)exponential functions, the application of sigmoidal fit functions to the HC_i time profiles may be more appropriate in certain cases. On the other hand, the fit

function does not make a difference in the resulting Cl production rates for a large Cl production and an almost immediate depletion of the HC_i. Some experiments instead show a delayed HC_i depletion that results (when applying sigmoidal functions) in an apparent increase of the production rate mainly in the first 30–40 min and a subsequent decrease similar to the (bi)exponential result. These various tendencies in the first 30–40 min (depending on the fit functions) may be considered as an effect of the limited time resolution (3 min cryotrap enrichment and 15 min for each total run) and an inhomogeneous mixing during the sampling time (3–4 min mixing time). However, the resulting total sources (over more than 60 min of the experiment) differ by 20% in extreme cases at most.

For typical [HC]_i concentrations of 10 ppb ($\sim 2.5 \times 10^{11}$ molecules cm⁻³), the approximate detection limit of the method for the radical concentrations is for Cl atoms 10⁴ molecules cm⁻³, for Br atoms 10⁹ molecules cm⁻³, and for OH 10⁶ molecules cm⁻³, leading to detectable production rates, dQ_X/dt , of about 10⁶ molecules cm⁻³s⁻¹ for Cl, 10⁸ molecules cm⁻³s⁻¹ for OH, and 10¹¹ molecules cm⁻³s⁻¹ for Br, depending on the various reactivities of the HCs that differ in this range. For example when Cl is present at significant levels, a 3 orders of magnitude higher Br concentration is needed to detect a contribution to the depletion of the HC_i. The detection limit and its uncertainty are characterized, for example, by the duration of the cold trap enrichment (currently 3 min) that limits the time resolution, by various wall loss rates compared to PFH, and by the fit functions that are applied to the profiles of each HC_i.

Alternatively to the evaluation method described above (when Br is not involved), one may integrate eq 2.2 and divide it by k_{OH} to solve the system graphically by exponential fits of the HC data for each measurement⁵¹

$$-\ln([HC]_i(\tau)/[HC]_{i,0})/k_{OH,i} = k_{Cl,i}/k_{OH,i} \int_0^\tau [Cl] dt + \int_0^\tau [OH] dt \quad (2.4)$$

This leads directly to time-integrated Cl and OH concentrations that are responsible for the measured HC depletion for each time of the sampling, whereas the initial fits of the

HC_i profiles lead to smoothed results for $\int [Cl] dt$ and $\int [OH] dt$.

Figure 2.4 compares the two evaluation methods based on experiment #6.2, where the resulting concentrations of the HC fit were integrated over time and plotted against the directly obtained, time-integrated results of the linear regression method. The absolute values and the time profiles are in very good agreement, except for the varying uncertainties that are caused by the statistical uncertainty of the combination of six Cl and OH results, each obtained by two HCs on the one hand and the standard error of one linear regression on the other hand.

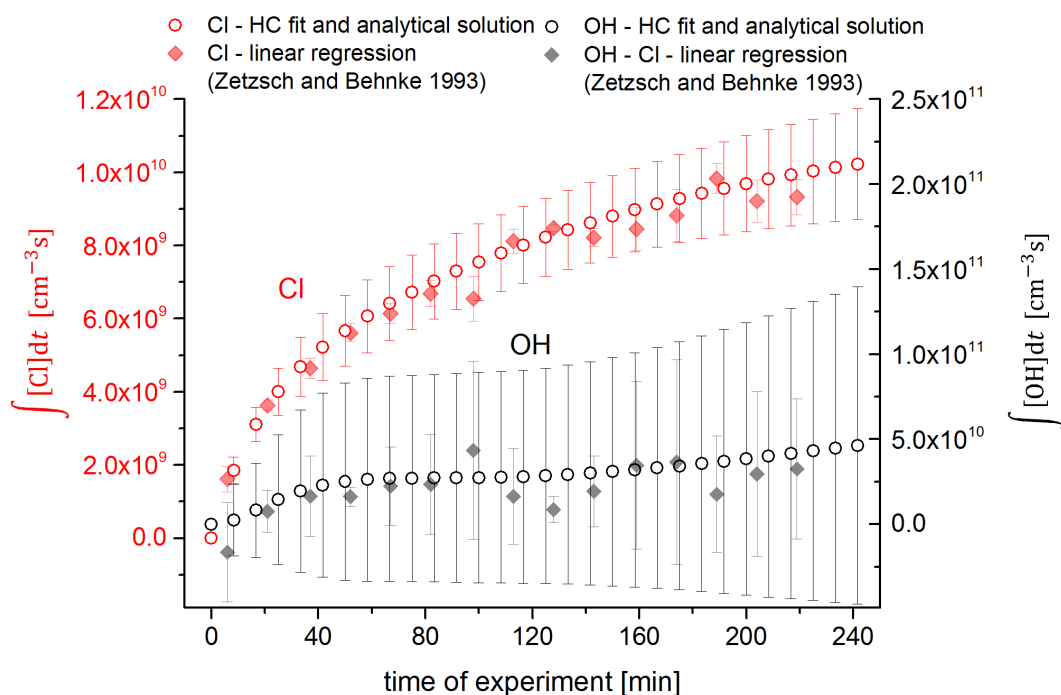


Figure 2.4: Time-integrated quasi-stationary Cl and OH concentrations derived from experiment #6.2 by the biexponential HC fit method described in section 2.2.3 (circles) in comparison to the evaluation proposed by Zetzsch and Behnke (diamonds).⁵¹

2.3.2 Blank Experiments with Iron-Free Salt Pans

In order to investigate the effects of Fe(III) enrichment in a salt sample, blank experiments were conducted by using iron free salts. Except for the catechol sample, all blank samples were milled and thus featured a finer grain size and a larger specific surface as compared to the ground and untreated samples.

Figures 2.5a and 2.5b present the Cl and Br production rates (dQ_x/dt) and the corresponding Cl and Br sources (Q_x) resulting from the blank experiments with pure NaCl (experiment #1) and with added NaBr (experiment #3). The graphs start where the irradiation of the sample was started ($t = 0$ min). The lower and upper margins of the bars represent the minimal and maximal values of dQ_x/dt and Q_x as described in section 2.2.3. The negative minimal and maximal uncertainties are drawn as thinner error bars for dQ_x/dt . Most measurements for Cl and Br from the blank samples are close to the detection limit and therefore show a large uncertainty. Further blank measurements include magnesium chloride, sodium oxalate, and catechol (experiments #2, #4, #5) and are shown in the Supporting Information.

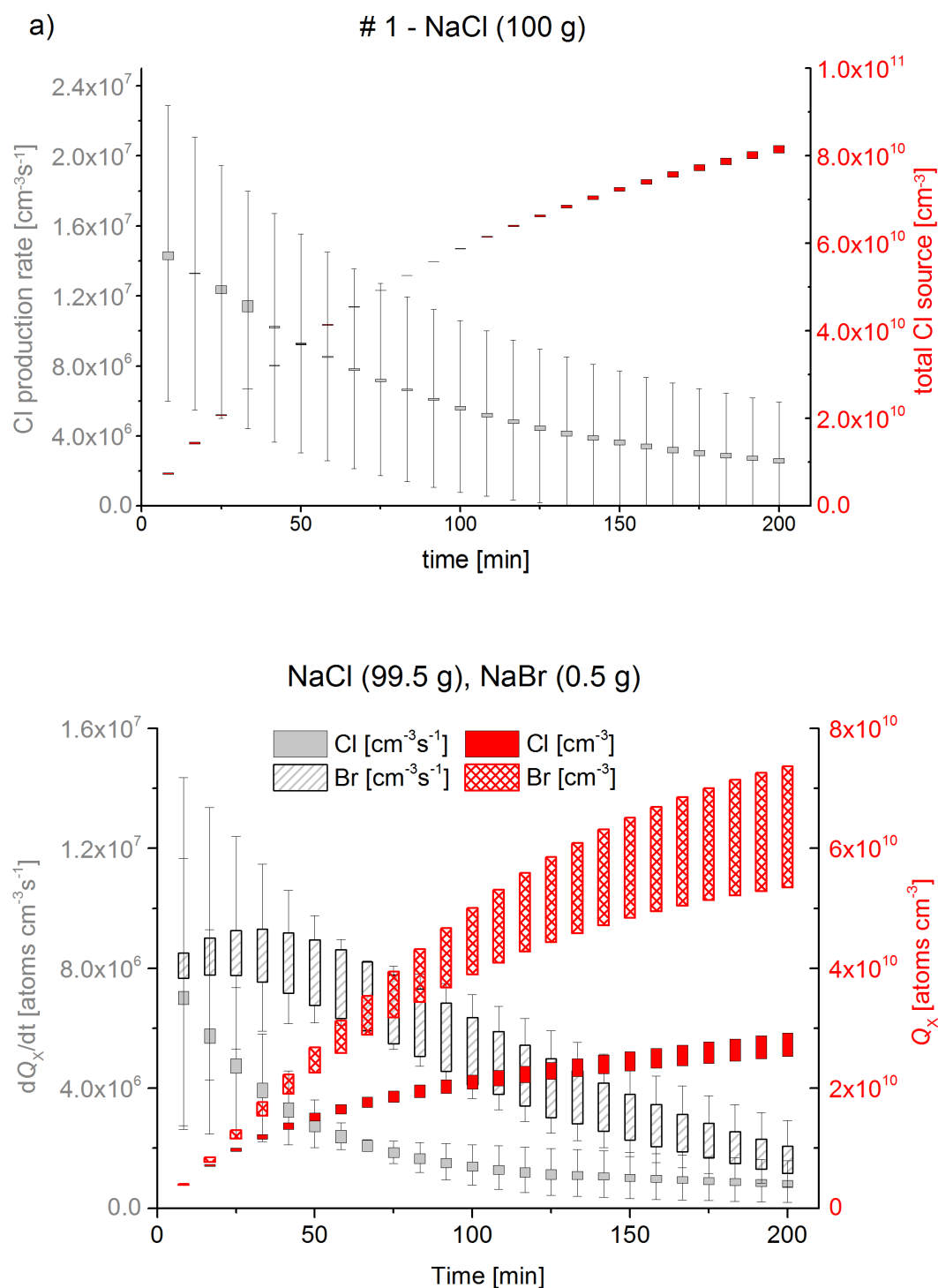


Figure 2.5 (a,b): Production rates of Cl and Br [$\text{atoms cm}^{-3}\text{s}^{-1}$] and the integrated total Cl and Br source [atoms cm^{-3}] during the blank experiments #1 and #3 (corresponding figures for the experiments #2 and #4 are shown in the Supporting Information). The salt compositions are given in the figures. The lower and upper margins of the bars represent the minimal and maximal values. For the production rate the negative minimum and the positive maximum uncertainties are included as thin error bars.

For the pure NaCl sample, a source of atomic Cl of $(4.1\text{--}4.2) \times 10^{10} \text{ cm}^{-3}$ was detected for the 1st hour, corresponding to production rates of $(0.8\text{--}1.5) \times 10^7 \text{ cm}^{-3} \text{ s}^{-1}$ (see Figure 2.5a or Table 2.1). Excluding the Fe(III)-induced chloride and bromide activation, this Cl₂ release can possibly be attributed to bromide impurities in the salt ($\text{Br}^- \leq 0.01\%$, according to the specifications of the manufacturer Sigma-Aldrich S9888, $\geq 99.0\%$) and to the observed NO_x impurities contained in the zero air and introduced due to the inherent air intrusion during the opening of the chamber required to change the salt samples. For such high Cl/Br ratios, bromide mainly induces the activation of chloride by the formation of BrCl¹⁶ that is released into the gas phase and rapidly photolyzed in our system ($J_{\text{BrCl}} = 7 \times 10^{-3} \text{ s}^{-1}$). The simultaneously produced Br atoms are below the detection limit due to the low reactivity of the HC_i toward Br. Assuming the release of Br atoms to be comparable with the detected Cl source and combining this assumption with the effect of bromide enrichment on the crystal surface,⁵² a trace impurity of 0.01% may be sufficient to be responsible for the detected Cl atoms.

Furthermore, there is the possibility of a direct activation by the heterogeneous reaction of NO_x trace impurities with the solid salt to subsequently release ClNO,⁵³ which could be photolyzed in our system to form Cl atoms ($J_{\text{ClNO}} = 1.8 \times 10^{-3} \text{ s}^{-1}$) or be hydrolyzed to form HCl and HONO and thus induce an enhanced OH production.⁵⁴ In the presence of O₃ (leading to N₂O₅ from NO_x), ClNO₂ could be formed⁵³ that is more stable against hydrolysis¹⁸ and can be photolyzed to form Cl and NO₂ ($J_{\text{ClNO}_2} = 2 \times 10^{-4} \text{ s}^{-1}$). This summarizes the activation of Cl via uptake of, for example, NO₂, N₂O₅, and O₃ on the deliquesced salt and concomitant release of photolyzable precursors.^{38,53} Throughout the experiments, typical O₃ and NO_x concentrations remained below 15 ppb ($\sim 3.8 \times 10^{11} \text{ molecules cm}^{-3}$) and 2 ppb ($\sim 5 \times 10^{10} \text{ molecules cm}^{-3}$) respectively, whereas a slight O₃ formation was observed in the course of the irradiation.

The resulting OH concentrations mainly ranged between 10^6 and $10^7 \text{ molecules cm}^{-3}$ as shown in Table 2.1. In our system, gaseous OH is mainly produced by NO_x impurities in the zero-air. The ongoing well-known photochemical cycle produces nitrogen monoxide which may reduce HO₂ radicals, which originate from the oxidation of hydrocarbons. Furthermore, NO can form O₃ via RO₂ and finally OH from photolysis of O₃ in the presence of water vapor. The known storage of NO_x in the FEP film and release under UV irradiation, mainly in the form of HONO,⁵⁵ can also form OH ($J_{\text{HONO}} = 1.5 \times 10^{-3} \text{ s}^{-1}$).

The contribution of the CH₄ impurity in the zero air (50–100 ppb) and of the O₃ formation during the experiment to the total Cl and OH reactivity in the system is lower than 5% for both radicals during the entire experiment and therefore neglected in the evaluation. Concerning Br, the reactivity of O₃ (formed during the experiments) can possibly influence the evaluation of the production rates and sources with respect to the low HC reaction rates toward Br. However, the Br-induced O₃ destruction recycles Br via BrO and HOBr and thus does not represent a final sink. At least during the first hour of the experiments, where the HC and O₃ reactivities are comparable and O₃ starts to form, the resulting Br concentrations are significant.

All experiments show a general trend to lower production rates with progressing irradiation time. A simple explanation for this tendency could be the evaporation of water from the QLM on the salt due to the radiative heating of the salt pan by the solar

simulator, thus diminishing the mobility of the halide ions. This may cause a surface “passivation” when the available halide ions have been consumed.³⁸

Despite the hygroscopic properties of MgCl_2 and the possibly more pronounced QLM,⁵⁶ a comparison of the Cl yields from the NaCl sample with the MgCl_2 sample shows a lower Cl_2 release. Also the addition of 2 g of sodium oxalate led to lower Cl activation with respect to pure NaCl. Catechol (that is very soluble and acts as a reducing agent) strongly inhibits the Cl_2 formation and shows a Cl production rate below the detection limit. Except for toluene, the depletion of the injected HC mixture was hardly observable; thus, the resulting Cl production rate and total Cl source could not be detected because no suitable fit function could be found for the alkanes.

The effect of bromide on a NaCl sample was observed by adding 0.5 g of NaBr to 99.5 g of NaCl. A Br source of $(2.6\text{--}3.1) \times 10^{10} \text{ cm}^{-3}$ was detected in the first hour, whereas the Cl source did not show a marked difference to the pure NaCl salt. During crystallization, bromide was enriched on the surface with respect to chloride;⁵² thus, the molar Cl/Br ratio and the resulting ratio in the QLM will probably be lower than the measured ratio in the saturated liquid phase (Cl/Br = 150) where much more water was used (section 2.3.4). Additionally, the activation mechanisms favor the production of Br_2 instead of BrCl at these Cl/Br ratios¹⁶ explaining the high Br source (Figure 2.5b). For example Hirokawa et al.⁵⁷ and Mochida et al.⁵⁸ found that the heterogeneous Br_2 formation through the uptake of O_3 on sea salt is much more effective, whereas a Cl_2 release was not observed in these studies. Oum et al.⁵⁹ proposed that gas-phase OH radicals can heterogeneously produce Cl_2 and Br_2 from sea salt.^{56,60,61} The uptake of OH on salt solutions and subsequent release of Br_2 , BrCl, and Br_2 have been investigated by Frinak and Abbatt,⁶² Park et al.,^{56,60,61} and Nissenon et al.⁶³ in detail. As O_3 ($10\text{--}20 \text{ ppb}$, $2.5\text{--}5 \times 10^{11} \text{ molecules cm}^{-3}$) and OH radicals ($10^6\text{--}10^7 \text{ molecules cm}^{-3}$) are formed during irradiation in our experiments, these mechanisms would explain the observed Cl and Br sources.

On the basis of the steady state concentrations of atomic Cl measured by Buxmann et al.⁴⁷ above a 0.33 g NaBr and 100 g NaCl salt mixture one can calculate Cl production rates of $(1.3\text{--}1.8) \times 10^7 \text{ cm}^{-3} \text{ s}^{-1}$ for the experiments with 200 ppb ozone at 67% RH. In comparison, our production rates vary from $(0.4\text{--}1.7) \times 10^7 \text{ cm}^{-3} \text{ s}^{-1}$. The given BrO production rates of 10–30 ppt/s (and thus the Br production), corresponding to $(2\text{--}7) \times 10^8 \text{ BrO atoms cm}^{-3} \text{ s}^{-1}$ at standard conditions, seem to be much higher in the work by Buxmann et al.⁴⁷ than that in our study, where $(2\text{--}8) \times 10^6 \text{ Br atoms cm}^{-3} \text{ s}^{-1}$ were detected in experiment #3. However, these results are difficult to compare due to the high ozone concentrations, the lower NaBr content, and the higher RH.

2.3.3 $\text{FeCl}_3 \cdot 6\text{H}_2\text{O}$ Containing Salts

Once dissolved in the aqueous phase, Fe(III) forms light-absorbing complexes with available ions and water molecules. The speciation mainly depends on salt composition, pH, and ionic strength in the solution and has a significant influence on the photoinduced radical formation. In the Fe(III)/water system, the main complexes are $\text{Fe}(\text{H}_2\text{O})_6^{3+}$ and $\text{Fe}(\text{H}_2\text{O})_5\text{OH}^{2+}$ at low pH, whereas in the presence of chloride anions, the more photosensitive $\text{Fe}(\text{H}_2\text{O})_5\text{Cl}^{2+}$ and $\text{Fe}(\text{H}_2\text{O})_4\text{Cl}_2^+$ complexes become important.^{33,36} For convenience, coordinated water molecules $(\text{H}_2\text{O})_x$ will be omitted in the following.

Photolysis of these complexes leads to OH and Cl radicals according to reactions (R2.1) – (R2.4).



Table 2.2 summarizes the main reaction pathways in chloride-dominated media and their forward (k_+) and backward (k_-) reaction rate constants. In the preponderant presence of chloride, OH^{\bullet} and Cl^{\bullet} will predominantly be scavenged by Cl^- to form the intermediates ClOH^- and $\text{Cl}_2^{\bullet-}$, respectively (Table 2.2, equilibria R2.5 and R2.7). Depending on the pH, ClOH^- can dissociate to Cl^{\bullet} (Table 2.2, equilibrium R2.6) that again produces $\text{Cl}_2^{\bullet-}$. Thus, the photolysis of FeOH^{2+} and $\text{Fe}(\text{OH})_2^+$, primarily producing OH^{\bullet} , finally forms Cl_2 ,⁷⁰ that is able to degas according to its physical solubility (Henry's law constant at 298 K: $6.2\text{--}9.5 \times 10^{-2} \text{ M atm}^{-1}$).⁷¹ However, the photolysis reactions (R2.3) and (R2.4), that directly produce Cl^{\bullet} and finally lead to a degassing of Cl_2 , are much more effective, based on the absorption cross sections and quantum yields.^{72,73} The degassing of Cl_2 slows down with increasing pH when the hydrolysis to the poorly degassing hypochlorous acid (ClOH) is favored between pH 4 and 7 (Henry's law constant at 298 K: $2.6\text{--}9.3 \times 10^2 \text{ M atm}^{-1}$).⁷¹ The high concentration of Cl^- and the subsequent scavenging of the radical intermediates Cl^{\bullet} and OH^{\bullet} (R2.5 and R2.7) will outmatch the reactions (R2.11), (R2.14), and (R2.15), involving Fe^{2+} and H_2O_2 .⁷⁰ Solely, Fe^{2+} may become a sink for $\text{Cl}_2^{\bullet-}$ with advanced photolytic reduction of Fe^{3+} after long irradiation times.

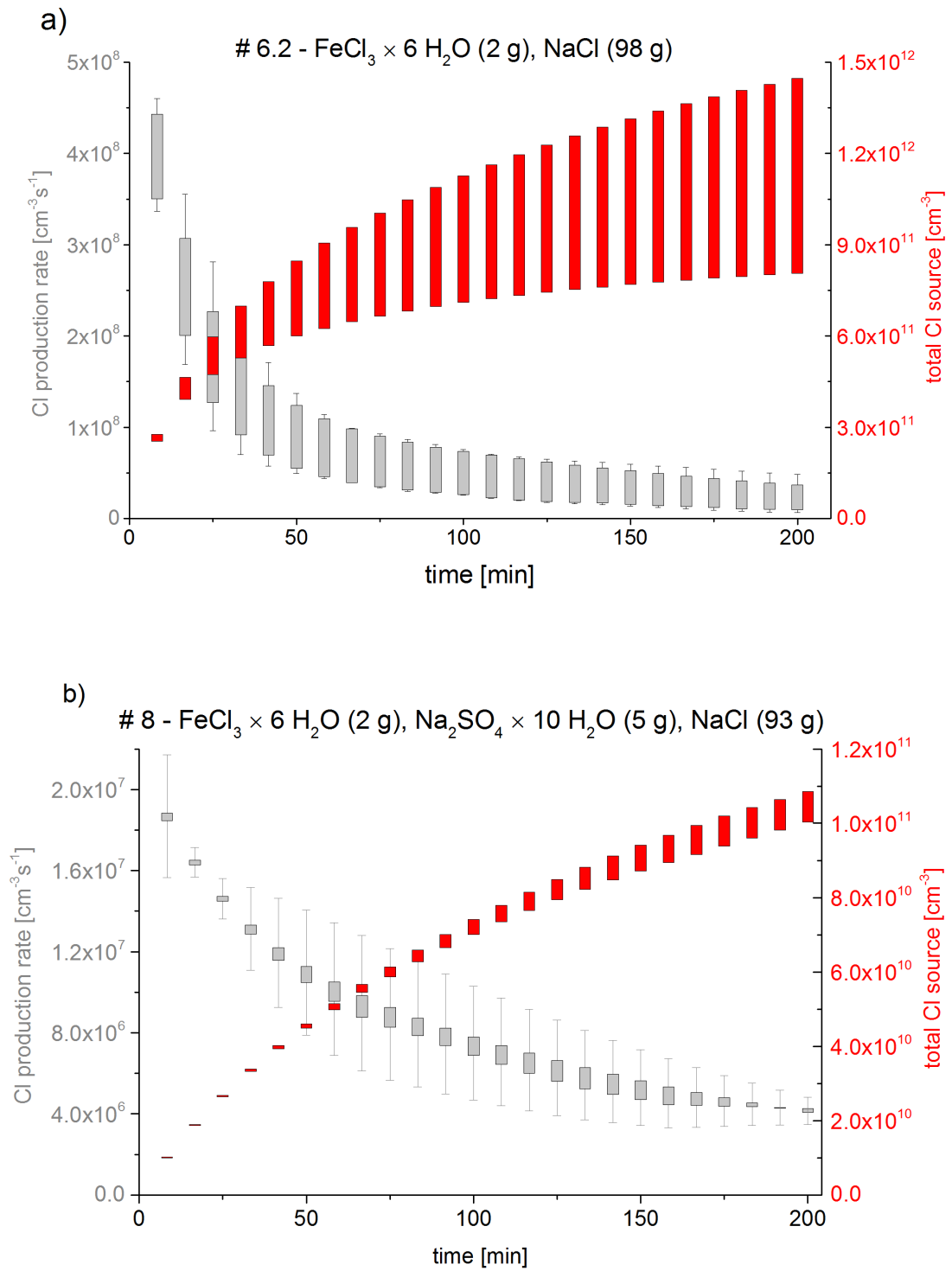
In comparison to the blanks, the addition of $\text{FeCl}_3 \cdot 6\text{H}_2\text{O}$ generally led to an increase in the observed gaseous Cl except for samples where sulfate was involved. The production rate showed a downward trend similar to that of the blank experiments. The reason is not only the drying out of the sample but also the formation of iron(II) via photoreduction (reactions R2.1 and R2.3) that becomes a sink for the radical intermediates Cl^{\bullet} , ClOH^- , and OH^{\bullet} or even directly reacts with $\text{Cl}_2^{\bullet-}$ (Table 2.2, reactions (R2.11)–(R2.14)), inhibiting the further formation of Cl_2 .³⁷ However, the reactions with Cl^- (Table 2.2, reactions R2.5 and R2.7) will dominate because Cl^- in the QLM is constantly provided by the bulk sample and the concentration is not expected to change significantly during irradiation.

The 2 g of $\text{FeCl}_3 \cdot 6\text{H}_2\text{O}$ /98 g of NaCl salt pan (experiment #6.1) showed an enormous Cl_2 release and consumed all of the injected alkanes totally within the first 30 min of irradiation.

Table 2.2: Rate Constants for Reactions and Equilibria, Involving Cl^\bullet , ClOH^\bullet , $\text{Cl}_2^{\bullet-}$, and OH^\bullet Radicals (given for zero ionic strengths).

Reaction	k_+ (forward)	k_- (backward)	No.
$\text{OH}^\bullet + \text{Cl}^- \rightleftharpoons \text{ClOH}^{\bullet-}$	$4.2 \times 10^9 \text{ M}^{-1} \text{ s}^{-1}$	$6.0 \times 10^9 \text{ s}^{-1}$	R5 ⁶⁴
$\text{ClOH}^{\bullet-} + \text{H}^+ \rightleftharpoons \text{Cl}^\bullet + \text{H}_2\text{O}$	$2.4 \times 10^{10} \text{ M}^{-1} \text{ s}^{-1}$	$1.8 \times 10^5 \text{ s}^{-1}$	R6 ⁶⁴
$\text{Cl}^\bullet + \text{Cl}^- \rightleftharpoons \text{Cl}_2^{\bullet-}$	$7.8 \times 10^9 \text{ M}^{-1} \text{ s}^{-1}$	$5.7 \times 10^4 \text{ s}^{-1}$	R7 ⁶⁴
$\text{Cl}^\bullet + \text{Cl}_2^{\bullet-} \rightleftharpoons \text{Cl}^- + \text{Cl}_2$	$1.4 \times 10^9 \text{ M}^{-1} \text{ s}^{-1}$		R8 ⁶⁴
$\text{Cl}_2^{\bullet-} + \text{Cl}_2^{\bullet-} \rightarrow \text{Cl}_3^- + \text{Cl}^-$	$3.1 \times 10^9 \text{ M}^{-1} \text{ s}^{-1}$		R9 ⁶⁵
$\text{Cl}_3^- \rightleftharpoons \text{Cl}_2 + \text{Cl}^-$	$K = 1.8 \times 10^{-1} \text{ M}^{-1}$		R10 ⁶⁶
$\text{Cl}^\bullet + \text{Fe}^{2+} \rightarrow \text{Cl}^- + \text{Fe}^{3+}$	$5.9 \times 10^9 \text{ M}^{-1} \text{ s}^{-1}$		R11 ⁶⁷
$\text{Cl}_2^{\bullet-} + \text{Fe}^{2+} \rightarrow 2\text{Cl}^- + \text{Fe}^{3+}$	$1.4 \times 10^7 \text{ M}^{-1} \text{ s}^{-1}$		R12 ⁶⁸
$\text{ClOH}^{\bullet-} + \text{Fe}^{2+} \rightarrow \text{Cl}^- + \text{OH}^- + \text{Fe}^{3+}$	$1.3 \times 10^8 \text{ M}^{-1} \text{ s}^{-1}$		R13 ⁶⁷
$\text{OH}^\bullet + \text{Fe}^{2+} \rightarrow \text{OH}^- + \text{Fe}^{3+}$	$2.7 \times 10^8 \text{ M}^{-1} \text{ s}^{-1}$		R14 ⁶⁹
$\text{OH}^\bullet + \text{OH}^\bullet \rightarrow \text{H}_2\text{O}_2$	$5.2 \times 10^9 \text{ M}^{-1} \text{ s}^{-1}$		R15 ⁶⁹

Due to the restricted time resolution with only 2 measuring points, the Cl source can only be estimated. The injected amount of HCs was increased for the next experiments. In experiment #6.2 the same sample as that in #6.1 was used, resulting in an up to 30 times higher production rate of Cl with respect to a pure 100 g of NaCl salt pan (see Figure 2.5a and 2.6a) without considering the additional effect of the probably smaller specific surface of the ground $\text{FeCl}_3 \cdot 6\text{H}_2\text{O}$ -containing samples and the reuse of the sample that had already been exposed to the simulated sunlight for 30 min. The total Cl source in the chamber increased up to $(6.3\text{--}8.9) \times 10^{11} \text{ atoms cm}^{-3}$ during 60 min of irradiation. Assuming that (without recycling) each Fe(III) species produces one Cl atom that leads to a degassing of $\frac{1}{2}$ Cl_2 molecule, at least a portion of 0.05–0.07% of the added Fe(III) is involved in the photoproduction of Cl_2 . A reduction of the FeCl_3 hexahydrate fraction in the salt from 2 g to 0.5 g in 99.5 g of NaCl (experiment #7.1) led to a slight decrease in the production rate and the total Cl source of only $(5.2\text{--}5.7) \times 10^{11} \text{ atoms cm}^{-3}$ during the first 60 min (Figure 2.7a, b, or Figure S2.2a in the Supporting Information). The enhanced activation can be attributed to the iron induced chlorine release mechanism as described above. Furthermore, the drop in pH due to the $\text{FeCl}_3 \cdot 6\text{H}_2\text{O}$ addition causes a shift in the speciation and supports the formation of the photosensitive FeCl_2^+ and FeCl^{2+} complexes as well as the degassing of Cl_2 (see section 2.3.4).



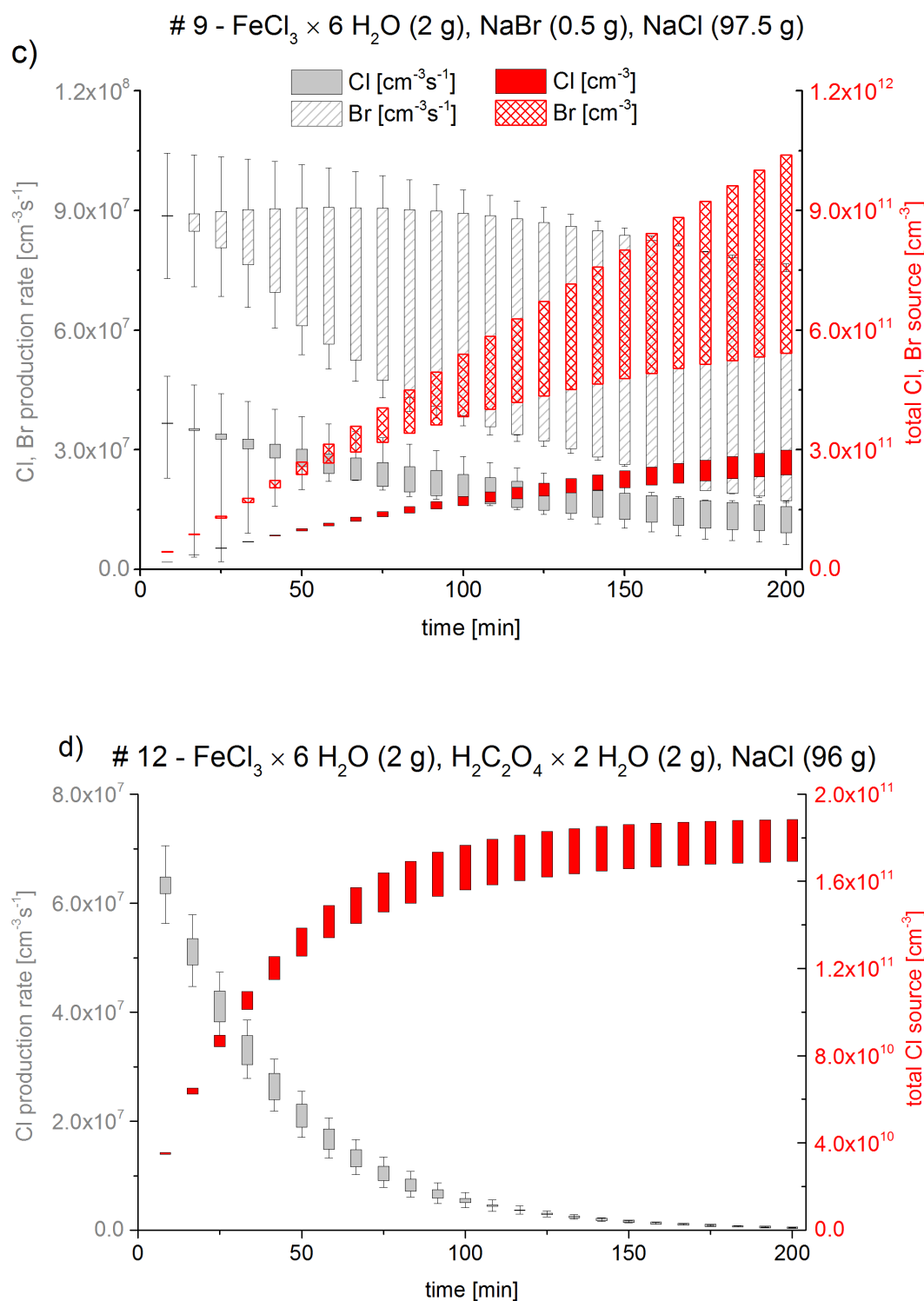


Figure 2.6 (a–d): Production rates of Br and Cl [atoms $\text{cm}^{-3}\text{s}^{-1}$] and the integrated total source of Cl and Br [atoms cm^{-3}] during the $\text{FeCl}_3 \cdot 6\text{H}_2\text{O}$ experiments #6.2 (a), #8 (b), #9 (c), and #12 (d) (Corresponding figures for the experiments #7.1, #10, and #13 are shown in the Supporting Information). The lower and upper margins of the bars represent the minimal and maximal values. For the production rate the negative minimum and the positive maximum uncertainties are included as thin error bars.

To investigate possible regeneration effects and check if the Cl source can become exhausted, experiment #7.1 was repeated five times without a change of the sample after dark periods of 1 night for experiments #7.1–7.3, of 1 week between #7.3 and #7.4, and of 3 nights between #7.4 and #7.5 without irradiation. A systematic tendency toward a lower Cl activation or an increased source after longer regeneration times are hardly noticeable (Figure 2.7a, b). Rather significant is the systematically higher Cl production rate (10^7 – 10^9 $\text{cm}^{-3}\text{s}^{-1}$) and thus the elevated Cl source in each run in comparison with the pure NaCl sample (0.8 – 1.5×10^7 $\text{cm}^{-3} \text{s}^{-1}$). Each resulting Cl source was at least above 10^{11} cm^{-3} after 100 min compared to $(5.8$ – $5.9) \times 10^{10}$ cm^{-3} for the blank experiment with 100 g of NaCl.

The addition of sodium sulfate and catechol to the 2 g of $\text{FeCl}_3 \cdot 6\text{H}_2\text{O}$ /98 g of NaCl mixture hindered the chloride activation drastically (Table 2.1 or Figure 2.6b). In both cases, the color of the sample changed to yellow and black, respectively, indicating a complex formation during the sample production process because sodium sulfate and catechol are usually colorless, although it does not seem to be in agreement with the speciation in chloride-dominated media (section 2.3.4). The observed yellow salt complexes in the sulfate sample are able to reduce the light intensity in the spectral region that is important for the photolysis of the Fe(III)-Cl complexes. The produced ferrous ions in reactions R2.1 and R2.3 prefer to form the stable FeSO_4 complex with the available sulfate ions ($\log K = 1.35$)⁷⁴ and thus interrupt the regeneration of Fe^{2+} to Fe^{3+} . Furthermore, SO_4^{2-} and HSO_4^- ions can act as scavenger for Cl^\bullet and OH^\bullet , producing sulfate anion radicals, and inhibit the formation of Cl_2 .³⁴ Thus, sulfate is able to strongly inhibit the radical production and Cl_2 release, as is observed in experiment #8 (Figure 2.6b). The Cl source is quantified to be even lower than that of the pure NaCl sample despite the same treatment (both milled). The inhibiting effect of catechol is even more intense and led to a Cl production rate below the detection limit, as compared to the blank experiment where only catechol (2 g) and NaCl (98 g) were present. Here, the well-known rapid redox reduction of Fe(III) to Fe(II) may play a decisive role, oxidizing catechol via quinone to muconic acid and finally in a few hours to CO_2 .⁷⁵

Two effects were observed for the $\text{Na}_2\text{C}_2\text{O}_4$ (2 g)/ $\text{FeCl}_3 \cdot 6\text{H}_2\text{O}$ (2 g)/NaCl(96 g) mixture. As discussed in section 2.3.4, oxalate forms a stable and dominant complex with Fe(III) that diminishes the Fe(III)-Cl complexation and thus the direct activation of chloride. Moreover, sodium oxalate shifts the sample pH to a less acidic range, where FeCl_2^+ starts to be reduced and the Cl_2 release is restricted by the formation of hypochlorous acid. Experiment #12 (Figure 2.6d) demonstrates the sensitivity to the pH by the use of oxalic acid instead of sodium oxalate, resulting in a more acidic pH of about 5. Due to this change, the Cl source in the first 60 min slightly increased from $(6.7$ – $6.9) \times 10^{10}$ to $(13$ – $15) \times 10^{10}$ cm^{-3} . According to Zuo and Hoigné,⁷⁶ the photolysis of the Fe(III)-oxalate complexes leads to a formation of H_2O_2 and thus stimulates the photo-Fenton reaction and the subsequent reoxidation of Fe(II). The thereby induced Fe(III) recycling and regeneration of photosensitive Fe(III)-chloride and hydroxy complexes explains the quite constant Cl production rate at later stages of the experiments when oxalate is involved. However, the high fraction of oxalate in the sample reduces the Fe(III) involved in the photoinduced Cl[•] production and thus reduces the total gaseous Cl source.

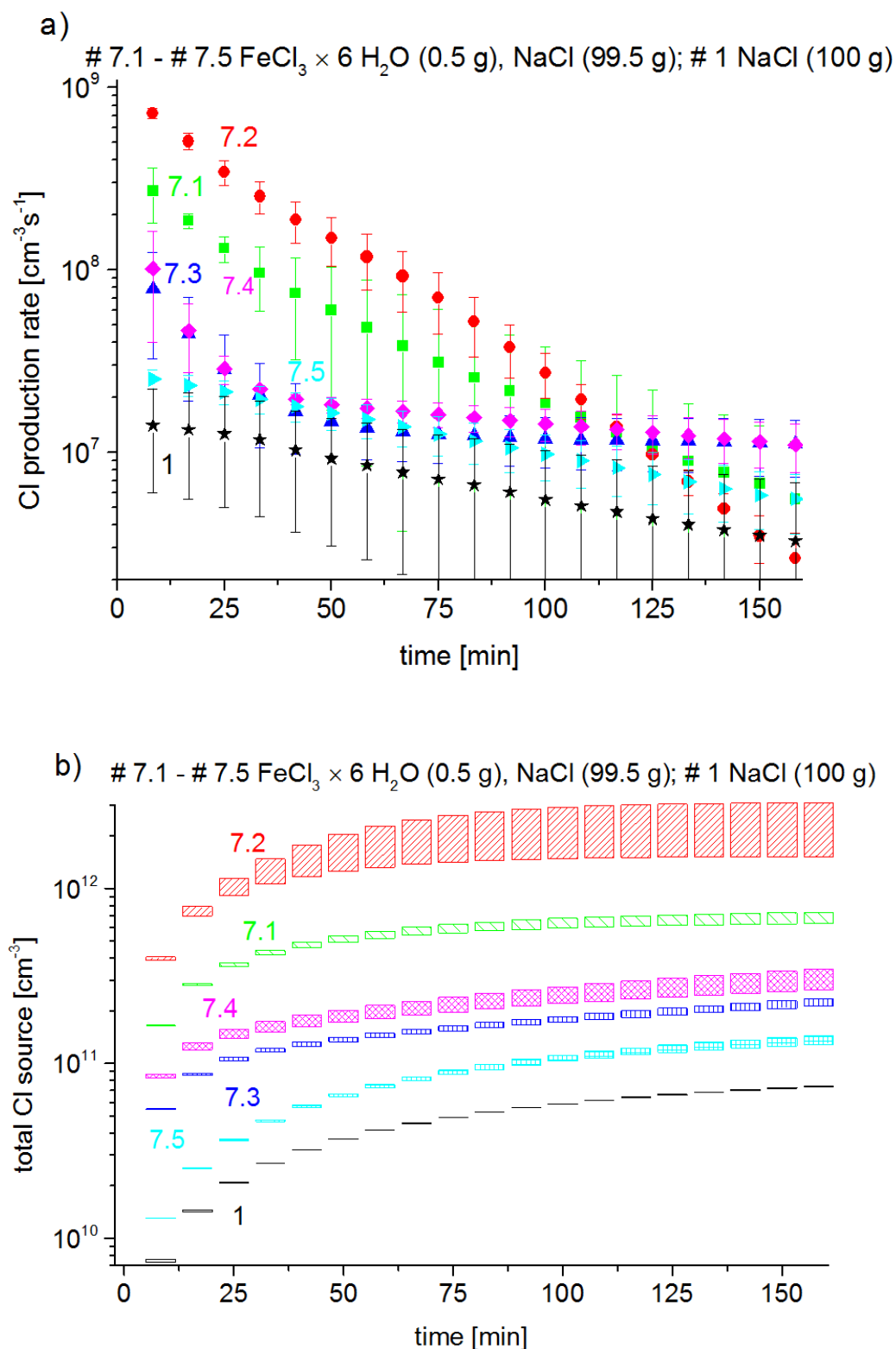


Figure 2.7 (a,b): Cl production rates [$\text{atoms cm}^{-3} \text{s}^{-1}$] detected in the repetitive irradiation of the 0.5 g of $\text{FeCl}_3 \cdot 6\text{H}_2\text{O}$ /99.5 g of NaCl sample (experiments #7.1–7.5) in comparison with the blank run on pure NaCl (experiment #1) (a) and the resulting total Cl source [atoms cm^{-3}] for the same experiments (b).

Experiment #13 demonstrates a combination of the effects from 2 g of oxalic acid and 5 g of sulfate on the 2 g of $\text{FeCl}_3 \cdot 6\text{H}_2\text{O}$ /91 g of NaCl sample. Though the sample was ground, a much lower Cl source of $(1.4\text{--}1.5) \times 10^{10} \text{cm}^{-3}$ was observed in the first hour compared to the untreated oxalic acid sample. The lower Cl production in comparison with the milled sulfate sample (experiment #8) can be ascribed to the larger grain size of the ground sample in experiment #13 and the combination of the radical scavenging effect of sulfate and the complexation of oxalate with Fe(III).

The influence of NaBr on the iron-induced chloride activation is similar to the effect on pure NaCl as a lower Cl production was observed in comparison with the respective sample without bromide (Figure 2.6c). The Br source in the presence of Fe(III) was a factor of 12 higher than that in the absence of Fe(III) in the first hour (Table 2.1), whereas the Cl source was 6–8 times lower due to the bromide addition. This implies that dissolved Fe(III) leads to a stronger preference of bromide activation even if Fe(III) prefers to complex with chloride (section 2.3.4). However, the photochemically formed Cl_2 seems not to degas completely but rather oxidize bromide to Br_2 as for example proposed by Mochida et al.⁷⁷ Furthermore, comparable to the blank sample, an enrichment of bromide on the surface and thus in the aqueous phase on the salt crystals is probable, and the activation of bromide and autocatalytic release of Br_2 instead of BrCl is preferred at this pH and Br^-/Cl^- ratio of 0.0067 in the liquid phase.¹⁶ In fact, Sadanaga et al.⁷⁸ reported an enhancement of the O_3 uptake and Br_2 release in the presence of Fe^{3+} in synthetic sea salt and suggested a Cl_2 release when bromide becomes deficient.

2.3.4 Speciation

The decisive factor for the photoinduced chlorine release is the fraction of photosensitive iron complexes in the water-chloride system, depending on the pH, molar fractions, and ionic strength. Table 2.3 gives an overview on the complexes and their equilibrium constants. Based on this data, the software PHREEQC⁸⁵ was employed for aqueous, geochemical calculations to derive the speciation as a function of pH in the QLM. To approximate the experimental conditions, small salt samples with equal molar ratios of the components were prepared in small Petri dishes, and 10 mL of bi-distilled water were added to obtain a saturated liquid layer on the salt crust. Using a pipette, 1 mL of the liquid phase was taken and diluted 1:10000 in order to analyze for the molar concentrations of iron and present anions by ICP-MS and IC. In this way, the molar ratios of the elements were determined and used as starting parameters for the speciation model.

This approach is rather qualitative because the process of adding water differs from the process of humidification by air moisture. The excess of water penetrates through the surface of the salt crystal and allows the bulk to dissolve, whereas the QLM on the crystals is only formed on the surface. Therefore, the obtained molar ratios could differ from the ratios in the bulk since, for example, bromide is enriched on the surface with respect to chloride during the drying process⁵². A further consequence of the partly heterogeneous crystallization of the salts is the variation of the liquid film thickness, depending on the hygroscopicity and composition of the different microcrystalline fractions of the salt pan.

Table 2.3: Equilibrium Constants ($\log_{10} K$) for the Formation of Low Molecular Weight Fe(III) Complexes with Several Ligands (including their dissociation constants) at Zero Ionic Strength and 298 K.

Equilibrium	$\log_{10} K$	No.
Water		
$\text{Fe}^{3+} + \text{H}_2\text{O} \rightleftharpoons \text{FeOH}^{2+} + \text{H}^+$	-2.19	R2.16 ⁷⁹
$\text{Fe}^{3+} + 2\text{H}_2\text{O} \rightleftharpoons \text{Fe}(\text{OH})_2^+ + 2\text{H}^+$	-5.67	R2.17 ⁷⁹
$\text{Fe}^{3+} + 3\text{H}_2\text{O} \rightleftharpoons \text{Fe}(\text{OH})_3 + 3\text{H}^+$	-12.0	R2.18 ⁷⁹
$\text{Fe}^{3+} + 4\text{H}_2\text{O} \rightleftharpoons \text{Fe}(\text{OH})_4^- + 4\text{H}^+$	-21.6	R2.19 ⁷⁹
Chloride		
$\text{Fe}^{3+} + \text{Cl}^- \rightleftharpoons \text{FeCl}^{2+}$	1.48	R2.20 ⁸⁰
$\text{Fe}^{3+} + 2\text{Cl}^- \rightleftharpoons \text{FeCl}_2^+$	2.13	R2.21 ⁸¹
$\text{Fe}^{3+} + 3\text{Cl}^- \rightleftharpoons \text{FeCl}_3$	1.13	R2.22 ⁸²
Bromide		
$\text{Fe}^{3+} + \text{Br}^- \rightleftharpoons \text{FeBr}^{2+}$	0.61	R2.23 ⁸³
$\text{Fe}^{3+} + 2\text{Br}^- \rightleftharpoons \text{FeBr}_2^+$	0.2	R2.24 ⁸³
Sulfate		
$\text{SO}_4^{2-} + \text{H}^+ \rightleftharpoons \text{HSO}_4^-$	1.99	R2.25 ⁶⁹
$\text{Fe}^{3+} + \text{SO}_4^{2-} \rightleftharpoons \text{FeSO}_4^+$	3.92	R2.26 ⁶⁹
$\text{Fe}^{3+} + 2\text{SO}_4^{2-} \rightleftharpoons \text{Fe}(\text{SO}_4)_2^-$	5.42	R2.27 ⁶⁹
Oxalate		
$\text{C}_2\text{O}_4^{2-} + \text{H}^+ \rightleftharpoons \text{HC}_2\text{O}_4^-$	4.18	R2.28 ⁸¹
$\text{HC}_2\text{O}_4^{2-} + \text{H}^+ \rightleftharpoons \text{H}_2\text{C}_2\text{O}_4$	1.31	R2.29 ⁴¹
$\text{Fe}^{3+} + \text{C}_2\text{O}_4^{2-} \rightleftharpoons \text{Fe}(\text{C}_2\text{O}_4)^+$	8.77	R2.30 ⁸¹
$\text{Fe}(\text{C}_2\text{O}_4)^+ + \text{C}_2\text{O}_4^{2-} \rightleftharpoons \text{Fe}(\text{C}_2\text{O}_4)_2^-$	6.52	R2.31 ⁸¹
$\text{Fe}(\text{C}_2\text{O}_4)_2^- + \text{C}_2\text{O}_4^{2-} \rightleftharpoons \text{Fe}(\text{C}_2\text{O}_4)_3^{3-}$	4.44	R2.32 ⁸¹
Catechol		
$\text{C}_6\text{H}_6\text{O}_2^{2-} + \text{H}^+ \rightleftharpoons \text{HC}_6\text{H}_6\text{O}_2^-$	13	R2.33 ⁸⁴
$\text{HC}_6\text{H}_6\text{O}_2^- + \text{H}^+ \rightleftharpoons \text{H}_2\text{C}_6\text{H}_6\text{O}_2$	9.25	R2.34 ⁸⁴
$\text{Fe}^{3+} + \text{H}_2\text{C}_6\text{H}_6\text{O}_2 \rightleftharpoons \text{Fe}(\text{C}_6\text{H}_6\text{O}_2)^+ + 2\text{H}^+$	1.37	R2.35 ⁴²
$\text{Fe}^{3+} + \text{C}_6\text{H}_6\text{O}_2^{2-} \rightleftharpoons \text{Fe}(\text{C}_6\text{H}_6\text{O}_2)^+$	20	R2.36 ⁸⁴
$\text{Fe}(\text{C}_6\text{H}_6\text{O}_2)^+ + \text{C}_6\text{H}_6\text{O}_2^{2-} \rightleftharpoons \text{Fe}(\text{C}_6\text{H}_6\text{O}_2)_2^-$	14.7	R2.37 ⁸⁴
$\text{Fe}(\text{C}_6\text{H}_6\text{O}_2)_2^- + \text{C}_6\text{H}_6\text{O}_2^{2-} \rightleftharpoons \text{Fe}(\text{C}_6\text{H}_6\text{O}_2)_3^{3-}$	9.01	R2.38 ⁸⁴

The equilibrium model in PREEQC is based on the MINTEQ database⁸⁶ and was extended for oxalate and catechol including the equilibrium constants listed in Table 2.3. For Fe^{3+} , Na^+ , Cl^- , SO_4^{2-} , HSO_4^- , and Br^- the activity coefficients were corrected for the ionic strength based on Pitzer's ion interaction approach⁸⁷ and the respective binary and ternary parameters listed in Tosca et al.⁸⁸ For the other ions, where to date no Pitzer parameters are available, the extended (or WATEQ) Debye-Hueckel equation was applied.^{89,90} The significance of this basic approach involves a large uncertainty because the extended Debye-Hueckel equation is limited to ionic strengths below 1 mol/L but in the case of predominant Cl^- concentrations still in good agreement with the Pitzer equations^{91,92} that are able to predict the activity coefficients in solutions with very high ionic strengths.⁹³ The modeled speciation only describes the equilibrium condition at the beginning of each experiment but is able to explain the precondition of the mechanism responsible for the various pathways of Cl_2 production. Detailed model studies, including reaction kinetics and absorptivities, have been performed elsewhere at lower Cl^- levels.^{35,44,69}

Figures 2.8a and b displays the calculated speciation equilibria for selected samples as a function of pH. The formed Fe(III) complexes are plotted as molar fraction of total Fe(III) dissolved in the QLM on the sample. Due to the high $\text{Cl}^-/\text{Fe(III)}$ ratio, no difference in speciation can be seen for the samples with 2 g and 0.5 g of $\text{FeCl}_3 \cdot 6\text{H}_2\text{O}$ except for the absolute concentrations that are shifted. In the expected very acidic pH range of the sample, FeCl_2^+ and FeCl^{2+} represent the highest fraction of Fe(III) species. These species have a much higher absorbance than the Fe(III)-hydroxo complexes.^{36,73} In particular, FeCl^{2+} has a two times higher quantum yield for photodissociation than FeOH^{2+} .³³ An even higher molar absorptivity in the visible region have Fe(III)-bromine complexes. In case of FeBr^{2+} this was shown by Rabinowitch and Stockmayer.⁹⁴ However, our model calculations show a negligible formation of Fe-Br complexes with respect to an assumed Cl^-/Br^- ratio of 150 in the quasi-liquid phase (see Figure S2.4b in the Supporting Information).

Adding sulfate to the modeled solutions does not significantly change the speciation at low pH on the condition that the molar $\text{Cl}^-/\text{SO}_4^{2-}$ ratio is 71, and therefore, this is only shown in the Supporting Information (Figure S2.4a). Adding oxalate instead has a significant impact on the speciation equilibrium (Figure 2.8b). The main complex that is present over a pH range from 1 to 7 is $\text{Fe}(\text{C}_2\text{O}_4)_3^{3-}$. Additionally, the sample pH is shifted to a less acidic range (see Figure 8a, b) where the less photoactive $\text{Fe}(\text{OH})_2^+$ starts to outbalance FeCl_2^+ . A further impact of oxalate in an irradiated system is the scavenging of OH^\bullet , comparable to sulfate.^{34,44}

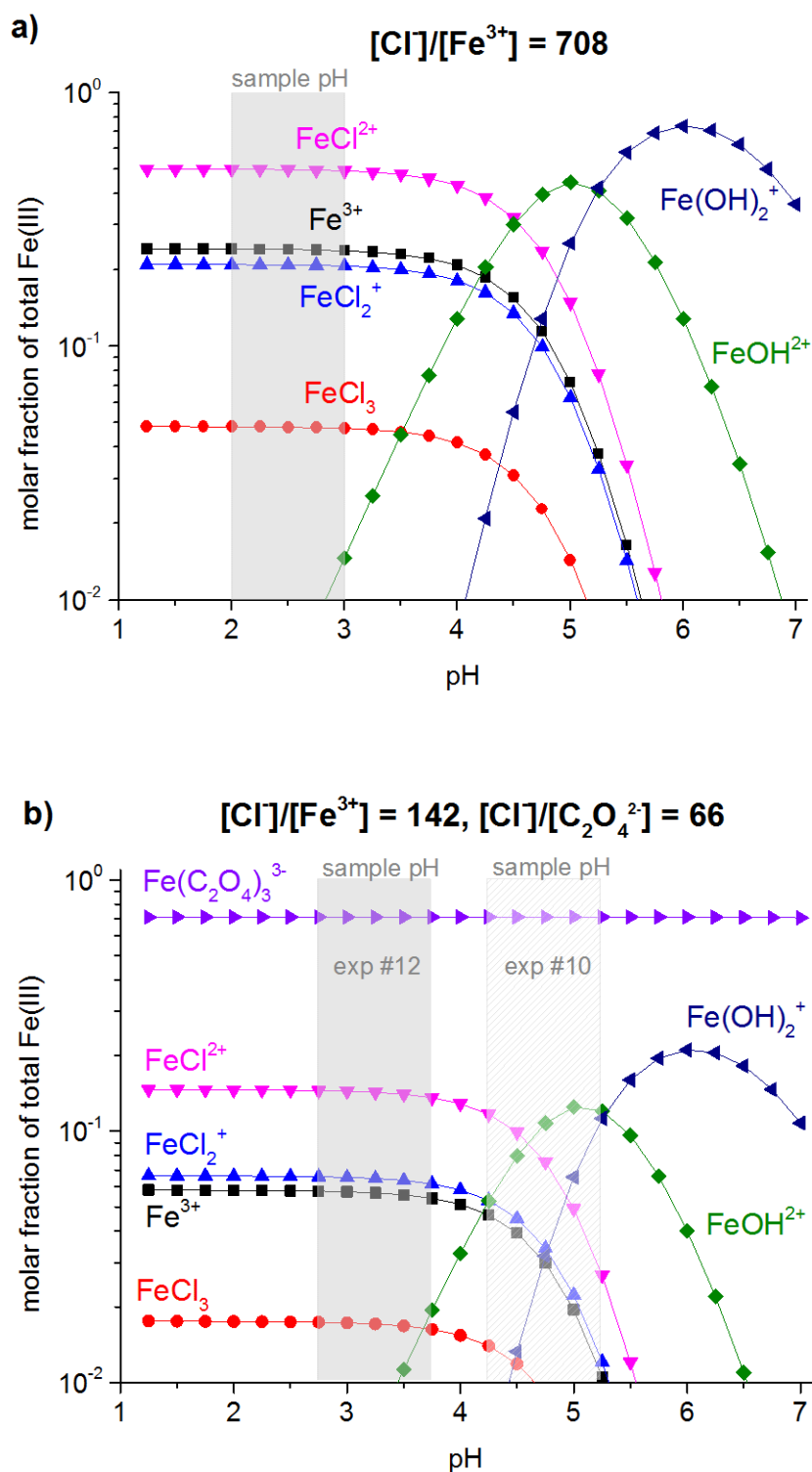


Figure 2.8 (a,b): Molar fraction of the formed Fe(III) species related to the total Fe(III) content in a saturated sodium chloride solution as a function of the pH (according to the PHREEQC model) for the sample compositions of experiments #7.1–7.5 (a) and experiments #10 and #12. The estimated range of the sample pH based on the measurements described in the text is shown in light gray. Corresponding figures for the other salt compositions are shown in the Supporting Information.

Concerning catechol, the induced Fe(III) complexes start to occur in a significant fraction as $\text{Fe}(\text{C}_6\text{H}_6\text{O}_6)^+$ at a pH higher than 3 (Supporting Information, Figure S2.4d). On the other hand, the measured sample pH is lower than 3, where mainly FeCl_2^+ is present. However, during the sample preparation, the salt appeared as dark black, indicating a complex formation with a strong light absorption. Catechol is known to reduce Fe^{3+} to Fe^{2+} at acidic pH^{75,95} and to form extremely stable chelate complexes.⁴⁵ The respective reactions are not included in the speciation model as only Fe(III) complexes are considered. The iron-free sample with catechol and NaCl instead appeared in a light gray color.

In general, the model calculations show that a low pH (<3) induces a large fraction of Fe-Cl complexes and inhibits the photo-Fenton reaction in terms of low OH^\cdot and H_2O_2 production. Thus a pH of 3 or slightly above would be optimal to warrant the formation of OH^\cdot and thus the reoxidation of the photodecomposed Fe(II)⁹⁵ for a continued, sustainable Cl_2^\cdot formation via the Fe(III) mechanism.

2.3.5 Environmental Significance

The influence of soluble iron on speciation and biochemistry plays an important role in nature, for example in brine-containing soils, intertidal zones, and coastal regions, or where dust or ash aerosols come into contact with sea salt.^{96,97} Recent model predictions extrapolated the present increase of ship traffic into the future and proposed that the soluble iron emitted from ships might contribute 30–60% to the soluble iron deposition in the high-latitude North Atlantic and North Pacific until the year 2100.⁹⁸ Furthermore, Zhu et al.⁹⁹ measured that only 7.5% of the soluble iron in marine aerosol particles is in the lower oxidation state Fe(II), and Schroth et al.¹⁰⁰ confirmed that Fe(III) is predominant, for example in soil particles from arid regions and in oil combustion products. Our work rather represents halogen release mechanisms above humidified salt sediment as it occurs in salty areas such as the Dead Sea or Australian salt lakes¹⁰¹, but the proposed mechanisms may also account for iron-containing saline aerosols.

While iron forms mainly complexes with organic ligands in seawater,¹⁰² the situation can change in sea salt aerosols where salinity increases and the pH drops below 2,¹⁰³ and our work indicates an additional potential impact of soluble iron on the atmosphere by the induced intrusion of Cl_2 and Br_2 . The varying content of soluble iron could have affected the tropospheric Cl and Br concentrations in the past. Chlorine is a strong oxidant and is highly reactive with organics having for example a 16 times higher reaction rate than OH^\cdot toward the climate forcing greenhouse gas methane. While it reacts relatively slowly with organics, it leads to surface-level O_3 destruction, mainly initiated by the autocatalytic release of bromine from sea salt.³⁸ When iron is present together with sea salt, the iron-induced halogen release could complement the classical release mechanisms via O_3 , NO_2 , or N_2O_5 .^{38,104} However, it still remains unclear if the natural iron-induced Cl_2 and Br_2 release plays a relevant role for the halogen activation in the atmosphere, as well as the implications of such rather local events on the global tropospheric chemistry, and, in particular, on variations of the atmospheric methane concentration. In reality, the ratio between the specific reaction surface and the volume in which the halogens are released is much higher in our simulation chamber than that in the affected parts of the atmosphere. The experimental conditions are chosen rather unrealistically (zero air

environment and pure salt samples) and the chamber leads to an enrichment of the released gas phase which helps to better investigate the mechanisms. For more significant conclusions on the environmental impact, aerosol experiments are needed where the specific reaction surface can be measured and the observations are easier to transfer to atmospheric conditions where aerosols have a higher global influence than salt brines.

2.4 Conclusions

The chlorine and bromine release from modeled salt pans under simulated solar light in a smog chamber made of Teflon was found to depend on the concentration of iron(III) and inorganic and organic additives. The plain NaCl/FeCl₃·6H₂O samples showed the highest chlorine release. The integrated Cl source in the first hour was about 20 times higher compared to that of the plain NaCl salt pan. The addition of sulfate and oxalate inhibited the activation of chloride significantly by forming complexes and by scavenging Cl atoms and OH radicals in the aqueous phase. Catechol inhibited the Cl₂ release below the detection limit. Adding bromide to the samples led to a slight decrease of released Cl₂, but simultaneously, a marked bromide activation was observed that increased when Fe(III) was present. This is probably caused by an enrichment of bromide in the QLM and by the drop in pH when Fe(III) is added. In summary, our study demonstrates the photocatalytic effect of Fe(III) causing gaseous Cl production and the influence of inorganic and organic contaminants including the underlying mechanisms that explain the various observed Cl and Br sources.

2.5 Associated Content

Compilation of relevant rate constants for reactions discussed in the text, corresponding figures (production rates, total sources) for the experiments #2, #4, #7.1, #10, #13, and additional, modeled speciation graphs for experiments #8, #9, #11, #13. This information is available free of charge via the Internet at <http://pubs.acs.org>.

2.6 Acknowledgments

We wish to thank Franz D. Oeste, gM-Ingenieurbüro Kirchhain, Germany, for advice, Agnes Bednorz and Andrej Einhorn for technical support and Dr. Gunter Ilgen and Dr. Sarmite Katkevica for the ICP-MS and IC measurements. This work was supported by the DFG within research unit 763 (HALOPROC). Sergej Bleicher was supported by Ries Consulting, Hosenfeld, Germany. The authors declare no competing financial interest.

2.7 References

- (1) Finlayson-Pitts, B. J. Chlorine Atoms as a Potential Tropospheric Oxidant in the Marine Boundary Layer. *Res. Chem. Intermed.* **1993**, *19*, 235–249.
- (2) Spicer, C. W.; Chapman, E. G.; Finlayson-Pitts, B. J.; Plastridge, R. A.; Hubbe, J. M.; Fast, J. D.; Berkowitz, C. M. Unexpectedly High Concentrations of Molecular Chlorine in Coastal Air. *Nature* **1998**, *394*, 353–356.
- (3) Platt, U.; Hönniger, G. The Role of Halogen Species in the Troposphere. *Chemosphere* **2003**, *52*, 325–338.

- (4) Osthoff, H. D.; Roberts, J. M.; Ravishankara, A. R.; Williams, E. J.; Lerner, B. M.; Sommariva, R.; Bates, T. S.; Coffman, D.; Quinn, P. K.; Dibb, J. E. High Levels of Nitryl Chloride in the Polluted Subtropical Marine Boundary Layer. *Nat. Geosci.* **2008**, *1*, 324–328.
- (5) Molina, M. J.; Rowland, F. S. Stratospheric Sink for Chlorofluoromethanes: Chlorine Atom-Catalysed Destruction of Ozone. *Nature* **1974**, *249*, 810–812.
- (6) Molina, M. J.; Tso, T.-L.; Molina, L. T.; Wang, F. C. Y. Antarctic Stratospheric Chemistry of Chlorine Nitrate, Hydrogen Chloride, and Ice: Release of Active Chlorine. *Science* **1987**, *238*, 1253–1257.
- (7) von Glasow, R. Atmospheric Chemistry: Wider Role for Airborne Chlorine. *Nature* **2010**, *464*, 168–169.
- (8) Thornton, J. A.; Kercher, J. P.; Riedel, T. P.; Wagner, N. L.; Cozic, J.; Holloway, J. S.; Dubé, W. P.; Wolfe, G. M.; Quinn, P. K.; Middlebrook, A. M. A Large Atomic Chlorine Source Inferred from Mid-Continental Reactive Nitrogen Chemistry. *Nature* **2010**, *464*, 271–274.
- (9) Phillips, G. J.; Tang, M. J.; Thieser, J.; Brickwedde, B.; Schuster, G.; Bohn, B.; Lelieveld, J.; Crowley, J. N. Significant Concentrations of Nitryl Chloride Observed in Rural Continental Europe Associated with the Influence of Sea Salt Chloride and Anthropogenic Emissions. *Geophys. Res. Lett.* **2012**, *39*, L10811.
- (10) Atkinson, R.; Baulch, D. L.; Cox, R. A.; Hampson, R. F.; Kerr, J. A.; Rossi, M. J.; Troe, J. Evaluated Kinetic, Photochemical and Heterogeneous Data for Atmospheric Chemistry: Supplement V. IUPAC Subcommittee on Gas Kinetic Data Evaluation for Atmospheric Chemistry. *J. Phys. Chem. Ref. Data* **1997**, *26*, 521–1011.
- (11) Lowe, D. C.; Allan, W.; Manning, M. R.; Bromley, T.; Brailsford, G.; Ferretti, D.; Gomez, A.; Knoben, R.; Martin, R.; Mei, Z., et al. Shipboard Determinations of the Distribution of ^{13}C in Atmospheric Methane in the Pacific. *J. Geophys. Res. D* **1999**, *104*, 26125–26135.
- (12) Allan, W.; Lowe, D. C.; Cainey, J. M. Active Chlorine in the Remote Marine Boundary Layer: Modeling Anomalous Measurements of $\delta^{13}\text{C}$ in Methane. *Geophys. Res. Lett.* **2001**, *28*, 3239–3242.
- (13) Platt, U.; Allan, W.; Lowe, D. Hemispheric Average Cl Atom Concentration from $^{13}\text{C}/^{12}\text{C}$ Ratios in Atmospheric Methane. *Atmos. Chem. Phys.* **2004**, *4*, 2393–2399.
- (14) Levine, J. G.; Wolff, E. W.; Jones, A. E.; Sime, L. C. The Role of Atomic Chlorine in Glacial-Interglacial Changes in the Carbon-13 Content of Atmospheric Methane. *Geophys. Res. Lett.* **2011**, *38*, L04801.
- (15) Finlayson-Pitts, B. J. Halogens in the Troposphere. *Anal. Chem.* **2009**, *82*, 770–776.
- (16) Fickert, S.; Adams, J. W.; Crowley, J. N. Activation of Br_2 and BrCl via Uptake of HOBr onto Aqueous Salt Solutions. *J. Geophys. Res. D* **1999**, *104*, 23719–23727.
- (17) Behnke, W.; Elend, M.; Krüger, U.; Zetzsch, C. The Influence of NaBr/NaCl Ratio on the Br^- -Catalysed Production of Halogenated Radicals. *J. Atmos. Chem.* **1999**, *34*, 87–99.
- (18) Behnke, W.; George, C.; Scheer, V.; Zetzsch, C. Production and Decay of ClNO_2 from the Reaction of Gaseous N_2O_5 with NaCl Solution: Bulk and Aerosol Experiments. *J. Geophys. Res. D* **1997**, *102*, 3795–3804.

- (19) Hunt, S. W.; Roeselová, M.; Wang, W.; Wingen, L. M.; Knipping, E. M.; Tobias, D. J.; Dabdub, D.; Finlayson-Pitts, B. J. Formation of Molecular Bromine from the Reaction of Ozone with Deliquesced NaBr Aerosol: Evidence for Interface Chemistry. *J. Phys. Chem. A* **2004**, *108*, 11559–11572.
- (20) Jobson, B. T.; Niki, H.; Yokouchi, Y.; Bottenheim, J.; Hopper, F.; Leaitch, R. Measurements of C₂–C₆ Hydrocarbons During the Polar Sunrise 1992 Experiment: Evidence for Cl Atom and Br Atom Chemistry. *J. Geophys. Res. D* **1994**, *99*, 25355–25368.
- (21) Zetzsch, C.; Behnke, W. Heterogeneous Photochemical Sources of Atomic Cl in the Troposphere. *Ber. Bunsen-Ges. Physik. Chem.* **1992**, *96*, 488–493.
- (22) Tuckermann, M.; Ackermann, R.; Götz, C.; Lorenzen-Schmidt, H.; Senne, T.; Stutz, J.; Trost, B.; Unold, W.; Platt, U. DOAS-Observation of Halogen Radical-Catalysed Arctic Boundary Layer Ozone Destruction during the ARCTOC-Campaigns 1995 and 1996 in Ny-Ålesund, Spitsbergen. *Tellus B* **1997**, *49*, 533–555.
- (23) Rudolph, J.; Ru B.; Thompson, A.; Anlauf, K.; Bottenheim, J. Halogen Atom Concentrations in the Arctic Troposphere Derived from Hydrocarbon Measurements: Impact on the Budget of Formaldehyde. *Geophys. Res. Lett.* **1999**, *26*, 2941–2944.
- (24) Spicer, C. W.; Plastridge, R. A.; Foster, K. L.; Finlayson-Pitts, B. J.; Bottenheim, J. W.; Grannas, A. M.; Shepson, P. B. Molecular Halogens before and during Ozone Depletion Events in the Arctic at Polar Sunrise: Concentrations and Sources. *Atmos. Environ.* **2002**, *36*, 2721–2731.
- (25) Ramacher, B.; Rudolph, J.; Koppmann, R. Hydrocarbon Measurements in the Spring Arctic Troposphere during the ARCTOC 95 Campaign. *Tellus B* **1997**, *49*, 466–485.
- (26) Stutz, J.; Hebestreit, K.; Alicke, B.; Platt, U. Chemistry of Halogen Oxides in the Troposphere: Comparison of Model Calculations with Recent Field Data. *J. Atmos. Chem.* **1999**, *34*, 65–85.
- (27) Stutz, J.; Ackermann, R.; Fast, J. D.; Barrie, L. Atmospheric Reactive Chlorine and Bromine at the Great Salt Lake, Utah. *Geophys. Res. Lett.* **2002**, *29*, 18.1–18.4.
- (28) Hebestreit, K.; Stutz, J.; Rosen, D.; Matveev, V.; Peleg, M.; Luria, M.; Platt, U. DOAS Measurements of Tropospheric Bromine Oxide in Mid-Latitudes. *Science* **1999**, *283*, 55–57.
- (29) Baker, A. K.; Rauthe-Schöch, A.; Schuck, T. J.; Brenninkmeijer, C. A. M.; van Velthoven, P. F. J.; Wisher, A.; Oram, D. E. Investigation of Chlorine Radical Chemistry in the Eyjafjallajökull Volcanic Plume Using Observed Depletions in Non-Methane Hydrocarbons. *Geophys. Res. Lett.* **2011**, *38*, L13801.
- (30) Bobrowski, N.; Hönninger, G.; Galle, B.; Platt, U. Detection of Bromine Monoxide in a Volcanic Plume. *Nature* **2003**, *423*, 273–276.
- (31) Eder, J. M. Über die Zersetzung des Eisenchlorides und einiger Organischer Ferridsalze im Lichte. *Monatsh. Chem.* **1880**, *1*, 755–762.
- (32) Langford, C. H.; Carey, J. H. The Charge Transfer Photochemistry of the Hexaaquoiron (III) Ion, the Chloropentaaquoiron (III) Ion, and the μ -Dihydroxo Dimer Explored with tert-Butyl Alcohol Scavenging. *Can. J. Chem.* **1975**, *53*, 2430–2435.
- (33) Nadtochenko, V. A.; Kiwi, J. Photolysis of FeOH²⁺ and FeCl²⁺ in Aqueous Solution. Photodissociation Kinetics and Quantum Yields. *Inorg. Chem.* **1998**, *37*, 5233–5238.

- (34) Machulek, A.; Moraes, J. E. F.; Okano, L. T.; Silverio, C. A.; Quina, F. H. Photolysis of Ferric Ions in the Presence of Sulfate or Chloride Ions: Implications for the Photo-Fenton Process. *Photochem. Photobiol. Sci.* **2009**, *8*, 985–991.
- (35) Machulek, A.; Vautier-Giongo, C.; Moraes, J. E. F.; Nascimento, C. A. O.; Quina, F. H. Laser Flash Photolysis Study of the Photocatalytic Step of the Photo-Fenton Reaction in Saline Solution. *Photochem. Photobiol. Sci.* **2006**, *82*, 208–212.
- (36) Vione, D.; Maurino, V.; Minero, C.; Calza, P.; Pelizzetti, E. Phenol Chlorination and Photochlorination in the Presence of Chloride Ions in Homogeneous Aqueous Solution. *Environ. Sci. Technol.* **2005**, *39*, 5066–5075.
- (37) Lim, M.; Chiang, K.; Amal, R. Photochemical Synthesis of Chlorine Gas from Iron(III) and Chloride Solution. *J. Photochem. Photobiol., A* **2006**, *183*, 126–132.
- (38) Finlayson-Pitts, B. J. The Tropospheric Chemistry of Sea Salt: A Molecular-Level View of the Chemistry of NaCl and NaBr. *Chem. Rev.* **2003**, *103*, 4801–4822.
- (39) Ewing, G. E. *H₂O on NaCl: From Single Molecule, to Clusters, to Monolayer, to Thin Film, to Deliquescence; Intermol Forces Clusters II Struct Bonding* 116, Springer, Berlin, Heidelberg, Germany, **2005**.
- (40) Kiwi, J.; Lopez, A.; Nadochenko, V. Mechanism and Kinetics of the OH-Radical Intervention during Fenton Oxidation in the Presence of a Significant Amount of Radical Scavenger (Cl⁻). *Environ. Sci. Technol.* **2000**, *34*, 2162–2168.
- (41) Moorhead, E. G.; Sutin, N. Rate and Equilibrium Constants for the Formation of the Monooxalate Complex of Iron(III). *Inorg. Chem.* **1966**, *5*, 1866–1871.
- (42) Mentasti, E.; Pelizzetti, E. Reactions Between Iron(III) and Catechol (o-Dihydroxybenzene). Part I. Equilibria and Kinetics of Complex Formation in Aqueous Acid Solution. *J. Chem. Soc., Dalton Trans.* **1973**, *23*, 2605–2608.
- (43) Weller, C.; Tilgner, A.; Bräuer, P.; Herrmann, H. Modeling the Impact of Iron-Carboxylate Photochemistry on Radical Budget and Carboxylate Degradation in Cloud Droplets and Particles. *Environ. Sci. Technol.* **2014**, *48*, 5652–5659.
- (44) Balmer, M. E.; Sulzberger, B. Atrazine Degradation in Irradiated Iron/Oxalate Systems: Effects of pH and Oxalate. *Environ. Sci. Technol.* **1999**, *33*, 2418–2424.
- (45) Hider, R. C.; Mohd-Nor, A. R.; Silver, J.; Morrison, I. E. G.; Rees, L. V. C. Model Compounds for Microbial Iron-Transport Compounds. Part 1. Solution Chemistry and Mossbauer Study of Iron(II) and Iron(III) Complexes from Phenolic and Catecholic Systems. *J. Chem. Soc., Dalton Trans.* **1981**, *2*, 609–622.
- (46) Tofan-Lazar, J.; Al-Abadleh, H. A. Surface Water Enhances the Uptake and Photoreactivity of Gaseous Catechol on Solid Iron(III) Chloride. *Environ. Sci. Technol.* **2013**, *394*–402.
- (47) Buxmann, J.; Balzer, N.; Bleicher, S.; Platt, U.; Zetzsch, C. Observations of Bromine Explosions in Smog Chamber Experiments above a Model Salt Pan. *Int. J. Chem. Kinet.* **2012**, *44*, 312–326.
- (48) Bleicher, S.; Buxmann, J. C.; Sander, R.; Riedel, T. P.; Thornton, J. A.; Platt, U.; Zetzsch, C. The Influence of Nitrogen Oxides on the Activation of Bromide and Chloride in Salt Aerosol. *Atmos. Chem. Phys. Discuss.* **2014**, *14*, 10135–10166.
- (49) Flynn, C. M. Hydrolysis of Inorganic Iron(III) Salts. *Chem. Rev.* **1984**, *84*, 31–41.

- (50) Behnke, W.; Holländer, W.; Koch, W.; Nolting, F.; Zetzsch, C. A Smog Chamber for Studies of the Photochemical Degradation of Chemicals in the Presence of Aerosols. *Atmos. Environ.* **1988**, *22*, 1113–1120.
- (51) Zetzsch, C.; Behnke, W. Heterogeneous Reactions of Chlorine Compounds. In *The Tropospheric Chemistry of Ozone in the Polar Regions*; Niki, H., Becker, K., Eds.; NATO ASI Series, Springer, Berlin, Heidelberg, Germany, **1993**; pp. 291–306.
- (52) Zangmeister, C. D.; Turner, J. A.; Pemberton, J. E. Segregation of NaBr in NaBr/NaCl Crystals Grown from Aqueous Solutions: Implications for Sea Salt Surface Chemistry. *Geophys. Res. Lett.* **2001**, *28*, 995–998.
- (53) Rossi, M. J. Heterogeneous Reactions on Salts. *Chem. Rev.* **2003**, *103*, 4823–4882.
- (54) Scheer, V.; Frenzel, A.; Behnke, W.; Zetzsch, C.; Magi, L.; George, C.; Mirabel, P. Uptake of Nitrosyl Chloride (NOCl) by Aqueous Solutions. *J. Phys. Chem. A* **1997**, *101*, 9359–9366.
- (55) Carter, W. P. L. Measurement and Modeling of NO_x Offgasing from FEP Teflon Chambers. *Proceedings of Sixth US/Germany Workshop on Ozone/Fine Particle*; Riverside California, October 4–6 **1999**.
- (56) Park, J.-H.; Christov, C. I.; Ivanov, A. V.; Molina, M. J. On OH Uptake by Sea Salt under Humid Conditions. *Geophys. Res. Lett.* **2009**, *36*, L02802.
- (57) Hirokawa, J.; Onaka, K.; Kajii, Y.; Akimoto, H. Heterogeneous Processes Involving Sodium Halide Particles and Ozone: Molecular Bromine Release in the Marine Boundary Layer in the Absence of Nitrogen Oxides. *Geophys. Res. Lett.* **1998**, *25*, 2449–2452.
- (58) Mochida, M.; Akimoto, H.; van den Bergh, H.; Rossi, M. J. Heterogeneous Kinetics of the Uptake of HOBr on Solid Alkali Metal Halides at Ambient Temperature. *J. Phys. Chem. A* **1998**, *102*, 4819–4828.
- (59) Oum, K. W.; Lakin, M. J.; DeHaan, D. O.; Brauers, T.; Finlayson-Pitts, B. J. Formation of Molecular Chlorine from the Photolysis of Ozone and Aqueous Sea-Salt Particles. *Science* **1998**, *279*, 74–76.
- (60) Park, J.-H.; Ivanov, A. V.; Molina, M. J. Effect of Relative Humidity on OH Uptake by Surfaces of Atmospheric Importance. *J. Phys. Chem. A* **2008**, *112*, 6968–6977.
- (61) Park, J.-H.; Ivanov, A. V.; Molina, M. J. Experimental Study on the Release of Cl₂ from NaCl upon OH Radical Uptake. *Microchem. J.* **2013**, *110*, 695–701.
- (62) Frinak, E. K.; Abbatt, J. P. D. Br₂ Production from the Heterogeneous Reaction of Gas-Phase OH with Aqueous Salt Solutions: Impacts of Acidity, Halide Concentration, and Organic Surfactants. *J. Phys. Chem. A* **2006**, *110*, 10456–10464.
- (63) Nissenon, P.; Wingen, L. M.; Hunt, S. W.; Finlayson-Pitts, B. J.; Dabdub, D. Rapid Formation of Molecular Bromine from Deliquesced NaBr Aerosol in the Presence of Ozone and UV Light. *Atmos. Environ.* **2014**, *89*, 491–506.
- (64) Yu, X.-Y. Critical Evaluation of Rate Constants and Equilibrium Constants of Hydrogen Peroxide Photolysis in Acidic Aqueous Solutions Containing Chloride Ions. *J. Phys. Chem. Ref. Data* **2004**, *33*, 747–763.
- (65) Elliot, A. J. A Pulse Radiolysis Study of the Temperature Dependence of Reactions Involving H, OH and e⁻_{aq} in Aqueous Solutions. *Radiat. Phys. Chem.* **1989**, *34*, 753–758.

- (66) Zimmerman, G.; Strong, F. C. Equilibria and Spectra of Aqueous Chlorine Solutions. *J. Am. Chem. Soc.* **1957**, *79*, 2063–2066.
- (67) Jayson, G. G.; Parsons, B. J.; Swallow, A. J. Some Simple, Highly Reactive, Inorganic Chlorine Derivatives in Aqueous Solution. Their Formation Using Pulses of Radiation and their Role in the Mechanism of the Fricke Dosimeter. *J. Chem. Soc., Faraday Trans. 1* **1973**, *69*, 1597–1607.
- (68) Thornton, A. T.; Laurence, G. S. Kinetics of Oxidation of Transition-Metal Ions by Halogen Radical Anions. Part I. The oxidation of Iron(II) by Dibromide and Dichloride Ions Generated by Flash Photolysis. *J. Chem. Soc., Dalton Trans.* **1973**, *8*, 804–813.
- (69) de Laat, J.; Le, T. G. Kinetics and Modeling of the Fe(III)/H₂O₂ System in the Presence of Sulfate in Acidic Aqueous Solutions. *Environ. Sci. Technol.* **2005**, *39*, 1811–1818.
- (70) King, W.; Aldrich, R. A.; Charnecki, S. E. Photochemical Redox Cycling of Iron in NaCl Solutions. *Mar. Chem.* **1993**, *44*, 105–120.
- (71) Sander, R. Compilation of Henry's Law Constants for Inorganic and Organic Species of Potential Importance in Environmental Chemistry, version 3. <http://www.henrys-law.org/henry.pdf> (**1999**).
- (72) Byrne, R. H.; Kester, D. R. Ultraviolet Spectroscopic Study of Ferric Equilibria at High Chloride Concentrations. *J. Solution Chem.* **1981**, *10*, 51–67.
- (73) Nadtochenko, V.; Kiwi, J. Primary Photochemical Reactions in the Photo-Fenton System with Ferric Chloride. 1. A Case Study of Xylidine Oxidation as a Model Compound. *Environ. Sci. Technol.* **1998**, *32*, 3273–3281.
- (74) de Laat, J.; Le, T. G.; Legube, B. A Comparative Study of the Effects of Chloride, Sulfate and Nitrate Ions on the Rates of Decomposition of H₂O₂ and Organic Compounds by Fe(II)/H₂O₂ and Fe(III)/H₂O₂. *Chemosphere* **2004**, *55*, 715–723.
- (75) Pracht, J.; Boenigk, J.; Isenbeck-Schröter, M.; Keppler, F.; Schöler, H. F. Abiotic Fe(III) Induced Mineralization of Phenolic Substances. *Chemosphere* **2001**, *44*, 613–619.
- (76) Zuo, Y.; Hoigné, J. Formation of Hydrogen Peroxide and Depletion of Oxalic Acid in Atmospheric Water by Photolysis of Iron(III)-Oxalato Complexes. *Environ. Sci. Technol.* **1992**, *26*, 1014–1022.
- (77) Mochida, M.; Hirokawa, J.; Kajii, Y.; Akimoto, H. Heterogeneous Reactions of Cl₂ with Sea Salts at Ambient Temperature: Implications for Halogen Exchange in the Atmosphere. *Geophys. Res. Lett.* **1998**, *25*, 3927–3930.
- (78) Sadanaga, Y.; Hirokawa, J.; Akimoto, H. Formation of Molecular Chlorine in Dark Condition: Heterogeneous Reaction of Ozone with Sea Salt in the Presence of Ferric Ion. *Geophys. Res. Lett.* **2001**, *28*, 4433–4436.
- (79) Baes, C. F.; Mesmer, R. E. *The Hydrolysis of Cations*; Wiley: New York, **1976**.
- (80) Kester, D. R.; Byrne, R. H.; Liang, Y.J.. Redox Reactions and Solution Complexes of Iron in Marine Systems. In: *Marine chemistry in the Coastal Environment*; Church, T. M., Ed.; American Chemical Society, Washington, DC, **1975**; Vol. 18, pp. 56–79.
- (81) Martell, A. E.; Smith, R. M. *Critical Stability Constants. Vol. 4. Inorganic Complexes*; Plenum; New York, **1976**.

- (82) Yatsimirskii, K. B.; Vasil'ev, V. P. *Instability Constants of Complex Compounds*; Pergamon Press; Oxford, U.K., **1960**.
- (83) Lister, M. W.; Rivington, D. E. Some Ferric Halide Complexes, and Ternary Complexes with Thiocyanate Ions. *Can. J. Chem.* **1955**, *33*, 1603–1613.
- (84) Avdeef, A.; Sofen, S. R.; Bregante, T. L.; Raymond, K. N. Coordination Chemistry of Microbial Iron Transport Compounds. 9. Stability Constants for Catechol Models of Enterobactin. *J. Am. Chem. Soc.* **1978**, *100*, 5362–5370.
- (85) Parkhurst, D. L.; Appelo, C. A. User's Guide to PHREEQC (Version 2): A Computer Program for Speciation, Batch-Reaction, One-Dimensional Transport, and Inverse Geochemical Calculations; U.S. Geological Survey: Washington, DC, **1999**.
- (86) Allison, J. D.; Brown, D. S.; Kevin, J. *MINTEQA2/PRODEFA2, A Geochemical Assessment Model for Environmental Systems: Version 3.0 User's Manual*; Environmental Research Laboratory, Office of Research and Development, U.S. Environmental Protection Agency; Athens, GA, **1991**.
- (87) Pitzer, K. S. Thermodynamics of Electrolytes. I. Theoretical Basis and General Equations. *J. Phys. Chem.* **1973**, *77*, 268–277.
- (88) Tosca, N. J.; McLennan, S. M.; Clark, B. C.; Grotzinger, J. P.; Hurowitz, J. A.; Knoll, A. H.; Schröder, C.; Squyres, S. W. Geochemical Modeling of Evaporation Processes on Mars: Insight from the Sedimentary Record at Meridiani Planum. *Earth Planet. Sci. Lett.* **2005**, *240*, 122–148.
- (89) Hückel, E. Zur Theorie konzentrierterer wässriger Lösungen starker Elektrolyte. *Phys. Z.* **1925**, *26*, 93–147.
- (90) Truesdell, A. H.; Jones, B. F. *WATEQ, A Computer Program for Calculating Chemical Equilibria of Natural Waters*; U.S. Department of the Interior, Geological Survey, **1973**.
- (91) Crowe, A. S., Longstaffe, F. J., Eds. *Extension of Geochemical Modelling Techniques to Brines: Coupling of the Pitzer Equations to PHREEQE*; Department of Geology, University of Alberta: Edmonton, Canada; **1987**; Vol. 1.
- (92) Merkel, B.; Planer-Friedrich, B. *Groundwater Geochemistry: A Practical Guide to Modeling of Natural and Contaminated Aquatic Systems*; Springer: Berlin, Heidelberg, Germany, **2008**.
- (93) Pitzer, K. S. Thermodynamics of Electrolytes. I. Theoretical Basis and General Equations. *J. Phys. Chem.* **1973**, *77*, 268–277.
- (94) Rabinowitch, E.; Stockmayer, W. H. Association of Ferric Ions with Chloride, Bromide and Hydroxyl Ions (A Spectroscopic Study). *J. Am. Chem. Soc.* **1942**, *64*, 335–347.
- (95) Machulek, A.; Moraes, J. E. F.; Vautier-Giongo, C.; Silverio, C. A.; Friedrich, L. C.; Nascimento, C. A. O.; Gonzalez, M. C.; Quina, F. H. Abatement of the Inhibitory Effect of Chloride Anions on the Photo-Fenton Process. *Environ. Sci. Technol.* **2007**, *41*, 8459–8463.
- (96) Spolaor, A.; Vallenga, P.; Cozzi, G.; Gabrieli, J.; Varin, C.; Kehrwald, N.; Zennaro, P.; Boutron, C.; Barbante, C. Iron Speciation in Aerosol Dust Influences Iron Bioavailability over Glacial-Interglacial Timescales. *Geophys. Res. Lett.* **2013**, *40*, 1618–1623.

- (97) Mahowald, N. M.; Engelstaedter, S.; Luo, C.; Sealy, A.; Artaxo, P.; Benitez-Nelson, C.; Bonnet, S.; Chen, Y.; Chuang, P. Y.; Cohen, D. D. Atmospheric Iron Deposition: Global Distribution, Variability, and Human Perturbations. *Annu. Rev. Mar. Sci.* **2009**, *1*, 245–278.
- (98) Ito, A. Global Modeling Study of Potentially Bioavailable Iron Input from Shipboard Aerosol Sources to the Ocean. *Global Biogeochem. Cycles* **2013**, *27*, 1–10.
- (99) Zhu, X.; Prospero, J. M.; Savoie, D. L.; Millero, F. J.; Zika, R. G.; Saltzman, E. S. Photoreduction of Iron(III) in Marine Mineral Aerosol Solutions. *J. Geophys. Res., D* **1993**, *98*, 9039–9046.
- (100) Schroth, A. W.; Crusius, J.; Sholkovitz, E. R.; Bostick, B. C. Iron Solubility Driven by Speciation in Dust Sources to the Ocean. *Nat. Geosci.* **2009**, *2*, 337–340.
- (101) Krause, T.; Tubbesing, C.; Benzing, K.; Schöler, H. F. Model Reactions and Natural Occurrence of Furans from Hypersaline Environments. *Biogeosci. Discuss.* **2013**, *10*, 17439–17468.
- (102) Rue, E. L.; Bruland, K. W. Complexation of Iron(III) by Natural Organic Ligands in the Central North Pacific as Determined by a New Competitive Ligand Equilibration/Adsorptive Cathodic Stripping Voltammetric Method. *Mar. Chem.* **1995**, *50*, 117–138.
- (103) Zhu, X.; Prospero, J. M.; Millero, F. J.; Savoie, D. L.; Brass, G. W. The Solubility of Ferric Ion in Marine Mineral Aerosol Solutions at Ambient Relative Humidities. *Mar. Chem.* **1992**, *38*, 91–107.
- (104) Finlayson-Pitts, B. J.; Ezell, M. J.; Pitts, J. N. Formation of Chemically Active Chlorine Compounds by Reactions of Atmospheric NaCl Particles with Gaseous N₂O₅ and ClONO₂. *Nature* **1989**, *337*, 241–244.

2.8 Supporting Information

Table S2.1: Rate constants for the reactions of methane and the reference hydrocarbons used as radical tracers for OH, Cl and Br in units of $\text{cm}^3 \text{s}^{-1}$ at 298 K (references in parentheses).

Hydrocarbon	k_{OH}	k_{Cl}	k_{Br}
Methane (CH_4)	6.7×10^{-15} (1)	1.07×10^{-13} (1)	4×10^{-24} (2)
2,2-Dimethylpropane (DMP)	8.3×10^{-13} (1)	1.1×10^{-10} (3)	$\leq 1 \times 10^{-20}$ (4)
2,2-Dimethylbutane (DMB)	2.2×10^{-12} (1)	1.7×10^{-10} (5)	–
2,2,4-Trimethylpentane (TMP)	3.3×10^{-12} (1)	2.3×10^{-10} (6)	6.8×10^{-15} (7)
Toluene	6.2×10^{-12} (8)	5.9×10^{-11} (9)	1.3×10^{-14} (10)
n-Perfluorohexane	–	–	–

2.8.1 Iron-free salt pans

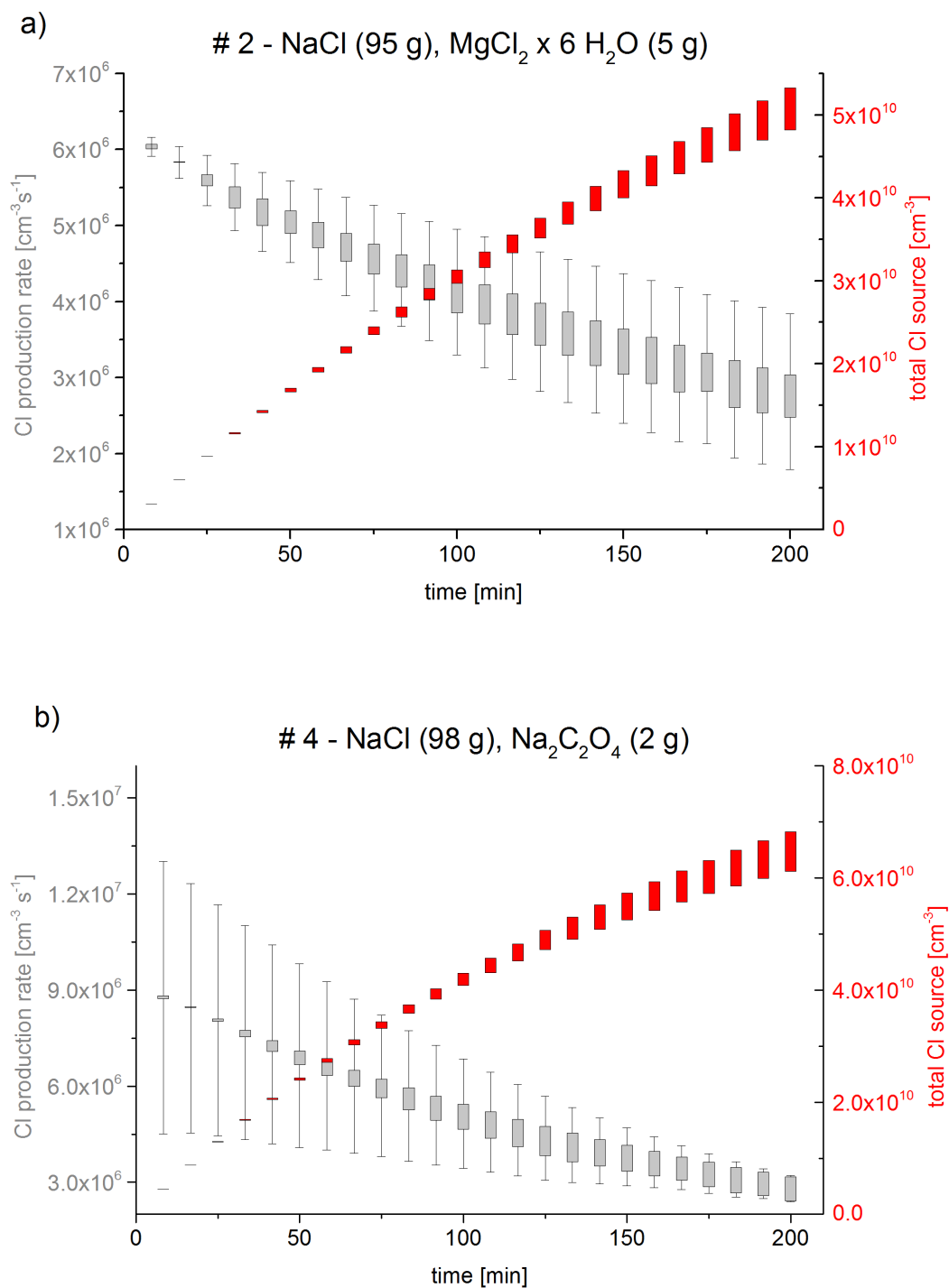
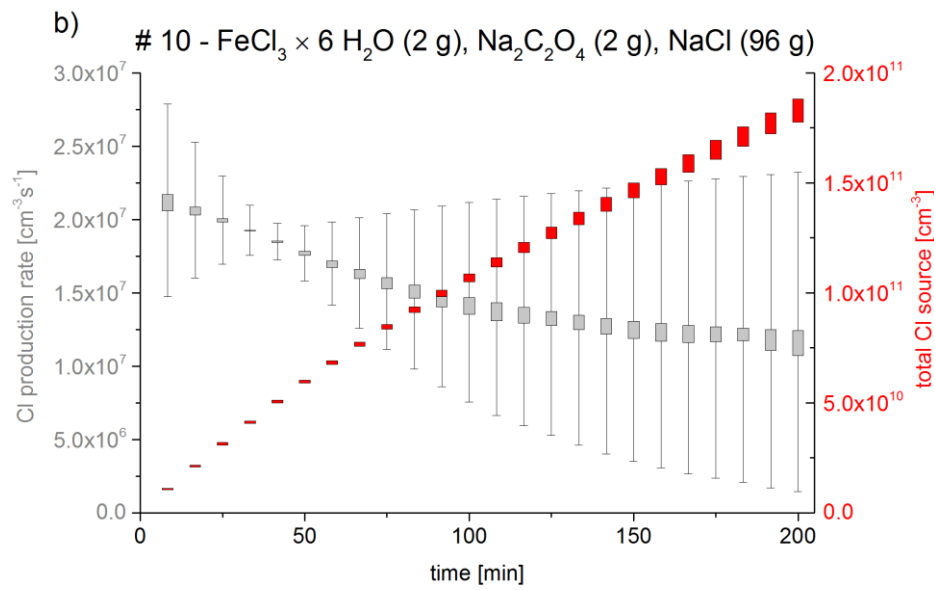
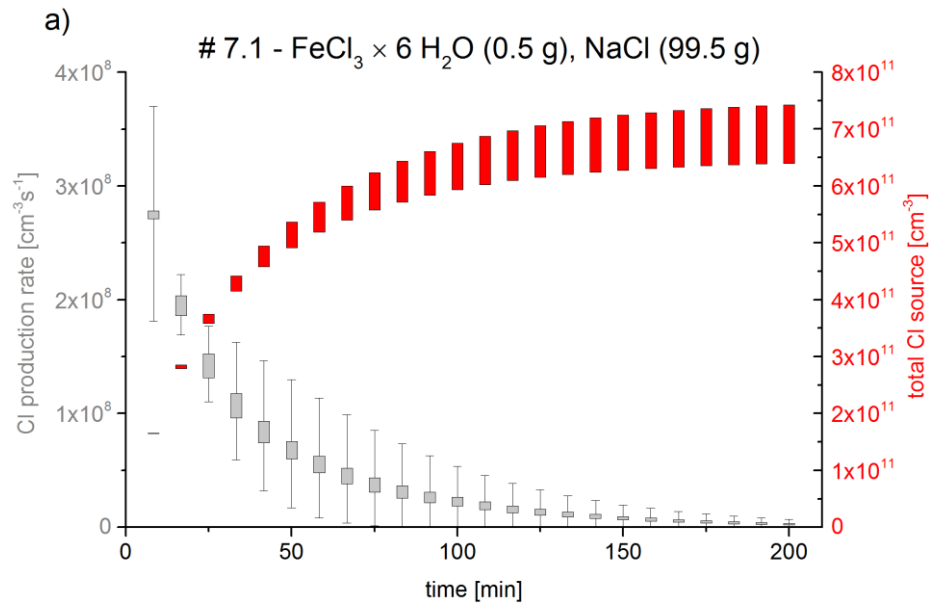


Figure S2.1a–b: Production rates of Cl and Br [atoms cm⁻³ s⁻¹] and the integrated total Cl and Br source [atoms cm⁻³] during the blank experiments #2 and #4. The salt compositions are given in the figures. The lower and upper margins of the bars represent the minimal and maximal values. For the production rate the negative minimum and the positive maximum uncertainties are included as thin error bars.

2.8.2 FeCl₃ containing salts



13 - $\text{FeCl}_3 \times 6 \text{H}_2\text{O}$ (2 g), $\text{H}_2\text{C}_2\text{O}_4 \times 2 \text{H}_2\text{O}$ (2 g), $\text{Na}_2\text{SO}_4 \times 10 \text{H}_2\text{O}$ (5 g), NaCl (91 g)

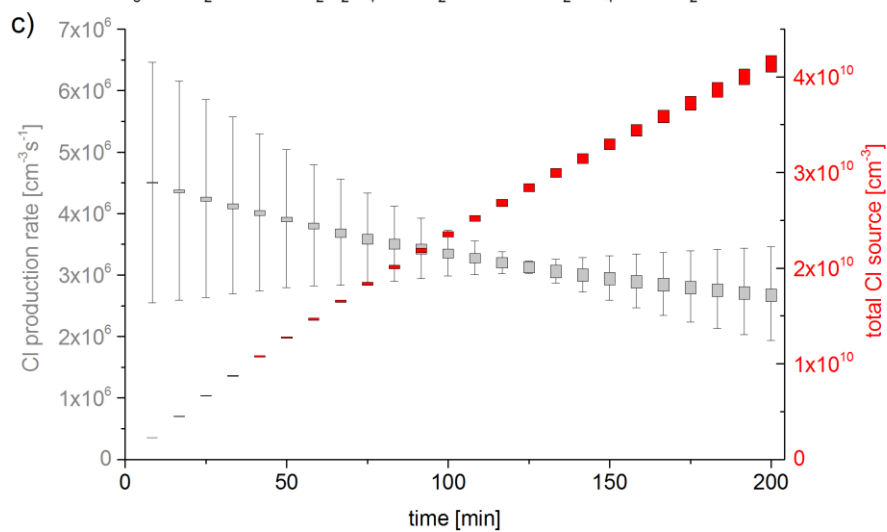
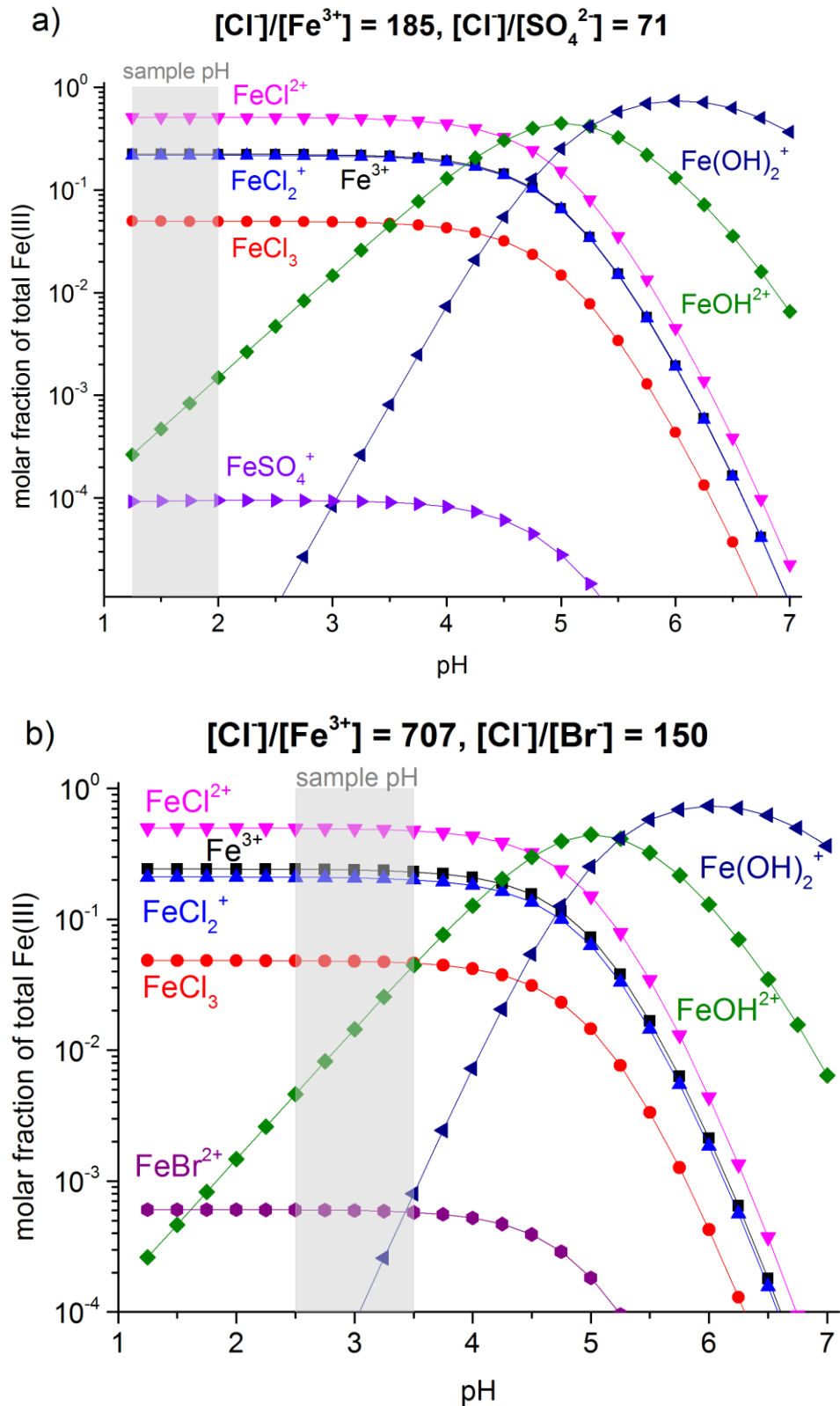
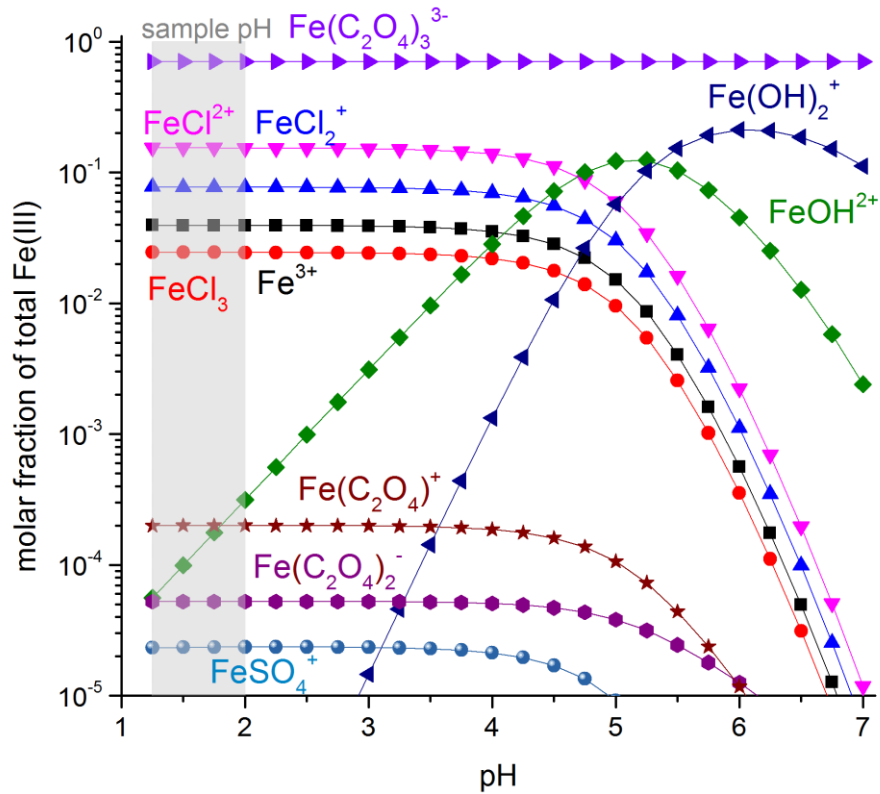


Figure S2.2a–c: Production rates of Br and Cl [$\text{atoms cm}^{-3}\text{s}^{-1}$] and the integrated total source of Cl and Br [atoms cm^{-3}] during the FeCl_3 experiments #7.1 (a), #10 (b), and #13 (c). The lower and upper margins of the bars represent the minimal and maximal values. For the production rate the negative minimum and the positive maximum uncertainties are included as thin error bars.

2.8.3 Speciation



c) $[\text{Cl}^-]/[\text{Fe}^{3+}] = 107$, $[\text{Cl}^-]/[\text{C}_2\text{O}_4^{2-}] = 50$, $[\text{Cl}^-]/[\text{SO}_4^{2-}] = 43$



d) $[\text{Cl}^-]/[\text{Fe}^{3+}] = 130$, $[\text{Cl}^-]/[\text{C}_6\text{H}_6\text{O}_2] = 53$

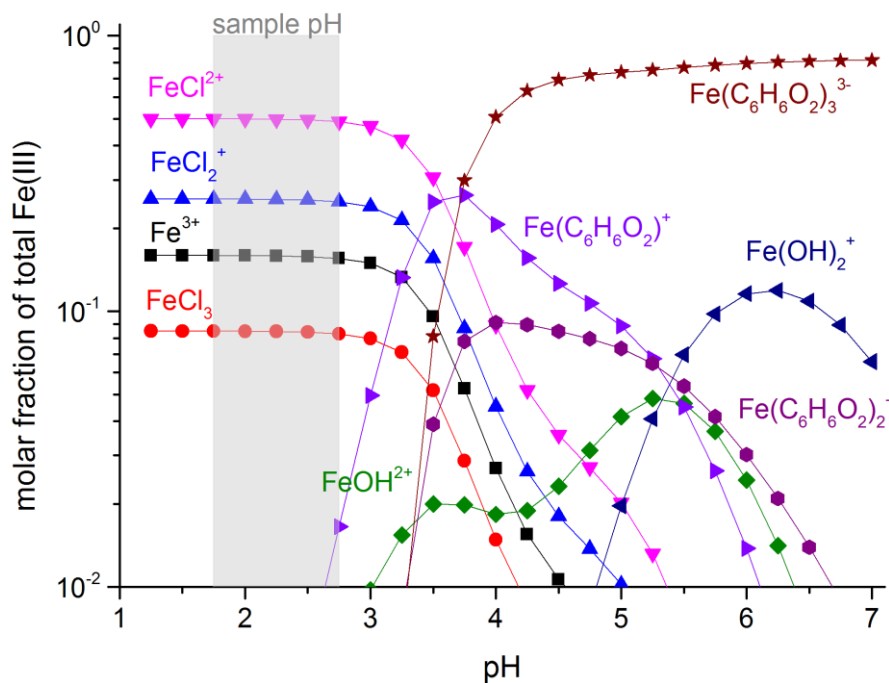


Figure S2.3a–d: Molar fraction of the formed Fe(III) species related to the total Fe(III) content in a saturated sodium chloride solution as a function of the pH (according to the PHREEQC model) for the sample compositions of experiment #8 (a), #9 (b), #13 (c) and #11 (d). The estimated range of the sample pH based on the measurements described in the text is shown in light gray.

2.8.4 References

- (1) Atkinson, R.; Baulch, D. L.; Cox, R. A.; Hampson, R. F.; Kerr, J. A.; Rossi, M. J.; Troe, J. Evaluated Kinetic, Photochemical and Heterogeneous Data for Atmospheric Chemistry: Supplement V. IUPAC Subcommittee on Gas Kinetic Data Evaluation for Atmospheric Chemistry. *J. Phys. Chem. Ref. Data* **1997**, *26*, 521–1011.
- (2) Baulch, D. L.; Duxbury, J.; Grant, S. J.; Montague, D. C. Evaluated Kinetic Data for High Temperature Reactions. Volume 4. Homogeneous Gas Phase Reactions of Halogen-and Cyanide-Containing Species. *J. Phys. Chem. Ref. Data* **1981**, *10*, 723.
- (3) Atkinson, R.; Aschmann, S. M. Kinetics of the Gas Phase Reaction of Cl Atoms with a Series of Organics at 296 ± 2 K and Atmospheric Pressure. *Int. J. Chem. Kinet.* **1985**, *17*, 33–41.
- (4) Amphlett, J. C.; Whittle, E. Bromination of Fluoroalkanes. Part 4. Kinetics of Thermal Bromination of Fluoroform and Pentafluoroethane. *Trans. Faraday Soc.* **1968**, *64*, 2130.
- (5) Jenkin, M. E.; Saunders, S. M.; Pilling, M. J. The Tropospheric Degradation of Volatile Organic Compounds: A Protocol for Mechanism Development. *Atmos. Environ.* **1997**, *31*, 81–104.
- (6) Aschmann, S. M.; Atkinson, R. Rate Constants for the Gas-Phase Reactions of Alkanes with Cl Atoms at 296 ± 2 K. *Int. J. Chem. Kinet.* **1995**, *27*, 613–622.
- (7) Barnes, I.; Bastian, V.; Becker, K. H.; Overath, R.; Tong, Z. Rate Constants for the Reactions of Br Atoms with a Series of Alkanes, Alkenes, and Alkynes in the Presence of O₂. *Int. J. Chem. Kinet.* **1989**, *21*, 499–517.
- (8) Atkinson, R. Kinetics and Mechanisms of the Gas-Phase Reactions of the Hydroxyl Radical with Organic Compounds under Atmospheric Conditions. *Chem. Rev.* **1986**, *86*, 69–201.
- (9) Shi, J.; Bernhard, M. J. Kinetic Studies of Cl-Atom Reactions with Selected Aromatic Compounds using the Photochemical Reactor-FTIR Spectroscopy Technique. *Int. J. Chem. Kinet.* **1997**, *29*, 349–358.
- (10) Bierbach, A.; Barnes, I.; Becker, K. H. Rate Constants of the Br⁻ Initiated Gas-Phase Oxidation of a Series of Alcohols, Furans and Benzenes at 300 ± 2 K. *Atmos. Environ.* **1999**, *33*, 2981–2992.

Chapter 3:

Iron(III)-Induced Activation of Chloride from Artificial Sea-Salt Aerosol

Julian Wittmer¹, Sergej Bleicher^{1,2}, Johannes Ofner³ and Cornelius Zetzsch¹

[1] Atmospheric Chemistry Research Unit, BayCEER, University of Bayreuth, Dr. Hans-Frisch Straße 1–3, 95448 Bayreuth, Germany

[2] now at: Department of Forensic Toxicology, Synlab MVZ Weiden GmbH, Zur Kesselschmiede 4, 92637 Weiden, Germany

[3] Division Environmental and Process Analytics, Institute of Chemical Technologies and Analytics, Vienna University of Technology, 1060 Vienna, Austria.

Reproduced with permission from Wittmer, J., Bleicher, S., Ofner, J., Zetzsch, C. Iron(III)-induced activation of chloride from artificial sea-salt aerosol. Environmental Chemistry 12(4), 461–475 (2015a). doi: 10.1071/EN14279. Copyright 2015 CSIRO Publishing.

Full text article: <http://www.publish.csiro.au/?paper=EN14279>

Special Issue: Naturally Produced Organohalogens – Atmosphere and Soil

Received: December 20, 2014

Accepted: March 27, 2015

Published: July 2, 2015

Environmental Context

Inorganic, natural aerosols (sea-salt, mineral dust, glacial flour) and contributions of anthropogenic components (fly ash, dust from steel production and processing, etc.) contain iron that can be dissolved as Fe^{III} in saline media. This study investigates photochemical processes in clouds and aerosols producing gas-phase Cl as a function of salt- and gas-phase composition employing a simulation chamber. Atomic Cl may contribute to the oxidative capacity of the troposphere, and our findings imply local sources.

Abstract

Artificial sea-salt aerosol, containing Fe^{III} at various compositions, was investigated in a simulation chamber (made of Teflon) for the influence of pH and of the tropospheric trace gases NO₂, O₃ and SO₂ on the photochemical activation of chloride. Atomic chlorine (Cl) was detected in the gas phase and quantified by the radical clock technique. Dilute brines with known Fe^{III} content were nebulised until the relative humidity reached 70–90 %. The resulting droplets (most abundant particle diameter: 0.35–0.46 μm, initial surface area: up to $3 \times 10^{-2} \text{ cm}^2 \text{ cm}^{-3}$) were irradiated with simulated sunlight, and the consumption of a test mixture of hydrocarbons was evaluated for Cl, Br and OH. The initial rate of atomic Cl production per aerosol surface increased with Fe^{III} and was $\sim 1.9 \times 10^{18} \text{ atoms cm}^{-2} \text{ s}^{-1}$ at Cl⁻/Fe^{III} = 13. The presence of NO₂ (~20 ppb) increased it to $\sim 7 \times 10^{18} \text{ atoms cm}^{-2} \text{ s}^{-1}$, the presence of O₃ (630 ppb) to $\sim 9 \times 10^{18} \text{ atoms cm}^{-2} \text{ s}^{-1}$ and the presence of SO₂ at 20 and 200 ppb inhibited the release slightly to ~ 1.7 and $\sim 1.1 \times 10^{18} \text{ atoms cm}^{-2} \text{ s}^{-1}$. The observed production of atomic Cl is discussed with respect to pH and speciation of the photolabile aqueous Fe^{III} complexes.

3.1 Introduction

Iron-containing aerosols have natural (e.g. mineral dust, glacial flour) or anthropogenic (combustion of fossil fuel, fuel-oil fly ash, metal processing industry, etc.) sources and represent (together with upwelling) the source of dissolved iron in offshore waters.^[1] The deposited dissolved iron, in the range of 0.26 Tg year⁻¹,^[2] has been suggested as being coupled to atmospheric carbon dioxide (CO₂) concentration by activation of the oceanic food chain ('Iron hypothesis').^[3-7] Apart from fertilisation of the oceans, iron is known to act as a catalyst in the photo-Fenton cycle in ferrous (Fe²⁺) and ferric (Fe³⁺) form, and it is utilised in wastewater treatment. Concerning the role of iron in the atmosphere, besides the proposed indirect CO₂ reduction, the interactions between gaseous and aqueous phases containing iron and other organic and inorganic compounds are of interest.

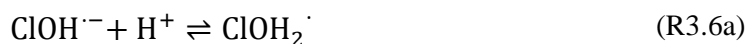
Reactive halogen species (RHS) have a large effect on the budget of ozone (O₃) and nitrogen oxides (NO_x), affecting the oxidation capacity of the atmosphere^[8,9] and interacting with secondary organic aerosols.^[10] In particular, the atomic chlorine radical (Cl) is an important atmospheric oxidant that can considerably influence the lifetime of methane (CH₄).^[11] For convenience, only aqueous-phase radicals will be marked with a dot in the following. The main mechanisms responsible for the activation of halides to reactive forms are well investigated, including heterogeneous activation by NO_x and O₃ and autocatalytic halogen activation by HOBr and HOCl.^[12,13] However, the potential role of iron in the release mechanisms of RHS remains unclear and is of special interest in the current work. Whereas a global tropospheric influence is questionable, the photochemistry of iron can significantly contribute to atomic Cl production in the gas phase, at least in some regions. Relevant iron-halide mixtures are present e.g. in coastal regions, intertidal zones, the combustion plumes of ships, volcanic plumes or brine-containing soils. In particular, hypersaline environments, such as the Dead Sea or Australian salt lakes,^[14] offer conditions that promote iron-induced halogen release, as recently investigated by Wittmer et al. for modelled salt surfaces.^[15] The present study, however, concentrates on the effect of Fe³⁺ in saline aerosols that can also be found in these regions and when mineral aerosol particles mix with sea salt. In particular, chloride (Cl⁻) enhances the dissolution of iron.^[16] The dominant presence of dissolved Fe³⁺ in saline aerosols and the photoreduction to Fe²⁺ were observed by several studies,^[17-19] but mainly with a focus on the role of the photochemistry of iron in the aqueous phase.^[20] Whereas the photolysis of ferric ions in saline media has been well investigated,^[21-23] less effort has been directed at the implications for the gas phase.

The photolysis of FeCl²⁺ and FeCl₂⁺ directly yields chlorine atoms (Cl[•]) in the liquid phase of the humid saline aerosol, and these react very fast with Cl⁻ to form Cl₂^{•-} (R3.1, reaction rate constant, $k = 2 \times 10^{10} \text{ M}^{-1} \text{ s}^{-1}$ ^[21]). The combination of Cl[•] with another Cl₂^{•-} (R3.2), or alternatively the combination of two Cl₂^{•-} (R3.3) and the dissociation of the produced Cl₃⁻ thereby (R3.4) leads to a degassing of Cl₂.^[24]





An alternative, indirect pathway for chloride activation is the photolysis of the slightly less photoactive species FeOH^{2+} , producing OH radicals in the liquid that again can form Cl^\bullet by ClOH^- .



A more detailed summary and description of Fe^{III} -induced Cl_2 formation can be found in Lim et al.^[24] or Wittmer et al.^[15]

In addition to the photosensitive iron-induced halogen release mechanism, further trace gas species, such as O_3 , NO_x and sulfur dioxide (SO_2), possibly influence Cl_2 release, mainly when dissolved in the aqueous phase where they can change the pH,^[25] coordinate with Fe^{2+} or Fe^{3+} ,^[26] scrub Cl^\bullet ^[22] or additionally activate halides by the known heterogeneous mechanisms.^[13] Concerning O_3 , Sadanaga et al.^[27] observed an enhancement of the O_3 uptake rate and Cl_2 release in the presence of water-soluble Fe^{3+} and O_3 in the dark. When SO_2 is involved, the absorbed amount is highly pH-dependent.^[28] The dissolved SO_2 is mainly in bisulfite and sulfite forms, which are oxidised to sulfate depending on the pH and the availability of catalysts such as Fe^{3+} .^[29,30] The presence of sulfate can strongly inhibit the chloride activation process by scavenging Cl^\bullet and OH^\bullet or forming stable complexes with ferrous ions.^[15,22] Apart from iron-influenced systems, polluted air masses considerably influence halogen activation in sea salt,^[8,12,31,32] as well as the environmental oxidation of Cl^- and Br^- by the triplet states of chromophoric dissolved organic matter.^[33] The present study aims at a deeper insight into the effects of Fe^{III} in saline media with a focus on a better quantification of surface-related gaseous Cl production and the effects of the trace gases mentioned above.

3.2 Experimental

3.2.1 Smog-Chamber Set-up

The experiments were conducted in a cylindrical Teflon smog chamber (fluorinated ethylene propylene, FEP 200A, DuPont, Wilmington, DE, USA) with a volume of more than 3500 L (diameter: 1.33 m, height: 2.5 m, surface/volume ratio: 3.8 m^{-1}). Here, the chamber and its analytical instrumentation are only briefly introduced. More detailed specifications can be found elsewhere.^[15,31,34]

The chamber was suspended above a solar simulator that generates a mean actinic flux comparable with the summer sun at 50° latitude. The chamber was equipped with a differential pressure sensor (Kalinsky Elektronik DS1) to monitor the slight overpressure

of 0.6–1 Pa, which was controlled by a continuous flow of 5–6 L min⁻¹ of hydrocarbon-free, humidified zero air (zero-air generator, cmc instruments, <1 ppb of O₃, <500 ppt NO_x, <100 ppb of CH₄) for all experiments. The temperature was adjusted to 20 °C and monitored by two light-shielded sensors (Rotronic, HC2-IC102) at different heights (bottom and top) to observe and avoid possible thermic layering. A Teflon fan inside the chamber assured constant mixing and kept temperature gradients below 1 °C. NO, NO_x and O₃ were monitored by chemiluminescence gas analysers (EcoPhysics, CLD 88p coupled with a photolytic converter, PLC 860 for NO and NO_x, and UPK 8001 for O₃).

Gas-phase Cl, Br and OH were indirectly quantified by the radical clock method,^[35] monitoring the consumption of selected hydrocarbons (2,2-dimethylpropane, DMP, Linde, ≥99 %; 2,2-dimethylbutane, DMB, Aldrich, ≥99 %; 2,2,4-trimethylpentane, TMP, Janssen ≥99 %; toluene, Tol, Aldrich ≥99.9 %) and *n*-perfluorohexane (PFH, Aldrich, ≥99 %) as inert standard. The concentrations of the hydrocarbons was measured at time intervals of 15 min by gas chromatography (GC, Siemens Sichromat 2, 50-m Al₂O₃-PLOT column, 0.25 mL min⁻¹ He as carrier gas) with a flame ionisation detector (FID), custom-built liquid nitrogen cryo-trap enrichment in glass-lined stainless-steel tubing and a Nafion tube counterflushed from outside with zero air to dry the sampling flux.^[15]

3.2.2 Sample Preparation and Chemicals used

An artificial seawater stock solution with a molar Cl⁻/Br⁻ ratio of 997 was prepared according to Kester et al.^[36] The mixture included NaCl (23.9 g L⁻¹), Na₂SO₄·10H₂O (9.1 g L⁻¹), KCl (0.68 g L⁻¹), NaHCO₃ (0.2 g L⁻¹), KBr (0.098 g L⁻¹), H₃BO₃ (0.026 g L⁻¹), NaF (0.003 g L⁻¹), MgCl₂ (5.1 g L⁻¹), and CaCl₂·2H₂O (1.5 g L⁻¹). Depending on the experiment, a specific amount of FeCl₃ was dissolved in the stock solution and diluted afterwards (1 : 28) to obtain a Cl⁻ concentration of 15–35 mmol L⁻¹ (Table 3.1) that provides optimal aerosol size distributions for long residence times of the suspended droplets. The aerosol production from the prepared solutions and the subsequent measurement are described in the following section. For the reference experiment with Fe^{III}-doped NaCl, the FeCl₃ was directly added to an 18 mmol L⁻¹ NaCl solution. The added amount of FeCl₃ and the resulting Cl⁻/Fe^{III} ratios are listed in Table 3.1. More details of the prepared artificial seawater are included in the Supplementary material (Table S3.1).

On the basis of the different sea-salt mixtures, the effect of various gas species was tested by adding O₃ from a silent ozoniser (Sorbios GSG 12) with an electrical discharge applied to pure oxygen (Rießner Gase, >99.995 %), NO₂ from a gas cylinder (Rießner Gase, 104 vpm (volume parts per million) NO₂ with a purity of 98 % in synthetic air), or SO₂ from a gas cylinder (Rießner Gase, 0.99 % SO₂ with a purity of 99.98 % in N₂ with a purity of 99.999 %).

Table 3.2: Compositions of the stock solutions obtained by adding FeCl₃ to the artificial seawater (prepared according to Kester et al.^[36]) or to a 1 g L⁻¹ NaCl solution and resulting molar Cl⁻/Fe^{III} ratios.

Manufacturer and specified purity (%)	weighted amount (g) in 1 L H ₂ O	Cl ⁻ /Fe ³⁺ (mol mol ⁻¹)	Cl ⁻ concentration in the nebulized solution (mmol L ⁻¹)
Added FeCl₃ to art. seawater			
Merck, for synthesis, ≥ 98 %	0.14	955	28
Merck, for synthesis, ≥ 98 %	1.36	101	29
Riedel - de Haën, sublimate, ≥ 99 %	2.67	53	30
Riedel - de Haën, sublimate, ≥ 99 %	13.04	13	37
Added FeCl₃ to 1 g/l NaCl			
Riedel - de Haën, sublimate, ≥ 99 %	0.278	13	18

3.2.3 Aerosol Production and Measurement

The sea-salt particles were generated by nebulising the prepared solutions (Table 1) with an ultrasonic nebuliser (Quick Ohm QUV-HEV FT25/16-A, 35 W, 1.63 MHz) at a starting relative humidity (RH) of ~40 % to avoid crystallisation.^[12] During injection (taking typically 30–50 min), the RH increased to 70–90 %. Thus, we can assume that the droplets equilibrate to form a saturated solution, leading to most abundant particle diameters between 350 and 460 nm based on the concentration of the stock solution and the final RH after injection.^[37] The size distributions were determined by an electrostatic classifier (TSI, 3071) in combination with a neutraliser (⁸⁵Kr) and a condensation nucleus counter (TSI, 3020). The scanning method and the multiple charge correction were applied with custom-written software.^[38] Typical size distributions, determined after 30–50 min of injection, are shown in Fig. 3.1 for different stock compositions. To avoid the condensation of the sea salt within the transfer line (~6.4 mm tube made of copper) and thus the dripping of solution inside the chamber, the tube was additionally heated by a heating wire to ~60–70 °C. During aerosol generation, the NO_x signal rose typically up to 3–5 ppb, probably originating from the sonochemical formation of nitrate and nitrite^[39] and including a possible cross-sensitivity of the NO_x analyser to nitrous acid (HONO).^[40]

The chamber walls were either cleaned with deionised water (Seralpur Pro 90 CN, <0.055 μS cm⁻¹), or the total FEP-Teflon film was exchanged after the experiment (depending on the risk of contamination expected for subsequent runs). To minimise the outgassing of gas-phase products,^[41] every new chamber was conditioned by adding O₃ at an RH of 50–80 % and irradiating for at least 4 h with the solar simulator and an additional UV lamp (Phillips TUV 55 W, λ = 253.7 nm).

After every experiment, the particles were collected by a Sioutas cascade impactor (SKC) in the aerodynamic diameter ranges of >2.5, 1–2.5, 0.5–1, 0.25–0.5 and <0.25 μm^[42] on

aluminium foil as a collection substrate. The impactor samples were analysed using an FEI Quanta 200 scanning-electron microscope (SEM), equipped with an energy-dispersive X-ray (EDX) detector for imaging (Octane Pro Silicon Drift (SDD) EDX detector from AMETEK). The hyperspectral data-cube from the SEM-EDX measurements was analysed using the software package *Imagelab* (Epina Software Laboratories, www.imagelab.at, accessed April 2015).^[43]

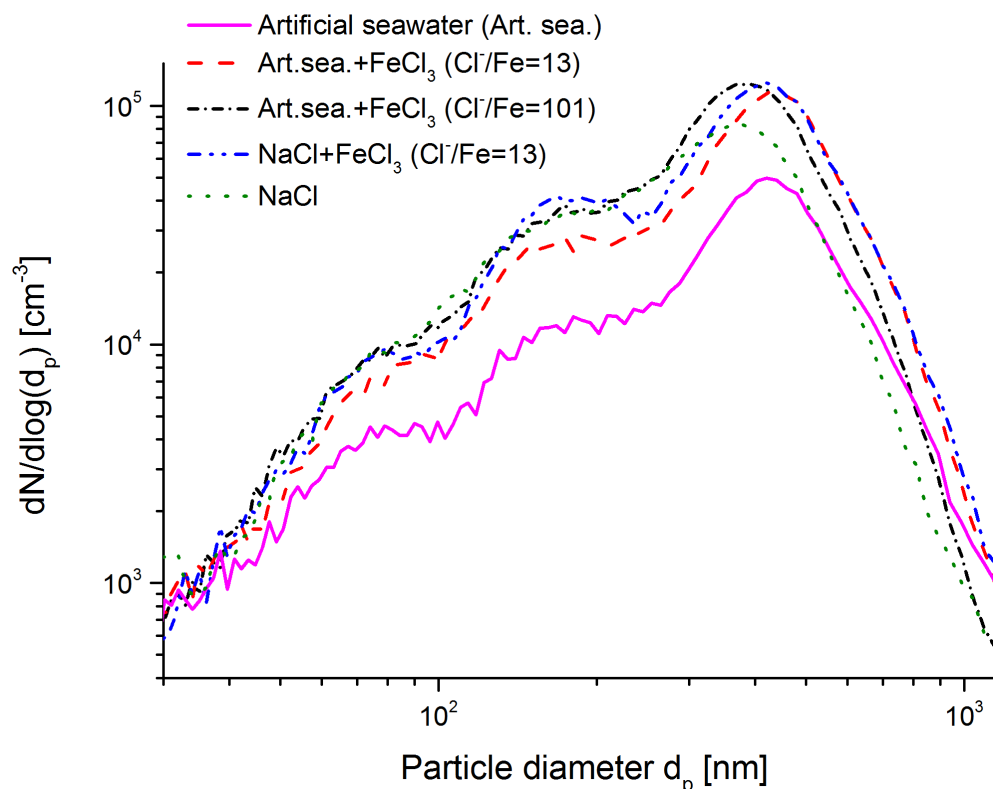


Figure 3.1: Typical initial (multiple-charge corrected) size distributions for aerosols generated by the ultrasonic nebuliser (30-50 min injection time) from various diluted stock solutions containing NaCl, FeCl₃ or artificial seawater. N, number density; d_p, particle diameter.

3.2.4 Data Analysis (Radical Clock)

The gas chromatograms were evaluated the same way as described before^[15] to quantify the quasi-stationary concentrations of Cl_{qs}, OH_{qs}, and Br_{qs} in the gas phase, based on the measured, dilution-corrected and smoothed hydrocarbon (HC_i) profiles, resulting in a system of four differential equations with three unknown variables according to:

$$(3.1)$$

where $k_{X,i}$ is the reaction rate constant of HC_i towards the radical X (X = Cl, Br, and OH; Table S2, Supplementary material). The corresponding total production, Q_X , and production rates dQ_X/dt are obtained by equalising sources and sinks in a photostationary steady-state:

$$Q_X = \int_0^{\tau} \sum_i k_{X,i} [\text{HC}_i]_t [\text{X}]_t dt \quad (3.2)$$

Considering a constant total reactivity of the chamber contents towards [X] on the one hand ($\sum_i k_{X,i} [\text{HC}_i]_0$) and only the reactivity of the measured hydrocarbons on the other hand ($\sum_i k_{X,i} [\text{HC}_i]_t$), which means either assuming that reaction products have the same reactivities as the HC_i or neglecting the reactivities of the reaction products totally, we obtain an estimate of the minimum and maximum Q_X and dQ_X/dt . These assumptions are reasonably valid for Cl atoms but less reliable for Br atoms and OH radicals, where the reactivities of reaction products may exceed the reactivities of the original hydrocarbons by far. However, they are valid at the very beginning of the irradiation, where the consumption of the hydrocarbons is still low.

The measurements of the particle size distributions (number density N , cm^{-3}) allow us to determine the available reaction surface area (A , $\text{m}^2 \text{m}^{-3}$) and the particle volume (V_{particle} , $\text{m}^3 \text{m}^{-3}$), which equals the liquid water content (LWC) plus the tare volume of the ions (radius, $r_{\text{Cl}^-} = 181$ pm, $r_{\text{SO}_4^{2-}} = 184$ pm, $r_{\text{Na}^+} = 102$ pm, $r_{\text{K}^+} = 137$ pm, $r_{\text{Mg}^{++}} = 72$ pm, $r_{\text{Ca}^{2+}} = 106$ pm, $r_{\text{Fe}^{+++}} = 49$ pm)^[44] at the adjusted RH. The measured LWC was corrected by considering the main ions as spherical. The contribution of deposited particles on the chamber walls to the activated Cl was considered by measuring the Cl activation of a totally wall-deposited aerosol load (*Chamber wall effects* section). The Cl production terms are normalised to obtain absolute production rates, dQ_{abs}/dt , and absolute total production Q_{abs} cm^{-2} of the aerosol surface. Therefore, the production rate (atoms $\text{cm}^{-3} \text{s}^{-1}$) is multiplied by the chamber volume, V_{chamber} , to obtain the total number of atoms produced per second. The result is divided by the actual active aerosol surface, which we define as the sum of (i) the measured aerosol surface when the lights were turned on ($A_{0,\text{light}}$) and its deposition rate, $\exp(-t_{\text{light}}/\tau_s)$, with the aerosol surface lifetime τ_s ; (ii) the active, deposited surface during the time of injection; and (iii) the active, deposited surface formed after the injection is finished (Eqn 3). Whereas (ii) is determined by assuming an approximately linear increase of the aerosol surface during injection and calculating the respective deposition until the injection is stopped ($t_{\text{inj, end}}$), (iii) is based on the measured aerosol surface area directly after injection ($A_{0,\text{inj}}$) and its deposition during the time t_{inj} , which starts when the injection ends. Both terms are multiplied by a factor of 0.2, which is the fraction of deposited surface area that contributes to the halogen activation (Section 3.3.1).

$$\frac{dQ_{\text{abs}}}{dt_{\text{light}}} = \frac{\frac{dQ_X}{dt_{\text{light}}} \times V_{\text{Chamber}}}{A_{0,\text{light}} \times \exp\left(-\frac{t_{\text{light}}}{\tau_s}\right) + 0.2 \times \left(\int_{t_{\text{inj, start}}}^{t_{\text{inj, end}}} \left(\frac{\Delta A_{0,\text{inj}}}{\Delta t_{\text{inj, end}}} \times \frac{t}{\tau_s} \right) dt + A_{0,\text{inj}} \times \left(1 - \exp\left(-\frac{t_{\text{inj}}}{\tau_s}\right)\right) \right)} \quad (3.3)$$

3.3 Results and Discussion

Table 3.2 presents an overview of the experiments performed, including $\text{Cl}^-/\text{Fe}^{\text{III}}$ ratios, pH of the diluted stock solution, gas-phase composition, initial reactivity of HCs against

Cl, OH, and Br, initial aerosol surface, resulting quasi-stationary concentrations and absolute production. Based on the two-to-five orders of magnitude lower reactivity of the applied HCs against Br and OH compared with Cl, depletion was dominated by the reaction with Cl, and no significant interpretation for Br and OH was possible in most cases. Before adding FeCl₃ to the samples, several Fe^{III}-free blank experiments were performed, including pure NaCl aerosol, artificial sea-salt aerosol and artificial sea-salt aerosol with O₃ and NO₂ addition respectively (see Table 3.2). Except for the artificial sea-salt aerosol with addition of 700 ppb O₃, Cl production was hardly detectable. Generally, no indication of Cl, Br or OH production was observed during the dark phases (aerosol, NO₂, O₃, SO₂ injections and waiting periods), based on the constant HC time profiles.

3.3.1 Chamber Wall Effects

Owing to flashovers in the classifier throughout some experiments caused by the high RH, only the measurements at the beginning of those experiments were evaluable. Therefore, the measurements after injection and when the lights were turned on were used to calculate the dilution-corrected loss by deposition, based on the mean dilution-corrected lifetimes $\tau_{N,S}$ (N = number density, s = total aerosol surface area) over the experiments without flashovers and neglecting the loss by coagulation. The deposition velocity depends on the salt concentration in the nebulised solution and thus on the mean particle diameter after injection. For instance, the artificial sea-salt solution and the pure NaCl solution gave lifetimes of $\tau_N = 24\,800$ s ($\tau_S = 30\,100$ s) and $\tau_N = 25\,000$ s ($\tau_S = 31\,100$ s). For the higher-concentration Fe^{III}-doped artificial seawater (29–35 mmol Cl⁻ L⁻¹), the most abundant particle diameters were between 430 and 460 nm, resulting in a faster sedimentation with $\tau_N = 4590 \pm 240$ s and $\tau_S = 6070 \pm 520$ s compared with $\tau_N = 6845$ s and $\tau_S = 8820$ s for the lower-concentration pure NaCl + FeCl₃ solution (24 mmol Cl⁻ L⁻¹) with most abundant particle diameters between 390 and 420 nm. The respective contour plots can be found in the Supplementary material (Fig. S1).

To quantify the particle deposition and its contribution to the active surface area (and thus to Cl activation), a test measurement was performed to determine the fraction of Cl release by the active wall surface compared with the active aerosol surface: the iron-doped artificial seawater sample (Cl⁻/Fe^{III} = 13) was injected and allowed to deposit totally for 17 h (<0.005 % of the surface area should have remained suspended) while keeping the RH at 80 %. Then the ‘aerosol-free’ chamber was irradiated, resulting in Cl production that was 20 ± 4 % compared with the actual production measured for the same sample in an aerosol experiment (see section 3.3.2). This production was evaluated by taking the mean of the quotient of each total production (deposited and not deposited) normalised by the respective initial *LWC* directly after injection. In Eqn 3, the contribution of deposited, active aerosol surface area is accounted for by adding 20 % of the deposited surface area since the time of injection to the surface area when the lights were turned on (corrected for deposition). The smaller active fraction when deposited on the wall can be explained by a physical surface reduction during the adhesion process of the droplets (possibly coagulating to larger droplets on the hydrophobic surface) and by an inhomogeneous irradiation of the chamber walls (especially the large fraction of wall surface perpendicular to the solar simulator), but also by a drying effect due to the heating

of the Teflon walls during irradiation. Fig. 3.2 demonstrates the contribution of active, deposited surface on the wall to the total active surface area during the experiment with Fe^{III}-doped, pH-adjusted (pH 2.1–2.3) artificial seawater (Cl⁻/Fe^{III} = 101). The figure additionally includes dQ_{abs}/dt and Q_{abs} , which are discussed in section 3.3.4.

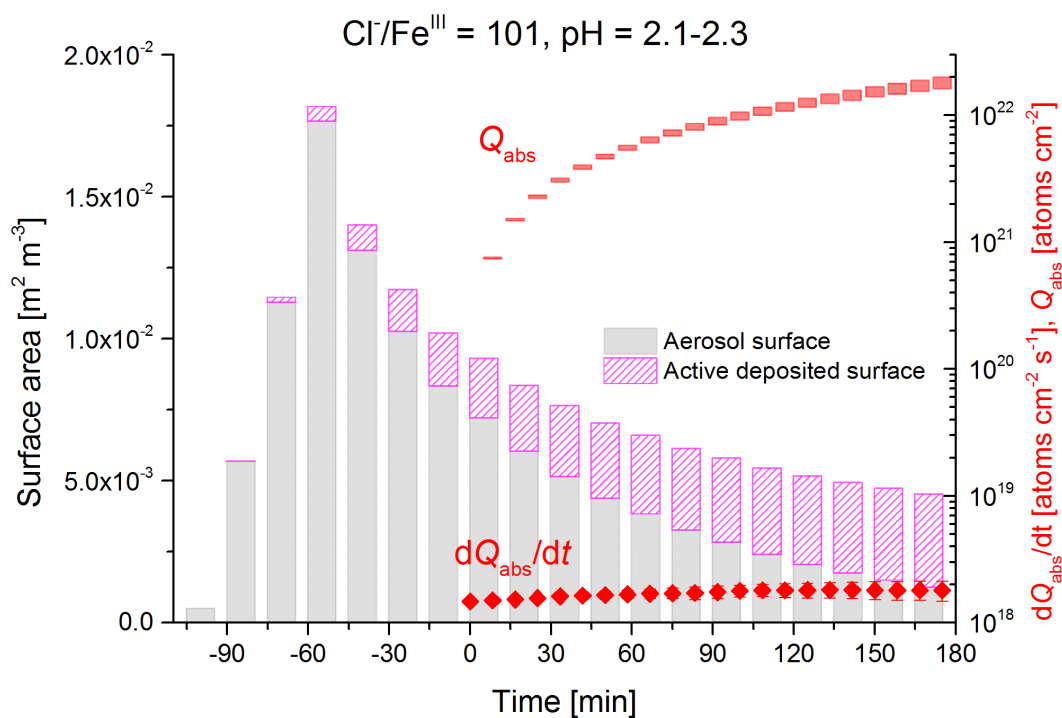


Figure 3.2: Time profile of the sum of the total measured aerosol surface area and the active deposited surface during the experiment with Fe^{III}-doped, pH-adjusted (pH = 2.1–2.3) artificial seawater (Cl⁻/Fe^{III} = 101) and the corresponding absolute gaseous mean Cl production rate (dQ_{abs}/dt) [atoms cm⁻² s⁻¹] and time integrated total Cl production Q_{abs} [atoms cm⁻²] of active aerosol surface. The light was switched on at 0 min.

Table 3.2: Molar $\text{Cl}^-/\text{Fe}^{\text{III}}$ ratio, pH of the diluted, nebulised stock solution, gas-phase composition within the smog chamber, total initial reactivity of the hydrocarbons in the chamber against Cl, OH and Br, total aerosol surface measured directly after injection, quasi-stationary Cl_{qs} , Br_{qs} and OH_{qs} concentrations during irradiation during the first hour, and resulting total Cl and Br production per square centimetre aerosol surface
n.d., not detected

$\text{Cl}^-/\text{Fe}^{3+}$	pH of diluted stock solution	Gas phase	Initial reactivity (s^{-1})			Initial aerosol surface area ($10^{-2} \cdot \text{m}^2 \cdot \text{m}^{-3}$)	Quasi-stationary concentration (atoms cm^{-3})			Total production Q_{abs} (atoms $\text{cm}^{-2} \cdot \text{h}^{-1}$)	
			Cl	OH	Br		$\text{Cl}_{\text{qs}} (\times 10^5)$	$\text{OH}_{\text{qs}} (\times 10^6)$	$\text{Br}_{\text{qs}} (\times 10^9)$	Cl ($\times 10^{19}$)	Br ($\times 10^{19}$)
∞^{A}	4.7–5.0	Zero air	182	4.5	0.0074	1.0	$\sim 0.1^{\text{F}}$	$\sim 1^{\text{F}}$	$\sim 1^{\text{F}}$	$\sim 0.6\text{--}0.7^{\text{F}}$	n.d. ^G
∞^{B}	4.8–5.1	Zero air	163	3.9	0.0063	2.3	~ 0.4	5.1	$< 1^{\text{G}}$	~ 0.8	n.d. ^G
∞^{A}	4.7–5.0	20 ppb NO_x	209	4.2	0.008	2.4	$\sim 0.1^{\text{F}}$	2	1.2	n.d. ^G	67–70
∞^{A}	4.7–5.0	700 ppb O_3	137	1.3	0.0053	2.2	4.9	17	9.4	4.6–7.3	162–279
955 ^C	4.5–4.8	Zero air	126	2.6	0.0039	1.2	$\sim 0.1^{\text{F}}$	2.3	$\sim 1^{\text{F}}$	$\sim 0.6\text{--}0.7^{\text{F}}$	n.d. ^G
101 ^C	3.9–4.2	Zero air	201	4.3	0.0077	2.5	0.5	1.2	3.8	1.1–1.2	177–196
101 ^{C,D}	2.1–2.3	Zero air	177	3.3	0.0046	1.8	1.9	2.2	2.7	8.8–9.6	184–216
101 ^C	3.9–4.2	20 ppb NO_x	196	3.9	0.0057	2.3	9.1	5	3	4.9–5.4	262–320
101 ^{C,D}	2.1–2.3	20 ppb NO_x	169	3.6	0.0053	2.3	5.4	3	$< 1^{\text{G}}$	11–13	n.d. ^G
51 ^C	3.3–3.6	Zero air	152	3.3	0.0052	3.2	1.9	5.4	1.2	2.2–2.5	29–32
13 ^B	1.9–2.2	Zero air	118	2.9		2.4	16.7	4.8	$< 1^{\text{G}}$	15–22	n.d. ^G
13 ^C	1.9–2.2	Zero air	125	2.4	0.0036	3.0	13.1	$< 1^{\text{G}}$	$< 1^{\text{G}}$	11–15	n.d. ^G
13 ^C	1.9–2.2	20 ppb NO_x	139	3.2	0.0051	3.1	65.1	$< 1^{\text{G}}$	$< 1^{\text{G}}$	26–86	n.d. ^G
13 ^C	1.9–2.2	630 ppb O_3	218	5.2	0.0085	3.4	40	13	13	29–74	299–814
13 ^C	1.9–2.2	~ 20 ppb SO_2	204	4.9	0.0078	1.9	4.3	2.1	3.7	10–11	204–222
13 ^C	1.9–2.2	> 200 ppb SO_2	178	4.4	0.0063	1.0	1.4	1.3	1.2	5.9–7.4	138–156

^A Fe^{III} -free artificial seawater stock solution.

^BNaCl stock solution.

^CArtificial seawater stock solution.

^DpH adjusted to 2.1–2.3.

^EMean steady-state concentrations during the first hour.

^FClose to the detection limit.

^GBelow the detection limit.

3.3.2 Iron(III)-Catalysed Cl Atom Production

Significant Cl activation was detected for every sample with $\text{Cl}^-/\text{Fe}^{\text{III}} < 101$ (Table 2), whereas Cl production was close to the detection limit during the blank experiments including Fe^{III} -free NaCl and artificial sea-salt aerosol in zero air. The effect of the constituents of the Fe^{III} -containing artificial seawater mixture was investigated by comparing the Cl release with a pure NaCl + FeCl_3 mixture. Both samples were prepared with a molar ratio of $\text{Cl}^-/\text{Fe}^{\text{III}} = 13$. Both experiments were conducted in the same manner and under the same conditions (21 ± 1 °C and 72 ± 2 % RH). After 45 min of aerosol injection and a 15-min waiting period, the light was turned on. The aerosol size distributions (Fig. 3.1) showed small differences, with a lower diameter for the most abundant particles but only a slightly lower surface-to-volume ratio for the artificial sea salt/ Fe^{III} mixture ($1.29 \times 10^7 \text{ m}^{-1}$) compared with the NaCl/ Fe^{III} mixture ($1.31 \times 10^7 \text{ m}^{-1}$) caused by the similar hydration behaviour at the given RH (Köhler theory).^[45] The Cl production rates and corresponding total production are shown in Fig. 3.3. Slightly higher Cl production of the pure NaCl/ Fe^{III} mixture was observed, which was probably caused by the speciation chemistry (as photolabile Fe^{III} -Cl complexes can form more easily in the absence of competing ions such as SO_4^{2-}).^[46] Considering the diluted stock solutions, the pH was between 1.9 and 2.2 for both experiments. The buffer effect of the added bicarbonate (0.2 g L^{-1}) in the artificial seawater is very low, considering the high amount of FeCl_3 added (13 g L^{-1}). Although the radical clock method is also able to quantify Br and OH, the depletion of HCs was dominated by Cl with its much higher reaction rate constants (Table S3.2, Supplementary material), which prevents significant interpretation of Br and OH (in most cases), which were close to the detection limit (Br $\sim 10^9$ molecules cm^{-3} ; OH $\sim 10^6$ molecules cm^{-3}).

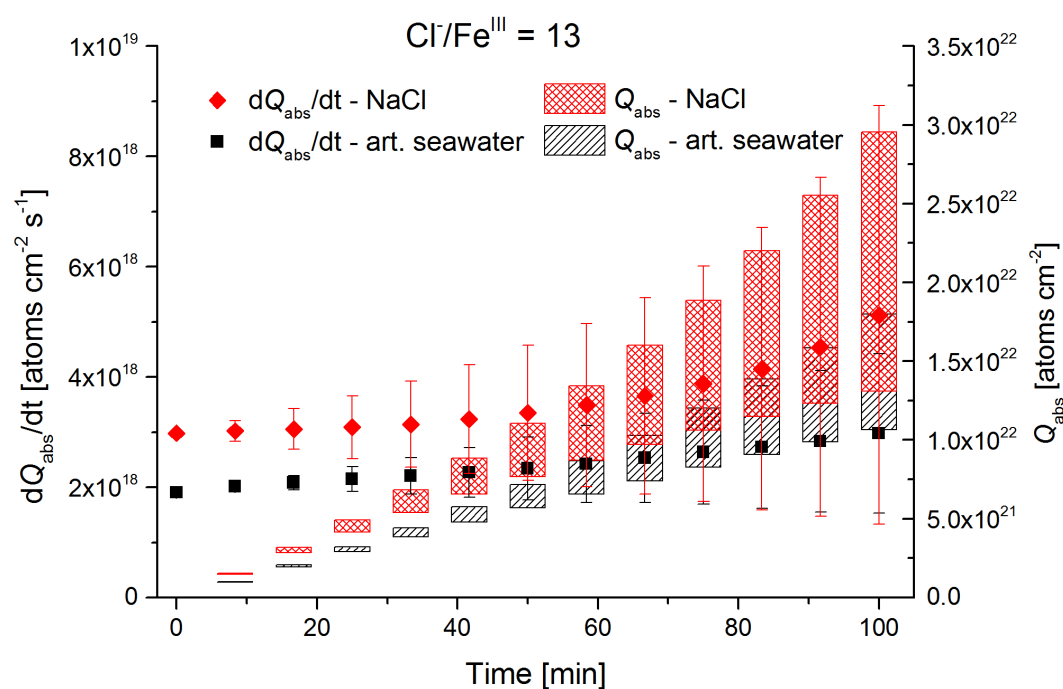


Figure 3.3: Absolute gaseous mean Cl production rate (dQ_{abs}/dt) [$\text{atoms cm}^{-2} \text{ s}^{-1}$] and time-integrated total minimum and maximum Cl production Q_{abs} [atoms cm^{-2}] of aerosol surface during the experiments with Fe^{III} -doped artificial seawater and NaCl with $\text{Cl}^-/\text{Fe}^{\text{III}} = 13$. The error bars for

dQ_{abs}/dt include the minimum and maximum production rates and the respective statistical uncertainty. The light was switched on at 0 min.

In order to determine the dependence of the chlorine activation on the $\text{Cl}^-/\text{Fe}^{\text{III}}$ ratio in the aerosol, a series of experiments with a $\text{Cl}^-/\text{Fe}^{\text{III}}$ ratio of (i) 13, (ii) 53, (iii) 101, (iv) 955 and (v) a blank without iron addition was conducted. Whereas no significant Cl concentration was detected for run (iv) and (v), (iii) resulted in a total Cl production of $(0.9\text{--}1.0) \times 10^{21}$ atoms cm^{-2} , run (ii) of $(2.3\text{--}2.6) \times 10^{21}$ atoms cm^{-2} , and run (i) of $(1.1\text{--}1.8) \times 10^{22}$ atoms cm^{-2} in the first 100 min (Fig. 3.4). This demonstrates a continuous increase in produced Cl with increasing fraction of Fe^{III} in the salt. A 1.9-times higher fraction of Fe^{III} results in a 2–3-times higher Cl production (comparing (iii) and (ii)), and 4.1 times more Fe^{III} results in 5–7-times higher Cl production (comparing (ii) and (i)). The higher amount of added FeCl_3 cannot only explain the disproportionately higher Cl activation. In fact, the shift in pH from adding 10 times more FeCl_3 (pH 4→2) is in addition responsible for a higher fraction of photolabile $\text{Fe}^{\text{III}}\text{-Cl}$ complexes (discussed in section 3.3.4). A slight decrease was observed for (iii), indicating exhaustion of the Cl source, whereas samples (i) and (ii) resulted in a more stable Cl production rate.

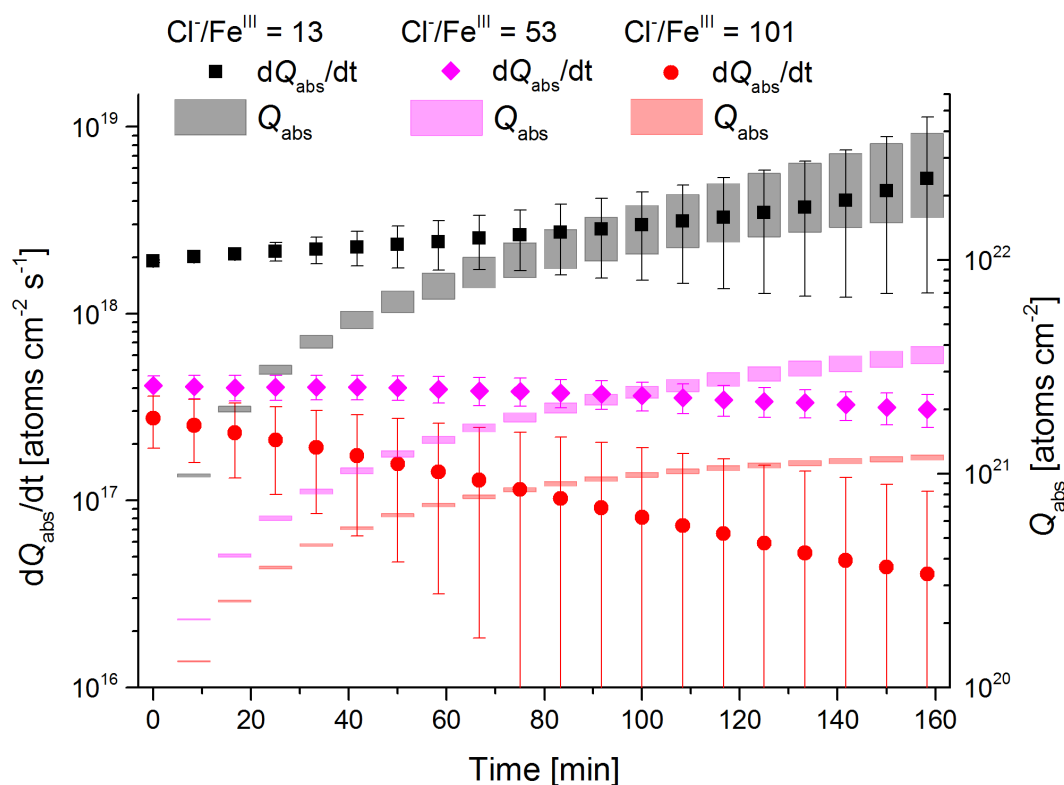


Figure 3.4: Absolute gaseous mean Cl production rate (dQ_{abs}/dt) [atoms cm^{-2} s^{-1}] and time-integrated total minimum and maximum Cl production Q_{abs} [atoms cm^{-2}] of aerosol surface during the experiments with Fe^{III} -doped artificial seawater at various Fe^{III} concentrations: $\text{Cl}^-/\text{Fe}^{\text{III}}$ = 13 (black), 53 (magenta), 101 (red). The light was switched on at 0 min.

3.3.3 Effects of NO_2 , O_3 , and SO_2

Experiments on the typical tropospheric traces and pollutants NO_2 , O_3 and SO_2 were performed by adding 20 ppb of NO_2 , 630 ppb of O_3 , and 20 and 200 ppb of SO_2 . These levels were chosen with the aim to better observe their effects and to obtain aerosol to

pollutant ratios approximately comparable with natural conditions (discussed in section 3.3.7). Figs 3.5 and 3.6 show the time profiles of the trace gases (corrected for dilution) combined with the results on Cl_{qs} , dQ_{abs}/dt and Q_{abs} obtained by the radical clock for the experiments with Fe^{III} -doped artificial seawater ($Cl^-/Fe^{III} = 13$) and addition of NO_2 and O_3 respectively. After the aerosol injection, the addition of NO_2 and a waiting period of 55 min (12 min in case of the O_3 experiment), the solar simulator was turned on (indicated by 0 min in the figures). For both experiments, significantly elevated Cl production was observed compared with the experiments in zero air. The higher Cl source is related to the additional activation mechanisms in the presence of O_3 and NO_x ,^[13] which are discussed in the following text. Fast formation of O_3 was observed in the NO_x experiment when the light was turned on, caused by the well-known photochemical cycle of NO , NO_2 and O_3 (photolysis rate coefficients: $J_{NO_2} = 6.7 \times 10^{-3} s^{-1}$, $J_{O_3} = 2 \times 10^{-4} s^{-1}$) on the one hand and the reoxidation of NO to NO_2 and OH by HO_2 (formed by the depletion of the injected HC_i) on the other hand. Therefore, the O_3 concentration exceeded the NO_x concentration in the course of the experiment, and the O_3 formation stopped when NO was depleted. Because O_3 is not present during the dark period, only negligible amounts of dark-phase nitrogen oxides like dinitrogen pentoxide (N_2O_5) could be present at the beginning of the irradiation and potentially explain the additional Cl source by the proposed heterogeneous activation mechanisms.^[12,13,32,47]

During irradiation, the presence of O atoms and O_3 formation can cause the formation of NO_3 and thus N_2O_5 , although NO_3 is extremely short-lived under our conditions ($J_{NO_3} = 0.11 s^{-1}$). At an NO_x concentration of 20 ppb, the proposed formation and photolysis of nitrosyl chloride (CINO) by NO_2 uptake of the sea-salt aerosol^[48–50] is too slow to contribute significantly to gaseous Cl production. For instance, Karlsson and Ljungström^[51] estimated a total CINO production of the order of 1.1×10^7 atoms cm^{-3} in a flow reactor at aerosol concentrations of $3 \times 10^5 cm^{-3}$ (surface/volume = $2 \times 10^7 m^{-1}$) when 50 ppb NO_2 was present. Owing to a photolysis rate of $J_{CINO} = 1.8 \times 10^{-3} s^{-1}$ in our chamber, this would result in comparable Cl production, whereas the actual total production in our experiments is of the order of $10^{12}–10^{13}$ atoms cm^{-3} and thus exceeds the production caused by CINO formation by far, even if Karlsson and Ljungström^[51] assume a sea-salt surface three orders of magnitude lower. The negligible influence of NO_2 - or N_2O_5 -induced Cl activation was confirmed by a blank experiment (iron-free artificial sea salt with 20 ppb NO_2 addition), where the artificial sea-salt aerosol without Fe^{III} was irradiated in the presence of 20 ppb NO_x and the quasi-stationary Cl concentration remained below 10^4 molecules cm^{-3} combined with a slower NO_x depletion (Supplementary material, Fig. S3.2). Rather, the formation of $XONO_2$ ($X = Cl, Br$) by XO (R3.7, R3.8), or HNO_3 by OH (R3.9) and the subsequent uptake by the aerosol may explain the NO_x loss,^[12,31,52] which predominantly ending up as nitrate (with a possible back-reaction pathway to N_2O_5 or XNO_2 by HNO_3 at low pH).^[13]



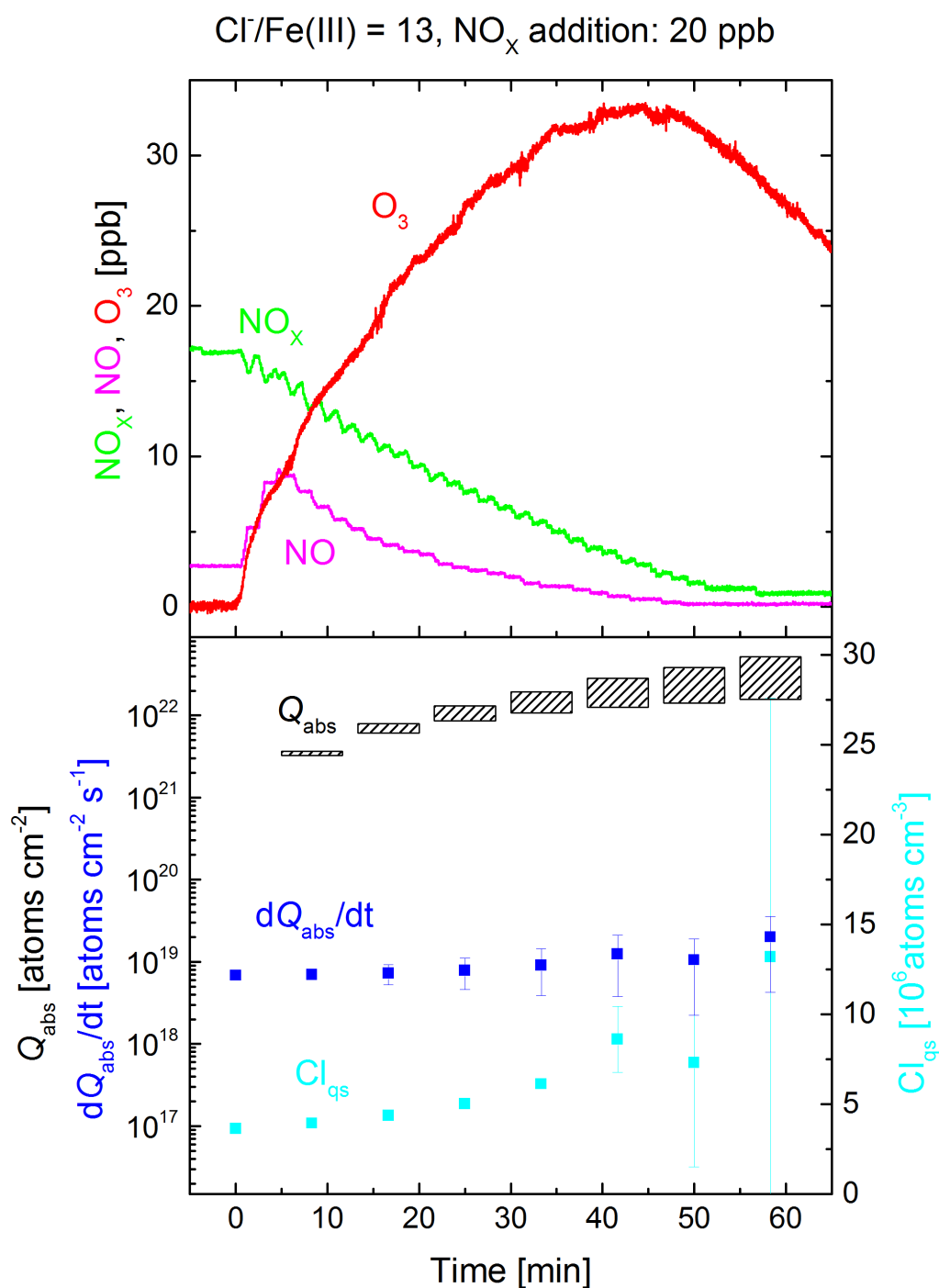
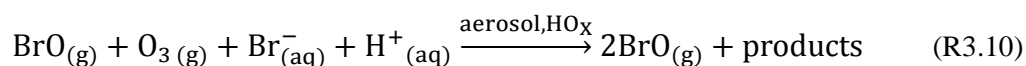


Figure 3.6: Time profiles of NO_x, NO and O₃ (upper box) and of the quasi-stationary Cl concentration (Cl_{qs}), the absolute gaseous mean Cl production rate (dQ_{abs}/dt) [atoms cm⁻² s⁻¹] and the time-integrated total minimum and maximum Cl production Q_{abs} (atoms cm⁻²) of aerosol surface (lower box) during the experiment with Fe^{III}-doped artificial seawater (Cl/Fe^{III} = 13) and 20 ppb NO_x. The light was switched on at 0 min.

The uptake of XONO₂ can result in additional X₂ or BrCl release, as e.g. summarised in the review by Rossi.^[13] The uptake of HNO₃ leads to an acidification of the aerosol and contributes to the reoxidation of Fe^{II} to Fe^{III} through photolysis and OH^{*} formation in the

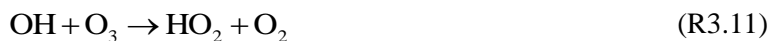
aqueous phase^[20] and thus is potentially responsible for the enhanced gaseous Cl production, according to the mechanisms described in the Introduction. Additionally, the uptake of HNO₃ leads to acid displacement with a subsequent release of HCl,^[53,54] whose reaction with OH is supposed to be a main Cl-atom source in the marine troposphere.^[55] In general, a low pH facilitates the release of HCl and other gaseous Cl precursors.^[25,31,56,57] For example, Keene and Savoie^[56] determined a gaseous HCl mixing ratio in the range of 0.1 ppb, and Keene et al.^[25] modelled HCl outgassing of 1 ppb day⁻¹ for acidified sea salt (pH 3). Transferred to our conditions with typical OH concentrations of 10⁶–10⁷ molecules cm⁻³ and a much higher LWC, this leads to gaseous Cl production rates in the range of 10⁹–10¹⁰ atoms cm⁻³ h⁻¹ and thus potentially contributes less than 10 % to the observed Cl production. This accounts also for the HCl formation caused by hydrogen abstraction during the consumption of the injected HC_i by Cl atoms. Furthermore, Zetzsch and Behnke^[58] investigated photochemical Cl production rates from 200 to 500 ppb O₃ and 300 ppb HCl in the presence of NaCl, Fe₂O₃ and SiO₂ aerosol. They concluded that the heterogeneous Cl⁻ activation exceeds the Cl source from the gas-phase reaction of OH and HCl by far.

Several effects were observed in the experiment where 630 ppb O₃ was added (Fig. 3.6). The total Cl production per hour is three to five times higher than the value obtained from the Fe^{III}-containing sample in zero air and is similar to the NO_x experiment (Table 3.2). However, the reactivity of O₃ towards Cl (~180 s⁻¹) is comparable with the total reactivity of the injected HC_i (~200 s⁻¹) and not considered in the calculation of the total production Q, as it does not represent a final sink but rather initiates a reaction cycle by HO₂ and HOCl where finally Cl₂ is produced.^[59,60] In addition, Sadanaga et al.^[27] observed enhanced O₃ uptake rates in the presence of water-soluble Fe^{III} in synthetic sea salt without irradiation. During the short dark period, O₃ depletion was hardly detectable, whereas we observed an approximately four times lower O₃ lifetime for the experiment with added Fe^{III} (~10⁴ s) compared with the pure artificial sea-salt sample (~4 × 10⁴ s). In general, the O₃ destruction is related to autocatalytic halogen activation where Br especially plays a dominant role.^[34] This difference possibly explains the much higher Cl and Br production (Fig. 3.6a, b) at the same level of quasi-stationary OH concentrations (~10⁷ molecules cm⁻³) for both experiments. Concerning Br production, the quasi-stationary Br concentration was again of the order of 10⁹ atoms cm⁻³ (close to the detection limit) and resulted in Q_{abs} values of (1–3) × 10²¹ atoms cm⁻² h⁻¹ for the iron-free and (3–8) × 10²¹ atoms cm⁻² h⁻¹ for the iron-doped sea salt. Adding O₃ to the iron-free aerosol, the significant enhancement in Cl production (~4–7 × 10¹⁹ atoms cm⁻² h⁻¹ from the iron-free sample in zero air to the iron-free sample with O₃ addition) is relatively low compared with the much stronger increase in Cl production when adding O₃ to the iron-containing sample (~2–5 × 10²⁰ atoms cm⁻² h⁻¹ from the iron-containing sample in zero air to the iron-containing sample with O₃ addition). This indicates that we observed an O₃-induced Cl and Br production that increases with addition of Fe^{III} (or decreasing aerosol pH) and contributes markedly to the enhanced iron-induced activation. Several mechanisms come into consideration for the observed effects. At these O₃ levels, a main mechanism (which is responsible for the high Cl and Br production and fast O₃ depletion) is the so-called ‘Bromine explosion’^[61] with the net reaction:



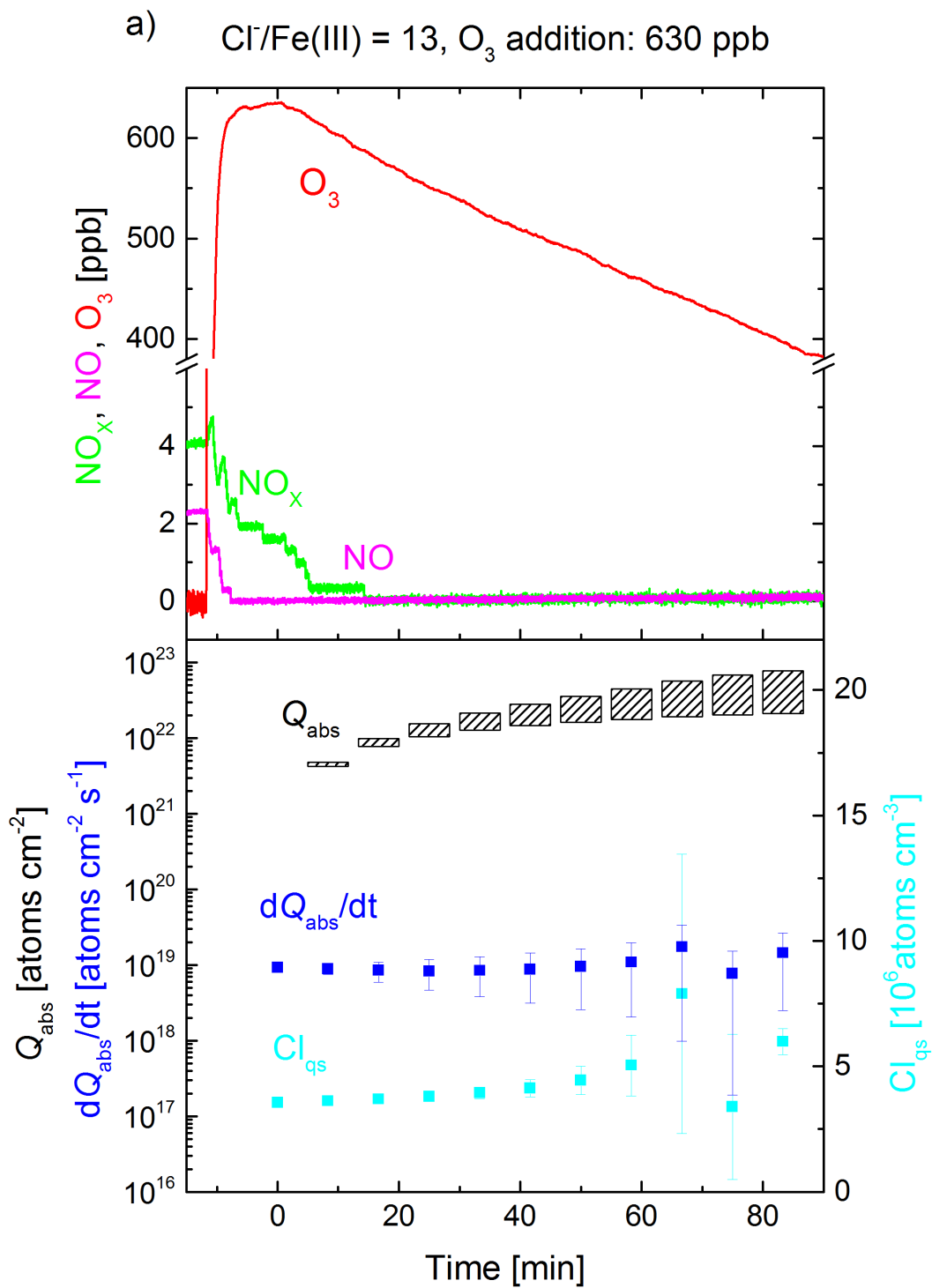
and the associated formation of OClO and ClO.^[34] However, it does not sufficiently explain the increase in production rates from $\sim 2 \times 10^{18}$ to $\sim 10^{19}$ atoms $\text{cm}^{-2} \text{s}^{-1}$ with O_3 addition when Fe^{III} is involved (Figs 3.3 and 3.6a), because the pH (when < 5) is supposed to have no large effect on the mechanism,^[25,62] and the additional Cl production rate (when estimated from the iron-free experiment) is $\sim 10^{18}$ atoms $\text{cm}^{-2} \text{s}^{-1}$ (Fig. 3.6b).

A further approach is the enhanced formation of H_2O_2 in the gas phase (R3.11, R3.12):



which enters the aqueous phase rapidly and oxidises Fe^{II} back to Fe^{III} , and is able to form HOCl^- or HOBr^- , which further dissociate and finally form Cl_2 or Br_2 .^[63]

Knipping et al.^[64] even report a direct uptake of OH and subsequent Cl_2 release from NaCl aerosols. Furthermore, NO_x (3–5 ppb is present after aerosol injection) forms NO_3 and N_2O_5 by O_3 during the dark phase, indicated by the loss of NO_x when O_3 is injected (Fig. 3.6a, b), and thus leads to HNO_3 formation in the aqueous phase with similar consequences to those described above (R3.9). NO_3 is able to efficiently produce atomic X from solid and humidified salts.^[65,66] Moreover, the uptake of N_2O_5 activates Cl^- by releasing ClNO_2 ^[47,67] (or even Cl_2 in a multistage process by ClNO_2 at acidic pH)^[68] and Br^- by releasing Br_2 or BrNO_2 ,^[69,70] which is photolysed to atomic X ($J_{\text{ClNO}_2} = 0.2 \times 10^{-3} \text{ s}^{-1}$, $J_{\text{BrNO}_2} = 3.7 \times 10^{-3} \text{ s}^{-1}$, $J_{\text{Br}_2} = 17 \times 10^{-3} \text{ s}^{-1}$). However, considering the low NO_x concentrations, the dark-phase activation mechanisms by NO_3 and N_2O_5 probably play an only minor role compared with autocatalytic light-induced activation. All given mechanisms favour the activation of bromide and could explain the high Br production rates in both O_3 experiments.



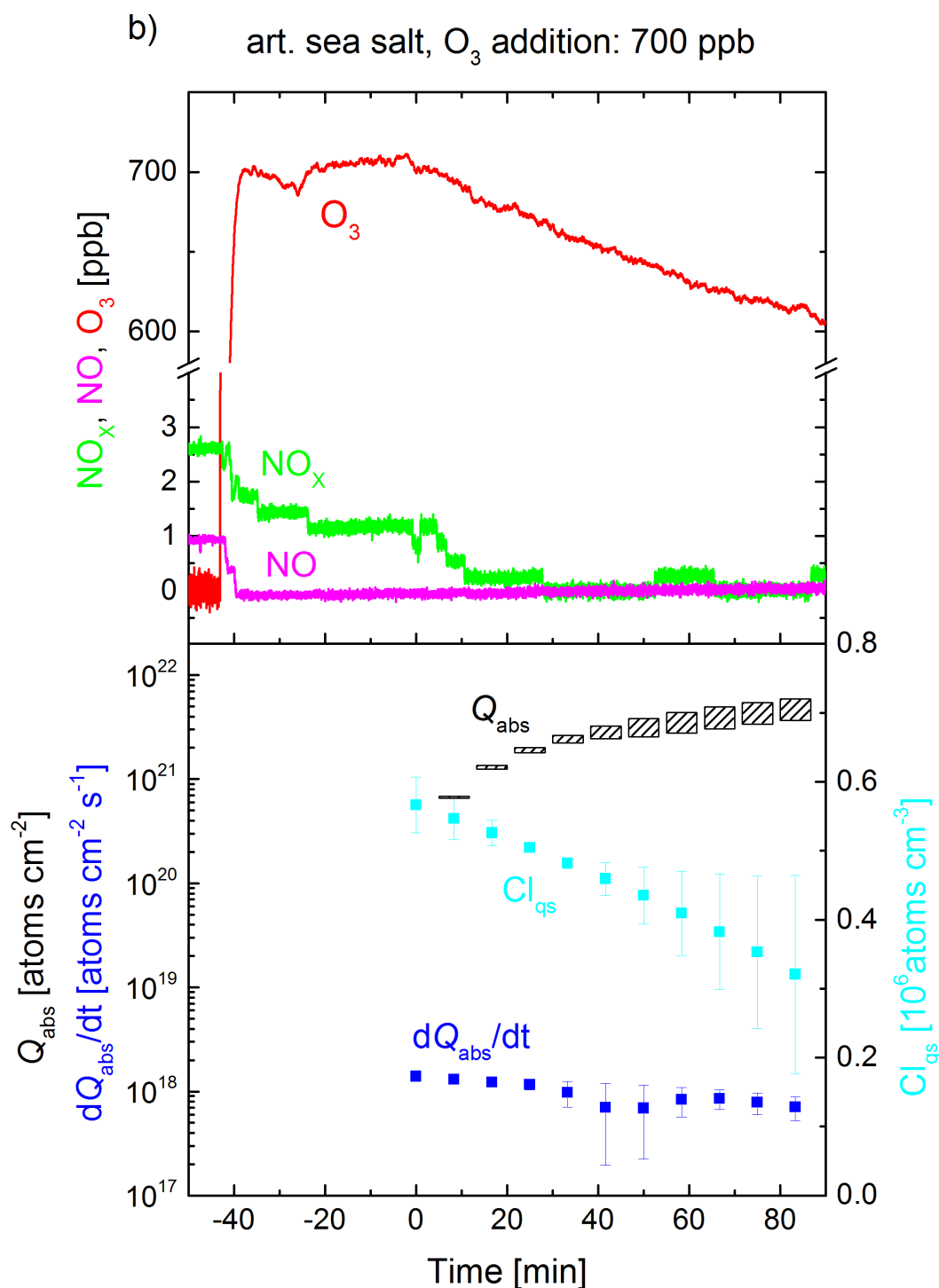


Figure 3.6a,b: Time profiles of NO_x, NO, and O₃ (upper box) and of the quasi-stationary Cl concentrations (Cl_{qs}), the absolute gaseous mean Cl production rate (dQ_{abs}/dt) [atoms cm⁻² s⁻¹] and of the time-integrated total minimum and maximum Cl production Q_{abs} [atoms cm⁻²] of aerosol surface (lower box) during the experiment with (a) Fe^{III}-doped artificial seawater (Cl⁻/Fe^{III} = 13) and 630 ppb O₃; and (b) a corresponding blank experiment with Fe^{III}-free artificial seawater and 700 ppb O₃. The light was switched on at 0 min.

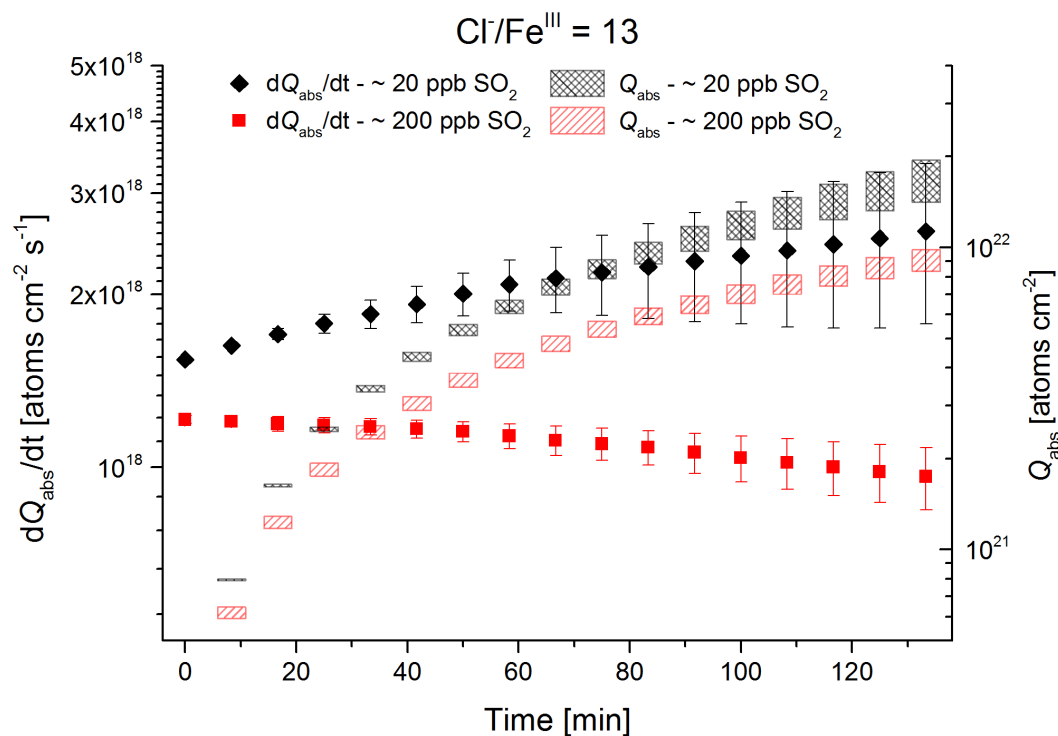


Figure 3.7: Absolute gaseous mean Cl production rate (dQ_{abs}/dt) [$\text{atoms cm}^{-2} \text{s}^{-1}$] and time-integrated total minimum and maximum Cl production Q_{abs} [atoms cm^{-2}] of aerosol surface during experiments with Fe^{III} -doped artificial seawater ($\text{Cl}^-/\text{Fe}^{\text{III}} = 13$) and different SO_2 mixing ratios in the chamber (~ 20 ppb, red; ~ 200 ppb, black). The light was switched on at 0 min.

In contrast to the reinforcing effects of NO_x and O_3 , the situation changes with SO_2 . Two experiments were conducted with SO_2 concentrations of ~ 20 and ~ 200 ppb and a waiting period of 45 min before turning the solar simulator on. Similarly to the effect of sulfate in a salt pan,^[15] SO_2 inhibited Cl production, because slightly lower dQ_{abs}/dt and Q_{abs} were observed (Fig. 3.7). Several studies have already examined the role and the uptake of SO_2 in combination with Fe^{III} and Fe^{II} for seawater. For example, Hoppel et al.^[28] report an uptake of $0.21\text{--}1.2 \text{ mmol L}^{-1}$ of nebulised seawater, which is in a similar range to the sulfate concentration of 1 mmol L^{-1} in the artificial seawater stock solution (which is nebulised in our case). However, we used a 29-times diluted stock solution to obtain size distributions with a maximum diameter of 400–450 nm. Additionally, the dissolution of SO_2 depends on further dissociation reactions in the aqueous phase that depend on pH, temperature and ion content.^[71] Therefore, the uptake rate of Hoppel et al. is only transferable with caution, but considering the less-concentrated stock solution, it should only be a small amount of SO_2 that dissolves in the aqueous phase of the aerosol, mainly in the form of bisulfite (HSO_3^-) given the pH range (2–6) of our samples. Especially at a low pH, where a high portion of dissolved Fe^{3+} is available, the oxidation of sulfite to sulfate is catalysed by Fe^{3+} .^[29] Moreover, a significant oxidation path is the reaction of sulfite with HOCl and HOBr , both of which can intervene in the autocatalytic halogen release.^[72,73] Although sulfate can strongly inhibit halogen activation, the effect of the freshly dissolved and oxidised SO_2 is probably very low with respect to the amount of sulfur that is already present in the artificial sea salt (section 3.2.2). A further influence of SO_2 is observed, concerning the quasi-stationary OH concentrations that are close to the detection limit of $10^6 \text{ molecules cm}^{-3}$ for both experiments, due to the oxidation of

SO₂ in the gas phase (SO₂ + OH → HOSO₂; $k = 1.3 \times 10^{-12} \text{ cm}^3 \text{ molecules}^{-1} \text{ s}^{-1}$),^[74] which competes with Cl production by HCl + OH ($k = 7.8 \times 10^{-13} \text{ cm}^3 \text{ molecules}^{-1} \text{ s}^{-1}$).^[75] Therefore, slightly lower Cl production is observed for the SO₂ experiments. In the extreme case of 200 ppb, Cl production decreases to ~70 % of that from the SO₂-free experiment.

3.3.4 Effect of pH and Fe^{III} Speciation Chemistry

To estimate the effect of the aerosol pH on Cl production, the pH of the diluted stock solution (Cl⁻/Fe^{III} = 101) was adjusted to pH 2.1–2.3 by gently adding 32 % HCl. The results demonstrate the immense effect of the pH (Fig. 3.2). The higher absolute production rate during the low-pH experiment led to eight times higher total Cl production per hour compared with the unadjusted sample (pH 3.9–4.2, Fig. 3.4; see also Table 3.2). There are multiple reasons for this effect. As evaluated in several studies for Fe^{III}-doped salts, the speciation chemistry of Fe^{III} strongly depends on the pH and ionic strength.^[15,24,76] Fig. 3.8a, b show the portions of the total Fe^{III} as Fe^{III} complexes as a function of the pH, calculated with an equilibrium model in PHREEQC.^[77] According to Wittmer et al., the model is based on the MINTEQ database,^[78] and the activity coefficients are corrected by the Pitzer ion interaction approach^[79] with the parameters listed in Tosca et al.^[80] The main equilibrium constants involving Fe^{III} are listed in the Supplementary material (Table S3.3). For some ions (e.g. F⁻), there are no Pitzer parameters available and the extended Debye–Hueckel equation^[81,82] was applied to calculate the respective activity coefficients. To get an insight into the processes during nebulisation and evaporation, the speciation was calculated for the diluted stock solution (Fig. 3.8a), which the nebuliser was filled with, as well as for the final aerosol (Fig. 3.8b), assuming a saturation in Cl⁻ (6.1 mol L⁻¹) and unchanged molar ratios towards the other constituents. This assumption is extremely simplified based on the complexity of a multicomponent salt system,^[45] and implies a similar hydration and solubility behaviour of NaCl and artificial sea salt but accounts for the fact that Na⁺ and Cl⁻ represent by far the main ions. For example, McCaffrey et al.^[83] measured similar Cl⁻ saturation concentrations in evaporating seawater whereas the concentration may change with increasing Fe^{III} content.

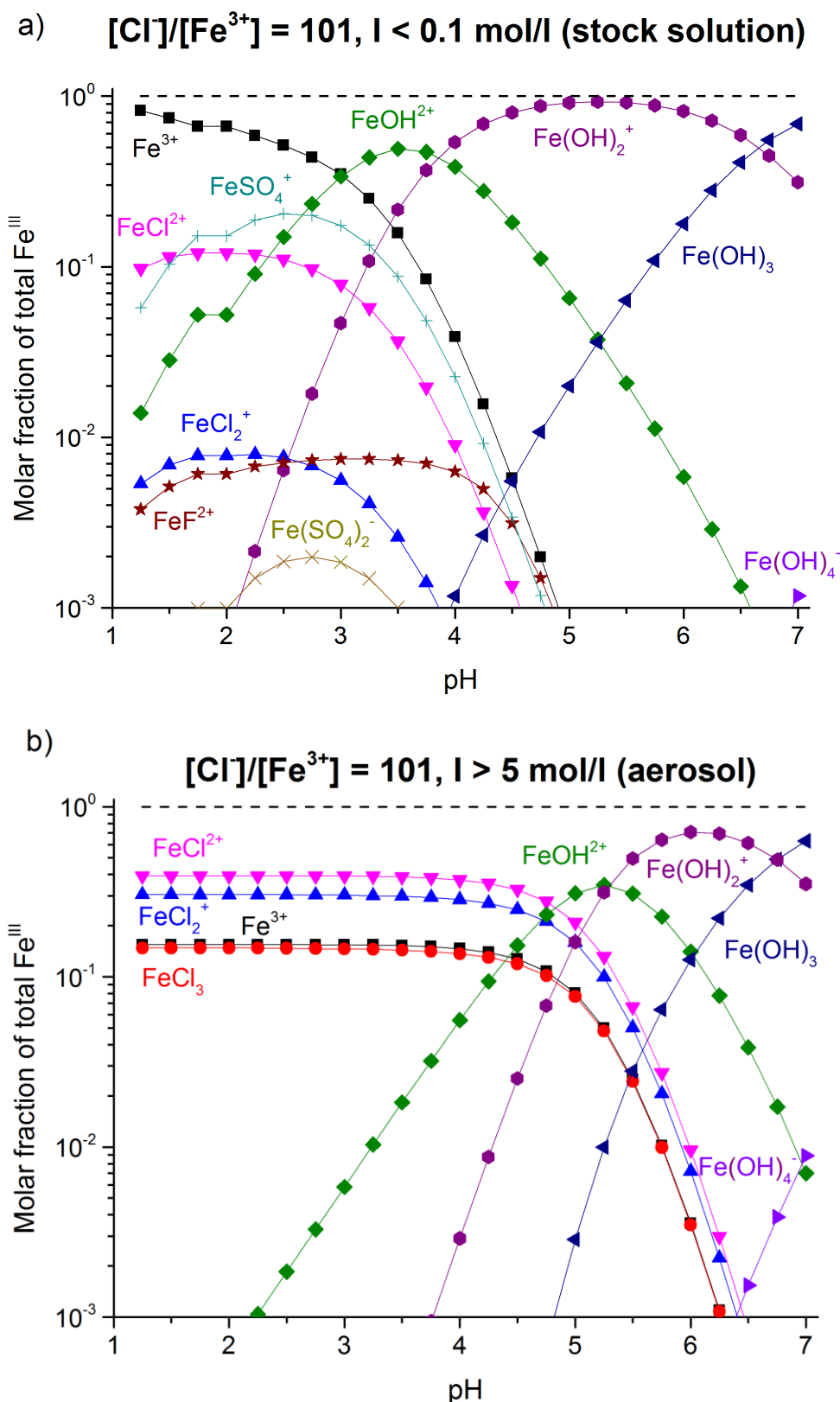


Figure 3.8a,b: Molar fraction of the formed Fe^{III} species relative to the total Fe^{III} content in Fe^{III} -doped artificial seawater ($\text{Cl}^-/\text{Fe}^{\text{III}} = 101$) as a function of pH (according to the PHREEQC model) of the low-concentration diluted stock solution before nebulising (a); and of the final, highly concentrated aqueous phase of the aerosol (b). The dashed line indicates a molar fraction of 1 (100 %).

Whereas high fractions of Fe^{3+} ions and Fe^{III} -hydroxy complexes are present in the stock solution, the decisive photosensitive Fe^{III} -Cl complexes start to form as a considerable fraction at pH 1–4.5 with increasing ionic strength (solvent concentrations). The pH of 4.5 is a turning point for the aerosol speciation, where mainly Fe^{III} -hydroxy complexes are present. Because Fe^{III} -Cl complexes comprise a fraction of less than 5 % in the stock solution at the given pH of 3.9–4.2 (and it takes some time until speciation equilibrium is reached during the transition from the low-concentration stock solution to the high-concentration liquid aerosol), the smaller amount of Fe^{III} -Cl complexes could explain the lower gaseous Cl production for the untreated sample. This situation changes when the pH is adjusted to 1.9–2.2 already in the diluted stock solution. At such low pH values, Fe^{III} -Cl complexes are formed much more easily. Furthermore, the solubility of Fe^{III} increases with decreasing pH, whereas more dissolved Fe^{III} becomes available on an absolute scale.^[46,84] Also, the formation of the highly soluble hypochlorous acid (HOCl ; Henry's law constant at 298 K: $2.6\text{--}9.3 \times 10^2 \text{ M atm}^{-1}$)^[85] predominates at a pH between 4 and 7 over Cl_2 , which is favoured at a pH lower than 4 and is much more easily released into the gas phase (Henry's law constant: $6.2\text{--}9.1 \times 10^{-2} \text{ M atm}^{-1}$).^[85] Similar observations were also made by Lim et al.,^[24] who ascribed the decreasing Cl_2 source with decreasing pH to the speciation chemistry and solubility of the various chlorine species.

3.3.5 SEM-EDX Results

Aerosol particles originating from the pure artificial sea water are mainly composed of NaCl , CaSO_4 , MgCl_2 and KCl (Fig. 3.9a). Whereas NaCl and CaSO_4 particles remain as single crystals, KCl and MgCl_2 exhibit some phase-mixing and a more amorphous structure. In the case of the FeCl_3 -containing artificial seawater, single NaCl and CaSO_4 crystals are also visible. Additionally, FeCl_3 is visible in the KCl – MgCl_2 phase (Fig. 3.9b). FeCl_3 appears to cover nearly all other particles like NaCl and CaSO_4 , thus indicating that all aerosol particles originating from the FeCl_3 -enriched artificial seawater are covered by an active Fe^{III} chloride-salt layer.

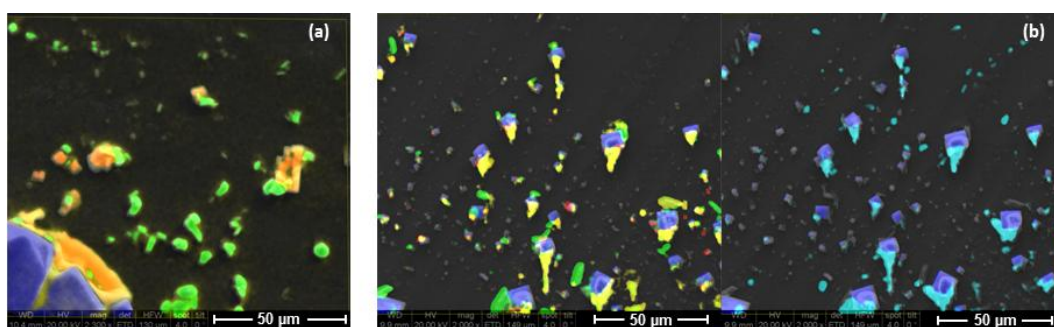


Figure 3.9a,b: Scanning electron microscope–energy dispersive X-ray (SEM-EDX) images of the aerosol particles of the pure sea-water (a), and FeCl_3 -containing sea-water (b) with NaCl (blue), CaSO_4 (green), MgCl_2 (yellow), KCl (red) and FeCl_3 (turquoise).

3.3.6 Fraction of Active Iron

Multiplying the initial LWC_0 (in $\text{dm}^3 \text{cm}^{-3}$) with the assumed saturation concentration of Cl^- (6.1 mol L^{-1}) in the aerosols produced and with Avogadro's constant ($N_A = 6 \times 10^{23} \text{ mol}^{-1}$) and dividing the molar $\text{Cl}^-/\text{Fe}^{\text{III}}$ ratio ($R_{\text{Cl/Fe}}$) in the stock solution yields the concentration of Fe^{III} in the chamber. The ratio of the minimum concentration of Cl atoms produced in the first hour of the experiments (Q_{min}) provides an estimation of the minimum fraction of active iron λ_{Fe} involved in Cl production:

$$\lambda_{\text{Fe}} = \frac{Q_{\text{min}} \times R_{\text{Cl/Fe}}}{LWC_0 \times 6.1 \times N_A} \quad (3.4)$$

assuming that each Fe^{III} produces $1/2\text{Cl}_2$ by excluding recycling effects and secondary activation mechanisms. The contribution of the tare volume of the ions to the measured LWC is $0.11 \times 10^{-9} \text{ m}^3 \text{m}^{-3}$ (considered in the calculation), whereas the influence of Fe^{3+} ions is negligible. Owing to the major assumption and unknown uncertainties ($R_{\text{Cl/Fe}}$ in the aerosol can differ from the bulk, or the concentration of Cl^- can vary depending on the composition and thus deliquescence of the aerosol), λ_{Fe} represents a rather qualitative value for relative comparisons between the experiments. Fig. 3.10 shows the results for all Fe^{III} -containing samples investigated, combined with the measured total minimum and maximum Cl production Q_{abs} during the first hour. Additionally, the corresponding initial minimum production rates are displayed in the Supplementary material (Fig. S3.3). Again, the increase in Q_{abs} for the artificial seawater samples with increasing Fe^{III} concentration ($\text{Cl}^-/\text{Fe}^{\text{III}} = 13, 53, 101$) is highlighted, although, λ_{Fe} is comparable, which indicates that similar Cl activation mechanisms are going on. This is also the case for the pure $\text{NaCl} + \text{Fe}^{\text{III}}$ sample where Q_{abs} and λ_{Fe} are higher, caused by the absence of competing ligands for Fe^{III} and thus a higher fraction of photolabile Fe^{III} -Cl complexes.

The presence of 20 ppb NO_x in the gas phase led to a considerable increase by a factor of 3–7 for Q_{abs} from the $\text{Cl}^-/\text{Fe}^{\text{III}} = 101$ and the $\text{Cl}^-/\text{Fe}^{\text{III}} = 13$ samples. The parallel increase of λ_{Fe} (even more than 100 %) is an artefact that actually represents the additional Cl activation mechanisms induced by NO_x ,^[13] as discussed in the section 3.3.3. The same applies for the experiment with 630 ppb O_3 . Decreasing the pH enhanced the activity of Fe^{III} , and more than 100 % of Fe^{III} seemed to be involved, which either is a consequence of recycling effects (reoxidation of Fe^{II} that was formed by photolysis of Fe^{III} complexes), or is caused by the uncertainty of λ_{Fe} . For the low-pH sample as well as for the untreated samples ($\text{Cl}^-/\text{Fe}^{\text{III}} = 13$ and 101), an increase in Q_{abs} and λ_{Fe} was observed with the addition of 20 ppb NO_x , which clearly demonstrates the NO_x -induced activation of chloride. The effect is not as pronounced at low aerosol pH.

SO_2 was able to slightly inhibit Cl production. In particular, high SO_2 mixing ratios decreased the Q_{abs} and thus the fraction of active iron. One can compare λ_{Fe} with the salt-pan measurements, where a proportion of 0.05–0.07 % of active Fe^{III} was determined.^[15] Considering a salt pan containing 0.5 g $\text{FeCl}_3 \cdot 6 \text{H}_2\text{O}$ and 99.5 g NaCl results in a total molar Fe^{III} content of 1.8×10^{-3} . This is quite high compared with the aerosol experiments with only $\sim 3 \times 10^{-6} \text{ mol Fe}^{\text{III}}$ at an LWC of $\sim 2.7 \times 10^{-9}$ but total Cl sources comparable with the salt-pan experiments. These large differences prove the small active

surface area of the salt pans compared with the homogeneously distributed and irradiated aerosol in the chamber.

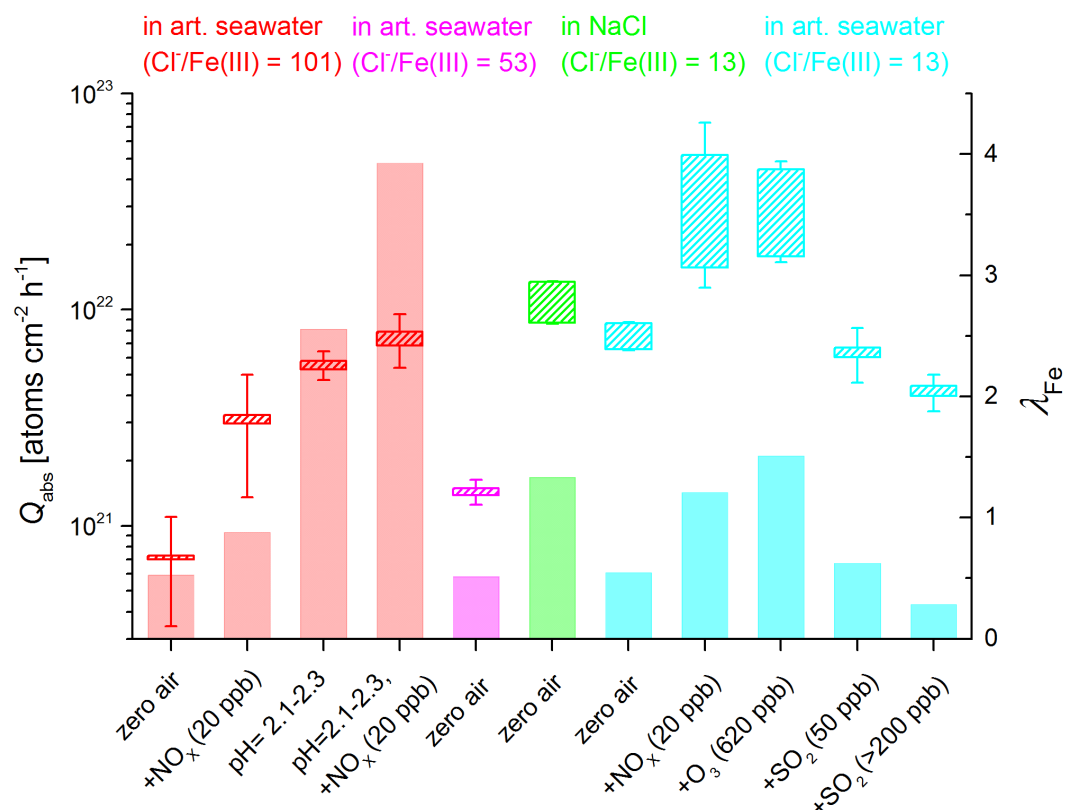


Figure 3.10: Overview of the minimum and maximum absolute Cl production Q_{abs} [atoms $\text{cm}^{-2} \text{h}^{-1}$] over the first hour and the corresponding fraction of active Fe^{III} (λ_{Fe}) for each experiment with Fe^{III} -containing samples and various air contaminants (NO_x , O_3 , SO_2).

3.3.7 Environmental Significance

The ratio of the concentrations of added pollutants and the generated aerosol concentrations ($2\text{--}6 \text{ mg m}^{-3}$) are approximately in agreement with the conditions for sea-salt aerosol over the ocean. Although the smog chamber helps to understand the mechanisms, it is difficult to transfer the results to large-scale atmospheric processes because the aerosol surface-to-volume ratio in the smog chamber is some orders of magnitude higher than in the atmosphere.

We investigated a very simplified system with no organic contaminants in the salt and under hydrocarbon-free conditions. Note that Fe complexes with oxygen-containing organics (such as phenolic compounds) can significantly increase the solubility of iron in seawater.^[86] However, complexation can strongly inhibit iron-induced chlorine activation,^[15] until the phenolic constituents are oxidised by OH^\cdot and Cl^\cdot from the photo-Fenton mechanism to the less-inhibiting but solubility-promoting oxalate. The soluble fraction of iron over the ocean ranges from 0 to 95 % as the bulk marine aerosol type reflects a mixing of multiple aerosol types, and solubility varies with the origin of the iron, aerosol size and composition.^[87–89] Moreover, the solubility increases owing to the

photoreduction of Fe^{III}, which is responsible for an Fe^{II} fraction in the aerosol of up to 50 % in remote marine areas.^[90] An additional crucial factor for the role of Fe^{III} photochemistry is the aerosol pH, which varies from 1–9, mainly depending on the origin and age of the aerosol and the corresponding altering processes.^[25,56]

Accounting for these effects in order to quantify iron-induced Cl production in the troposphere, a sophisticated large-scale model would be required. Based on a mean molar Cl⁻/Fe ratio of 100–200 in the marine aerosol (central Atlantic),^[91] on the lower fraction of dissolved Fe^{III} in the aerosol that can form photolabile complexes, and on the 20–200-times larger aerosol surface area in the chamber compared with the Atlantic aerosol,^[92] the mean natural contribution of Fe^{III}-induced Cl activation cannot compete with alternative mechanisms on a global scale (also indicated by Cl below the detection limit in our experiment with Cl⁻/Fe^{III} = 997). However, it may become important on a local scale with a larger Fe^{III} burden exposed to saline media, e.g. ship plumes or other iron-containing combustion aerosols^[93] or where soil dust comes into contact with sea salt, but also in brine-containing soils^[94] or salt lakes such as the Dead Sea or Australian salt lakes.^[14]

Furthermore, iron-doped sea-salt aerosols have been proposed as a method for climate engineering, aiming to enhance CH₄ depletion with higher Cl levels in the marine boundary layer and to simultaneously fertilise the oceans.^[95] Based on our results, one may try to estimate the feasibility of such a project. For our conditions, increasing the mean molar Cl⁻/Fe^{III} ratio to, say, 50 by adding Fe^{III} would have significant effects on Cl production and thus reduce the lifetime of CH₄. Transferred to the global production rate of sea salt Cl⁻ of 1785 Tg year⁻¹,^[96] an annual contribution of 56 Tg year⁻¹ of pure Fe^{III} (that dissolves totally in the sea-salt aerosol) would be needed. In addition, the effect of enhanced Cl production has to be scaled down by the much lower typical aerosol surface in the marine boundary layer (~60–200 μm² cm⁻³ ^[91]) compared with our experiments (~10 000–30 000 μm² cm⁻³). Thus, an increase of Cl surface production by a factor of 4 in the chamber (which is the case for Cl⁻/Fe^{III} = 51 compared with the blank) would result in an increase of ~2.5 % transferred to the marine boundary layer, neglecting any effect of dissolved organics or gas-phase species. A mixture with Cl⁻/Fe^{III} = 13 would need 220 Tg year⁻¹ of Fe^{III} and result in ~17–19 % increase in Cl production. Note that the increase of atomic Cl does not directly correlate with a reduction of the CH₄ lifetime owing to the flat vertical profile of CH₄ (almost evenly distributed over the total troposphere)^[91] compared with the Cl-producing sea salt (confined to <1 km above the oceans, the marine sea-salt layer)^[91] and thus more inefficient depletion, apart from technical challenges and other potential implications for the ecosystem.

3.4 Conclusions

In the present work, we confirmed and quantified Cl formation processes induced by the photochemistry of Fe^{III} dissolved in the liquid aerosol phase. We found that depending on the Fe^{III} loading in the artificial sea-salt aerosol, an enormous amount of chlorine can be activated. The initial production rates varied from ~1.9 × 10¹⁸ atoms cm⁻² s⁻¹ (Cl⁻/Fe^{III} = 13) to ~2.8 × 10¹⁷ atoms cm⁻² s⁻¹ (Cl⁻/Fe^{III} = 101), whereas no significantly enhanced Cl production was detected for Cl⁻/Fe^{III} = 955 compared with the Fe^{III}-free salt. The

differences can mainly be explained by the amount of Fe^{III} and the corresponding speciation of Fe^{III} complexes that depend on the pH.

The presence of 20 ppb NO_x or 630 ppb O_3 considerably increased the initial Cl production rate to $\sim 7 \times 10^{18}$ atoms $\text{cm}^{-2} \text{s}^{-1}$ ($\text{Cl}^-/\text{Fe}^{\text{III}} = 13$) and $\sim 9 \times 10^{18}$ atoms $\text{cm}^{-2} \text{s}^{-1}$ ($\text{Cl}^-/\text{Fe}^{\text{III}} = 13$) respectively (as compared with the blank value of 2×10^{18} atoms $\text{cm}^{-2} \text{s}^{-1}$), owing to the well-known halogen activation processes and potential pH effects. Gas-phase SO_2 instead slightly inhibited Cl production to ~ 1.7 and $\sim 1.1 \times 10^{18}$ atoms $\text{cm}^{-2} \text{s}^{-1}$, by adding ~ 20 ppb and >200 ppb SO_2 respectively. The strong effect of the aerosol pH on Fe^{III} speciation and subsequent Cl formation was demonstrated by comparing two samples with an equal $\text{Cl}^-/\text{Fe}^{\text{III}}$ ratio of 101 but a pH adjusted to 2.1–2.3 and 3.9–4.2. Here, the production rate increased by almost an order of magnitude for the more acidic pH. An approach to calculate the active fraction of Fe^{III} involved in Cl production confirms a higher λ_{Fe} with lower pH, highlights recycling effects and identifies additional activation mechanisms where NO_x and O_3 are involved. In natural environments, these processes may occur in natural salty media at high dissolved Fe^{III} concentrations and locally contribute to photochemical Cl formation.

3.5 Associated Content

The supplementary material (available on the journal's website at http://www.publish.csiro.au/?act=view_file&file_id=EN14279_AC.pdf) includes more details on the artificial seawater composition (Table S1), the rate constants of the applied HCs towards the radicals (Table S3.2), the main equilibrium constants for important Fe^{III} complexes, the contour plots of selected experiments (Fig. S3.1), the NO_x , NO, and O_3 time profiles for the Fe^{III} -free experiment with 20 ppb NO_2 addition (Fig. S3.2) and an overview of the initial minimum absolute Cl production rate (Fig. S3.3).

3.6 Acknowledgements

We thank Franz D. Oeste, gM-Ingenieurbüro Kirchhain, Germany, for advice, Agnes Bednorz and Andrej Einhorn for technical support and Elisabeth Eitenberger and Gernot Friedbacher (Vienna University of Technology) for operating the electron microscope. This work was supported by the Deutsche Forschungsgemeinschaft (DFG) within research unit 763 (HALOPROC) and by Ries Consulting GmbH&Co Betriebs KG, Hosenfeld.

3.7 References

- [1] I. Y. Fung, S. K. Meyn, I. Tegen, S. C. Doney, J. G. John, Bishop, James K. B., Iron supply and demand in the upper ocean. *Global Biogeochem. Cycles* **2000**, *14*, 281. doi:10.1029/1999GB900059
- [2] M. S. Johnson, N. Meskhidze, Atmospheric dissolved iron deposition to the global oceans: effects of oxalate-promoted Fe dissolution, photochemical redox cycling, and dust mineralogy. *Geosci. Model Dev.* **2013**, *6*, 1137. doi:10.5194/gmd-6-1137-2013
- [3] A. Martínez-García, D. M. Sigman, H. Ren, R. F. Anderson, M. Straub, D. A. Hodell, S. L. Jaccard, T. I. Eglinton, G. H. Haug, Iron fertilization of the subantarctic ocean during the last ice age. *Science* **2014**, *343*, 1347. doi:10.1126/science.1246848
- [4] A. Martínez-García, A. Rosell-Melé, S. L. Jaccard, W. Geibert, D. M. Sigman, G. H. Haug, Southern Ocean dust-climate coupling over the past four million years. *Nature* **2011**, *476*, 312. doi:10.1038/nature10310
- [5] J. H. Martin, S. E. Fitzwater, R. M. Gordon, Iron deficiency limits phytoplankton growth in Antarctic waters. *Global Biogeochem. Cycles* **1990**, *4*, 5. doi:10.1029/GB004i001p00005
- [6] S. Blain, B. Quéguiner, L. Armand, S. Belviso, B. Bombled, L. Bopp, A. Bowie, C. Brunet, C. Brussaard, F. Carlotti, U. Christaki, A. Corbière, I. Durand, F. Ebersbach, J.-L. Fuda, N. Garcia, L. Gerringa, B. Griffiths, C. Guigue, C. Guillerm, S. Jacquet, C. Jeandel, P. Laan, D. Lefèvre, C. Lo Monaco, A. Malits, J. Mosseri, I. Obernosterer, Y.-H. Park, M. Picheral, P. Pondaven, T. Remenyi, V. Sandroni, G. Sarthou, N. Savoye, L. Scouarnec, M. Souhaut, D. Thuiller, K. Timmermans, T. Trull, J. Uitz, P. van Beek, M. Veldhuis, D. Vincent, E. Viollier, L. Vong, T. Wagener, Effect of natural iron fertilization on carbon sequestration in the Southern Ocean. *Nature* **2007**, *446*, 1070. doi:10.1038/nature05700
- [7] R. T. Pollard, I. Salter, R. J. Sanders, M. I. Lucas, C. M. Moore, R. A. Mills, P. J. Statham, J. T. Allen, A. R. Baker, Bakker, Dorothee C. E., M. A. Charette, S. Fielding, G. R. Fones, M. French, A. E. Hickman, R. J. Holland, J. A. Hughes, T. D. Jickells, R. S. Lampitt, P. J. Morris, F. H. Nedelec, M. Nielsdottir, H. Planquette, E. E. Popova, A. J. Poulton, J. F. Read, S. Seeyave, T. Smith, M. Stinchcombe, S. Taylor, S. Thomalla, H. J. Venables, R. Williamson, M. V. Zubkov, Southern Ocean deep-water carbon export enhanced by natural iron fertilization. *Nature* **2009**, *457*, 577. doi:10.1038/nature07716
- [8] R. von Glasow, P. J. Crutzen, Tropospheric halogen chemistry. *Treatise on Geochemistry*, **2003**, Vol. 4, pp 1–67 (Elsevier-Pergamon: Oxford, UK).
- [9] U. Platt, G. Hönninger, The role of halogen species in the troposphere. *Chemosphere* **2003**, *52*, 325. doi:10.1016/S0045-6535(03)00216-9
- [10] J. Ofner, N. Balzer, J. Buxmann, H. Grothe, P. Schmitt-Kopplin, U. Platt, C. Zetzsch, Halogenation processes of secondary organic aerosol and implications on halogen release mechanisms. *Atmos. Chem. Phys.* **2012**, *12*, 5787. doi:10.5194/acp-12-5787-2012
- [11] R. von Glasow, Atmospheric chemistry: Wider role for airborne chlorine. *Nature* **2010**, *464*, 168. doi:10.1038/464168a

- [12] B. J. Finlayson-Pitts, The tropospheric chemistry of sea salt: A molecular-level view of the chemistry of NaCl and NaBr. *Chem. Rev.* **2003**, *103*, 4801. doi:10.1021/cr020653t
- [13] M. J. Rossi, Heterogeneous reactions on salts. *Chem. Rev.* **2003**, *103*, 4823. doi:10.1021/cr020507n
- [14] T. Krause, C. Tubbesing, K. Benzing, H. F. Schöler, Model reactions and natural occurrence of furans from hypersaline environments. *Biogeosciences* **2014**, *11*, 2871. . doi:10.5194/bg-11-2871-2014
- [15] J. Wittmer, S. Bleicher, C. Zetzsch, Iron(III)-induced activation of chloride and bromide from modeled salt pans. *J. Phys. Chem. A* **2014**, *119*, 4373. [published online early 22 September 2014], doi:10.1021/jp508006s.
- [16] H. Fu, D. M. Cwiertny, G. R. Carmichael, M. M. Scherer, V. H. Grassian, Photoreductive dissolution of Fe-containing mineral dust particles in acidic media. *J. Geophys. Res.* **2010**, *115*, D11304. doi:10.1029/2009JD012702..
- [17] X. Zhu, J. M. Prospero, D. L. Savoie, F. J. Millero, R. G. Zika, E. S. Saltzman, Photoreduction of iron(III) in marine mineral aerosol solutions. *J. Geophys. Res.* **1993**, *98*, 9039. doi:10.1029/93JD00202
- [18] W. L. Miller, D. King, J. Lin, D. R. Kester, Photochemical redox cycling of iron in coastal seawater. *Marine Chem.* **1995**, *50*, 63. doi:10.1016/0304-4203(95)00027-O
- [19] R. L. Siefert, S. O. Pehkonen, Y. Erel, M. R. Hoffmann, Iron photochemistry of aqueous suspensions of ambient aerosol with added organic acids. *Geochim. Cosmochim. Ac.* **1994**, *58*, 3271. doi:10.1016/0016-7037(94)90055-8
- [20] D. Vione, V. Maurino, C. Minero, E. Pelizzetti, Harrison, Mark A J, R.-I. Olariu, C. Arsene, Photochemical reactions in the tropospheric aqueous phase and on particulate matter. *Chem. Soc. Rev.* **2006**, *35*, 441.
- [21] V. A. Nadtochenko, J. Kiwi, Photolysis of FeOH^{2+} and FeCl^{2+} in aqueous solution. photodissociation kinetics and quantum yields. *Inorg. Chem.* **1998**, *37*, 5233. doi:10.1021/ic9804723
- [22] A. Machulek, Moraes, José Ermírio F, L. T. Okano, C. A. Silvério, F. H. Quina, Photolysis of ferric ions in the presence of sulfate or chloride ions: implications for the photo-Fenton process. *Photochem. Photobiol. Sci.* **2009**, *8*, 985. doi:10.1039/b900553f
- [23] D. Whitney King, R. A. Aldrich, S. E. Charnecki, Photochemical redox cycling of iron in NaCl solutions. *Marine Chem.* **1993**, *44*, 105. doi:10.1016/0304-4203(93)90196-U
- [24] M. Lim, K. Chiang, R. Amal, Photochemical synthesis of chlorine gas from iron(III) and chloride solution. *J. Photoch. Photobio. A: Chemistry* **2006**, *183*, 126. doi:10.1016/j.jphotochem.2006.03.005
- [25] W. C. Keene, R. Sander, A. A. Pszenny, R. Vogt, P. J. Crutzen, J. N. Galloway, Aerosol pH in the marine boundary layer. *J. Aerosol Sci.* **1998**, *29*, 339. doi:10.1016/S0021-8502(97)10011-8
- [26] J. de Laat, T. G. Le, Kinetics and Modeling of the $\text{Fe}^{\text{III}}/\text{H}_2\text{O}_2$ System in the Presence of Sulfate in Acidic Aqueous Solutions. *Environ. Sci. Technol.* **2005**, *39*, 1811. doi:10.1021/es0493648
- [27] Y. Sadanaga, J. Hirokawa, H. Akimoto, Formation of molecular chlorine in dark condition: Heterogeneous reaction of ozone with sea salt in the presence of ferric ion. *Geophys. Res. Lett.* **2001**, *28*, 4433. doi:10.1029/2001GL013722

- [28] W. Hoppel, L. Pasternack, P. Caffrey, G. Frick, J. Fitzgerald, D. Hegg, S. Gao, J. Ambrusko, T. Albrecht, Sulfur dioxide uptake and oxidation in sea-salt aerosol. *J. Geophys. Res.* **2001**, *106*, 27575. doi:10.1029/2000JD900843
- [29] M. Novič, I. Grgić, M. Poje, V. Hudnik, Iron-catalyzed oxidation of S^{IV} species by oxygen in aqueous solution: Influence of pH on the redox cycling of iron. *Atmos. Environ.* **1996**, *30*, 4191. doi:10.1016/1352-2310(96)00137-9
- [30] J.-Z. Zhang, F. J. Millero, The rate of sulfite oxidation in seawater. *Geochim. Cosmochim. Ac.* **1991**, *55*, 677. doi:10.1016/0016-7037(91)90333-Z
- [31] S. Bleicher, J. C. Buxmann, R. Sander, T. P. Riedel, J. A. Thornton, U. Platt, C. Zetzsch, The influence of nitrogen oxides on the activation of bromide and chloride in salt aerosol. *Atmos. Chem. Phys. Discuss.* **2014**, *14*, 10135. doi:10.5194/acpd-14-10135-2014
- [32] W. Behnke, C. Zetzsch, Heterogeneous photochemical formation of Cl atoms from NaCl aerosol, NO_x and ozone. *J. Aerosol Sci.* **1990**, *21*, S229. doi:10.1016/0021-8502(90)90226-N
- [33] M. Brigante, M. Minella, G. Mailhot, V. Maurino, C. Minero, D. Vione, Formation and reactivity of the dichloride radical in surface waters: A modelling approach. *Chemosphere* **2014**, *95*, 464. doi:10.1016/j.chemosphere.2013.09.098
- [34] J. Buxmann, N. Balzer, S. Bleicher, U. Platt, C. Zetzsch, Observations of bromine explosions in smog chamber experiments above a model salt pan. *Int. J. Chem. Kinet.* **2012**, *44*, 312. doi:10.1002/kin.20714
- [35] W. Behnke, W. Holländer, W. Koch, F. Nolting, C. Zetzsch, A smog chamber for studies of the photochemical degradation of chemicals in the presence of aerosols. *Atmos. Environ.* **1988**, *22*, 1113. doi:10.1016/0004-6981(88)90341-1
- [36] D. R. Kester, I. W. Duedall, D. N. Connors, R. M. Pytkowicz, Preparation of artificial seawater. *Limnol. Oceanogr.* **1967**, *12*, 176. doi:10.4319/lo.1967.12.1.0176
- [37] K. Zhang, E. Knipping, A. Wexler, P. Bhavsar, G. Tonnesen, Size distribution of sea-salt emissions as a function of relative humidity. *Atmos. Environ.* **2005**, *39*, 3373. doi:10.1016/j.atmosenv.2005.02.032
- [38] N. Balzer, Kinetische Untersuchungen der Halogen-Aktivierung einer simulierten Salzpflanze in einer Smogkammer **2012**, Ph.D thesis; University of Bayreuth, Germany.
- [39] Supeno, P. Kruus, Sonochemical formation of nitrate and nitrite in water. *Ultrason. Sonochem.* **2000**, *7*, 109. doi:10.1016/S1350-4177(99)00043-7
- [40] T. B. Ryerson, E. J. Williams, F. C. Fehsenfeld, An efficient photolysis system for fast-response NO₂ measurements. *J. Geophys. Res.* **2000**, *105*, 26447. doi:10.1029/2000JD900389
- [41] N. A. Kelly, Characterization of fluorocarbon-film bags as smog chambers. *Environ. Sci. Technol.* **1982**, *16*, 763. doi:10.1021/es00105a007
- [42] C. Misra, M. Singh, S. Shen, C. Sioutas, P. M. Hall, Development and evaluation of a personal cascade impactor sampler (PCIS). *J. Aerosol Sci.* **2002**, *33*, 1027. doi:10.1016/S0021-8502(02)00055-1
- [43] H. Lohninger, J. Ofner, Multisensor hyperspectral imaging as a versatile tool for image-based chemical structure determination. *Spectrosc. Eur.* **2014**, No. 26, 6.

- [44] R. D. Shannon, Revised effective ionic radii and systematic studies of interatomic distances in halides and chalcogenides. *Acta Cryst. A* **1976**, *32*, 751. doi:10.1107/S0567739476001551
- [45] I. N. Tang, A. C. Tridico, K. H. Fung, Thermodynamic and optical properties of sea salt aerosols. *J. Geophys. Res.* **1997**, *102*, 23269. doi:10.1029/97JD01806
- [46] F. J. Millero, Solubility of Fe^{III} in seawater. *Earth Planet. Sc. Lett.* **1998**, *154*, 323. doi:10.1016/S0012-821X(97)00179-9
- [47] J. A. Thornton, J. P. Kercher, T. P. Riedel, N. L. Wagner, J. Cozic, J. S. Holloway, W. P. Dubé, G. M. Wolfe, P. K. Quinn, A. M. Middlebrook, B. Alexander, S. S. Brown, A large atomic chlorine source inferred from mid-continental reactive nitrogen chemistry. *Nature* **2010**, *464*, 271. doi:10.1038/nature08905
- [48] W. H. Schroeder, P. Urone, Formation of nitrosyl chloride from salt particles in air. *Environ. Sci. Technol.* **1974**, *8*, 756. doi:10.1021/es60093a015
- [49] B. J. Finlayson-Pitts, Reaction of NO₂ with NaCl and atmospheric implications of NOCl formation. *Nature* **1983**, *306*, 676. doi:10.1038/306676a0
- [50] W. Behnke, H.-U. Krüger, V. Scheer, C. Zetzsch, Formation of ClNO₂ and HONO in the presence of NO₂, O₃ and wet NaCl aerosol. *J. Aerosol Sci.* **1992**, *23*, 933. doi:10.1016/0021-8502(92)90565-D
- [51] R. Karlsson, E. Ljungström, Nitrogen dioxide and sea salt particles—A laboratory study. *J. Aerosol Sci.* **1995**, *26*, 39. doi:10.1016/0021-8502(94)00098-J
- [52] A. Saiz-Lopez, R. von Glasow, Reactive halogen chemistry in the troposphere. *Chem. Soc. Rev.* **2012**, *41*, 6448. doi:10.1039/c2cs35208g
- [53] De Haan, D. O., B. J. Finlayson-Pitts, Knudsen cell studies of the reaction of gaseous nitric acid with synthetic sea salt at 298 K. *J. Phys. Chem. A* **1997**, *101*, 9993. doi:10.1021/jp972450s
- [54] T. D. Saul, M. P. Tolocka, M. V. Johnston, Reactive uptake of nitric acid onto sodium chloride aerosols across a wide range of relative humidities. *J. Phys. Chem. A* **2006**, *110*, 7614. doi:10.1021/jp060639a
- [55] W. Behnke, V. Scheer, C. Zetzsch, Production of a photolytic precursor of atomic Cl from aerosols and Cl⁻ in the presence of O₃, in *Naturally-produced organohalogenes* (Eds A. Grimvall, E. de Leer) **1995**, pp. 375-384 (Springer: Dordrecht, Netherlands).
- [56] W. C. Keene, D. L. Savoie, The pH of deliquesced sea-salt aerosol in polluted marine air. *Geophys. Res. Lett.* **1998**, *25*, 2181. doi:10.1029/98GL01591
- [57] P. Brimblecombe, S. L. Clegg, The solubility and behaviour of acid gases in the marine aerosol. *J. Atmos. Chem.* **1988**, *7*, 1. doi:10.1007/BF00048251
- [58] C. Zetzsch, W. Behnke, Heterogeneous reactions of chlorine compounds, in *The tropospheric chemistry of ozone in the polar regions* (Eds. Niki, H., Becker, K. H.) **1993**, pp. 291–306 (Springer: New York).
- [59] S. Pechtl, R. von Glasow, Reactive chlorine in the marine boundary layer in the outflow of polluted continental air: A model study. *Geophys. Res. Lett.* **2007**, *34*, L11813. doi:10.1029/2007GL029761
- [60] C. B. Faxon, D. T. Allen, Chlorine chemistry in urban atmospheres: A review. *Environ. Chem.* **2013**, *10*, 221. doi:10.1071/EN13026

- [61] M. Hausmann, U. Platt, Spectroscopic measurement of bromine oxide and ozone in the high Arctic during Polar Sunrise Experiment 1992. *J. Geophys. Res.* **1994**, *99*, 25399. doi:10.1029/94JD01314
- [62] S. Fickert, J. W. Adams, J. N. Crowley, Activation of Br₂ and BrCl via uptake of HOBr onto aqueous salt solutions. *J. Geophys. Res.* **1999**, *104*, 23719. doi:10.1029/1999JD900359
- [63] K. W. Oum, Formation of molecular chlorine from the photolysis of ozone and aqueous sea-salt particles. *Science* **1998**, *279*, 74. doi:10.1126/science.279.5347.74
- [64] E. M. Knipping, M. J. Lakin, K. L. Foster, P. Jungwirth, D. J. Tobias, R. B. Gerber, D. Dabdub, B. J. Finlayson-Pitts, Experiments and simulations of ion-enhanced interfacial chemistry on aqueous NaCl aerosols. *Science* **2000**, *288*, 301. doi:10.1126/science.288.5464.301
- [65] S. Seisel, F. Caloz, F. F. Fenter, van den Bergh, Hubert, M. J. Rossi, The heterogeneous reaction of NO₃ with NaCl and KBr: A nonphotolytic source of halogen atoms. *Geophys. Res. Lett.* **1997**, *24*, 2757. doi:10.1029/97GL02857
- [66] Y. Rudich, R. K. Talukdar, A. R. Ravishankara, Fox, R. W., Reactive uptake of NO₃ on pure water and ionic solutions. *J. Geophys. Res.* **1996**, *101*, 21023. doi:10.1029/96JD01844
- [67] W. Behnke, C. George, V. Scheer, C. Zetzsch, Production and decay of ClNO₂ from the reaction of gaseous N₂O₅ with NaCl solution: Bulk and aerosol experiments. *J. Geophys. Res.* **1997**, *102*, 3795. doi:10.1029/96JD03057
- [68] J. M. Roberts, H. D. Osthoff, S. S. Brown, A. R. Ravishankara, N₂O₅ oxidizes chloride to Cl₂ in acidic atmospheric aerosol. *Science* **2008**, *321*, 1059. doi:10.1126/science.1158777
- [69] F. F. Fenter, F. Caloz, M. J. Rossi, Heterogeneous Kinetics of N₂O₅ Uptake on Salt, with a Systematic Study of the Role of Surface Presentation (for N₂O₅ and HNO₃). *J. Phys. Chem.* **1996**, *100*, 1008. doi:10.1021/jp9503829
- [70] B. J. Finlayson-Pitts, F. E. Livingston, H. N. Berko, Synthesis and identification by infrared spectroscopy of gaseous nitryl bromide, BrNO₂. *J. Phys. Chem.* **1989**, *93*, 4397. doi:10.1021/j100348a005
- [71] M. E. Gebel, B. J. Finlayson-Pitts, J. A. Ganske, The uptake of SO₂ on synthetic sea salt and some of its components. *Geophys. Res. Lett.* **2000**, *27*, 887. doi:10.1029/1999GL011152
- [72] R. Vogt, P. J. Crutzen, R. Sander, A mechanism for halogen release from sea-salt aerosol in the remote marine boundary layer. *Nature* **1996**, *383*, 327. doi:10.1038/383327a0
- [73] R. C. Troy, D. W. Margerum, Non-metal redox kinetics: hypobromite and hypobromous acid reactions with iodide and with sulfite and the hydrolysis of bromosulfate. *Inorg. Chem.* **1991**, *30*, 3538. doi:10.1021/ic00018a028
- [74] R. Atkinson, D. L. Baulch, R. A. Cox, J. N. Crowley, R. F. Hampson, R. G. Hynes, M. E. Jenkin, M. J. Rossi, J. Troe, Evaluated kinetic and photochemical data for atmospheric chemistry: Volume I - gas phase reactions of O_x, HO_x, NO_x and SO_x species. *Atmos. Chem. Phys.* **2004**, *4*, 1461. doi:10.5194/acp-4-1461-2004

- [75] R. Atkinson, D. L. Baulch, R. A. Cox, J. N. Crowley, R. F. Hampson, R. G. Hynes, M. E. Jenkin, M. J. Rossi, J. Troe, Evaluated kinetic and photochemical data for atmospheric chemistry: Volume III – gas phase reactions of inorganic halogens. *Atmos. Chem. Phys.* **2007**, 7, 981. doi:10.5194/acp-7-981-2007
- [76] V. Nadochenko, J. Kiwi, Primary photochemical reactions in the photo-fenton system with ferric chloride. 1. A case study of xylydine oxidation as a model compound. *Environ. Sci. Technol.* **1998**, 32, 3273. doi:10.1021/es970962e
- [77] D. L. Parkhurst, C. A. Appelo, *User's guide to PHREEQC (Version 2): A computer program for speciation, batch-reaction, one-dimensional transport, and inverse geochemical calculations* **1999**, pp. 99-4259 (US Geological Survey:Denver, CO, USA).
- [78] J. D. Allison, D. S. Brown, K. J. Novo-Gradac, *MINTEQA2/PRODEFA2, A Geochemical Assessment Model for Environmental Systems: Version 3.0 User's Manual* **1991** (Environmental Research Laboratory, Office of Research and Development, US Environmental Protection Agency, Athens, GA).
- [79] K. S. Pitzer, Thermodynamics of electrolytes. I. Theoretical basis and general equations. *J. Phys. Chem.* **1973**, 77, 268. doi:10.1021/j100621a026
- [80] N. J. Tosca, S. M. McLennan, B. C. Clark, J. P. Grotzinger, J. A. Hurowitz, A. H. Knoll, C. Schröder, S. W. Squyres, Geochemical modeling of evaporation processes on Mars: Insight from the sedimentary record at Meridiani Planum. *Earth and Planet. Sc. Lett.* **2005**, 240, 122. doi:10.1016/j.epsl.2005.09.042
- [81] A. H. Truesdell, B. F. Jones, WATEQ, a computer program for calculating chemical equilibria of natural waters. *US Geol. Surv. J. Res.* **1974**, 2, 233.
- [82] E. Hückel, Zur Theorie konzentrierterer wässeriger Lösungen starker Elektrolyte. *Phys. Z* **1925**, 26, 93.
- [83] M. A. McCaffrey, B. Lazar, H. D. Ho, The evaporation path of seawater and the coprecipitation of Br⁻ and K⁺ with halite. *J.Sediment. Petrol.* **1987**, 57, 928.
- [84] X. Liu, F. J. Millero, The solubility of iron in seawater. *Marine Chem.* **2002**, 77, 43. doi:10.1016/S0304-4203(01)00074-3
- [85] R. Sander, Compilation of Henry's Law constants for inorganic and organic species of potential importance in environmental chemistry. *Ver.* 3, **1999**. Available at <http://www.henry-law.org/henry.pdf> [verified May 2013].
- [86] K. Kuma, J. Nishioka, K. Matsunaga, Controls on iron (III) hydroxide solubility in seawater: the influence of pH and natural organic chelators. *Limnol. Oceanogr.* **1996**, 41, 396. doi:10.4319/lo.1996.41.3.0396
- [87] E. R. Sholkovitz, P. N. Sedwick, T. M. Church, A. R. Baker, C. F. Powell, Fractional solubility of aerosol iron: Synthesis of a global-scale data set. *Geochim. Cosmochim. Ac.* **2012**, 89, 173. doi:10.1016/j.gca.2012.04.022
- [88] A. R. Baker, T. D. Jickells, M. Witt, K. L. Linge, Trends in the solubility of iron, aluminium, manganese and phosphorus in aerosol collected over the Atlantic Ocean. *Marine Chem.* **2006**, 98, 43. doi:10.1016/j.marchem.2005.06.004
- [89] R. L. Siefert, A. M. Johansen, M. R. Hoffmann, S. O. Pehkonen, Measurements of trace metal (Fe, Cu, Mn, Cr) oxidation states in fog and stratus clouds. *J. Air Waste Manag. Assoc.* **1998**, 48, 128. doi:10.1080/10473289.1998.10463659

- [90] G. Zhuang, Z. Yi, R. A. Duce, P. R. Brown, Chemistry of iron in marine aerosols. *Global Biogeochem. Cycles* **1992**, *6*, 161. doi:10.1029/92GB00756
- [91] P. Warneck, Chemistry of the natural atmosphere, 2nd edn **1999** (Academic Press:San Diego, CA).
- [92] C. D. O'Dowd, E. Becker, M. Kulmala, Mid-latitude North-Atlantic aerosol characteristics in clean and polluted air. *Atmos. Res.* **2001**, *58*, 167. doi:10.1016/S0169-8095(01)00098-9
- [93] A. Ito, Global modeling study of potentially bioavailable iron input from shipboard aerosol sources to the ocean. *Global Biogeochem. Cycles* **2013**, *27*, 1. doi:10.1029/2012GB004378
- [94] N. M. Mahowald, S. Engelstaedter, C. Luo, A. Sealy, P. Artaxo, C. Benitez-Nelson, S. Bonnet, Y. Chen, P. Y. Chuang, D. D. Cohen, F. Dulac, B. Herut, A. M. Johansen, N. Kubilay, R. Losno, W. Maenhaut, A. Paytan, J. M. Prospero, L. M. Shank, R. L. Siefert, Atmospheric iron deposition: global distribution, variability, and human perturbations. *Ann. Rev. Mar. Sci.* **2009**, *1*, 245. doi:10.1146/annurev.marine.010908.163727
- [95] F. D. Meyer-Oeste, *Method for cooling the troposphere*, *Int. Patent CA 2748680 A1*, **2010**.
- [96] W. C. Keene, Khalil, M. Aslam K., D. J. Erickson, A. McCulloch, T. E. Graedel, J. M. Lobert, M. L. Aucott, S. L. Gong, D. B. Harper, G. Kleiman, P. Midgley, R. M. Moore, C. Seuzaret, W. T. Sturges, C. M. Benkovitz, V. Koropalov, L. A. Barrie, Y. F. Li, Composite global emissions of reactive chlorine from anthropogenic and natural sources: Reactive chlorine emissions inventory. *J. Geophys. Res.* **1999**, *104*, 8429. doi:10.1029/1998JD100084

3.8 Supplementary Material

Table S3.1: Applied composition of the prepared artificial seawater according to Kester et al.^[1]

Salt	Manufacturer	weighted amount [g] in 1 L H ₂ O
Artificial seawater		
NaCl	Sigma-Aldrich, ACS	23.9
Na ₂ SO ₄ x 10 H ₂ O	Merck, ACS	9.09
KCl	Roth, ACS	0.68
NaHCO ₃	Merck, for analysis	0.20
KBr	Merck, for analysis	0.098
H ₃ BO ₃	Grüssing GmbH, 99.5 %	0.026
NaF	Riedel de Haën, for analysis	0.003
MgCl ₂	Sigma Aldrich, 98 %	5.07
CaCl ₂ x 2 H ₂ O	Grüssing, 99%	1.52

Table S3.2: Rate constants for the reactions of methane and the reference hydrocarbons used as radical tracers for OH, Cl and Br in units of cm³ s⁻¹ at 298 K.

Hydrocarbon	k _{OH} (cm ³ s ⁻¹)	k _{Cl} (cm ³ s ⁻¹)	k _{Br} (cm ³ s ⁻¹)
Methane (CH ₄)	6.7 × 10 ⁻¹⁵ [2]	1.07 × 10 ⁻¹³ [2]	4 × 10 ⁻²⁴ [3]
2,2-Dimethylpropane (DMP)	8.3 × 10 ⁻¹³ [2]	1.1 × 10 ⁻¹⁰ [4]	≤ 1 × 10 ⁻²⁰ [5]
2,2-Dimethylbutane (DMB)	2.2 × 10 ⁻¹² [2]	1.7 × 10 ⁻¹⁰ [6]	–
2,2,4-Trimethylpentane (TMP)	3.3 × 10 ⁻¹² [2]	2.3 × 10 ⁻¹⁰ [7]	6.8 × 10 ⁻¹⁵ [8]
Toluene	6.2 × 10 ⁻¹² [9]	5.9 × 10 ⁻¹¹ [10]	1.3 × 10 ⁻¹⁴ [11]
n-Perfluorohexane	–	–	–

Table S3.3: Main equilibrium constants ($\log_{10} K$) for the formation of low molecular weight Fe^{III} complexes with several ligands at zero ionic strength and 298 K.

Equilibrium Constants	$\log_{10} K$
Water	
$\text{Fe}^{3+} + \text{H}_2\text{O} \rightleftharpoons \text{FeOH}^{2+} + \text{H}^+$	-2.19 ^[12]
$\text{Fe}^{3+} + 2\text{H}_2\text{O} \rightleftharpoons \text{Fe}(\text{OH})_2^+ + 2\text{H}^+$	-5.67 ^[12]
$\text{Fe}^{3+} + 3\text{H}_2\text{O} \rightleftharpoons \text{Fe}(\text{OH})_3 + 3\text{H}^+$	-12.0 ^[12]
$\text{Fe}^{3+} + 4\text{H}_2\text{O} \rightleftharpoons \text{Fe}(\text{OH})_4^- + 4\text{H}^+$	-21.6 ^[12]
Chloride	
$\text{Fe}^{3+} + \text{Cl}^- \rightleftharpoons \text{FeCl}^{2+}$	1.48 ^[13]
$\text{Fe}^{3+} + 2\text{Cl}^- \rightleftharpoons \text{FeCl}_2^+$	2.13 ^[14]
$\text{Fe}^{3+} + 3\text{Cl}^- \rightleftharpoons \text{FeCl}_3$	1.13 ^[15]
Bromide	
$\text{Fe}^{3+} + \text{Br}^- \rightleftharpoons \text{FeBr}^{2+}$	0.61 ^[16]
$\text{Fe}^{3+} + 2\text{Br}^- \rightleftharpoons \text{FeBr}_2^+$	0.2 ^[16]
Fluoride	
$\text{Fe}^{3+} + \text{F}^- \rightleftharpoons \text{FeF}^{2+}$	6.2 ^[17]
$\text{Fe}^{3+} + 2\text{F}^- \rightleftharpoons \text{FeF}_2^+$	10.8 ^[17]
$\text{Fe}^{3+} + 3\text{F}^- \rightleftharpoons \text{FeF}_3$	14 ^[17]
Sulfate	
$\text{Fe}^{3+} + \text{SO}_4^{2-} \rightleftharpoons \text{FeSO}_4^+$	3.92 ^[18]
$\text{Fe}^{3+} + 2\text{SO}_4^{2-} \rightleftharpoons \text{Fe}(\text{SO}_4)_2^-$	5.42 ^[18]

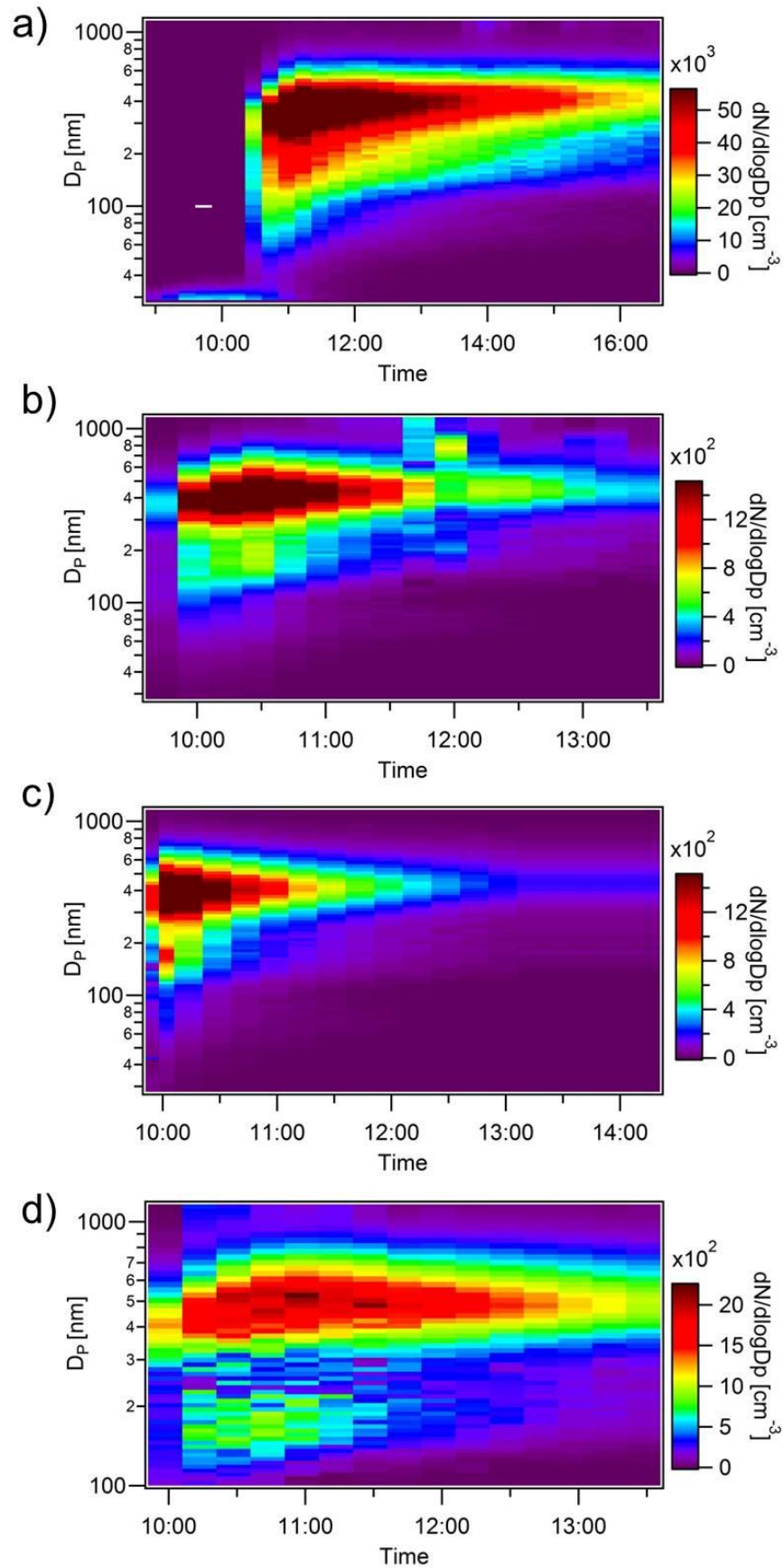


Figure S3.1a-d: Contour plots of selected experiments with nebulized a) NaCl (1 g L⁻¹), b) NaCl+FeCl₃ (~ 18 mmol L⁻¹ Cl⁻, Cl⁻/Fe^{III} = 13), c) artificial seawater + FeCl₃ (~ 29 mmol L⁻¹ Cl⁻, Cl⁻/Fe^{III} = 101) and d) artificial seawater + FeCl₃ (~ 37 mmol L⁻¹ Cl⁻, Cl⁻/Fe^{III} = 13)

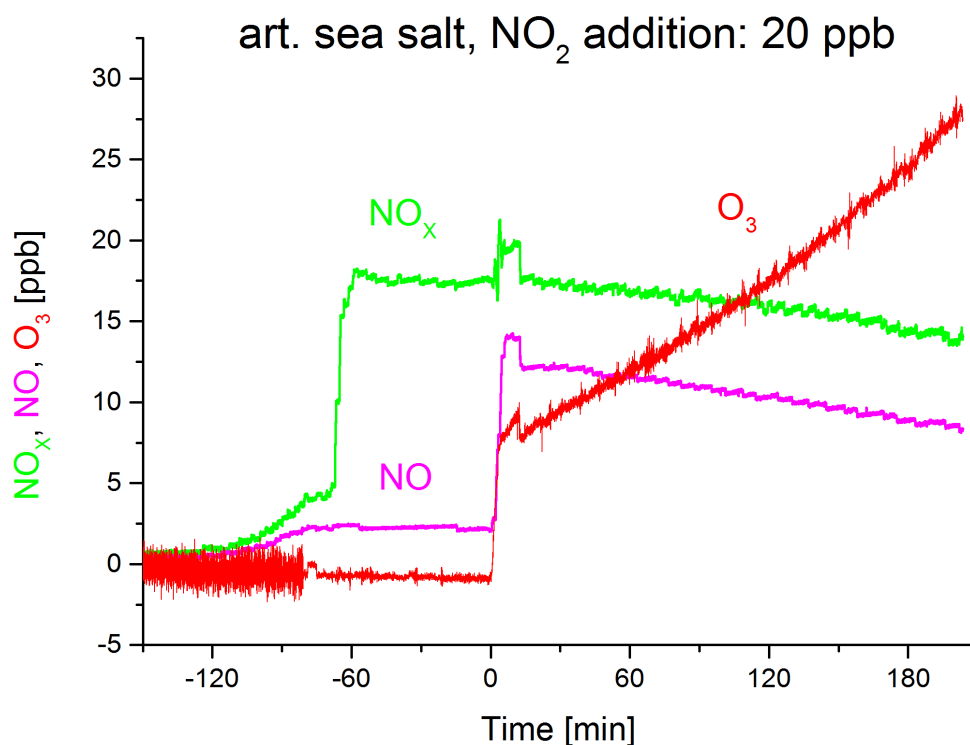


Figure S3.2: Time profiles of NO_x , NO , and O_3 during the experiment with Fe^{III} -free artificial seawater and 20 ppb NO_2 .

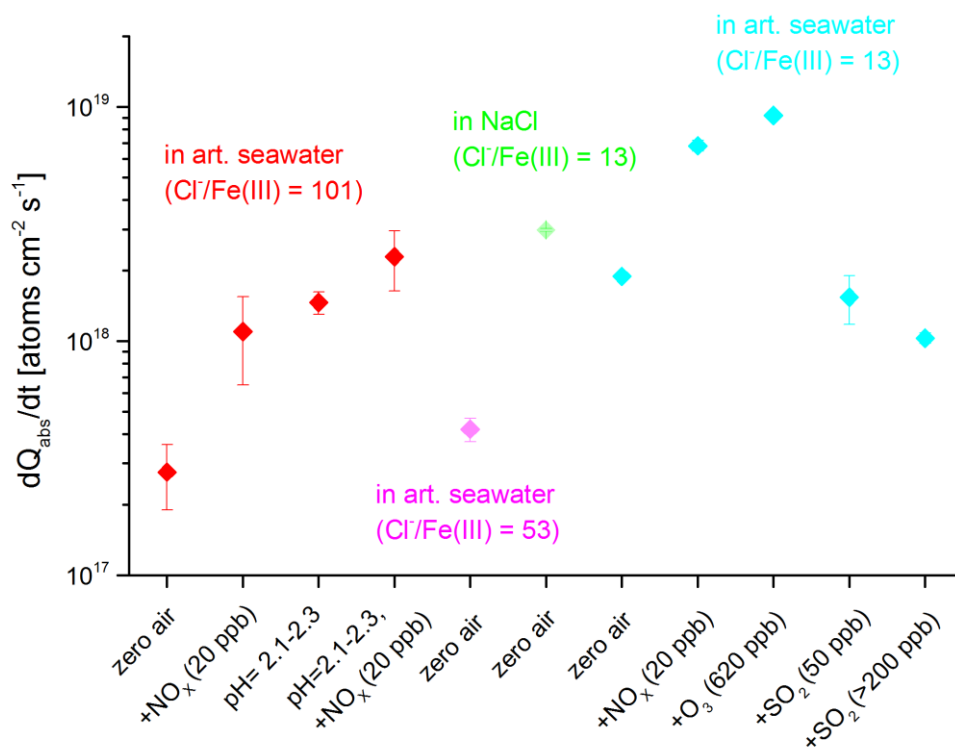


Figure S3.3: Overview of the initial minimum absolute Cl production rate dQ_{abs}/dt [atoms $\text{cm}^{-2} \text{s}^{-1}$] for each experiment with Fe^{III} containing samples and various air contaminants (NO_x , O_3 , SO_2).

References

- [1] D. R. Kester, I. W. Duedall, D. N. Connors, R. M. Pytkowicz, Preparation of artificial seawater. *Limnol. Oceanogr.* **1967**, *12*, 176.doi:10.4319/lo.1967.12.1.0176.
- [2] R. Atkinson, D. L. Baulch, R. A. Cox, R. F. Hampson, J. A. Kerr, M. J. Rossi, J. Troe, Evaluated Kinetic, Photochemical and Heterogeneous Data for Atmospheric Chemistry: Supplement V. IUPAC Subcommittee on Gas Kinetic Data Evaluation for Atmospheric Chemistry. *J. Phys. Chem. Ref. Data* **1997**, *26*, 521.doi:10.1063/1.556011.
- [3] D. L. Baulch, J. Duxbury, S. J. Grant, D. C. Montague, Evaluated Kinetic Data for High Temperature Reactions. Volume 4. Homogeneous Gas Phase Reactions of Halogen- and Cyanide-Containing Species. *J. Phys. Chem. Ref. Data* **1981**, *10*, 723.
- [4] R. Atkinson, S. M. Aschmann, Kinetics of the gas phase reaction of Cl atoms with a series of organics at 296 ± 2 K and atmospheric pressure. *Int. J. Chem. Kinet.* **1985**, *17*, 33.doi:10.1002/kin.550170105.
- [5] J. C. Amphlett, E. Whittle, Bromination of fluoroalkanes. Part 4. Kinetics of thermal bromination of fluoroform and pentafluoroethane. *Trans. Faraday Soc.* **1968**, *64*, 2130.doi:10.1039/tf9686402130.
- [6] M. E. Jenkin, S. M. Saunders, M. J. Pilling, The tropospheric degradation of volatile organic compounds: a protocol for mechanism development. *Atmos. Environ.* **1997**, *31*, 81.doi:10.1016/S1352-2310(96)00105-7.
- [7] S. M. Aschmann, R. Atkinson, Rate constants for the gas-phase reactions of alkanes with Cl atoms at 296 ± 2 K. *Int. J. Chem. Kinet.* **1995**, *27*, 613.doi:10.1002/kin.550270611.
- [8] I. Barnes, V. Bastian, K. H. Becker, R. Overath, Z. Tong, Rate constants for the reactions of Br atoms with a series of alkanes, alkenes, and alkynes in the presence of O₂. *Int. J. Chem. Kinet.* **1989**, *21*, 499.doi:10.1002/kin.550210703.
- [9] R. Atkinson, Kinetics and mechanisms of the gas-phase reactions of the hydroxyl radical with organic compounds under atmospheric conditions. *Chem. Rev.* **1986**, *86*, 69.doi:10.1021/cr00071a004.
- [10] J. Shi, M. J. Bernhard, Kinetic studies of Cl atom reactions with selected aromatic compounds using the photochemical reactor-FTIR spectroscopy technique. *Int. J. Chem. Kinet.* **1997**, *29*, 349.
- [11] A. Bierbach, I. Barnes, K. H. Becker, Rate constants of the Br[•] initiated gas-phase oxidation of a series of alcohols, furans and benzenes at 300 ± 2 K. *Atmos. Environ.* **1999**, *33*, 2981.doi:10.1016/S1352-2310(99)00084-9.
- [12] C. F. Baes, R. E. Mesmer, The hydrolysis of cations, **1976** (Wiley: New York).
- [13] D. R. Kester, R. H. Byrne, Y.-J. Liang, Redox reactions and solution complexes of iron in marine systems, in *Marine chemistry in the Coastal Environment, Vol. 18* (Ed. Church, T. M.) **1975**, pp. 56-79(American Chemical Society: Washington, DC).
- [14] A. E. Martell, R. M. Smith, *Critical Stability Constants. Volume 4. Inorganic Complexes*, **1976** (Plenum: New York)
- [15] K. B. Yatsimirskii, V. P. Vasil'ev, Instability constants of complex compounds, **1960** (Pergamon Press: Oxford).

- [16] M. W. Lister, D. E. Rivington, Some ferric halide complexes, and ternary complexes with thiocyanate ions. *Can. J. Chem.* **1955**, *33*, 1603. doi:10.1139/v55-194
- [17] D. K. Nordstrom, E. A. Jenne, Fluorite solubility equilibria in selected geothermal waters. *Geochim. Cosmochim. Ac.* **1977**, *41*, 175. doi:10.1016/0016-7037(77)90224-1.
- [18] J. de Laat, T. G. Le, Kinetics and Modeling of the Fe^{III}/H₂O₂ System in the Presence of Sulfate in Acidic Aqueous Solutions. *Environ. Sci. Technol.* **2005**, *39*, 1811. doi:10.1021/es0493648.

Chapter 4:

Photochemical Activation of Chlorine by Iron-Oxide Aerosol

Julian Wittmer¹ and Cornelius Zetzsch^{1,2}

[1] Atmospheric Chemistry Research Unit, BayCEER, University of Bayreuth, Dr. Hans-Frisch Straße 1–3, 95448 Bayreuth, Germany

[2] Max Planck Institute for Chemistry, Hahn-Meitner-Weg 1, 55128 Mainz, Germany

Reproduced with permission from Wittmer, J. and Zetzsch, C. Photochemical Activation of Chlorine by Iron-Oxide Aerosol. J. Atm. Chem. doi: 10.1007/s10874-016-9336-6. Copyright Springer Science +Business Media Dodrecht 2016.

Full text article: <http://link.springer.com/article/10.1007/s10874-016-9336-6>

Special Issue: Natural Halocarbons in the Atmosphere

Received: October 1, 2015

Accepted: March 31, 2016

First online: April 14, 2016

Acknowledgments

We wish to thank Dr. Catherine McCammon, BGI Bayreuth, Germany, for the Mössbauer spectroscopy of our samples, Johannes Thiessen for the BET analysis, Dipl.-Ing. Franz D. Oeste and Dr. Sergej Bleicher for advice, and Agnes Bednorz and Andrej Einhorn for technical support. This work was supported by the German Research Foundation (DFG) within research unit 763 (HALOPROC) grant ZE792/5-2.

Abstract

The photochemical activation of chlorine by dissolved iron in artificial sea-salt aerosol droplets and by highly dispersed iron oxide (Fe_2O_3) aerosol particles (mainly hematite, specific surface $\sim 150 \text{ m}^2 \text{ g}^{-1}$) exposed to gaseous HCl, was investigated in humidified air in a Teflon simulation chamber. Employing the radical-clock technique, we quantified the production of gaseous atomic chlorine (Cl) from the irradiated aerosol. When the salt aerosol contained Fe_2O_3 at pH 6, no significant Cl production was observed, even if the dissolution of iron was forced by “weathering” (repeatedly freezing and thawing for five times). Adjusting the pH in the stock suspension to 2.6, 2.2, and 1.9 and equilibrating for one week resulted in a quantifiable amount of dissolved iron (0.03 , 0.2 , and 0.6 mmol L^{-1} , respectively) and in gaseous Cl production rates of ~ 1.6 , 6 , and $8 \times 10^{21} \text{ atoms cm}^{-2} \text{ h}^{-1}$, respectively. In a further series of experiments, the pure Fe_2O_3 aerosol was exposed to various levels of gaseous hydrogen chloride (HCl). The resulting Cl production rates ranged from $8 \times 10^{20} \text{ Cl atoms cm}^{-2} \text{ h}^{-1}$ (at $\sim 4 \text{ ppb HCl}$) to $5 \times 10^{22} \text{ Cl atoms cm}^{-2} \text{ h}^{-1}$ (at $\sim 350 \text{ ppb HCl}$) and confirmed the uptake and conversion of HCl to atomic Cl (at HCl to Cl conversion yields of 2–5 %, depending on the relative humidity). The Fe_2O_3 experiments indicate that iron-induced Cl formation may be important for highly soluble combustion-aerosol particles in marine environments in the presence of gaseous HCl.

4.1 Introduction

Iron is an essential element of the lithosphere, hydrosphere and biosphere, which is demonstrated by its manifold chemistry having significant implications on the atmosphere. As a bioelement, it mediates metabolic processes and thus indirectly affects the atmospheric carbon footprint. In the atmosphere, iron is mainly present in aerosol particles in form of solid oxides arising naturally basically from arid continental regions (~95 %) or from anthropogenic combustion processes (~5 %; Luo et al. 2008). Volcanic eruptions may significantly contribute to the iron budget in some periods (Duggen et al. 2007). Mineral aerosol particles influence the absorption and reflection of solar radiation, cloud condensation and the gas-phase chemistry. Concerning the latter, in particular the (aqueous) surface chemistry is decisive. The dissolution of ferric oxides in the aqueous phase (e.g. atmospheric waters or quasi-liquid aerosol layer) is driven by salinity, pH, organic (e.g. humic like substances; Al-Abadleh 2015) and inorganic (e.g. chloride; Liu and Millero 2002) or ligands and induces Fenton-like processes that lead to aqueous-phase radicals when exposed to sunlight. Lim et al. (2006), Wittmer et al. (2015a) and Wittmer et al. (2015b) demonstrated that such a system leads to gaseous halogen formation in the presence of halides. The halogen formation is initiated by the photolytic reduction of Fe^{III}-chloride complexes (Miller et al. 1995; Nadochenko and Kiwi 1998).

The global average iron solubility in aerosol-particle suspensions is estimated to ~1–2% (Jickells and Spokes 2001), whereas measurements and estimates of the fraction of soluble iron in marine aerosol range from 0–95% depending on the origin of the iron-containing aerosol (e.g. combustion or mineral dust; Schroth et al. 2009), the aerosol pH (Keene et al. 1998), age, size and composition (Zhu et al. 1993; Siefert et al. 1998; Baker et al. 2006; Baker and Croot 2010; Sholkovitz et al. 2012). Atmospheric processing can considerably influence the iron solubility (Mahowald et al. 2009). Rubasinghege et al. (2010) demonstrated the significant role of size and anions in the dissolution of FeOOH. In this context, the interaction between iron-containing particles and gaseous HCl is still relatively unexplored. Zhang and Iwasaka (2001) investigated the Cl deposition on dust particles in a marine atmosphere. Moreover, Sullivan et al. (2007b) determined a Cl mass fraction of 4–9 % in dust particles during a major dust storm and ascribed the enrichment in Cl to the heterogeneous HCl uptake. The behavior of HCl remains unclear when a large fraction of iron oxide is involved in the aerosol (e.g. combustion aerosol particles). The potential uptake may lead to a photochemical activation of chloride, similar to halide media doped with Fe^{III} (Wittmer et al. 2015a; Wittmer et al. 2015b). The mean natural gaseous HCl concentration in the boundary layer is ~200 ppt (Graedel and Keene 1996) with an annual HCl production rate of 7.6 Tg yr⁻¹ (Erickson et al. 1999). Main sources are the dechlorination (e.g. by acid displacement in sea salt), volcanoes, and anthropogenic activities (e.g. coal combustion or biomass burning). The main sink is the heterogeneous deposition on surfaces (Keene et al. 1999). The chemical reaction (mainly with OH) and subsequent Cl production is not an efficient net sink based on the further reactions of Cl with hydrocarbons via H abstraction and thus a regeneration of HCl.

Behnke and Zetzsch (1990) already determined an enhanced production of atomic Cl from HCl uptake at high ozone (O₃) concentrations and relative humidities in the presence of SiO₂ and Fe₂O₃ aerosol particles. Here, we take up the topic of the

atmospheric impact of iron oxides exposed to halide media. In particular, we investigated the iron-induced Cl activation from Fe₂O₃-containing sea-salt aerosol particles or from pure iron-oxide aerosol in the presence of HCl. In the latter case, we explored the uptake of gaseous HCl and its heterogeneous conversion into Cl. The study simulated conditions where Fe₂O₃-containing sea-salt aerosol or pure iron-oxide aerosol are exposed to sunlight in remote marine environments at low trace gas concentrations.

4.2 Experimental

The experimental set-up was equal to the set-up in Wittmer et al. (2015b). All experiments were conducted at 20°C in a Teflon smog chamber (Fluorinated Ethylene Propylene - FEP 200A, DuPont, Wilmington, DE, USA) with a volume of ~3.5 m³ that is continuously flushed with hydrocarbon-free, humidified (temperature-controlled three-neck bottle filled with deionized water (Seralpur pro 90 cn, <0.055 μS cm⁻¹)) zero air (zero-air-generator, cmc instruments, <1 ppb O₃, <0.5 ppb NO_x, <100 ppb CH₄) to replenish the air consumption of the connected analyzers (EcoPhysics, CLD 88p coupled with a photolytic converter, PLC 860 for NO and NO_x, and UPK 8001 for O₃) and to maintain a slight overpressure (0.3–1 Pa). The chamber is suspended above a solar simulator, providing an actinic flux comparable to the tropospheric sunlight on the 50th latitude in the tropospheric summer. More detailed specifications can be found elsewhere (Buxmann et al. 2012; Bleicher et al. 2014; Wittmer et al. 2015a). After every experiment, the chamber was either cleaned by deionized water or the whole Teflon film was exchanged. In both cases, the chamber was (re-)conditioned by irradiation with four UV lamps (Phillips TUV 55W, λ = 253.7 nm) in the presence of >1 ppm O₃ at high RH.

In principle, two types of experiments were performed. The first series of experiments consisted of the nebulizing (Ultrasonic nebulizer: Quick Ohm QUV-HEV FT25/16-A, 35 W, 1.63 MHz) and irradiating of an artificial sea-salt stock solution (containing 824 mg L⁻¹ NaCl, 314 mg L⁻¹ Na₂SO₄ × 10 H₂O, 176 mg L⁻¹ MgCl₂, 52 mg L⁻¹ CaCl₂ × 2 H₂O, 24 mg L⁻¹ KCl, 6.9 mg L⁻¹ NaHCO₃, 3.4 mg L⁻¹ KBr, 0.9 mg L⁻¹ H₃BO₃, and 0.1 mg L⁻¹ NaF; Kester et al. 1967) doped with Fe₂O₃ (Sicotrans Orange L2515D, BASF) with a specific surface area: 152 m² g⁻¹ (according to a BET measurement at the Faculty of Engineering Sciences, University of Bayreuth). The Mössbauer analysis of Sicotrans Orange (evaluated by the Bavarian Research Institute of Experimental Geochemistry and Geophysics at Bayreuth using the program MossA; Prescher et al. 2012) revealed the dominant presence of Fe³⁺ in the form of α-Fe₂O₃ (hematite), a phase containing paramagnetic Fe³⁺ and a fraction of Fe²⁺ and/or Fe³⁺ showing slow paramagnetic relaxation (Fig. 4.1).

In addition to an untreated run, the dissolution of Fe₂O₃ in the sea salt was promoted by acidification or repeated freezing/thawing processes. For each experiment, 17 mg of Fe₂O₃ were stirred into 100 mL of the artificial seawater solution to obtain a molar ratio of ~0.08 between solid (and dissolved) iron and Cl⁻. This contribution is comparable to the largest Fe^{III} concentration in Wittmer et al. (2015b) where FeCl₃ was dissolved in artificial seawater. The powder formed a suspension with Fe₂O₃ grains sinking to the bottom within 3–5 min. Therefore, the flask was shaken before filling ~50 ml into the nebulizer. For some samples, the pH was reduced to 2.6, 2.2 and 1.9 (measured by a pH

meter, pH 3110, WTW) by adding 30, 55 and 110 μL of HCl (Sigma-Aldrich ACS, 37%), respectively. In this way, the Cl^- concentration in the stock solution increased from 28 to 31.6, 34.6 and 41 mmol L^{-1} . After 16 h, 113 h and 186 h, an aliquot of each sample was passed through a 0.025 μm filter (Whatman Anotop 10 Plus) combined with a 0.45 μm pre-filter (Millipore), to determine the amount of dissolved iron (Fe_d) by ICP-OES (Central Analytics, BayCEER, University of Bayreuth). The obtained filtrated solution may contain smaller iron colloids ($<0.025 \mu\text{m}$) that would also be detected by ICP-OES and may distort the given Fe_d concentrations. However, the amount of iron from colloids is rather negligible with regard to the sample without pH adjustment, where the remaining colloids did not lead to a detectable amount of iron (detection limit $\sim 0.001 \text{ mmol L}^{-1}$).

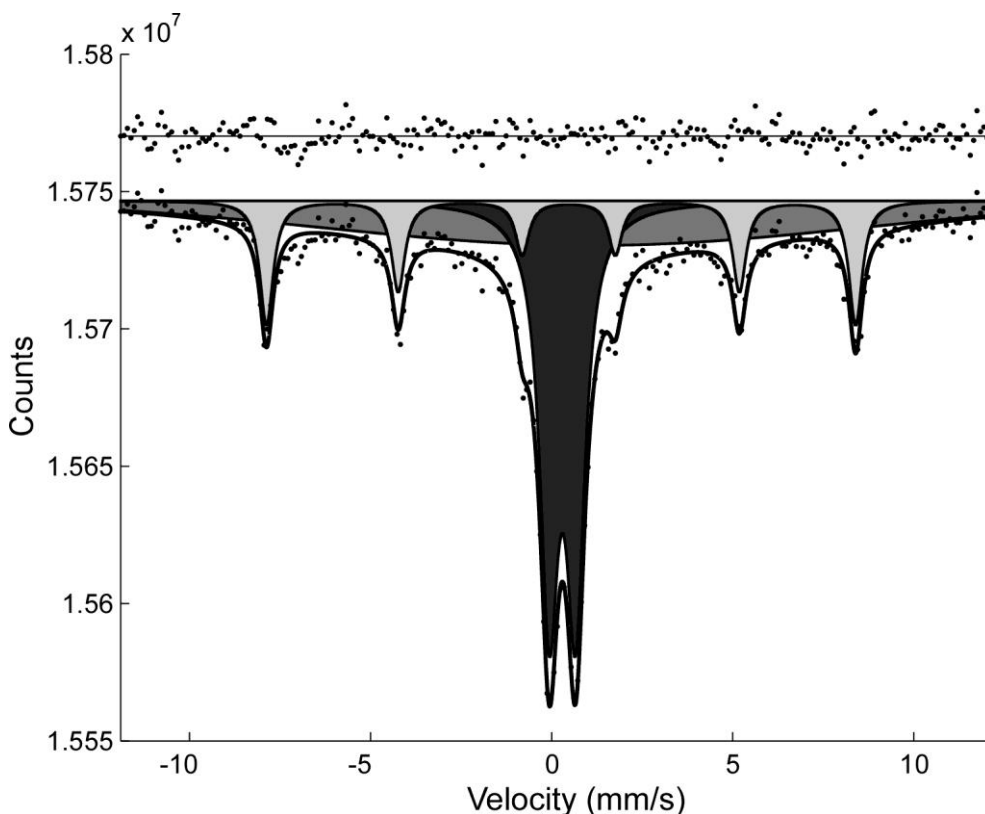


Fig. 4.1 Room temperature Mössbauer spectrum of Sicotrans Orange L 2515. The spectrum is fitted to a magnetic sextet assigned to $\alpha\text{-Fe}_2\text{O}_3$ (light grey, 19 %), a quadrupole doublet assigned to Fe^{3+} (dark grey, 39 %) and a broad absorption assigned to Fe^{2+} and/or Fe^{3+} (medium grey, 42 %). The relative areas of the different components indicate roughly the relative abundance of the different iron species. The residual (difference between the fitted curve and experimental data) is shown above the spectrum and the velocity scale is relative to $\alpha\text{-Fe}_2\text{O}_3$. The spectrum was collected for 13 days and was evaluated by Dr. Catherine McCammon (BGI Bayreuth, Germany) using the program MossA (Prescher et al. 2012)

In a second series of experiments, hydrated Fe_2O_3 or SiO_2 aerosol particles were generated by nebulizing a suspension of the Sicotrans Orange powder or Aerosil 200 (Evonik Industries, specific surface of $200 \text{ m}^2 \text{ g}^{-1}$) in water. The resulting aerosol particles were exposed to various levels of gaseous (evaporated) HCl by injecting known amounts of concentrated hydrochloric acid (Sigma-Aldrich, ACS, 37 %).

The aerosol was produced in accordance to Wittmer et al. (2015b), with the only difference that pure nitrogen was applied for injection to avoid the sonochemical formation of nitrate and nitrite (Supeno and Kruus 2000). The aerosol size distributions and concentrations were monitored by an electrostatic classifier (TSI, 3071) in combination with a bipolar neutralizer (^{85}Kr) and a condensation nucleus counter (TSI, 3020). Scanning and data evaluation were performed by a custom written software (Balzer 2012). Typical resulting size distributions, obtained after 30–60 min of injection, are shown in Fig. 4.2. Based on these distributions (measured every 15 min), the aerosol surface is calculated. For some distributions, a slightly bi- or trimodal shape is recognizable probably caused by the laminar and turbulent coagulation during the nebulization process at high temperatures and number densities within the nebulizer (Wang et al. 2008). For the suspensions of Aerosil 200 and Sicotrans Orange in deionized water, we observed a less effective ultrasonic aerosol production indicated by much lower aerosol loads at comparable injection times to the artificial seawater experiments. The determined surface lifetimes were $\tau_s = 4510 \pm 952 \text{ s}$ for the pure Fe_2O_3 aerosol and $\tau_s \sim 4800 \pm 800 \text{ s}$ for the Fe_2O_3 +artificial seawater aerosol. Note that the specific surface of the aerosol particles is much larger due to the formation of porous agglomerates.

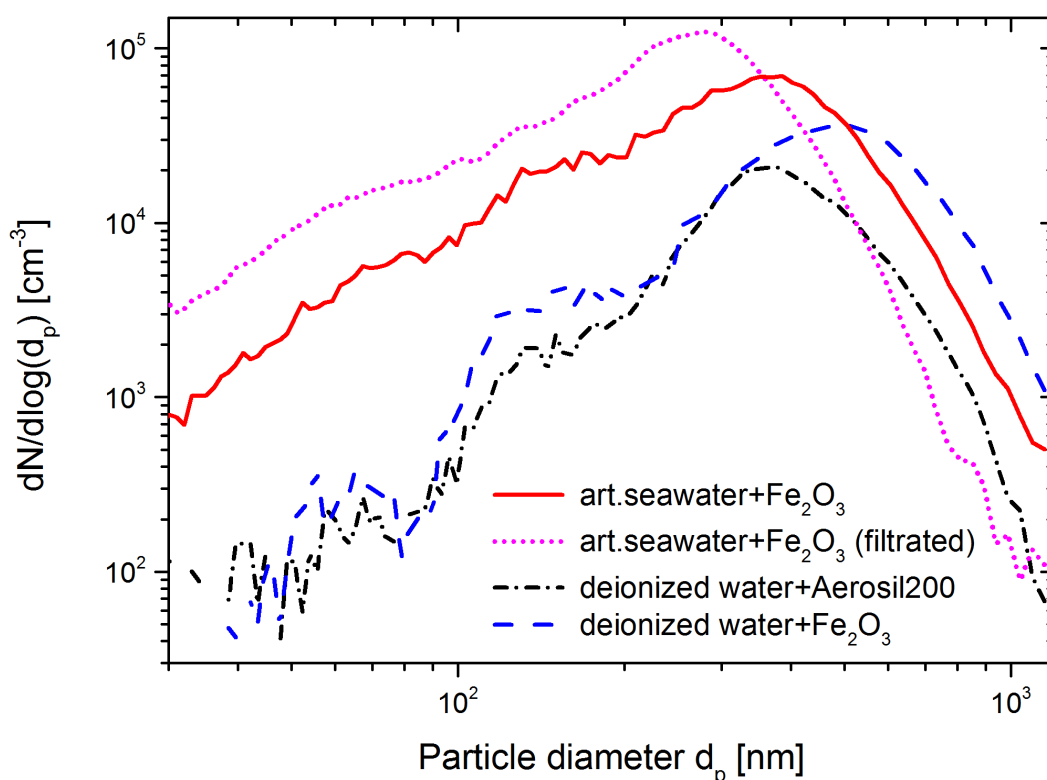


Fig. 4.2 Initial (multiple-charge corrected) size distributions for aerosol particles generated by the ultrasonic nebulizer (30 – 60 min injection time) from the stock solutions (filtrated and unfiltered

artificial seawater, doped with Fe₂O₃, Aerosil 200 in deionized water, and Fe₂O₃ in deionized water)

The production rates and total production of Cl and OH radicals were determined by the radical clock method (Behnke et al. 1988; Zetzsch and Behnke 1993), monitoring the degradation pattern of selected hydrocarbons (2,2-dimethylpropane, Linde, ≥ 99%; 2,2-dimethylbutane, Aldrich, ≥ 99 %; 2,2,4-trimethylpentane, Janssen ≥ 99%; toluene, Aldrich ≥ 99.9%) by a gas chromatograph with flame ionization detector (Siemens Sichromat 2) with a capillary column (Al₂O₃-PLOT) equipped with a custom-built liquid nitrogen cooled cryo-trap enrichment (sampling flow 100 mL min⁻¹ dried by a Nafion dryer). The combined time profiles of the hydrocarbons allow us to quantify the quasistationary radical concentrations based on the individual rate constants (k_{Cl,i}; k_{OH,i}) of the hydrocarbons (HC_i) towards Cl and OH.

$$-\frac{d\ln[\text{HC}_i]}{dt} = k_{\text{Cl},i}[\text{Cl}] + k_{\text{OH},i}[\text{OH}] \quad (4.1)$$

These quasistationary concentrations of the radicals were corrected for the reactivity of the system according to Wittmer et al. (2015a) leading to a minimum (considering the actual, measured hydrocarbon concentrations) and maximum (assuming a reactivity of the degradation products comparable to the initial reactivity of the system) total production Q_{Cl} and production rate dQ_{Cl}/dt .

$$\frac{dQ_{\text{Cl}}}{dt} = \sum_i k_{\text{Cl},i}[\text{HC}_i]_t [\text{Cl}]_t \quad (4.2)$$

Q_{Cl} and dQ_{Cl}/dt are corrected for the chamber volume and normalized by the effective active aerosol surface A_{eff} , considering the actual measured aerosol surface and the active, deposited surface that forms due to the deposition on the Teflon walls.

$$\frac{dQ_{\text{abs}}}{dt} = \frac{\frac{dQ_{\text{Cl}}}{dt} \times V_{\text{Ch}}}{A_{\text{eff}}(t)} \quad (4.3)$$

The detailed calculation of A_{eff} is described in Wittmer et al. (2015b). The result is the (minimum and maximum) total production (rate) Q_{abs} (dQ_{abs}/dt) of Cl radicals per square centimeter of aerosol surface.

4.3 Results and Discussion

4.3.1 Cl Production from Fe₂O₃ in Artificial Sea-Salt Aerosol

Fig. 4.3 displays the measured iron concentrations as a function of time for each sample. As already explored in precipitation studies, the equilibration takes at least 7 days to stoichiometry (Kuma et al. 1996; Liu and Millero 2002).

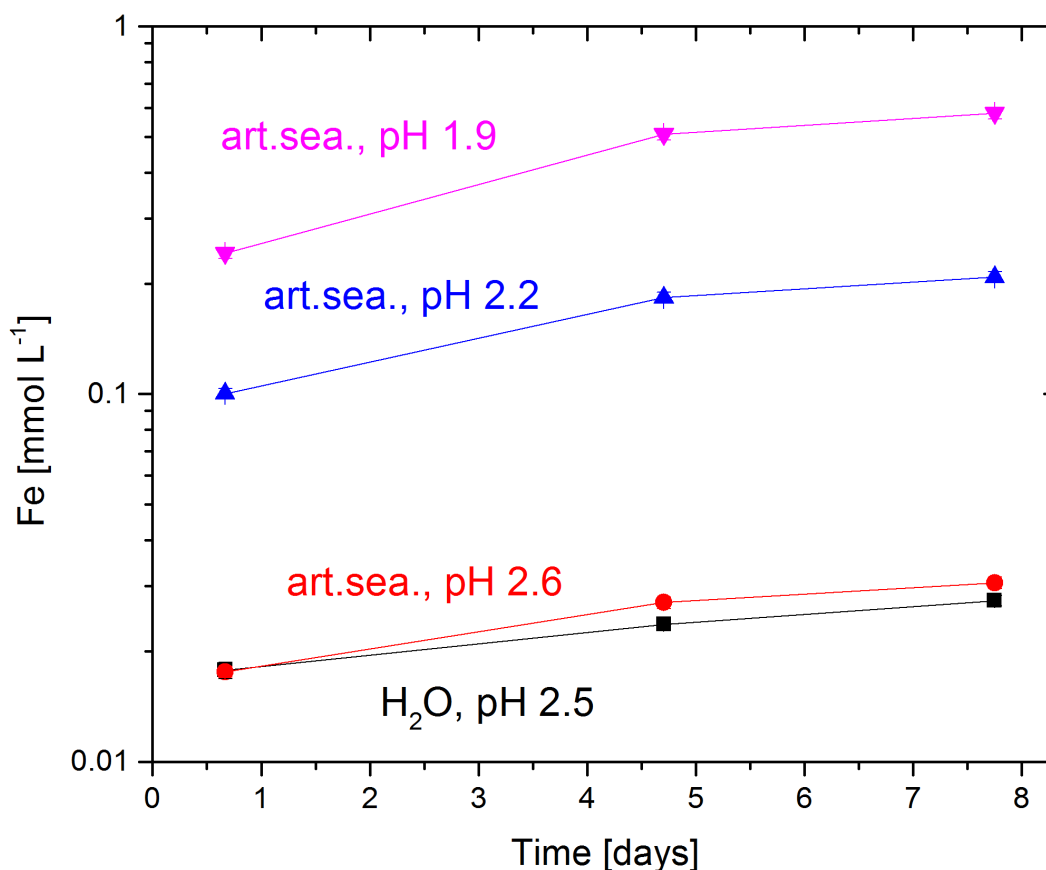


Fig. 4.3 The concentration of quasi-dissolved iron in artificial seawater and deionized water at various pHs and 25°C as a function of time. The samples were passed through a 0.025- μm filter (Whatman Anotop 10 Plus) combined with a 0.45 μm pre-filter (Millipore) and the iron content was determined by ICP-OES

The dissolution proceeds via



and depends on the further stepwise formation of Fe^{III}-hydroxy and Fe^{III}-chloride complexes (Liu and Millero 2002; Wittmer et al. 2015a), explaining the strong increase of dissolved iron with pH (Fig. 4.3). For instance, Nadtochenko and Kiwi (1998) and Wittmer et al. (2015b) identified FeCl²⁺ and FeCl₂⁺ (R4.6, R4.7, Table 4.1) as the key complexes (coordinated water molecules omitted) that are dominant in the acidic pH range (< 4.5) at high salinity and form Cl radicals in the aqueous phase that combine and lead to degassing of Cl₂. At higher pH, FeOH²⁺ and Fe(OH)₂⁺ (R4.2, R4.3, Table 4.1) become relevant as a source of OH radicals (classical photo-Fenton) but can also form Cl₂

in the presence of Cl^- . For a more detailed discussion of the speciation parameters and the kinetic mechanism of the Cl_2 production, we refer to Wittmer et al. (2015b). The sea-salt matrix promotes the dissolution of iron as indicated by the larger amount of dissolved iron in the sea-salt sample (pH 2.6, 30 μL HCl added) compared to the sample with 17 mg Fe_2O_3 in 100 mL deionized water (pH 2.5, 40 μL HCl added). The dissolution of Fe_2O_3 finally resulted in Fe_d/Cl^- ratios of ~ 0.001 (pH 2.6), ~ 0.006 (pH 2.2) and ~ 0.014 (pH 1.9) in the artificial seawater solutions. The filtrated samples of Fe_2O_3 -doped artificial seawater and deionized water without pH adjustment did not contain detectable amounts of iron ($< 0.0001 \text{ mmol L}^{-1}$). The high sensitivity of Fe_d toward small changes in pH was already explored by Zhu et al. (1992) in detail. For hematite, they found a variation in solubility of 4 orders of magnitude in the pH range from 0.5 to 2.

Table 4.1 Relevant equilibria influencing the speciation of iron complexes in a saline solution.



In the first experiment, the Fe_2O_3 – artificial seawater mixture without pH adjustment was applied. The time profiles of the hydrocarbons did not show a significant depletion, implying a Cl production rate below the detection limit ($< 5 \times 10^{17} \text{ atoms cm}^{-2} \text{ s}^{-1}$). One main reason is the low fraction of dissolved Fe_2O_3 as indicated by the pH of 6 and by an iron concentration of the filtrated aliquot below the detection limit (Table 4.2). E.g. Byrne and Kester (1976), Kuma et al. (1996) and Liu and Millero (2002) determined a very low amount of dissolved Fe^{III} from Fe^{III} -hydroxides in seawater at this pH range (e.g. $5.53 \times 10^{-14} \text{ mol kg}^{-1}$ for Fe_2O_3 in seawater at pH 5 (Zhu et al. 1992) or $\log[\text{Fe}^{\text{III}}] = -6.8$ at pH 5 for ferric hydroxide (Liu and Millero 2002). Even if the pH and the ionic strength change after nebulization, the time to reach the dissolution equilibrium during the experiment (typically 3 h) is quite short. Therefore, the high ionic strength in the produced aerosol has a negligible effect in this short timescale compared to the pH of the stock solution. Concerning the change of ion concentrations from the initial solution to the aerosol phase, one may assume a saturated salt solution ($\sim 6.1 \text{ mol Cl}^- \text{ L}^{-1}$) after a rapid equilibration of the liquid aerosol phase with its surrounding.

To alternatively accelerate and promote the dissolution of the iron oxide, an aliquot of the Sicotrans-artificial seawater mixture was frozen at -20°C for 1–3 hours and thawed again at 20°C for five times. Jeong et al. (2012) determined a greatly enhanced dissolution due to this process at acidic pH conditions (pH 2–4) in the dark. However, we did not observe an effect related to the Fe^{III} -induced Cl production. The impact of the accelerated dissolution was below the detection limit. Based on the significant detection starting from a molar $\text{Fe}^{\text{III}}/\text{Cl}^- > 0.001$ (see Table 4.2), we conclude that at least $\sim 1\%$ of the added Fe_2O_3 has to be dissolved in artificial seawater to detect a gaseous Cl production.

Although, accelerating the iron-oxide dissolution rates more than 2 times by freezing (Jeong et al. 2012), the dissolved fraction remains far below 1 %, justified by the very low solubility value of $\log[\text{Fe}^{\text{III}}] = -11.0$ for artificial seawater at 25°C and pH = 8.1 (Liu and Millero 2002).

In contrast to the samples without pH adjustment, the nebulization and irradiation of the pH adjusted samples resulted in a significant Cl production. Fig. 4.4 shows the Cl production and the Fe_d/Cl^- ratio in the nebulized solution as a function of the pH. The Cl source clearly increases with increasing acidity and thus with the amount of dissolved iron and the increasing Fe/Cl^- . At the highest pH of 2.6 in this series ($\text{Fe}/\text{Cl}^- = 0.001$) we observed a Cl production of $(1.6\text{--}1.7) \times 10^{21}$ atoms $\text{cm}^{-2} \text{h}^{-1}$, at pH 2.2 ($\text{Fe}/\text{Cl}^- = 0.006$) the Cl production was $(5.6\text{--}6.6) \times 10^{21}$ atoms $\text{cm}^{-2} \text{h}^{-1}$, and it was $(7.0\text{--}9.3) \times 10^{21}$ Cl atoms $\text{cm}^{-2} \text{h}^{-1}$ at the lowest pH of 1.9 ($\text{Fe}/\text{Cl}^- = 0.014$). The increase shows a non-linear relation with pH (or amount of dissolved iron) that is discussed in the following.

Table 4.2: Overview on pH and molar Fe_d/Cl^- ratio (Fe_d = total amount of dissolved iron) of the nebulized artificial seawater (100 ml) + Fe_2O_3 (17 mg) suspensions, total initial reactivities of the injected hydrocarbons towards Cl and OH, initial active aerosol surface at the beginning of irradiation, resulting quasistationary Cl_{qs} and OH_{qs} concentrations during the first hour and the resulting total Cl production per cm^{-2} aerosol surface during the first hour

pH	Molar Fe_d/Cl^- ratio	Fe_d (mmol L^{-1}) ^c	Initial reactivity (s^{-1})		Initial A_{eff} ($10^{-3} \cdot \text{m}^2 \text{m}^{-3}$)	X_{qs} ($10^5 / 10^6$ atoms cm^{-3}) ^d		$Q_{\text{Cl,abs}}$ (10^{21} atoms $\text{cm}^{-2} \text{h}^{-1}$)
			Cl	OH		Cl	OH	
6	$<3 \times 10^{-5}$	$<0.001^e$	86	1.5	42.1	$<0.1^e$	10	$<1^e$
6 ^a	$<3 \times 10^{-5}$	$<0.001^e$	101	2.1	49	$<0.1^e$	3	$<1^e$
2.6	0.001	0.031	118	2.3	19.3	1.8	2.6	1.6–1.7
2.6 ^b	0.001	0.031	110	2.6	12.8	4.7	5.6	5.6–6.8
2.2	0.006	0.21	106	2.5	14.3	5.5	2.4	5.6–6.6
1.9	0.014	0.58	100	2.5	16.8	10	n.d. ^f	7.0–9.3

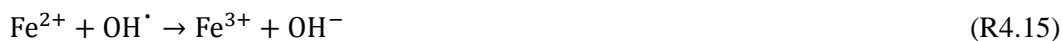
^aFive times frozen and thawed, ^bFiltrated, ^cafter 7 days of equilibration, ^dmean steady state concentrations during the 1st hour, ^ebelow the detection limit, ^fbelow the detection limit because of too high Cl concentration.

The fraction of active iron (λ_{Fe}) was calculated according to Wittmer et al. (2015b), resulting in 2010 % for pH 2.6, 1220 % for pH 2.2, and 620 % for pH 1.9. These high iron activities of more than 100 % indicate a multiple recycling process of the dissolved iron or even a further dissolution of Fe_2O_3 in the quasi-liquid layer of the aerosol. The contribution of additional Cl activation mechanisms due to zero air impurities (e.g. O_3 and NO_x) is supposed to be small when comparing the values to the relatively low λ_{Fe} of 50–150 % obtained in Wittmer et al. (2015b) for iron-doped artificial sea-salt aerosol exposed to O_3 and NO_x . Furthermore, the decrease of λ_{Fe} with lower pH demonstrates the non-linear relation of pH and Cl production (the ratio between produced Cl and Fe_d decreases with lowering the pH but should be constant in a linear relation). This is in contrast to the results in Wittmer et al. (2015b), where λ_{Fe} increases when decreasing the

pH from 4 to 2.2. The discussed samples in the present study are in the pH range from 1.5 to 3, where the fractions of the Fe^{III}-Cl complexes are stable. However, the fractions of Fe^{III}-hydroxy complexes (FeOH²⁺, Fe(OH)₂⁺) decrease significantly with increasing acidity (Wittmer et al. 2015b) and the photochemical formation of OH[•] radicals and H₂O₂ (R4.9), and thus the re-oxidation of Fe^{II} to Fe^{III} (R4.10), becomes inefficient (λ_{Fe} decreases).



Indeed the highly concentrated Cl⁻ anion scavenges OH[•] to form Cl₂^{•-} and potentially degassing Cl₂ (R4.11-R4.14), but inhibits the catalyzing effect of iron in case of low OH[•] concentrations (R4.9, R4.10, R.15, Kiwi et al. 2000; Machulek et al. 2006).



Moreover, Machulek et al. (2007) related the decreasing efficiency of the Fenton process from pH 3 to 1 to the reduction of Fe^{III} by H₂O₂ (R4.16) that depends on acidity, and to the dominant formation of the less reactive Cl₂^{•-} radical (and not OH[•]). The potential formation of oxoiron (IV) (FeO²⁺) at this pH range may also influence the OH[•] formation (Pignatello et al., 1999).



To investigate possible matrix and dissolution effects in the aerosol phase, a filtrated aliquot of the pH 2.6 sample was nebulized and irradiated in order to compare the results to the run including solid Fe₂O₃. The comparison led to a 3.5–4 times higher Cl production of the filtrated experiment ($5.6\text{--}6.8 \times 10^{21}$ Cl atoms cm⁻² h⁻¹). The strong increase may originate from the larger specific aerosol surface based on the smaller most abundant particle diameter for the filtrated sample (surface to volume ratio: 1.79×10^7 m⁻¹) compared to the unfiltrated sample (surface to volume ratio: 1.50×10^7 m⁻¹), as illustrated in Fig. 4.2. The higher surface to volume ratio may cause an enhanced availability of iron, indicated by the high λ_{Fe} of 7840 %.

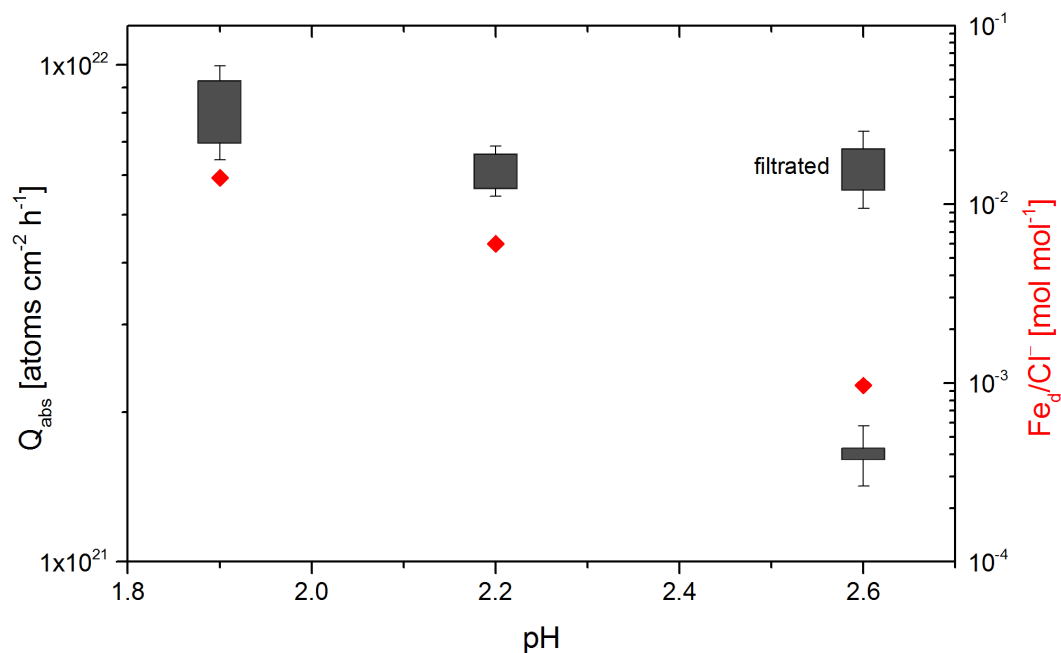


Fig. 4.4 Total amount of Cl atoms per hour and per cm² aerosol surface produced at various pHs (HCl additions) by the nebulized suspensions of Fe₂O₃ in artificial seawater (black bars, left ordinate) and the corresponding Fe_d/Cl⁻ ratios determined for the filtrated aliquots (red diamonds, right ordinate). In each experiment, the Fe₂O₃-artificial seawater suspension was nebulized except for the labeled experiment where a filtrated solution was applied. The lower and upper margins of the bars represent the minimal and maximal values. The error bars represent the respective negative minimum and the positive maximum uncertainty

4.3.2 Cl Production from HCl Uptake on Fe₂O₃

We explored the heterogeneous Cl production from Fe₂O₃ aerosol particles by the uptake of HCl in a series of experiments. It should be noted that the given HCl concentrations may contain an uncertainty of 50 % based on the adsorption on the FEP-Teflon walls (Zetzsch and Behnke 1993), but due to the same conditions for every experiment a relative comparison is still significant. An aerosol-free experiment resulted in a production of $(2.6\text{--}2.7) \times 10^{10}$ Cl atoms cm⁻³ h⁻¹ ($\sim 7.4 \times 10^6$ Cl atoms cm⁻³ s⁻¹) at a quasistationary OH concentration of $\sim 2 \times 10^6$ cm⁻³. The theoretical Cl production rate at 345 ppb HCl and 2×10^6 cm⁻³ OH is 1.28×10^7 cm⁻³ s⁻¹ ($k_{\text{HCl}+\text{OH}} = 7.6 \times 10^{-13}$ cm³ molecules⁻¹ s⁻¹ at 20°C, Atkinson et al. 2007) based on the homogeneous gas-phase reaction



Assuming that Cl is formed only homogeneously in this experiment implies a reproducibility (ρ) of 56–59 %, comparing the amount of HCl retrieved from the measured Cl production and the injected amount of HCl. The measured, lower value is probably caused by injection and adsorption losses of HCl (and thus lower gaseous HCl concentrations than calculated).

To distinguish the iron-induced, heterogeneous Cl formation from the fraction of Cl formed by the reaction of gaseous HCl with OH and by non-iron induced, heterogeneous Cl formation, several blank runs were conducted. The relevant OH concentrations in

these experiments originate from trace impurities of NO_x (Wittmer et al. 2015a) and from photolysis of HONO degassing from the Teflon film (background OH production rate in dry zero air $\sim 10^7$ molecules cm⁻³ s⁻¹, Bartolomei et al. 2015). As might be expected, the injection and irradiation of pure iron-oxide aerosol resulted in Cl concentrations below the detection limit, since no chlorine is present in the system to be activated. Further experiments included the injection and irradiation of 5 μL HCl (~ 345 ppb gas phase mixing ratio in the smog chamber) in the presence of non-catalytic, UV transparent SiO₂ aerosol particles (Aerosil 200) at 40–50% RH.

The addition of SiO₂ left the OH concentrations unaffected, but enhanced the formation of Cl atoms to $(1.1\text{--}1.2) \times 10^{11}$ Cl atoms cm⁻³ h⁻¹ (related to the aerosol surface: $2.6\text{--}2.7 \times 10^{21}$ Cl atoms cm⁻² h⁻¹) compared to the aerosol-free blank experiment. The approximately four times higher Cl production is caused by the increase hydrophilic surface available for heterogeneous reaction (according to the experience of Zetzsch and Behnke, 1993, with Aerosil 200 and Sicotrans orange in FEP-Teflon bags in comparison with blank runs).. Although, the additional aerosol surface of 0.018 m² m⁻³ is quite low compared to the wall surface (3.8 m² m⁻³), the surrounding aqueous layer of the aerosol (due to the nebulization of a suspension) absorbs gaseous HCl, enabling the dissociated Cl⁻ anions to be converted to gaseous Cl radicals by the known activation processes (e.g. Rossi 2003). Once highly soluble HOCl_(g) is formed via O₃ (from the NO_x impurities) and HO₂ (from the degradation of hydrocarbons), it rapidly leads to degassing of photolabile Cl₂ ($J_{\text{Cl}_2} = 1.55 \times 10^{-3}$ s⁻¹), particularly on an acidic surface containing Cl⁻ in the absence of Br⁻ (e.g. Vogt et al. 1996):



Moreover, the uptake of OH and subsequent reaction with Cl⁻_(aq) may also contribute to this process (Knipping et al. 2000). As already mentioned above, the heterogeneous Cl production from HCl was also reported by Zetzsch and Behnke (1993), who measured an eight times higher maximum Cl formation in the presence of SiO₂ aerosol particles as compared to the blank run.

When Fe₂O₃ aerosol particles and 5 μL HCl were added, the Cl production was significantly enhanced to $(2.6\text{--}3.0) \times 10^{11}$ Cl atoms cm⁻³ h⁻¹ (related to the aerosol surface: $5.7\text{--}6.6 \times 10^{22}$ Cl atoms cm⁻² h⁻¹) at a mean OH concentration of $\sim 5 \times 10^6$ cm⁻³. The higher quasistationary OH concentration in the Fe₂O₃ experiment at comparable hydrocarbon reactivities were caused by the slightly higher RH (~ 60 %), but also by an enhanced HC oxidation by Cl and subsequent HO₂ and OH formation. Zetzsch (1987) and Behnke and Zetzsch (1988) detected elevated OH concentrations, in the presence of Fe₂O₃ aerosol (containing Cl⁻, SO₄²⁻, and NO₃⁻) and O₃ as well. As indicated by the depletion of 28.9 ppb of hydrocarbons by the reaction with Cl during the first 150 min, the contribution of HCl formed by the depletion of hydrocarbons remains below 10 % (assuming no further reactivity of the reaction products). This also applies to the other experiments with varying HCl concentrations (Table 4.3).

The iron-free blank experiments represent a background value for the HCl conversion by OH and additional heterogeneous processes. To better compare the background formation with the iron induced Cl formation, the measured Cl production in the SiO₂ experiment is

subtracted by the result in the aerosol-free experiment and normalized by the aerosol surface to obtain a heterogeneous and homogeneous background production. Thus, a heterogeneous contribution of 3–3.5 % ($Q_{\text{bg,het}} = 2.0\text{--}2.1 \times 10^{21}$ Cl atoms $\text{cm}^{-2} \text{h}^{-1}$) and a homogeneous contribution of ~9–10 % ($Q_{\text{bg,hom}} = 2.6\text{--}2.7 \times 10^{10}$ Cl atoms $\text{cm}^{-3} \text{h}^{-1}$) to the iron-induced Cl production was estimated for the experiments applying 5 μL HCl (Fig. 4.5). The homogeneous contribution may rise with increasing OH concentrations at similar hydrocarbon reactivities and HCl concentrations. Assuming a proportional increase of $Q_{\text{bg,hom}}$ with increasing OH concentrations means a maximum effective homogeneous fraction of ~23–25 % of produced Cl in the Fe_2O_3 experiment (comparing the OH concentration of $2 \times 10^6 \text{ cm}^{-3}$ in the aerosol-free experiment with $5 \times 10^6 \text{ cm}^{-3}$ in the 5 μL HCl experiment). However, this number represents an upper limit of homogeneous contribution based on the assumption of a constant HCl concentration with time (justified by the “recycling” of HCl due to hydrocarbon degradation) without injection and adsorption losses.

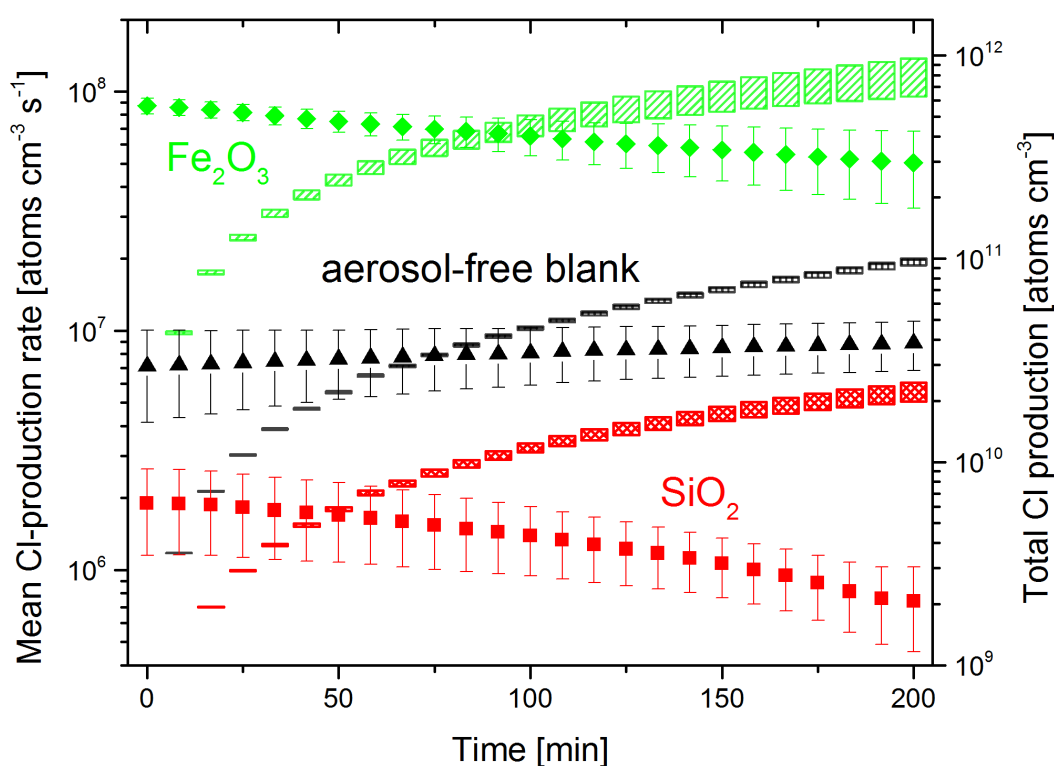


Fig. 4.5 Mean Cl production rate (symbols, left ordinate) and total Cl production (bars, right ordinate) of the Fe_2O_3 , SiO_2 and aerosol free experiments with 5 μL HCl injected, respectively. For a better comparison of the Fe_2O_3 and the heterogeneous Cl production evaluated in the SiO_2 experiments, the values for SiO_2 were corrected for the homogeneous production and normalized with the ratio of the surface areas ($A_{\text{SiO}_2}/A_{\text{Fe}_2\text{O}_3}$)

Table 4.3: Overview on the experiments with nebulized deionized water (200 ml) + Fe₂O₃ (0.5 g) or SiO₂ suspensions and varying HCl injections. Total initial reactivities of the injected hydrocarbons towards Cl and OH, initial active aerosol surface at the beginning of irradiation, relative humidity, resulting quasistationary Cl_{qs} and OH_{qs} concentrations during the first hour, the resulting absolute (Q_{abs}) and corrected (Q_{eff}) total Cl productions per cm⁻² aerosol surface during the first hour are listed

Injected HCl [μL] / HCl mixing ratio [ppb]	Initial reactivity (s ⁻¹)		Aerosol material	Initial A_{eff} (10 ⁻³ ·m ² m ⁻³)	RH [%]	X_{qs} concentration (10 ⁵ / 10 ⁶ radicals cm ⁻³) ^a		$Q_{\text{Cl,abs}}$ (10 ²¹ atoms cm ⁻² h ⁻¹)	$Q_{\text{Cl,eff}}$ (10 ²¹ atoms cm ⁻² h ⁻¹)
	Cl	OH				Cl	OH		
5 / 345	164	3.9	blank	0	40	0.5	2	n.d. ^c	n.d. ^c
5 / 345	135	3.1	SiO ₂	19	52	2.6	2	2.6–2.7	2.0–2.1
0 / 0	174	4.2	Fe ₂ O ₃	8.0	76	< 0.1 ^b	10	< 1 ^b	< 1 ^b
0.6 / 41	113	2.6	Fe ₂ O ₃	5.6	52	1.2	7.4	3.6–3.8	0.77–0.83
1.2 / 83	119	2.9	Fe ₂ O ₃	4.1	59	1.5	4.6	6.4–6.6	2.8–2.9
2.5 / 173	161	4.1	Fe ₂ O ₃	1.9	76	1.2	6.9	15–16	2.3–2.8
2.5 / 173	147	3.7	Fe ₂ O ₃	1.1	42	4.2	3.3	90–104	78–91
3.5 / 242	128	3.0	Fe ₂ O ₃	4.2	57	4.9	8.5	21–23	13–14
5 / 345	169	4.1	Fe ₂ O ₃	1.5	61	4.9	5	57–66	41–49

^amean steady state concentrations during the 1st hour, ^bbelow the detection limit, ^cnot evaluable since no aerosol phase present

In the following, the background Cl production is subtracted in order to calculate an effective Cl production Q_{eff} from the determined total production at time t :

$$Q_{\text{eff}}(t) = \frac{(Q_{\text{Cl}}(t) - \rho \times [\text{OH}] \times [\text{HCl}] \times k_{\text{HCl}+\text{OH}} \times t) \times V_{\text{Ch}}}{A_{\text{eff}}(t)} - Q_{\text{bg,het}}(t) \quad (4.4)$$

where $Q_{\text{Cl}}(t)$ is the integrated total Cl production (atoms cm^{-3}) at time t , $[\text{OH}]$ and $[\text{HCl}]$ are the quasistationary OH and HCl concentrations (assumed to be constant), V_{Ch} is the chamber volume, $A_{\text{eff}}(t)$ is the effective surface area (consisting of the measured aerosol surface and the wall contribution, see Wittmer et al. 2015b), and $Q_{\text{bg,het}}$ the integrated heterogeneous background production at time t . The calculation of Q_{eff} strengthens the comparison of the experiments with various amounts of injected HCl and spares respective blank experiments.

Fig. 4.6 illustrates Q_{eff} for various amounts of HCl injected at a RH of 52–61 %. The lower and upper margins of the bars represent the minimal and maximal values. The error bars represent the respective negative minimum and the positive maximum uncertainty (calculated based on statistical evaluation; Wittmer et al. 2015b). With increasing HCl concentrations an expected increase of Q_{eff} was observed from $\sim 0.8 \times 10^{21}$ Cl atoms $\text{cm}^{-2} \text{h}^{-1}$ (for 0.6 μL HCl) to $(41\text{--}49) \times 10^{21}$ Cl atoms $\text{cm}^{-2} \text{h}^{-1}$ (for 5 μL HCl). A not considered influence on the Q_{eff} determination is the wall loss of HCl (by water on the Teflon film or the dry Teflon film). Important hints that the RH affects the gaseous HCl concentration give the experiments with the same amount of HCl injected (2.5 μL) at different RH (42 % and 76 %). The low RH experiment resulted in a significantly higher Cl production ($78\text{--}91 \times 10^{21}$ Cl atoms $\text{cm}^{-2} \text{h}^{-1}$) compared to the high RH run ($2.3\text{--}2.8 \times 10^{21}$ Cl atoms $\text{cm}^{-2} \text{h}^{-1}$). Based on the measurements by Svensson et al. (1987) and the formula given by Wahner et al. (1998) the amount of water adsorbed on the Teflon film is $\sim 3.7 \text{ mg m}^{-2}$ at 42 % RH (low RH case), $\sim 6 \text{ mg m}^{-2}$ at 60 % RH, and $\sim 10 \text{ mg m}^{-2}$ at 75 % RH (high RH case). The exponential increase of adsorbed water with increasing RH may intensify the wall sink for HCl and thus explain the strong effect on the Cl production as observed in our experiments. When adsorbed on the “iron-free” Teflon film, HCl contributes to a negligible extent to the halogen activation. E.g. Buxmann et al. (2015) did not find a contribution of deposited HCl and HBr in a comparable system. The number of adsorbed layers on the aerosol particles may dilute the QLM and additionally retarding the activation, even if the layer thickness changes slowly at this RH range (Cwiertny et al. 2008).

In order to estimate the efficiency of the HCl to Cl conversion on the aerosol particles, the fraction of activated chlorine (φ_{Cl}) was calculated by dividing the total (molar) amount of produced Cl atoms Q_{Cl} (including the homogeneous background correction) by the total (molar) amount of injected HCl (HCl_{inj}):

$$\varphi_{\text{Cl}}(t) = \frac{Q_{\text{Cl}}(t) - \rho \times [\text{OH}] \times [\text{HCl}] \times k_{\text{HCl}+\text{OH}} \times t}{\text{HCl}_{\text{inj}}} \quad (4.5)$$

The resulting conversion rate during the first hour against the initial aerosol surface is shown in Fig. 4.7. No clear dependence of φ_{Cl} on the provided aerosol surface was

noticed. The various runs show a comparable HCl conversion in the range of 2-5 % except for the value obtained from the high RH experiment (ϕ_{Cl} below 1 %).

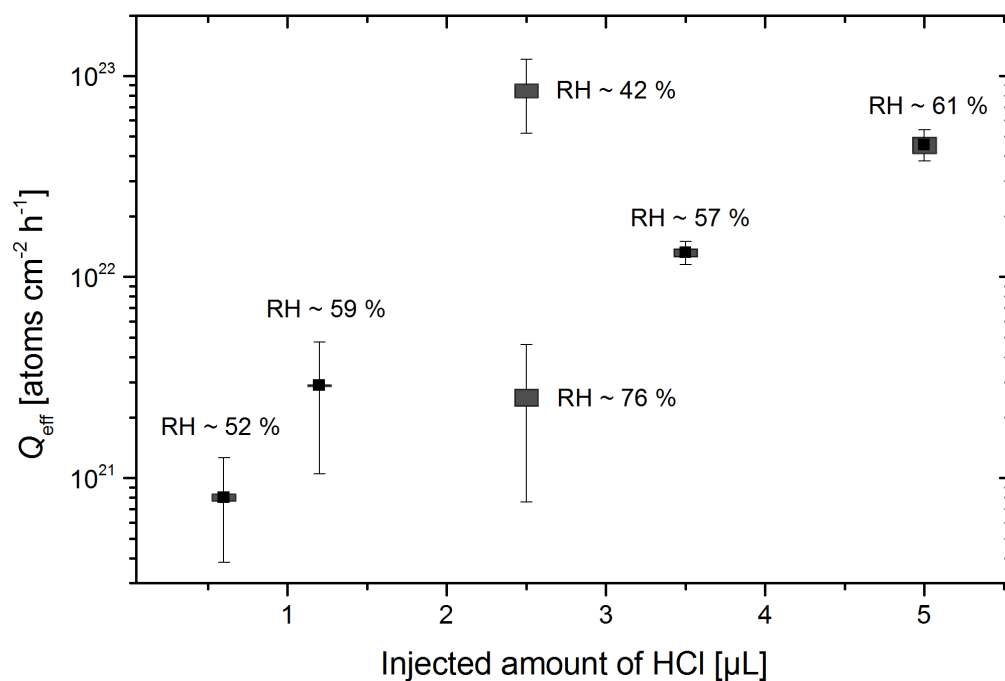


Fig. 4.6 Total amount of Cl atoms per hour and per cm^2 aerosol surface (corrected for the heterogeneous and homogeneous background) produced at various HCl concentrations. The RH is labeled for each experiment. The lower and upper margins of the bars represent the minimal and maximal values. The error bars represent the respective negative minimum and the positive maximum uncertainty

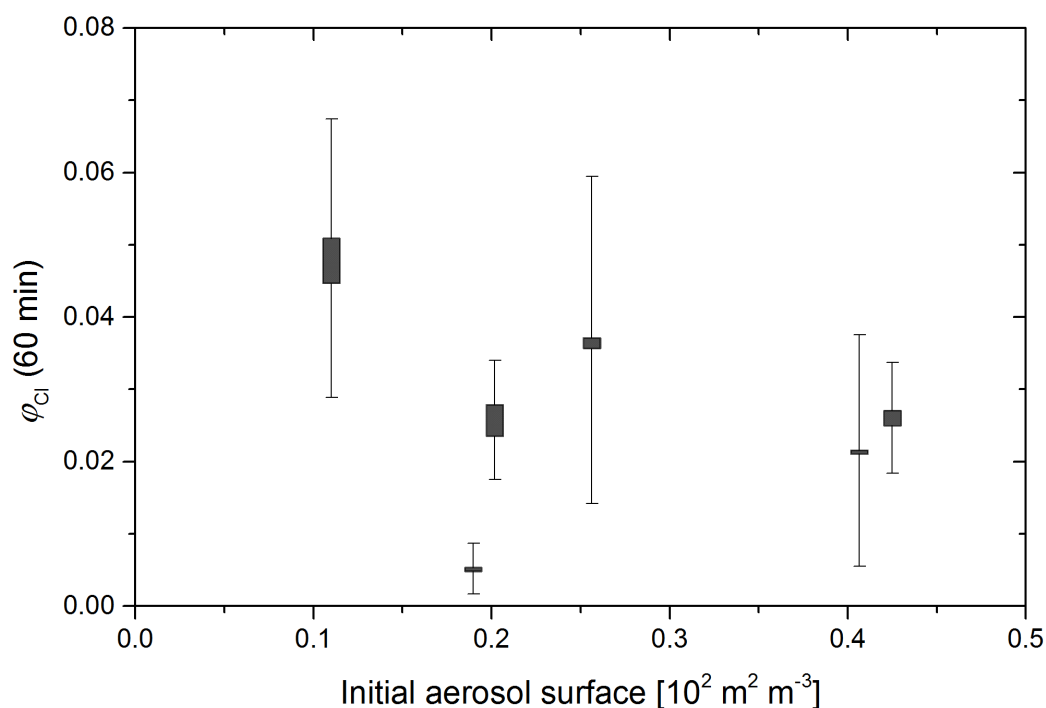


Fig. 4.7: Conversion rate ϕ_{Cl} of HCl to Cl within the first hour against the initial aerosol surface for the performed Fe_2O_3 experiments with various amounts of HCl added. The lower and upper

margins of the bars represent the minimal and maximal values. The error bars represent the respective negative minimum and the positive maximum uncertainty

4.4 Environmental Significance

Our results indicate that iron-containing aerosol can become photochemically active during atmospheric processing, especially in marine environments when it comes into contact with sea salt or HCl. The pH of aged sea-salt aerosol is typically in the acidic range from 2 to 4, e.g. depending on the air pollutants and the RH (Keene and Savoie 1998). At this pH, Fe₂O₃ is dissolved in significant amounts (see section 3.1), whereas the solubility of other natural iron oxides, such as FeOOH, can even be higher (Zhu et al. 1992). In particular, the iron-induced Cl production may become important concerning aerosol particles with a large fraction of (soluble) iron (e.g. combustion products, volcanic aerosol). For instance, a notable amount of iron-containing aerosol particles and HCl (and other acidic gases) are present in volcanic plumes (Delmelle et al. 2007) and a significant contribution to the observed Cl activation (Gliß et al. 2015) is thinkable.

The iron solubility (and thus the photochemical activity) is a complex function of surface area to volume ratio (Baker and Croot 2010), acid and cloud processing depending on the atmospheric residence time (Zhu et al. 1992; Zhuang et al. 1992; Shi et al. 2009) and the buffer ability. The latter is based on carbonate minerals (e.g. CaCO₃ and MgCO₃) and thus limits the dissolution of iron into the aqueous aerosol phase (Meskhidze 2005). Ito and Feng (2010) modelled that only a small fraction of iron dissolves in the coarse-mode dust particles (<0.2 %), whereas a significant fraction dissolves in the fine-mode dust particles (1–2%) above the North Pacific Ocean. In particular, the submicron particles can become very acidic by reaction with HCl or sulfuric acid (Sullivan et al. 2007a; Sullivan et al. 2007b), and laboratory studies support that the acid processing is the dominant mechanism for iron dissolution in mineral dust during transport (Shi et al. 2012). Potential sources of acidity are trace-gas pollutants (e.g. SO₂, HNO₃, N₂O₅ or HCl). On average, mineral dust particles contain ~3.5 % of iron (Duce and Tindale 1991). The HCl uptake on mineral dust is mainly ascribed to the reaction with CaCO_{3(s)} to form CaCl_{2(aq)} (Tobo et al. 2009). Therefore, HCl can play an important role in forming a deliquescent layer on the particle surface, as Ca-rich dust particles can be converted to aqueous droplets (Tobo et al. 2010). In our study, we found direct evidence that HCl is also taken up by Fe₂O₃ and thus may initiate a catalytic Cl activation cycle in natural environments. The activation may be strengthened in the morning hours after an HCl enrichment in the aerosol during the nighttime. A rough estimate of the uptake coefficient γ (according to Kolb et al. (2010)), based on the calculation of the first order rate constant of the heterogeneous HCl reaction from the measured Cl production rates, leads to a γ between 10⁻⁴ and 10⁻⁵, as compared to $\gamma = 0.14$ for HCl on CaCO₃ (Santschi and Rossi 2006).

In general, iron oxides originating from combustion contain a much higher fraction of soluble iron than natural mineral dust (Sedwick et al. 2007; Sholkovitz et al. 2012). Main reasons are the fine mode of the combustion aerosol particles, the missing buffer ability and the presence of acidic gases in combustion plumes. Recently, Wang et al. (2015) estimated a mean combustion source of 5.3 Tg yr⁻¹ total Fe from 1960–2007 with particle sizes of >10 μm (72 %), 1–10 μm (27 %) and <1 μm (1 %) but an increasing fraction of

particles $<1 \mu\text{m}$ since 2000. Fine-grained aerosol particles, produced by combustion, contain 77–81 % soluble iron (Schroth et al. 2009). As a consequence, combustion iron represents typically less than 5 % of total iron deposited over much open ocean regions but can reach fractions up to 20 % close to the continent (Luo et al. 2008). To interpret our results in a larger context, the explored mechanism could be integrated in halogen activation models for tropospheric aerosol particles and clouds (e.g. Herrmann et al. 2003; Tilgner et al. 2013).

4.5 Conclusions

This study demonstrates the gaseous, iron-catalyzed formation of Cl by uptake of HCl on pure iron-oxide aerosol and iron-oxide dispersed ion in sea-salt aerosol in dependence on the pH. When Fe_2O_3 (Sicotrans Orange, L2515D, BASF) was embedded in an untreated sea-salt matrix, neither a significant amount of dissolved iron nor a significant gaseous Cl production was observed. Adjusting the pH below 3 led to a detectable fraction of dissolved iron that causes significant gaseous Cl productions of $(1.6\text{--}1.7) \times 10^{21}$ Cl atoms $\text{cm}^{-2} \text{h}^{-1}$ (pH 2.6), $(5.6\text{--}6.6) \times 10^{21}$ Cl atoms $\text{cm}^{-2} \text{h}^{-1}$ (pH 2.2) and $(7.0\text{--}9.3) \times 10^{21}$ Cl atoms $\text{cm}^{-2} \text{h}^{-1}$ (pH 1.9). An alternative acceleration of the iron-oxide dissolution by the freezing process (without pH adjustment) could not be observed within the detection limits of our system.

Furthermore, we found evidence for the direct uptake of gaseous HCl on pure iron-oxide aerosol particles and a thereby induced iron-catalyzed production of Cl in the gas phase that can be distinguished significantly from the heterogeneous and homogeneous background production processes of Cl. The various amounts of injected HCl resulted in HCl to Cl conversion rates of 2–5 % at corrected total Cl productions (Q_{eff}) from $\sim 0.8 \times 10^{21}$ Cl atoms $\text{cm}^{-2} \text{h}^{-1}$ (at ~ 41 ppb HCl) to $(41\text{--}49) \times 10^{21}$ Cl atoms $\text{cm}^{-2} \text{h}^{-1}$ (at ~ 345 ppb HCl), whereas the conversion depends on RH and the subsequent uncertainty in the HCl concentrations due to the adsorption effects on the chamber wall and injection losses.

Our findings are of great interest for the processing of iron-containing aerosol in the atmosphere and particularly may become important for the increasing amount of highly soluble combustion aerosol particles in marine environments.

4.6 References

- Al-Abadleh, H. A. Review of the bulk and surface chemistry of iron in atmospherically relevant systems containing humic-like substances. *RSC Adv.* (2015). doi: 10.1039/C5RA03132J
- Atkinson, R., Baulch, D. L., Cox, R. A., Crowley, J. N., Hampson, R. F., Hynes, R. G., Jenkin, M. E., Rossi, M. J., Troe, J. Evaluated kinetic and photochemical data for atmospheric chemistry: Volume III – Gas phase reactions of inorganic halogens. *Atmos. Chem. Phys.* (2007). doi: 10.5194/acp-7-981-2007
- Baker, A. R., Croot, P. L. Atmospheric and marine controls on aerosol iron solubility in seawater. *Marine Chem.* (2010). doi: 10.1016/j.marchem.2008.09.003
- Baker, A. R., Jickells, T. D., Witt, M., Linge, K. L. Trends in the solubility of iron, aluminium, manganese and phosphorus in aerosol collected over the Atlantic Ocean. *Marine Chem.* (2006). doi: 10.1016/j.marchem.2005.06.004
- Balzer, N., Kinetische Untersuchungen der Halogen-Aktivierung einer simulierten Salzpflanze in einer Smogkammer, PhD thesis. University of Bayreuth, Germany (2012). <https://epub.uni-bayreuth.de/162/>
- Bartolomei, V., Gomez Alvarez, E., Wittmer, J., Tlili, S., Streckowski, R., Temime-Roussel, B., Quivet, E., Wortham, H., Zetzsch, C., Kleffmann, J., Gligorovski, S. Combustion processes as a source of high levels of indoor hydroxyl radicals through the photolysis of nitrous acid. *Environ. Sci. Technol.* (2015). doi: 10.1021/acs.est.5b01905
- Behnke, W., Holländer, W., Koch, W., Nolting, F., Zetzsch, C. A smog chamber for studies of the photochemical degradation of chemicals in the presence of aerosols. *Atmos. Environ.* (1988). doi: 10.1016/0004-6981(88)90341-1
- Behnke, W., Zetzsch, C. The generation of radicals on aerosol surfaces. *Air Poll. Res. Rep.* 17, 119–124 (1988)
- Behnke, W., Zetzsch, C. Heterogeneous production of Cl atoms under simulated tropospheric conditions in a smog chamber. In: Restelli G., Angeletti G. (eds.) *Physico-Chemical Behaviour of Atmospheric Pollutants.* pp 277–282. Springer, Dordrecht (1990)
- Bleicher, S., Buxmann, J. C., Sander, R., Riedel, T. P., Thornton, J. A., Platt, U., Zetzsch, C. The influence of nitrogen oxides on the activation of bromide and chloride in salt aerosol. *Atmos. Chem. Phys. Discuss.* (2014). doi: 10.5194/acpd-14-10135-2014
- Buxmann, J., Balzer, N., Bleicher, S., Platt, U., Zetzsch, C. Observations of bromine explosions in smog chamber experiments above a model salt pan. *Int. J. Chem. Kinet.* (2012). doi: 10.1002/kin.20714
- Buxmann, J., Bleicher, S., Platt, U., Glasow, R. von, Sommariva, R., Held, A., Zetzsch, C., Ofner, J. Consumption of reactive halogen species from sea-salt aerosol by secondary organic aerosol: Slowing down bromine explosion. *Environ. Chem.* (2015). doi: 10.1071/EN14226
- Byrne, R. H., Kester, D. R. Solubility of hydrous ferric oxide and iron speciation in seawater. *Marine Chem.* (1976). doi: 10.1016/0304-4203(76)90012-8

- Cwiertny, D. M., Young, M. A., Grassian, V. H. Chemistry and photochemistry of mineral dust aerosol. *Annu. Rev. Phys. Chem.* (2008). doi: 10.1146/annurev.physchem.59.032607.093630
- Delmelle, P., Lambert, M., Dufrêne, Y., Gerin, P., Óskarsson, N. Gas/aerosol–ash interaction in volcanic plumes: New insights from surface analyses of fine ash particles. *Earth Planet. Sci. Lett.* (2007). doi: 10.1016/j.epsl.2007.04.052
- Duce, R. A., Tindale, N. W. Atmospheric transport of iron and its deposition in the ocean. *Limnol. Oceanogr.* (1991). doi: 10.4319/lo.1991.36.8.1715
- Duggen, S., Croot, P., Schacht, U., Hoffmann, L. Subduction zone volcanic ash can fertilize the surface ocean and stimulate phytoplankton growth: Evidence from biogeochemical experiments and satellite data. *Geophys. Res. Lett.* (2007). doi: 10.1029/2006GL027522
- Erickson, D. J., Seuzaret, C., Keene, W. C., Gong, S. L. A general circulation model based calculation of HCl and ClNO₂ production from sea salt dechlorination: Reactive chlorine emissions inventory. *J. Geophys. Res.* (1999). doi: 10.1029/98JD01384
- Gliß, J., Bobrowski, N., Vogel, L., Pöhler, D., Platt, U. OCIO and BrO observations in the volcanic plume of Mt. Etna – implications on the chemistry of chlorine and bromine species in volcanic plumes. *Atmos. Chem. Phys.* (2015). doi: 10.5194/acp-15-5659-2015
- Graedel, T. E., Keene, W. C. The budget and cycle of earth's natural chlorine. *Pure Appl. Chem.* (1996). doi: 10.1351/pac199668091689
- Herrmann, H., Majdik, Z., Ervens, B., Weise, D. Halogen production from aqueous tropospheric particles. *Chemosphere* (2003). doi: 10.1016/S0045-6535(03)00202-9
- Ito, A., Feng, Y. Role of dust alkalinity in acid mobilization of iron. *Atmos. Chem. Phys.* (2010). doi: 10.5194/acp-10-9237-2010
- Jeong, D., Kim, K., Choi, W. Accelerated dissolution of iron oxides in ice. *Atmos. Chem. Phys.* (2012). doi: 10.5194/acp-12-11125-2012
- Jickells, T. D., Spokes, L. J. Atmospheric iron inputs to the oceans. *IUPAC series on analytical and physical chemistry of environmental systems* 7, 85–122 (2001)
- Keene, W. C., Khalil, M. Aslam K., Erickson, D. J., McCulloch, A., Graedel, T. E., Lobert, J. M., Aucott, M. L., Gong, S. L., Harper, D. B., Kleiman, G., Midgley, P., Moore, R. M., Seuzaret, C., Sturges, W. T., Benkovitz, C. M., Koropalov, V., Barrie, L. A., Li, Y. F. Composite global emissions of reactive chlorine from anthropogenic and natural sources: Reactive chlorine emissions inventory. *J. Geophys. Res.* (1999). doi: 10.1029/1998JD100084
- Keene, W. C., Sander, R., Pszenny, A. A., Vogt, R., Crutzen, P. J., Galloway, J. N. Aerosol pH in the marine boundary layer. *J. Aerosol Sci.* (1998). doi: 10.1016/S0021-8502(97)10011-8
- Keene, W. C., Savoie, D. L. The pH of deliquesced sea-salt aerosol in polluted marine air. *Geophys. Res. Lett.* (1998). doi: 10.1029/98GL01591
- Kester, D. R., Duedall, I. W., Connors, D. N., Pytkowicz, R. M. Preparation of artificial seawater. *Limnol. Oceanogr.* (1967). doi: 10.4319/lo.1967.12.1.0176

- Kiwi, J., Lopez, A., Nadtochenko, V. Mechanism and kinetics of the OH-radical intervention during Fenton oxidation in the presence of a significant amount of radical scavenger (Cl⁻). *Environ. Sci. Technol.* (2000). doi: 10.1021/es991406i
- Knipping, E. M., Lakin, M. J., Foster, K. L., Jungwirth, P., Tobias, D. J., Gerber, R. B., Dabdub, D., Finlayson-Pitts, B. J. Experiments and simulations of ion-enhanced interfacial chemistry on aqueous NaCl aerosols. *Science* (2000). doi: 10.1126/science.288.5464.301
- Kolb, C. E., Cox, R. A., Abbatt, J. P. D., Ammann, M., Davis, E. J., Donaldson, D. J., Garrett, B. C., George, C., Griffiths, P. T., Hanson, D. R., Kulmala, M., McFiggans, G., Pöschl, U., Riipinen, I., Rossi, M. J., Rudich, Y., Wagner, P. E., Winkler, P. M., Worsnop, D. R., O' Dowd, C. D. An overview of current issues in the uptake of atmospheric trace gases by aerosols and clouds. *Atmos. Chem. Phys.* (2010). doi: 10.5194/acp-10-10561-2010
- Kuma, K., Nishioka, J. U., Matsunaga, K. Controls on iron(III) hydroxide solubility in seawater: The influence of pH and natural organic chelators. *Limnol. Oceanogr.* (1996). doi: 10.4319/lo.1996.41.3.0396
- Lim, M., Chiang, K., Amal, R. Photochemical synthesis of chlorine gas from iron(III) and chloride solution. *J. Photochem. Photobiol., A* (2006). doi: 10.1016/j.jphotochem.2006.03.005
- Liu, X., Millero, F. J. The solubility of iron in seawater. *Marine Chem.* (2002). doi: 10.1016/S0304-4203(01)00074-3
- Luo, C., Mahowald, N., Bond, T., Chuang, P. Y., Artaxo, P., Siefert, R., Chen, Y., Schauer, J. Combustion iron distribution and deposition. *Global Biogeochem. Cycles* (2008). doi: 10.1029/2007GB002964
- Machulek, A., Vautier-Giongo, C., Moraes, José E F, Nascimento, Claudio A O, Quina, F. H. Laser flash photolysis study of the photocatalytic step of the photo-Fenton reaction in saline solution. *J. Photochem. Photobiol.* (2006). doi: 10.1562/2005-05-28-RA-548
- Machulek, A., Moraes, José E. F., Vautier-Giongo, C., Silverio, C. A., Friedrich, L. C., Nascimento, Cláudio A. O., Gonzalez, M. C., Quina, F. H. Abatement of the inhibitory effect of chloride anions on the photo-Fenton process. *Environ. Sci. Technol.* (2007). doi: 10.1021/es071884q
- Mahowald, N. M., Engelstaedter, S., Luo, C., Sealy, A., Artaxo, P., Benitez-Nelson, C., Bonnet, S., Chen, Y., Chuang, P. Y., Cohen, D. D., Dulac, F., Herut, B., Johansen, A. M., Kubilay, N., Losno, R., Maenhaut, W., Paytan, A., Prospero, J. M., Shank, L. M., Siefert, R. L. Atmospheric iron deposition: global distribution, variability, and human perturbations. *Ann. Rev. Mar. Sci.* (2009). doi: 10.1146/annurev.marine.010908.163727
- Meskhidze, N. Dust and pollution: A recipe for enhanced ocean fertilization? *J. Geophys. Res.* (2005). doi: 10.1029/2004JD005082
- Miller, W. L., King, D., Lin, J., Kester, D. R. Photochemical redox cycling of iron in coastal seawater. *Marine Chem.* (1995). doi: 10.1016/0304-4203(95)00027-O

- Nadtochenko, V. A., Kiwi, J. Photolysis of FeOH^{2+} and FeCl^{2+} in aqueous solution. Photodissociation kinetics and quantum yields. *Inorg. Chem.* (1998). doi: 10.1021/ic9804723
- Pignatello, J. J., Liu, D., Huston, P. Evidence for an additional oxidant in the photoassisted Fenton reaction. *Environ. Sci. Technol.* (1999). doi: 10.1021/es980969b
- Prescher, C., McCammon, C., Dubrovinsky, L. MossA: A program for analyzing energy-domain Mössbauer spectra from conventional and synchrotron sources. *J. Appl. Crystallogr. (J. Appl. Crystallogr.)* (2012). doi: 10.1107/S0021889812004979
- Rossi, M. J. Heterogeneous reactions on salts. *Chem. Rev.* 103, 4823–4882 (2003)
- Rubasinghege, G., Lentz, R. W., Scherer, M. M., Grassian, V. H. Simulated atmospheric processing of iron oxyhydroxide minerals at low pH: roles of particle size and acid anion in iron dissolution. *Proc. Natl. Acad. Sci. USA* (2010). doi: 10.1073/pnas.0910809107
- Santschi, C., Rossi, M. J. Uptake of CO_2 , SO_2 , HNO_3 and HCl on calcite (CaCO_3) at 300 K: mechanism and the role of adsorbed water. *J. Phys. Chem. A* (2006). doi: 10.1021/jp056312b
- Schroth, A. W., Crusius, J., Sholkovitz, E. R., Bostick, B. C. Iron solubility driven by speciation in dust sources to the ocean. *Nature Geosci.* (2009). doi: 10.1038/ngeo501
- Sedwick, P. N., Sholkovitz, E. R., Church, T. M. Impact of anthropogenic combustion emissions on the fractional solubility of aerosol iron: Evidence from the Sargasso Sea. *Geochem. Geophys. Geosyst.* (2007). doi: 10.1029/2007GC001586
- Shi, Z., Krom, M. D., Bonneville, S., Baker, A. R., Jickells, T. D., Benning, L. G. Formation of iron nanoparticles and increase in iron reactivity in mineral dust during simulated cloud processing. *Environ. Sci. Technol.* (2009). doi: 10.1021/es901294g
- Shi, Z., Krom, M. D., Jickells, T. D., Bonneville, S., Carslaw, K. S., Mihalopoulos, N., Baker, A. R., Benning, L. G. Impacts on iron solubility in the mineral dust by processes in the source region and the atmosphere: A review. *Aeolian Res.* (2012). doi: 10.1016/j.aeolia.2012.03.001
- Sholkovitz, E. R., Sedwick, P. N., Church, T. M., Baker, A. R., Powell, C. F. Fractional solubility of aerosol iron: Synthesis of a global-scale data set. *Geochim. Cosmochim. Ac.* (2012). doi: 10.1016/j.gca.2012.04.022
- Siefert, R. L., Johansen, A. M., Hoffmann, M. R., Pehkonen, S. O. Measurements of trace metal (Fe, Cu, Mn, Cr) oxidation states in fog and stratus clouds. *J. Air Waste Manag. Assoc.* (1998). doi: 10.1080/10473289.1998.10463659
- Sullivan, R. C., Guazzotti, S. A., Sodeman, D. A., Prather, K. A. Direct observations of the atmospheric processing of Asian mineral dust. *Atmos. Chem. Phys.* (2007a). doi: 10.5194/acp-7-1213-2007
- Sullivan, R. C., Guazzotti, S. A., Sodeman, D. A., Tang, Y., Carmichael, G. R., Prather, K. A. Mineral dust is a sink for chlorine in the marine boundary layer. *Atmos. Environ.* (2007b). doi: 10.1016/j.atmosenv.2007.05.047
- Supeno, Kruus, P. Sonochemical formation of nitrate and nitrite in water. *Ultrason. Sonochem.* (2000). doi: 10.1016/S1350-4177(99)00043-7

- Svensson, R., Ljungström, E., Lindqvist, O. Kinetics of the reaction between nitrogen dioxide and water vapour. *Atmos. Environ.* (1987). doi: 10.1016/0004-6981(87)90315-5
- Tilgner, A., Bräuer, P., Wolke, R., Herrmann, H. Modelling multiphase chemistry in deliquescent aerosols and clouds using CAPRAM3.0i. *J. Atmos. Chem.* (2013). doi: 10.1007/s10874-013-9267-4
- Tobo, Y., Zhang, D., Matsuki, A., Iwasaka, Y. Asian dust particles converted into aqueous droplets under remote marine atmospheric conditions. *Proc. Natl. Acad. Sci. USA* (2010). doi: 10.1073/pnas.1008235107
- Tobo, Y., Zhang, D., Nakata, N., Yamada, M., Ogata, H., Hara, K., Iwasaka, Y. Hygroscopic mineral dust particles as influenced by chlorine chemistry in the marine atmosphere. *Geophys. Res. Lett.* (2009). doi: 10.1029/2008GL036883
- Vogt, R., Crutzen, P. J., Sander, R. A mechanism for halogen release from sea-salt aerosol in the remote marine boundary layer. *Nature* (1996). doi: 10.1038/383327a0
- Wahner, A., Mentel, T. F., Sohn, M. Gas-phase reaction of N₂O₅ with water vapor: Importance of heterogeneous hydrolysis of N₂O₅ and surface desorption of HNO₃ in a large Teflon chamber. *Geophys. Res. Lett.* (1998). doi: 10.1029/98GL51596
- Wang, R., Balkanski, Y., Boucher, O., Bopp, L., Chappell, A., Ciais, P., Hauglustaine, D., Peñuelas, J., Tao, S. Sources, transport and deposition of iron in the global atmosphere. *Atmos. Chem. Phys.* (2015). doi: 10.5194/acp-15-6247-2015
- Wang, W.-N., Purwanto, A., Lenggoro, I. W., Okuyama, K., Chang, H., Jang, H. D. Investigation on the Correlations between Droplet and Particle Size Distribution in Ultrasonic Spray Pyrolysis. *Ind. Eng. Chem. Res.* (2008). doi: 10.1021/ie070821d
- Wittmer, J., Bleicher, S., Zetzsch, C. Iron(III)-induced activation of chloride and bromide from modeled salt pans. *J. Phys. Chem. A* (2015a). doi: 10.1021/jp508006s
- Wittmer, J., Bleicher, S., Ofner, J., Zetzsch, C. Iron(III)-induced activation of chloride from artificial sea salt aerosol. *Environ. Chem.* (2015b). doi: 10.1071/EN14279
- Zetzsch, C. Simulation of atmospheric photochemistry in the presence of solid airborne aerosols. In: *Dechema-Monographien*, vol 104. pp 187–213. Verlag Chemie, Weinheim, Germany (1987)
- Zetzsch, C., Behnke, W. Heterogeneous reactions of chlorine compounds. In: Niki H., Becker K.H. (eds.) *The Tropospheric Chemistry of Ozone in the Polar Regions*. pp 291–306. Springer, Berlin Heidelberg (1993)
- Zhang, D., Iwasaka, Y. Chlorine deposition on dust particles in marine atmosphere. *Geophys. Res. Lett.* (2001). doi: 10.1029/2001GL013333
- Zhu, X., Prospero, J. M., Millero, F. J., Savoie, D. L., Brass, G. W. The solubility of ferric ion in marine mineral aerosol solutions at ambient relative humidities. *Marine Chem.* (1992). doi: 10.1016/0304-4203(92)90069-M
- Zhu, X., Prospero, J. M., Savoie, D. L., Millero, F. J., Zika, R. G., Saltzman, E. S. Photoreduction of iron(III) in marine mineral aerosol solutions. *J. Geophys. Res.* (1993). doi: 10.1029/93JD00202
- Zhuang, G., Yi, Z., Duce, R. A., Brown, P. R. Chemistry of iron in marine aerosols. *Global Biogeochem. Cycles* (1992). doi: 10.1029/92GB00756

Acknowledgements

I am very grateful to my supervisor Prof. Dr. Cornelius Zetzsch for providing me the opportunity to realize my PhD at the Atmospheric Chemistry Research Unit, for his support and advice at any time, for the many constructive discussions and ideas and for the freedom to implement own creativity.

Special thanks go to Dr. Sergej Bleicher and Dr. Stefan Gonser (Nino) for giving me support, advice and motivation and by the way becoming close friends.

I am grateful to all critical proof readers who tortured themselves through this manuscript and the included publications. Thanks to Sergej, Nino, Johannes, Peter, Tobi and Sarmite.

I would like to thank all my former and current colleagues at the BayCEER for the pleasant time with a lot of scientific and private discussions, support and a nice working atmosphere.: Katharina Kamilli, Dr. Sarmite Katkevica, Lukas Fasbender, Prof. Dr. Andreas Held, Agnes Bednorz, Andrej Einhorn, Dr. Johannes Ofner, Paulo Alarcon, Dr. Matthias Sörgel, Dr. Lei Han, the Central Analytic team, Sebastian Schmitt, Kerstin Hofmann, Alex Guhr, Valeska Scharsich, Anne Genslein, Mirella Glor, Gerhard Kürfner, Gerhard Müller, Uwe Hell and everyone else that crossed my way.

I would also like to thank my external colleagues Franz D. Oeste, Stefan Schmitt, Dr. Nicole Bobrowski, Dr. Joelle Buxmann, Prof. Dr. Ulrich Platt, Dr. Marcello Liotta, Dr. Rolf Sander, Tobias Sattler, Dr. Enno Bahlmann, Prof. Dr. Heinfried Schöler, Dr. Markus Greule, Prof. Dr. Frank Keppler, Dr. Vincent Bartolomei, Dr. Brice Temime-Roussel, Dr. Elena Gomez Alvarez, Dr. Rafael Strekowski, Dr. Saso Gligorovski, Dr. Eoin Wilson, Dr. Dean Venables, Dr. Catherine McCammon, Johannes Thiessen for the constructive cooperations and advices during my time in Bayreuth.

This work was supported by the Deutsche Forschungs Gemeinschaft (DFG) within research unit 763 (HALOPROC) grant ZE792/5-2 and by Ries Consulting GmbH&Co Betriebs KG, Hosenfeld.

For the great time in Bayreuth during my rare free time I am extremely grateful to Sergej, Nino, Kathi, Lukas and the Ironmen, everyone I got to know and all guys who visited me from far home. In particular, I want to thank the glorious BTS tennis team including Heiko, Benni, Thorsten, Micha, Christopher, Basti, Jörg, Markus, Fabian, Andi and Werner for the awesome time crowned with a double championship!

Last but not least I would like to thank my friends and my family, especially my parents, brother, sister-in-law and nephew for supporting me during my whole life. Finally, I am deeply grateful to Ramona for her support, patience, flexibility and love.

(Eidesstattliche) Versicherungen und Erklärungen

(§ 5 Nr. 4 PromO)

Hiermit erkläre ich, dass keine Tatsachen vorliegen, die mich nach den gesetzlichen Bestimmungen über die Führung akademischer Grade zur Führung eines Doktorgrades unwürdig erscheinen lassen.

(§ 8 S. 2 Nr. 5 PromO)

Hiermit erkläre ich mich damit einverstanden, dass die elektronische Fassung meiner Dissertation unter Wahrung meiner Urheberrechte und des Datenschutzes einer gesonderten Überprüfung hinsichtlich der eigenständigen Anfertigung der Dissertation unterzogen werden kann.

(§ 8 S. 2 Nr. 7 PromO)

Hiermit erkläre ich eidesstattlich, dass ich die Dissertation selbständig verfasst und keine anderen als die von mir angegebenen Quellen und Hilfsmittel benutzt habe.

(§ 8 S. 2 Nr. 8 PromO)

Ich habe die Dissertation nicht bereits zur Erlangung eines akademischen Grades anderweitig eingereicht und habe auch nicht bereits diese oder eine gleichartige Doktorprüfung endgültig nicht bestanden.

(§ 8 S. 2 Nr. 9 PromO)

Hiermit erkläre ich, dass ich keine Hilfe von gewerblichen Promotionsberatern bzw. -vermittlern in Anspruch genommen habe und auch künftig nicht nehmen werde.

Bayreuth, den 2016-05-08

.....

Julian Daniel Wittmer